DISSERTATION

# DEVELOPMENT OF ELECTROCHEMICAL ASSAYS AND BIOSENSORS FOR DETECTION OF ZIKA VIRUS

Submitted by

Jessica Filer

Graduate Degree Program in Cell and Molecular Biology

In partial fulfillment of the requirements

For the Degree of Doctor of Philosophy

Colorado State University

Fort Collins, Colorado

Spring 2019

Doctoral Committee:

Advisor: Brian Geiss
Co-Advisor: Tom Chen

Charles Henry
Jeff Wilusz
Greg Ebel

# ABSTRACT

## DEVELOPMENT OF ELECTROCHEMICAL ASSAYS AND BIOSENSORS FOR DETECTION OF ZIKA VIRUS

Zika virus (ZIKV) emerged as a significant public health concern after the 2015-2016 outbreak in South and Central America. Severe neurological complications and birth defects in adults and children respectively underscore the need for quick and accurate diagnosis so that proper medical observation and intervention can be done. Electrochemical assays and biosensors are attractive as alternative diagnostic tools due to their sensitivity and ease of miniaturization. This dissertation describes three novel electrochemical assays and biosensors to detect ZIKV specific nucleic acid, antibodies, and virus particles.

A nuclease protection ELISA (NP-ELISA) was developed for nucleic acid detection by enzymatic readout. The assay was validated using synthetic complementary oligos for absorbance, chemiluminescence, and electrochemical enzymatic readout. Two horseradish peroxidase substrates, 3,3',5,5'-Tetramethylbenzidine (TMB) and hydroquinone, were characterized electrochemically and compared for electrochemical assay use. Electrochemical TMB readout demonstrated better sensitivity compared to all tested detection modalities with a limit of detection of $3.72\times10^{3}$ molecules $mL^{-1}$, which compares well to the amount of ZIKV RNA in clinical samples and to other approved assays like the CDC's Trioplex assay.

For serological analysis, a capacitive microwire biosensor was developed and validated using immunized mouse sera to detect a ZIKV antibody response. Measurements were taken through a wide serial dilution range of $1:10^{18}$ to $1:10^{3}$ and two dilutions ($1:10^{12}$ and $1:10^{6}$) were used for analysis for optimal sensitivity. A statistically significant immune response was

detected four days after immunization at a $1{:}10^{12}$ dilution and was specific for ZIKV when compared with Chikungunya virus (CHIKV). These results indicate that serological analysis can be performed four days earlier with the wire sensor compared to ELISAs using ultra-dilute samples. The sensor also was used to differentiate between IgG and IgM antibodies and compared well with ELISA results.

Lastly, an impedance array sensor was designed and validated for detection of ZIKV particles. The array allows for simultaneous handling of many electrodes, which increases throughput compared to other biosensor designs. The sensor demonstrated good sensitivity with an LOD of 22.4 focus forming units (FFU) which compares well to other reported sensors. In addition, it was optimized for specificity and tested using Sindbis virus (SINV) as a negative control. These novel platforms comprise new advancements in biosensor technology by simplifying existing assays, increasing sensitivity, and providing a new platform for handheld measurements.

# ACKNOWLEDGEMENTS

The pursuit of scientific and technological advancement is a community effort and I have a large network of mentors, colleagues, family, and friends who have played crucial roles in the completion of this dissertation research. First and foremost, I want to thank my advisor, Brian Geiss, for his patient instruction and constant encouragement. He has taught me not only technical knowledge, but also how to think critically, analytically, and scientifically. Looking back on my years as a graduate student, I am thankful for this wonderful opportunity he has given me that has allowed me to grow not only in knowledge, but also in character. The most important lessons I learned during this time were not details about viruses or lab techniques or even related to science at all. They were lessons in resilience, perseverance, relationships, motivation, self-awareness, humility, and grace. I am a better person today for having Brian as my mentor. And I cannot thank him enough. I also want to thank my committee members Tom Chen, Chuck Henry, Jeff Wilusz, and Greg Ebel who have coached me in my scientific and professional development. They have pushed me out of my comfort zone and highlighted weaknesses and areas for improvement. Under their guidance, I have been able to improve on many skills and knowledge sets including communication, data analysis, and virology.

In addition to my faculty mentors, I want to thank my peer and post-doc mentors who I have grown to value not only as colleagues, but as friends. Members of the Geiss Lab have supported me throughout the years, sat through multiple iterations of my defense presentation, and gave constructive feedback to improve. Kristen Bullard-Feibelman in particular always made time to answer all of my questions and helped me to become self-sufficient at virus work and protein purification. Rob Channon worked individually with me for two years explaining electrochemistry and voltammetry analysis so that I could understand it and run experiments on

my own. It was an honor to collaborate with Lei Wang on her wire sensor project and I picked up many concepts and tricks from her during our time as lab partners that advanced my understanding of biosensor development. The wire sensor development, statistical analysis, figure generation was done by Lei and we collaborated together to compose the manuscript which has been partially incorporated into this dissertation. And Lang Yang has been my lab partner and friend all these years, patiently tutoring me in advanced mathematics, circuit analysis, electronics, and engineering. Lang not only did most of the photolithography for electrode array fabrication and Matlab processing to calculate charge transfer resistance from our impedance data, but he also spent many long evenings with me, helping and teaching me to troubleshoot electronic and engineering problems. If I can call myself an interdisciplinary scientist, it is because I have stood on the shoulders of these excellent scientists and engineers.

I am also fortunate to have a large support network of family members who have carried me through this degree. My in-laws, Bob, Sherrie, and Alec Filer have helped, supported, and believed in me. And it is impossible to count the number of phone calls I made to my parents, Archie and Karen Cole, and my brother, Denny. They all have celebrated even the smallest victories and lamented every failed experiment with me. But the greatest recognition goes to my husband, Alan, without whom I could not have completed this degree. He spent countless nights listening to my doubts, frustrations, and insecurities and no matter how many times I begged to give up, Alan would gently remind me that I should not quit and helped me to find purpose in my work. He cooked meals for me, helped me practice for presentation after presentation, proofread papers and emails, recommended experiments to try, and even joined me on occasion in lab to keep me company on weekends or late nights. Most of all, Alan has never wavered in his confidence of my capability. On those nights when I hated research and thought I'd never measure up as a scientist, he believed that I could. That I wasn't a failure. I was learning. I am

grateful for his steady presence and influence in my life, helping me grow emotionally, intellectually, and spiritually. My dearest love, thank you.

Lastly, I have been blessed by God with great educational opportunities in life and it is thus my responsibility to share these blessings with others. I will strive every day to use the skills and knowledge I have cultivated through graduate school to make the world a better place.

TABLE OF CONTENTS

ABSTRACT ..... ii

ACKNOWLEDGEMENTS ..... iv

Chapter 1 – Literature Review ..... 1

Introduction ..... 1

Virion Structure and Neutralization ..... 2

RNA Genome Structure ..... 3

Flavivirus Replication Cycle ..... 5

Attachment and Entry ..... 5

Fusion ..... 8

Translation ..... 8

Replication ..... 9

Assembly and Maturation ..... 10

History and Emergence of Zika Virus as a Human Pathogen ..... 11

Zika Virus Clinical Appearance and Pathogenesis ..... 16

Neurological Complications in Adults ..... 16

Congenital ZIKV Syndrome ..... 18

Antibody Dependent Enhancement of Flavivirus Infection ..... 19

Diagnosis of Zika Virus ..... 20

Chapter 2 – Electrochemical Biosensors and Assays: An Introduction for Biologists ..... 25

Purpose ..... 25

Basic Sensor Concepts ..... 25
Electrochemical Principles ..... 26
Common Electrochemical Techniques ..... 29
Voltammetry ..... 29
Electrochemical Impedance Spectroscopy ..... 31
Field Effect Transistor Biosensors ..... 35
Surface Functionalization and Chemistry ..... 35
Adsorption of Biorecognition Probe ..... 36
Covalent Coupling ..... 39
Affinity-based Immobilization ..... 40
Blocking ..... 40
History of Electrochemical Biosensor Research ..... 42
Nanotechnology in Biosensor Development ..... 45
Noble Metal Nanoparticles ..... 46
Conclusion ..... 48

Chapter 3 – A Nuclease Protection ELISA Assay for Colorimetric and Electrochemical Detection of Nucleic Acid ..... 57
Introduction ..... 57
Materials and Methods ..... 59
Materials ..... 59
Hybridization and Digestion ..... 60
Absorbance Detection ..... 60
Chemiluminescence Detection ..... 61
Electrochemical Detection ..... 61

Results and Discussion ..... 62

Optimization of Nuclease Protection ..... 62

NP-ELISA Specificity ..... 63

Increasing NP-ELISA Sensitivity Through Chemiluminescent Detection ..... 64

Electrochemical Characterization of Hydroquinone/Benzoquinone and 3,3',5,5'-Tetramethylbenzidine ..... 65

Increasing NP-ELISA Sensitivity Through Electrochemical Detection ..... 68

Sensitivity of Electrochemical Detection ..... 69

Conclusion ..... 70

Chapter 4 – An Ultrasensitive Capacitive Microwire Sensor for Pathogen-Specific Antibody Responses ..... 78

Introduction ..... 78

Materials and Methods ..... 80

Study Design ..... 80

Materials ..... 80

Surface Functionalization of the Working Electrode ..... 81

Fabrication of the Microwire Chip ..... 82

Capacitance Readout ..... 83

Mouse Serum Analysis ..... 83

ELISA Analysis of anti-Zika IgM and IgG Levels in Mouse Sera ..... 83

Results and Discussion ..... 84

Sensor Design and Working Principles ..... 84

Detection of anti-ZIKV Antibodies During an Immunization Time Course ..... 85

Specificity Tests with Mouse Sera ..... 88

Isotyping of Antibodies in Mouse Serum Samples ..... 89

Conclusion ..... 90

Chapter 5 – Design and Optimization of Electrode Surface Chemistry for a Novel Electrode Array Sensor ..... 96

Introduction ..... 96

Materials and Methods ..... 97

Materials ..... 97

Electrode Fabrication ..... 98

PDMS Fabrication ..... 99

Surface Functionalization of the Electrodes ..... 99

Electrochemical Measurements ..... 100

ELISA Characterization ..... 100

4G2 Production and Purification ..... 100

Virus Production and Quantitation ..... 101

Results and Discussion ..... 102

Sensor Principles ..... 102

Sensor Characterization ..... 103

Sensor Optimization and Specificity ..... 104

Concentration Dependent Sensing of ZIKV ..... 106

Conclusion ..... 107

Chapter 6 – Conclusion ..... 116

Summary ..... 116

Future Directions ..... 117

References ..... 120

Appendix A – Characterization of Engineered β-galactosidase Enzyme for Protein Fragment Complementation ..... 188

Introduction ..... 188

Materials and Methods ..... 189

Materials ..... 189

Site Directed Mutagenesis ..... 190

Protein Purification and Characterization ..... 191

Results and Discussion ..... 192

Conclusion ..... 196

# CHAPTER 1 - LITERATURE REVIEW

## Introduction

Flaviviruses are positive-sense RNA viruses with a ~50 nm enveloped particle and a ~11 kb genome. The flavivirus genus is composed of 71 antigenically related viruses and includes clinically relevant viruses such as yellow fever virus (YFV), West Nile virus (WNV), dengue virus (DENV), Japanese encephalitis virus (JEV), tick borne encephalitis Virus (TBEV), and Zika virus (ZIKV). The name flavivirus is derived from the latin word, flavus, for yellow and is a reference to the genus type species, YFV. Although they were originally classified under the Togaviridae family in 1974, flaviviruses were determined to be sufficiently different from other Togaviridae members (e.g. alphaviruses) such that they were classified under a separate family, Flaviviridae, in 1984 (1). Because most flaviviruses are arthropod-borne viruses (arboviruses), areas of active transmission are based on the geographical distribution of their respective vectors and animal reservoirs (2). Within the genus, the flaviviruses are classified into clusters based on their vector (mosquito, tick, or no known vector) (3). They are additionally classified into serocomplexes based on cross-neutralization of the viruses with polyclonal sera (4) with cross-neutralization between serocomplexes being possible (5), but rare (4). ZIKV, the primary focus of this review, is a member of the Spondweni Virus (SPOV) serocomplex which contains only ZIKV and SPOV, its closest relative (6). However, a super serogroup containing at least DENV and ZIKV was recently classified using antibodies against a previously unknown quaternary epitope (7). Three genetic lineages of ZIKV have been identified: East African, West African, and Asian (8).

ZIKV is typically transmitted by a bite from *Aedes Aegypti* or *Aedes Albopictus* mosquitos, though vertical transmission from mother to fetus may also occur. It is unique among

arboviruses in that it can also be transmitted sexually. The virus typically causes a mild, self-limiting, febrile illness and may include symptoms of rash, conjunctivitis, arthralgia, retro-orbital pain, myalgia, and headache (9–11). Vomiting and diarrhea have been reported but are less common (12–14).

## Virion Structure and Neutralization

Like other flaviviruses, the mature ZIKV particle is 50 nm in diameter with a nucleocapsid core, lipid membrane envelope, and protein shell composed of E and M proteins (15). The E protein forms 90 antiparallel dimers that lay flat against the surface and cover the M protein. Three sets of dimers are arranged into 30 "rafts" that form a herringbone-like array.

The E protein monomer consists of three structural ectodomains, two stem helices, and two transmembrane helices. Ectodomain I (DI) sits in the middle of the monomer and connects ectodomain II (DII) and ectodomain III (DIII) with flexible hinges. It acts like a bridge to help to stabilize the structure of the E protein and also carries the protein's glycosylation site, Asn154 (15). Some earlier African strains of ZIKV, however, have a mutation at this residue that precludes glycosylation. Comparison with other strains from this time period suggests that this mutation may be a result of passaging the virus in a laboratory environment (16).

DI is connected to DII by four polypeptide chains. DII is an elongated, finger-like domain that is involved in hydrophobic dimerization of the two monomers (17). It also contains the hydrophobic fusion loop that inserts into the endosomal membrane during fusion (18). In the homodimer conformation, the fusion loop of one monomer is hidden by DI and DII of the second monomer (19). Structural rearrangements in the acidic endosome expose the fusion loop and allow it to insert into the membrane. DIII is connected to the other end of DI by a single polypeptide linker. It is an immunoglobulin-like domain at the C-terminus of the protein that extends out slightly from the smooth surface of the mature particle (20). Its immunoglobulin-

like structure as well as mutagenesis studies have revealed that DIII is involved in attachment and interactions with cell receptors for entry (20). DIII is connected to two C-terminal stem anchor domains that anchor the ectodomain to the viral membrane by interactions with two co-linear transmembrane domains. These transmembrane domains do not extend past the membrane, nor do they interact with the nucleocapsid (NC) (21).

The human humoral response against ZIKV and other flaviviruses is dominated by broadly flavivirus-reactive antibodies against the E protein (22–26), though antibodies may also be elicited against the prM/M (23), C (27), and NS1 (28) proteins. The flavivirus E protein has numerous type-specific and cross-reactive epitopes that are classified into four groups by the potency of neutralization and the degree of cross-reactivity: fusion loop epitopes, envelope dimer epitopes, DIII epitopes, and quaternary epitopes (reviewed in (29, 30)). Antibodies against fusion loop epitopes make up the largest proportion of anti-E protein antibodies (31, 32). These cross-reactive epitopes are poorly neutralizing and are implicated in antibody dependent enhancement (ADE) of flavivirus infection (33, 34). Envelope dimer epitopes represent another class of cross-reactive epitopes that are comprised of residues across both dimer subunits. Epitopes along the lateral ridge of DIII are type-specific and potently neutralizing. While these epitopes are immunodominant in mice, they make up only a small proportion of the human antibody response. Quaternary epitopes are also type-specific and are comprised of residues across different dimers in the virion structure. Antibodies against these epitopes only recognize E protein in the context of the virion structure and do not recognize soluble recombinant E protein.

## RNA Genome Structure

The flavivirus genome is a single stranded, positive sense RNA with a singular open reading frame (ORF) and a type I 5’ cap. At either end of the ORF lie the 5’ and 3’ untranslated

regions (UTRs). Both UTRs have significant conserved secondary structure that functions to cyclize the genome into a panhandle shape and is also essential for replication and host evasion.

The 5' UTR of the ZIKV genome is about 107 nucleotides in length (35). Although the sequence may vary between species, the secondary structure is highly conserved (36). It consists of two stem loop structures, that are separated by poly(U) sequences. Stem loop A (SLA) is a Y-shaped structure that is ~70 nucleotides in length. It contains the promoter region that directly interacts with the NS5 polymerase to initiate synthesis of the negative sense template at the 3' end (37, 38). The presence of SLA is required for cap formation and removal of this region completely kills viral replication (39). Stem loop B (SLB) is somewhat shorter than SLA at 30 nucleotides in length and terminates at the AUG start codon. This stem loop contains the 5' upstream AUG region (UAR) that is one of three flavivirus cyclization elements. These elements facilitate long-range interactions between the 5' and 3' UTRs that are essential for cyclization and replication of the genome (40). Just downstream of the 5' UTR is the second cyclization element termed the 5' conserved sequence (CS) (35, 41). It lies within the capsid gene and, together with the UAR sequence, the 5' CS hybridizes with its complementary 3' CS to cyclize the genome and form a panhandle shape.

The 3' UTR varies by species from 400-600 nucleotides in length and comprises of three domains. Domain I lies immediately after the stop codon of the ORF. It consists of two stem loop structures termed stem loop (SL) 1 and 2 (or alternatively known as xrRNA1 and xrRNA2) (36). The tops of SL1 and 2 interact with motifs just downstream of the respective loop to form pseudoknots (PK1 and PK2) that are resistant to degradation by host exonuclease XRN1 (35, 42). As the enzyme moves down the strand to degrade it, it stalls as it hits SL1 (42, 43). This stalling process inactivates the enzyme and causes it to fall off the RNA. In doing so, flaviviruses reduce XRN1 exonuclease activity which subsequently reduces degradation of viral

RNA. The remaining intact RNA, about 0.5kb, is known as subgenomic flavivirus RNA (sfRNA). In addition to dysregulating the mRNA decay pathway by inhibiting XRN1, sfRNA acts as an immune antagonist (discussed below) (42).

Domain II of the 3' UTR consists of the dumbbell structures (DB) 1 and 2. In some species of flaviviruses DB1 and DB2 contain the repeated conserved sequence 2 (RCS2) (DENV, JEV) and conserved sequence 2 (CS2) (DENV, WNV, JEV) respectively (36). The dumbbell structures also interact with downstream sequences to form PK3 and PK4. Although the mechanism is not yet clear, DB1 and DB2 have been shown to be essential for replication and translation (44). Domain III is the most conserved structured region of the 3' UTR and contains the CS1 sequence immediately upstream of a short hairpin (sHP) structure. It also contains the 3' stem loop (3'SL) wherein lies the 3'CS and 3'UAR sequences that are involved in cyclization. The 3'SL is essential for viral replication and deleting the region completely abolishes replication (45).

## Flavivirus Replication Cycle

As mentioned previously, the flavivirus genome consists of a 5' cap, the 5' and 3' UTR, and an open reading frame that encodes a singular polyprotein. This polyprotein is later cleaved into three structural proteins (C, M, E) that are involved in NC assembly and seven nonstructural proteins (NS1, NS2A, NS2B, NS3, NS4A, NS4B, and NS5) that function in translation, replication, modulation of host cell processes.

### *Attachment and Entry*

The replication cycle begins with attachment and entry of the virus into the cell. Attachment and recognition of the virus is poorly understood but involves interactions between cell receptors and the E glycoprotein on the virion surface. Glycosaminoglycans (GAGs) like heparin-sulfate proteoglycans are thought to act as an initial low-affinity co-receptor for

attachment (3). These long polysaccharide chains are linked to serine residues on surface proteins called proteoglycans and are present on all cell types in mammalian tissues. Because GAGs are sulfated molecules, they present a dense, negatively charged surface that is typically involved in binding protein ligands at the cell surface (46). Similarly, positively charged GAG-binding motifs of the E protein interact with the negative sulfate groups of the GAG to facilitate adhesion of the virus particle (47, 48).

Besides the GAG co-receptor, several putative cell attachment factors have been identified and may be used in combination to promote entry into the cell (reviewed in (49)). Of these, three receptor families are the best characterized for flavivirus entry. C-type lectin receptors (CLRs) and phosphatidylserine (PS) receptors will be described below. Entry of opsonized virus by Fcγ receptors will be discussed in a later section.

CLRs are a class of pathogen recognition receptors (PRRs) that are expressed in innate immune cells such as macrophages and immature dendritic cells (DCs). They use carbohydrate recognition domains (CRDs) to bind carbohydrate moieties present on the surface of various pathogens, including flaviviruses (50). Mammalian CLRs like DC-SIGN have been shown to bind flaviviruses at the conserved glycosylated Asn154 in the protein (or Asn153 in DENV) (51–57). Mannose receptor (MR) is additional mammalian CLR that has been shown to bind to glycosylated Asn67 of DENV (58, 59). Likewise in mosquitos, mosGCTL-1 is a CLR involved in WNV entry in *Culex* mosquitos (60) and mosGCTL-7 was recently reported as a CLR for JEV entry in *Aedes Aegypti* (61).

Typically, binding of a virus to CLRs will induce internalization, degradation, and processing for antigen presentation. However, the acidic environment of the lysosome promotes fusion with the endosomal membrane, allowing the flavivirus to subvert the cell's degradation mechanisms. Furthermore, two recent reports demonstrated that cells expressing internalization-

deficient DC-SIGN could still support infection with JEV (51) and DENV (62). These data suggest that CLRs may not act as the main entry receptor but function as an attachment factor or co-receptor.

As shown for Vaccinia virus which also obtains its membrane from the ER (63), flaviviruses are thought to acquire an apoptotic-like membrane as they bud into the ER. Because the luminal-facing membrane is enriched in PS, the virus membrane will likewise have large quantities of PS like that found on the plasma membrane of apoptotic cells, a phenomenon termed apoptotic mimicry (64). TIM and TAM transmembrane proteins represent two families of receptors for PS or phosphatidylethanolamine (PE) which are involved in clearance of apoptotic cells and also play a role in regulating the immune response (64). TIM (T-cell immunoglobulin and mucin domain) proteins bind PS or PE on apoptotic cell membranes directly through a conserved metal ion-dependent ligand-binding site (MILIBS) (65). These proteins have been shown to bind PS or PE present in the WNV (66, 67) and DENV (68, 69) membrane. Likewise, TAM (TYRO3, AXL, and MER) proteins are receptor tyrosine kinases (RTKs) that bind PS indirectly through bridging molecules like Gas6 (70) or ProS (71). Both DENV (68) and ZIKV (72–76) have been shown to associate with AXL via Gas6 or ProS bridging. However, two recent reports demonstrated that ZIKV infection occurs even in the absence of TAM receptors (74, 77). These results suggest that PS receptors may act, like CLRs or GAGs, as an attachment factor to concentrate the virus on the cell surface where it can engage its *bona fide* entry receptor. This entry receptor has yet to be found.

Although TIM and TAM receptors may not be the *bona fide* entry receptor for flaviviruses, the fact that they bind to PS or PE on the virion surface is intriguing. Mature flavivirus particles have a smooth surface covered in E protein that is thought to prevent access to the envelope membrane (78) and raises the question of how TIM and TAM receptors access

the underlying lipids. As one possible explanation, dynamic motion of the flexible surface E proteins may briefly expose the membrane and allow cell receptors to bind (79). This phenomenon is known as virus breathing (30). Alternatively, the cleavage of prM during particle maturation is known to be inefficient and "spiky" regions of partially mature particles may provide access to the membrane (49). Or lastly, many structural studies grow virus at 28˚C in mosquito cells, which produces the smooth virions that are thought to infect human cells (80). However, DENV virions were recently shown to have a bumpy surface when grown at physiological temperatures of 37˚C that exposes the membrane underneath (79). This likely explains how the viral membrane is exposed to bind to TIM and TAM receptors.

*Fusion*

Once the virion is internalized by clathrin-mediated endocytosis, the acidification of the endosome causes a conformational change from its metastable pre-fusion structure to its post-fusion stable structure. The anti-parallel homodimers of the E protein initially dissociate into monomers and subsequently form parallel homotrimers in an irreversible manner (81, 82). This configuration forces EDII outward from the surface where the fusion loop is inserted into the endosomal membrane. The E protein then folds back onto itself and brings the two membranes into close proximity for fusion (83, 84).

*Translation*

After fusion, the nucleocapsid is released into the cytoplasm, where it dissociates from the RNA genome. The dissociation process is poorly understood, but it does not require the capsid to be degraded (85). Garcia-Blanco et al have proposed that elongating ribosomes may be responsible for dissociating the RNA from the capsid, but they concede that other pH-dependent mechanisms and/or ribosomal interactions may be important (86). The genome is then localized to the rough ER where it acts as an mRNA for host-driven translation of the polyprotein. There,

eIF4E recognizes the 5' cap and recruits the 43S pre-initiation complex (87). The 5'cHP secondary structure guides this complex to the start codon (88) where it binds the 60S ribosomal subunit and forms the full 80S complex for elongation.

The open reading frame is translated directly onto the ER membrane as a single polyprotein that anchors itself in the membrane with multiple transmembrane helices. Signal peptides throughout the polyprotein translocate the NS1, prM, and E proteins into the ER lumen while the C, NS3, and NS5 proteins are translocated into the cytoplasm. The polyprotein is then post-translationally cleaved into its structural and nonstructural proteins by host signalase in the lumen and viral NS2B/3 protease in the cytoplasm (78).

*Replication*

Once cleaved, NS1, NS4A, and NS4B cooperatively induce membrane rearrangements in the ER and form vesicle packets (VPs) (89–91). There, the NS proteins all associate with one another to form the replication complex (RC). The NS2B and NS4B transmembrane proteins anchor the RC to the VP membrane by interactions with the NS3 protease and helicase domains respectively (92). NS5 subsequently associates with the anchored RC by interactions between the NS5 RNA-dependent RNA polymerase (RdRp) domain and the NS3 helicase domain (92).

Replication starts with synthesis of the negative sense strand from the positive sense genome. The NS5 RdRp recognizes the 5'SLA promoter region and starts de novo RNA synthesis at the 3' end of the cyclized genome (93, 94). Once synthesized, the negative strand remains based paired with the positive strand to form a double stranded intermediate (95). This intermediate is then unwound by the NS3 helicase, releasing the positive strand for translation or packaging. The 3' end of the negative strand binds to the template channel of the NS5 RdRp to start synthesis (92). Afterwards, the new double stranded product is released for further rounds of replication.

The single stranded positive sense RNA is modified post-transcriptionally with a type I cap as it is released from the unwound double stranded product. NS3 triphosphatase activity removes the γ phosphate from the triphosphate at the 5' end of the positive strand (96). Afterwards, the NS5 methyltransferase (MTase) domain binds a GMP molecule and transfers it to the new diphosphate group (97). The MTase then uses AdoMet as a donor for methyl groups that are transferred sequentially to the N7 position of the guanine and the ribose 2'O position of the first nucleotide. The RNA may also be methylated internally at the N6 position of adenosine ($m^6A$) by cellular MTases (35, 98, 99). $m^6A$ methylation is common in eukaryotic mRNA and is also commonly found as a modification towards the 3' end of DENV and YFV genomes. In ZIKV, $m^6A$ methylation may be used by the host to suppress replication (99).

*Assembly and Maturation*

During translation, the prM and E proteins form heterodimers (100) that then group into trimeric spikes. These trimers associate with C protein bound to a single RNA genome and bud into the ER lumen by undefined processes (78). This process is likely coordinated between the C protein and the membrane proteins, E and prM (101). The resulting immature particle is slightly larger than its mature counterpart at 60nm in diameter and is composed of 60 trimeric spikes. At the tip of each heterodimer, the pr domain of the prM protein covers the fusion loop (102). This prevents irreversible, pH-dependent conformational changes that may inactivate the virus. The immature particle is transported through the trans-Golgi network (TGN) where the surface proteins are glycosylated. As the acidity increases, the trimeric spikes rearrange and rotate into flat, anti-parallel homodimers of E protein. This rearrangement opens the cleavage site for prM, allowing it to be cleaved by host endoprotease, furin. The pr peptide continues to protect the fusion loop until the mature particle is released into the neutral extracellular matrix to restart the cycle.

## The History and Emergence of Zika Virus as a Human Pathogen

Zika virus (ZIKV) was first isolated by Dick et al in 1947 from a rhesus monkey during a yellow fever (YFV) surveillance program (103). The program was implemented in a small forest called Zika in southern Uganda where caged rhesus monkeys were placed in the canopy and monitored for signs of illness. When blood from a pyretic rhesus monkey was injected into an uninfected monkey, serum from the inoculated monkey neutralized the isolated viral agent. Blood was also injected intracerebrally or intraperitoneally into mice. Mice that were injected intraperitoneally showed no signs of illness while those that received intracerebral injections developed symptoms. ZIKV was isolated again almost a year later in a series of mosquito catches in the same area (103) and both of these isolated strains were then passaged in mice (104). As the virus adapted to the mice, the frequency of neurological symptoms such as motor weakness and paralysis increased. These mice demonstrated histopathological changes in the central nervous system including neural degeneration. These data suggested early on that ZIKV is neurotropic. Furthermore, infant mice exhibited more pronounced pathology than their adult counterparts providing early evidence that ZIKV infection is harmful to neurological development.

Early serological studies suggested that ZIKV infection in humans was common in Uganda (105, 106) and was also present in other areas of the world such as India (107), Malaysia (108), and the Philippines (109). In 1954, a case of febrile illness in humans was reported by Macnamara (110) and was misidentified as ZIKV infection (111–113). Three patients were seen in a rural Nigerian clinic during an outbreak of jaundice purportedly caused by YFV. The virus was isolated from one patient and identified as ZIKV by a neutralization test with monkey sera against a range of viruses. The other two patients were diagnosed by seroconversion against the isolated virus. Their symptoms included fever, headache, joint pain, retro-orbital pain, and mild

diarrhea. Two patients also had evidence of jaundice, though the possibility of co-infection could not be ruled out. Although these patients were the only confirmed diagnoses, the author noted the prevalence of other, similar cases during the jaundice epidemic. This led Macnamara to suggest a link between ZIKV infection and hepatitis. To test this relationship, Bearcroft inoculated himself with the virus isolated by Macnamara (114). He experienced symptoms of headache, fever, and malaise that resolved within a week, but showed no evidence of jaundice. Although a conclusion could not be drawn from these isolated cases, it is likely that the relationship between the isolated virus and jaundice was a result of a co-infection.

Macnamara's isolate that Bearcroft injected himself with was later identified as Spondweni virus (SPOV) (111–113), the closest viral relative to ZIKV (115). Therefore, the first ZIKV infection in man was actually reported ten years later by Simpson in 1964 (111). Simpson became ill while doing laboratory research on ZIKV in Uganda. He reported no break in lab technique and had visited Zika Forest three weeks prior where he was bitten by mosquitos. He reported similar symptomology to that described by Bearcroft with headache, fever and malaise but also developed a macropapular rash that covered his upper body. The virus was identified as ZIKV using anti-sera against different viruses, including SPOV. Simpson's recovery time was also shorter than Bearcroft's with symptoms resolving within five days instead of seven.

After the re-identification of Macnamara's isolate as SPOV, two strains of ZIKV were isolated in Lunyo Forest (near Zika Forest in Uganda) from *Aedes africanus* mosquitos in 1958 by Weinbren et al (116). These strains were identified as ZIKV using anti-sera to a variety of viruses, though cross-neutralization to SPOV was not tested. Mice that were inoculated with this virus showed similar neuropathological changes as those reported by Dick et al including neural degeneration and brain softening (104). Other pathological changes like myocarditis and skeletal

myositis (viral infection of the heart and skeletal muscle tissues respectively) were also reported in infant mice.

ZIKV continued to be regularly isolated during the 1960's from only *A. africanus* mosquitos in Zika Forest (117). For the first time in 1969, ZIKV was isolated outside of Uganda in a mosquito other than *A. africanus*. It was isolated from *Aedes aegypti* mosquitos in Malaysia (118), supporting the serological evidence that ZIKV was circulating at this time in Malaysia in addition to other parts of Southeast Asia including Thailand and Vietnam (119).

A laboratory acquired ZIKV infection was reported in 1973 (120), almost ten years after Simpson's illness. The infectious agent was identified as ZIKV by hemagglutination inhibition, complement fixation, and neutralization tests. Symptoms included fever, chills, retro-orbital pain, and joint pain and they completely resolved in a week. The course of illness in this report was like that described by Bearcroft (114), with no evidence of a rash. Although ZIKV infection has been described without rash (121), the authors did not test for cross-neutralization with SPOV nor did they describe isolated agents being used in the laboratory at that time. Because the symptomology of SPOV and ZIKV are extremely similar, it is unclear if this lab infection is a true case of ZIKV or if it is another instance of SPOV infection misdiagnosed as ZIKV.

For the next several decades, isolated cases and serological evidence of ZIKV infection were reported in Nigeria (122, 123), Indonesia (124, 125), Uganda (126), and Pakistan (127). By 2007, only 14 confirmed cases of ZIKV infection were reported in the literature (111, 120, 122, 124, 128). This changed in 2007 when a ZIKV outbreak occurred on Yap Island in Micronesia (129). During this time, an increase in febrile illness was noted by local physicians that included symptoms of fever, rash, conjunctivitis, and joint pain. A few of these patients tested positive for Dengue virus (DENV) IgM, but the differences in clinical presentation from previous DENV outbreaks, which normally does not present with rash, raised suspicion of a different causative

agent. Samples tested for viral RNA by RT-PCR tested positive for ZIKV and an in-depth analysis revealed that an estimated 5005 individuals (73% of the population) had been infected with ZIKV. Not only was this outbreak the first instance of ZIKV transmission outside of Africa or Asia, it was also the first report of a large outbreak of ZIKV.

During the next six years, only six other cases of ZIKV infection were reported (130–133). In one report, two scientists became infected with ZIKV in 2008 during field work for a mosquito study in Senegal (133). One of these patients transmitted the virus to his wife, who had not traveled recently. Although the evidence was circumstantial, the authors suspected sexual transmission as none of the other family members became ill. This report represents the first known instance of human sexual transmission of ZIKV or any other arbovirus.

In 2013, another ZIKV outbreak was reported in French Polynesia with an estimated 19,000 suspected cases (66% of the total population) (134, 135). Phylogenetic studies revealed that the etiological agent was most closely related to the Cambodia 2010 strain of ZIKV, indicating the spread from Asia into the Pacific Islands (134). Notably, this outbreak represented the first documented case of neurological manifestations of ZIKV infection in humans. A woman with serological evidence of a recent ZIKV infection developed Guillan-Barré syndrome (GBS) (136). GBS is an autoimmune disorder that can be triggered by infection or vaccination and is characterized by ascending muscular weakness and/or paralysis that develops days to weeks after an infection (137). Furthermore, a retrospective study of the 2013 outbreak found a link between ZIKV infection in pregnant women and microcephaly in infants (135). Microcephaly is a congenital abnormality characterized by a small head circumference that is at least 2 standard deviations smaller than the average and it is often accompanied by other birth defects, abnormalities, or cognitive impairments. The incidence of microcephaly is usually very low (~2 cases per 10,000 births (138)), but this study estimated that pregnant women who are

infected with ZIKV in their first trimester give birth to microcephalic infants at a rate of 95 cases per 10,000 births.

Before the end of the French Polynesian outbreak, 26 cases of ZIKV were imported to New Caledonia by travelers (139). These cases led to autochthonous transmission (14) that started an outbreak which lasted for more than six months (139). About a month after the New Caledonia ZIKV outbreak was declared, another outbreak was announced in the Cook Islands in early 2014 (140). Over the course of the next year, ZIKV continued to spread by imported cases to other Pacific islands including Easter Island (141), Vanuatu (142), the Solomon Islands (143), and Fiji (144). In March 2015, an outbreak of febrile, dengue-like illness was reported in Bahia, Brazil (145). Differential diagnosis was done by testing sera from 24 individuals with RT-PCR for DENV, WNV, ZIKV, CHIKV, and Mayaro virus. Almost a third of the patients tested positive for ZIKV. Researchers initially thought that the virus was introduced to Brazil during the 2014 soccer World Cup (146), but no countries with reported ZIKV transmission participated in the World Cup and it is more likely that it was introduced into Brazil in August 2014 from one of the Pacific Islands during the Va'a World Sprint Championship canoe race (147).

After the initial outbreak in Bahia, ZIKV continued to spread to other Brazilian states causing over 64,000 confirmed cases in Brazil alone by the end of 2016 (148). Additionally, approximately six months after the start of the outbreak, public health officials reported an increase in the incidence of microcephaly from 0.6 case per 10,000 lives births to 2.8 cases per 10,000 live births (149). By the end of November, 2015, the incidence had increased to almost 10 cases per 10,000 live births (150). This twenty-fold increase in incidence led the World Health Organization (WHO) to declare a public health emergency of international concern (PHEIC) on February 1, 2016 and allocate over $50 million to surveillance and research on ZIKV (151). The virus continued to spread over the next few years throughout Central and

South America (152, 153), the Caribbean (154), Pacific Islands (142, 155), Southeast Asia (156–158), and Africa (159). The 2015-2016 PHEIC was officially declared over on November 18, 2016 (160), but endemic transmission and its large burden on public health remains a large concern.

## Zika Virus Clinical Appearance and Pathogenesis

Up to 80% cases of ZIKV infection are asymptomatic (129) and symptomatic infection typically presents as a mild, self-limiting illness that may cause a fever, macropapular rash, myalgia, and conjunctivitis, arthralgia, retro-orbital pain, and headache (9–11). Vomiting (12) and diarrhea (13, 14) are rare but may also occur. Laboratory findings often note mild thrombocytopenia (low platelet count) or leucopenia (low white blood cell count) (9, 10), but severe thrombocytopenia leading to subcutaneous bleeding has also been reported (12, 161). Treatment is supportive as there are currently no antivirals or vaccines available and the infection typically clears within a week of symptom onset.

### *Neurological Complications in Adults*

For approximately 1% of symptomatic ZIKV patients, the illness manifests with severe neurological complications (162). Reported neurological sequelae include Guillan Barré syndrome (136, 157, 163–165), transverse myelitis (162, 166, 167), encephalitis (168–170), and optic neuritis (171, 172). Guillan Barré syndrome (GBS) is a rare neurological disorder that arises from autoimmune damage to the peripheral nervous system. There are several clinical variants but acute motor axonal neuropathy (AMAN) and acute motor sensory axonal neuropathy (AMSAN) are the two that are associated with ZIKV infection (173). It is still unclear how ZIKV induces GBS, but the proposed mechanism is that molecular mimicry of ZIKV antigens, generate cross-reactive anti-carbohydrate antibodies that bind to axonal membrane elements like gangliosides and induce macrophage-mediated damage (174). The damage to these components

disrupts nerve conduction and causes an ascending paralysis that starts in the legs and may last months or even years. Furthermore, the condition can become fatal if the autonomic nervous system is affected and causes organ failure with mortality rates ranging from 3% - 7% (175). For ZIKV-induced GBS, an increased prevalence of facial weakness and paresthesia, difficulty swallowing, shortness of breath, and pain are reported compared to GBS with other etiologies (176). Transverse myelitis (TM) is a similar autoimmune condition characterized by immune-mediated damage to the spinal cord which causes weakness in the legs and sometimes the arms. It is not known whether ZIKV causes TM by viral infection or inflammation-mediated damage or whether it involves molecular mimicry or superantigens (173).

A few case reports have documented ZIKV-associated encephalitis (169, 170), meningoencephalitis (168), and cerebellitis (177). For a virus to cause neurological disease, it must be neuroinvasive (the ability of the virus to enter the central nervous system, CNS) and neurotropic (the ability of the virus to infect and replicate in neuronal cells). Neuroinvasiveness and neurovirulence are properties of many flaviviruses like WNV and JEV that cause encephalitis and other neurological complications (178). The neuropathogenesis of these viruses is poorly understood but mechanisms of flavivirus neuroinvasiveness are thought to include hematogenous transport (i.e. during viremia, the virus infects the CNS via the circulatory system by crossing a cytokine-induced permeabilized blood-brain barrier) (179) and retrograde axonal transport (i.e. the virus infects peripheral nerve cells and travels to the CNS) (180). The E protein, particularly DIII and DII, is thought to be a major determinant of neurotropism and although the identity of neuronal flavivirus receptors remains elusive, heat shock protein 70 (Hsp70) and membrane glycoproteins have been shown to mediate JEV and WNV entry respectively *in vitro* (181, 182). Damage to the CNS tissue occurs mainly through apoptosis, necrosis, and bystander damage resulting from the $CD8^+$ T-cell response (178). Although it may

be reasonable to hypothesize that ZIKV may cause encephalitis in adults by similar means, these manifestations are rare in adults and ZIKV is more commonly associated with autoimmune conditions like GBS and TM. Furthermore, while WNV and JEV show tropism for mature neuron cells, astrocytes, and glial cells (178), ZIKV has been shown to readily infect proliferative brain regions that are prevalent in the developing fetus (183–188), though some conflicting reports suggest enhanced virulence in differentiated neuronal brain cells (189) and the presence of ZIKV in cerebrospinal fluid in adult macaques - perhaps due to passive spillover from high viremia in immunosuppressed mice (190). These data, combined with the rarity of encephalitic and similar case reports in the literature suggest that ZIKV neuropathogenesis is unlikely to occur readily in adults and likely occurs by mechanisms related to its role in ZIKV congenital syndrome such as infection of adult multipotent neural stem cells (191).

*Congenital ZIKV Syndrome*

ZIKV infection in pregnant women is linked to severe birth defects including microcephaly (174–176), ocular abnormalities (195–198), brain calcifications (199), and intrauterine growth restriction (200, 201) that are collectively known as congenital ZIKV syndrome. Microcephaly is caused by disorders that induce cell death and cause failure to divide and differentiate of neural progenitor cells (202) and ZIKV has been shown *in vitro* to dysregulate cell growth and proliferation (183, 186) and inhibit differentiation (203). *In vitro* work has shown that ZIKV may do this by inhibiting the Akt-mTOR pathway in neural progenitor cells which is essential for brain development and regulating autophagy (204). These data agree with the virus's ability to induce autophagy in umbilical vein endothelial cells (205). ZIKV has also been shown to induce neurological disease in mouse (187, 206, 207) and non-human primate fetuses (208–211). These reports suggest involvement of glial cells and upregulation of microRNAs, but the mechanism of neuropathogenesis remains unclear.

Furthermore, the incidence of ZIKV-associated microcephaly differs between regions with a nine-fold increase in microcephaly in Brazil and a four-fold increase in Columbia following respective outbreaks. These data imply the involvement of additional considerations such as socioeconomic factors on the incidence of ZIKV-associated microcephaly (212).

### *Antibody Dependent Enhancement of Flavivirus Infection*

Antibody-dependent enhancement (ADE) is a phenomenon characterized by enhanced viral entry and infection of cells via non-neutralizing antibody. It was first observed in 1930 (213) and the first experiments on ADE of viral infection were done in the 1960's (214, 215). Since then, the phenomenon has been well established for DENV (216–224) and it is hypothesized to be responsible for the development of a severe form of dengue fever (DF) known as dengue hemorrhagic fever/dengue shock syndrome (DHF/DSS) (225, 226). Although still not entirely understood, many of the underlying molecular mechanisms have been elucidated. After a primary DENV infection with one of the four serotypes, ADE occurs during a secondary infection with a different serotype (187). When a secondary DENV infection occurs, memory B cells from the primary infection dominate the immune response, which is a phenomenon known as "original antigenic sin" (228, 229). These B cells are activated to produce antibody that is cross-reactive and will bind to the secondary serotype with low affinity but will not neutralize the virus. This immune complex can then interact with the Fcγ receptor (FcγR) of an FcγR-bearing cell (230–233) (e.g. monocyte, dendritic cell, or macrophage), and is internalized via clathrin-coated pits (234–236). This mechanism increases the number of infected cells and is termed extrinsic ADE (237, 238). Inside the endosome, the acidic pH allows the viral E protein to initiate membrane fusion with the endosomal membrane (81, 239, 240). Once in the cytoplasm, the virus suppresses type I interferon signaling, blocking the innate antiviral response (241). This increases viral replication in the cell, a process is termed intrinsic

ADE (237, 242). Extrinsic and intrinsic ADE together lead to higher viremia and altered levels for cytokines such as IL-10, IL-12, IFN-γ, and TNFα (242–248). Further cell signaling increases vascular permeability and leads to fluid loss into the surrounding tissue and DHF (242). The corresponding drop in blood volume results in DSS marked by hemoconcentration and hypotension that can lead to hypovolemic shock and death (249–251).

However, research has demonstrated that DENV infection can be enhanced by sera against other flaviviruses, including ZIKV (214, 221, 252, 253). Recently, a research group showed that ZIKA antibodies could enhance DENV infection in mice (31) and ZIKV enhancement was also recently shown to occur in the presence of DENV antibodies (33, 254–256). Recent work analyzed the reactivity and specificity of ZIKV and DENV antibodies and they found that antibodies reactive to the DI/DII domains of the E protein were cross-reactive between the ZIKV and DENV E proteins, but DIII-reactive antibodies were not (257). Furthermore, mice that were previously injected with DI/DII-reactive antibodies showed enhanced mortality and weight loss when infected with DENV. Collectively, these studies suggest that heterologous ADE may occur during human infection and could be responsible for many complications that arise from DENV infection. Enhancement of ZIKV infection is also suspected to be involved in the onset of neurological complications (258). Given the large burden of DENV and ZIKV complications, heterologous enhancement between ZIKV and DENV has major implications for public health and further research is necessary to elucidate the role of ADE in ZIKV and DENV pathogenesis.

## Diagnosis of Zika Virus

Because complications associated with ZIKV infection are so severe, it is critical that patients are quickly and accurately diagnosed to facilitate proper monitoring and medical intervention. There are no FDA-approved diagnostic tools yet available for laboratory ZIKV

testing but there are currently ten assays that can be used for clinical diagnosis of ZIKV infection under Emergency Use Authorization (EUA) (259). For early diagnosis (<14 days after symptom onset), the CDC recommends nucleic acid testing (NAT) on serum and urine (260). Typically, this is done with real time RT-PCR assays such as the Trioplex Assay, which can test for ZIKV, DENV, and CHIKV simultaneously. While the Trioplex assay demonstrates good specificity and is very sensitive (limit of detection (LOD) equals $2.45\times10^3$ genome copy equivalents (GCE)/mL) (261), the assay is very technical and requires the design of three sequence-specific probes in conserved regions of the ZIKV genome with expensive fluorescent and quenching tags (261). Because PCR cannot detect RNA directly, a reverse transcription step must also be included to detect RNA viruses such as ZIKV. This increases assay time, labor, and reagent cost. Besides the reagent requirements, the instrumentation for real time PCR is also expensive (~$15k USD), making it inaccessible in resource-poor areas where the virus circulates (262, 263).

Alternative NAT methods that have been developed in the last two years to increase assay simplicity while maintaining high specificity and sensitivity mostly include CRISPR-based diagnostics and loop-mediated isothermal amplification (LAMP) based assays. Two CRISPR-based diagnostics have been described by Gootenberg et al (264) and Myhrvold et al (265) that employ a SHERLOCK (specific high-sensitivity enzyme reporter unlocking) platform. The SHERLOCK platform uses Cas13a-mediated cleavage of collateral reporter-RNAs for specific detection of an RNA target. The assay was designed to be instrument-free by Myhrvold et al for use as a point-of-care assay and demonstrated attomolar RNA detection in clinical samples in under two hours. Two LAMP assays have been developed by Castro et al (266) and Guo et al (267) that respectively use real time analysis and fluorescence analysis to monitor the RNA response in clinical samples. Although sensitive, both assays require expensive instrumentation.

A point-of-care colorimetric LAMP assay was developed by Calvert et al (268). As the nucleic acid is amplified, it releases protons which reduce the pH as detected by a colorimetric pH indicator. The reported limit of detection was $2\text{-}3\times10^3$ copies/mL which compares well with the CDC's Trioplex assay.

If the patient sample is collected >14 days after symptom onset or if the sample tested negative by NAT, serological testing is recommended. This is typically done with the CDC's Zika MAC-ELISA which detects anti-ZIKV IgM (269) and positive or inconclusive results are confirmed using plaque reduction neutralization testing (PRNT) (270). Besides the CDC MAC-ELISA, other ZIKV immunoassays have been developed by public health and commercial bodies. An evaluation comparing commercial immunoassays by Euroimmun, Abcam, Novatech, and InBios found that while the assays had decent specificity, most had poor sensitivity ranging from 37% to 65% (271). Another report compared immunoassays developed by the CDC and Centro Nacional de Diagnóstico y Referencia (CNDR) and found that the CNDR immunoassay had higher sensitivity than the CDC MAC-ELISA (94.5% vs 70.1%) as well as better specificity (85.6% vs 82.8%) (272). The improved performance of the CNDR assay compared to the CDC's is attributed to its use of an antibody against DIII of the ZIKV E protein which has higher neutralization capacity and has higher specificity.

The performance of ELISAs are generally limited by poor sensitivity (271), poor specificity due to cross-reactivity with other flaviviruses (273), and long processing times (272). A prominent need for improved diagnostics has galvanized the development of new techniques for ZIKV serological testing. Several fluorescent techniques have been published recently. An indirect immunofluorescence (IIF) assay developed by De Ory et al was used to test characterized serum samples and showed high sensitivity (96.8%), but it suffered poor specificity (72.5%) and is also limited to use with expensive fluorescent microscopes (274). Wong et al

developed a multiplex microsphere immunoassay (MIA) based on fluorescence that used seven ZIKV antigens in a single well format to combine the sensitivity of anti-E protein detection with the differential power of detecting virus-specific antibodies against the NS proteins (275). This assay demonstrated good sensitivity and had a fast turnaround time of less than four hours. Although there was extensive cross-reactivity for most of the antigens used, the combination of seven antigens in a single assay increased diagnostic power. To increase the throughput of the classical PRNT, Koishi et al developed a fluorescent neutralization test using quantitative immunofluorescence to measure the amount of neutralizing antibody in a serological sample (276). The fluorescence assay compared well to the classical PRNT, increased throughput, and demonstrated half the cross-reactivity with DENV than the MAC-ELISA but could not differentiate between acute and past infections and required specialized laboratory equipment and space to perform.

Biosensors, as reviewed in Chapter 2, are attractive as new diagnostic tools due to their high sensitivity and ease of miniaturization for point-of-care measurements. In the past year, several groups have reported biosensor designs to diagnose ZIKV infection. Cabral-Miranda et al used a screen-printed carbon electrode modified with carbon nanotubes (to enhance conductivity) with immobilized anti-ZIKV DIII to detect an anti-ZIKV serological response (277). Their sensor was 10,000 times more sensitive than the compared ELISA and exhibited no cross reactivity when tested with DENV+ serum. Furthermore, the sensor could differentiate between IgM and IgG using a secondary antibody.

Biosensors are also commonly developed to detect antigen during the acute phase of infection. Afsahi et al designed a graphene-based field effect biosensor to detect ZIKV NS1 protein and demonstrated a limit of detection of 0.45 nM and good selectivity when compared to JEV NS1 (278). The sensor was not compared to relevant cross-reactive agents such as DENV

and it is unclear whether the sensor could be used for differential diagnosis in regions where ZIKV and DENV co-circulate. A paper-based sensor by Draz et al labeled target ZIKV with platinum nanoprobes to measure the impedance signal from virus lysate (279) and is an inexpensive approach amenable for point-of-care detection.

Although new diagnostics tend to improve one or a few parameters (e.g. sensitivity, specificity, portability, cost-effectiveness), integrating these properties remains a challenge. The ideal diagnostic tool will demonstrate high sensitivity and specificity balanced with miniaturization, portability, and inexpensiveness. Subsequent chapters will describe proofs of concept for electrochemical assays and biosensors with large potential as point-of-care tools.

# CHAPTER 2 - ELECTROCHEMICAL BIOSENSORS AND ASSAYS: AN INTRODUCTION FOR BIOLOGISTS (280)

## Purpose

Clinical diagnostics is becoming an increasingly interdisciplinary field that requires extensive collaboration between molecular biologists, analytical chemists, electrochemists, engineers, materials scientists, and computer scientists. To facilitate effective development of new diagnostic tools, a basic understanding of these disciplines is required. Because this manuscript is written for a biological audience, the purpose of this chapter is to introduce the basic principles of electrochemistry, electrical engineering, surface chemistry, and nanotechnology as it pertains to electrochemical biosensor and assay development. Many excellent introductory materials exist for these topics, but they are often mathematically dense and contain extraneous information not pertinent to biosensor development. The goal of this chapter is to introduce the biologist to electrochemical biosensors and assays from a streamlined, conceptual perspective.

## Basic Sensor Concepts

According to the International Union of Pure and Applied Chemistry (IUPAC), a biosensor is a device that converts a biorecognition (e.g. affinity binding such as that between an antibody and antigen) or biocatalytic (e.g. an enzymatic reaction) event into an analytical signal proportional to the target concentration (281). A biosensor consists of an analyte, bioreceptor, transducer, signal processor, and display (282) (Figure 2.1). Analyte refers to the target molecule that is being detected while the bioreceptor is a biomolecule such as an antibody that binds the analyte. The bioreceptor is usually immobilized onto the transducer which converts energy from the biorecognition event into a quantifiable signal. The signal processor conditions

the signal, subtracting noise and amplifying the signal which can then be displayed through a user interface.

All biosensors share six properties that reflect the quality of its operation (282). Selectivity refers to the bioreceptor's ability to distinguish between and bind to the analyte versus other components in the matrix. The concentrations of analyte that produce a linear change in signal response are collectively defined as the linear range (283). The sensitivity of the biosensor refers to the slope of this linear range (284), or the smallest change in analyte concentration that stimulates a signal change. Related to the sensitivity is the limit of detection (LOD) or the lowest concentration of analyte that can be detected (285).

A biosensor's ability to generate the same signal response for the same analyte concentration under different conditions is its reproducibility (286). Finally, stability is the consistency of a signal in response to environmental or kinetic influences such as temperature or dissociation of the bound analyte (282).

Biosensors are very diverse and can be categorized according to the bioreceptor or the transduction method. Bioreceptors used in biosensor research include enzymes (287), antibodies (288), antigen/substrate, DNA (289), aptamers (290), and even whole cells (291). Most biosensors employ either electrochemical (292) or optical (293) transduction techniques, though acoustic biosensors have also been reported (294). Electrochemical biosensors and assays will be the focus of this review.

## Electrochemical Principles

Electrochemistry is the study of the flow and transfer of electrons between chemical species and the factors that affect this process (295). This electron transfer typically occurs as a result of chemical changes involving the oxidation or reduction of species (296). These reactions are termed redox reactions and each half of the reaction (e.g. the oxidation or reduction) is

termed a “half-cell”. The movement and flow of these electrons and charges is termed current. Many different techniques exist that analyze such electrochemical processes and characteristics, but most of these techniques employ common equipment and principles (295).

Most electrochemical reactions are analyzed in an electrochemical cell consisting of three electrodes and an electrolyte (Figure 2). The working electrode (WE) is the electrode that drives the electrochemical reaction of interest by applying a potential relative to the reference electrode (RE). Potential refers to the available electron energy that can drive reactions and the amount of work required to move a test charge from one electrode to the other (297). Physically, the magnitude of the potential results from charge present in excess to the metal’s innate amount of charge. This is driven by an external power supply that drives electrons into or out of an electrode (298). Potential was historically termed electromotive force and is thus denoted with the letter E.

Because E measures the work to move charges from one point to another, measuring this electron energy is, by definition, done relative to a reference point. The reference electrode is made of stable components that exist in equilibrium. For example, the standard hydrogen electrode (SHE) is made of inert platinum with adsorbed hydrogen gas. The SHE lies in a contained solution of hydrogen ions and it undergoes a half-cell reaction at equilibrium (299).

$$2H^{+}(aq) + 2e^{-} \leftrightarrow H_2\,(g)$$

By convention, the potential of the entire redox reaction is reported in terms of the reduction half-cell potential (295). The potential of the half-cell reaction at the SHE has been arbitrarily assigned a potential of 0 V and it is stable over time and across temperature (300). This fixed, stable potential between the electrode and electrolyte acts as a reference that can be used to measure the relative potential of the other electrodes (296). Other common reference electrodes have a different half-cell potential relative to the SHE. For example, a silver-silver chloride RE

is made of a silver wire coated with AgCl and is contained in a KCl solution. The equilibrium of this half-cell reaction

$$AgCl\ (s) + \ e^{-} \ \leftrightarrow \ Ag\ (s) + Cl^{-}\ (aq)$$

occurs at 0.222V vs SHE RE (299). It is thus common to denote the potential in terms of the reference electrode used (e.g. one might say 1.7V vs Ag/AgCl), but the potential of any given half-cell with respect to a given RE can be converted to terms relative to SHE by subtracting the potential of the RE half-cell potential relative to SHE.

Redox reactions involving the reduction or oxidation of a species cause a direct transfer of charge across the electrode/electrolyte interface (Figure 2.3). Reduction involves an electron transfer from the electrode to the chemical species in solution whereas oxidation transfers an electron from the species back to the electrode. This type of electrochemical current is known as Faradaic current and it is driven by the difference in potential between the WE and RE. The potential difference between the WE and RE is known as the cell potential and it influences the direction and rate of charge transfer across the electrode/electrolyte interface. Chemical reactions subsequently occur at the WE surface due to the potential difference between the electrode and electrolyte (e.g. the interfacial potential difference) (295). For current to flow, we must have a complete circuit. The counter electrode (CE) serves this purpose. As a reduction occurs at the WE, a complementary oxidation happens at the CE, creating a full electrical circuit that allows current to flow (296) (Figure 2.2).

However, the interfacial potential does more than drive redox reactions. It also causes charges to accumulate or move out of the interfacial region without transferring across to the electrode (301). The accumulated charge at the electrode-electrolyte interface behaves like a capacitor that stores charge and is called double layer capacitance (302). Like a capacitor, the composition and length of the double layer influences the amount of stored charge or capacitance

as well as the rate of charge transfer. Unlike a capacitor, however, as the potential changes, so too does the structure of the double layer. At positive potentials, anions in solution accumulate at the interface whereas cations accumulate when negative potentials are applied to the electrode. As charges move in or out of the double layer, a non-Faradaic current flows (Figure 2.4). This capacitive or charging current seeks to equilibrate the double layer and may be transient or continuous (303). If a single change in potential occurs, the charging current will dissipate over time as the double layer equilibrates. On the other hand, a continuous change in potential will produce a continuous charging current.

## Common Electrochemical Techniques

### *Voltammetry*

Amperometry is a technique that measures the current over time at a fixed potential. Voltammetric methods like cyclic voltammetry are a subset of amperometry that measure the current response as the WE is scanned through a defined range of potentials. This scan is known as a potential sweep. For a given redox couple, as the electrode is scanned toward lower potentials, it will drive the reduction of the species. As the electrode is scanned back towards higher potentials, the species will be oxidized again. The potentials where reduction and oxidation occur generate respective peaks in current and produce the characteristic "duck-shaped" voltagramm shown in Figure 2.5 using ferricyanide ($Fe(CN_6)^{3-}$) and ferrocyanide ($Fe(CN_6)^{4-}$) as a model redox couple. Starting from point A, the potential is scanned towards lower potentials and $Fe(CN_6)^{3-}$ begins to reduce to $Fe(CN_6)^{4-}$. The current increases as $Fe(CN_6)^{3-}$ is continuously reduced until it reaches a peak at point C. This peak occurs because $Fe(CN_6)^{3-}$ is depleted from electrode surface and buildup of $Fe(CN_6)^{4-}$ limits mass transport of $Fe(CN_6)^{3-}$ to the electrode surface (296). During this time, the current decreases until the potential reaches point D, known as the switching potential ($E_\lambda$). The scan then reverses direction and begins to

sweep towards higher potentials. With plenty of newly formed $Fe(CN_6)^{4-}$ at the electrode surface, the current again steadily increases in the same manner until the species is depleted at point F. Here the current becomes limited by mass transport again and begins to fall off until the scan is completed. The potential where the peak current ($i_p$) occurs is known as the peak potential ($E_p$). The difference between the two peak potentials ($\Delta E_p$) provides information about the reversibility of the redox reaction. An ideal, reversible system will have a $\Delta E_p$ of 59mV, though in practice this value is closer to 70-80mV. When a reaction is quasi-reversible or irreversible, more energy is required to complete the reaction, causing reduction to happen at increasingly negative potentials and oxidation at increasingly positive potentials. This results in a larger $\Delta E_p$. Halfway between the two $E_p$ lies the half-wave potential, $E_{1/2}$. This corresponds to the potential where the concentrations of the oxidized and reduced species at the electrode surface are the same and the reaction lies in equilibrium. $E_{1/2}$ is typically close to the formal potential, $E^{0'}$, which corresponds to the potential that is measured when the concentrations of the reduced and oxidized species are equal (295).

When redox reactions are not taking place, background current can still flow between the electrodes and corresponds to the capacitive non-Faradaic current (296). When analyzing low quantities of redox species, this non-Faradaic current may interfere with accurate measurements of Faradaic current (303). Pulse voltammetry techniques like square wave voltammetry (SWV) increase sensitivity to Faradaic currents by subtracting background capacitive currents (304). Briefly, SWV applies a staircase series of forward and reverse potential pulses of a fixed length of time. Current is measured at the end of each pulse, after charging currents have dissipated, and the difference in current is plotted against the difference in potential between the forward and reverse pulses.

Conventional electrodes are typically an insulator-enclosed wire with an exposed disk ranging from 1 – 10 mm in diameter (305). Microelectrodes, with a diameter of less than 25 μm, exhibit different electrochemical behavior and have several advantages compared to conventional electrodes. Diffusion of a species to the planar surface of a conventional electrode is almost entirely linear and imposes limits on the current to yield peak currents in the voltagramm (Figure 2.6). In contrast, the planar surface of a microelectrode is significantly smaller and radial diffusion to the edges of the disk have a much larger contribution (306). This "edge effect" creates a hemispherical region from which species can diffuse and increases the transport rate of species to the electrode surface (305, 306) (Figure 2.6c). Thus, the redox species diffuses to the electrode surface as quickly or even faster than electron transfer can occur. The current is not limited by mass transport in this case and does not fall off, which produces a steady-state voltagramm (Figure 2.6d). Just as reversibility can be determined by $\Delta E_p$ of a traditional voltagramm, the slope of the sigmoidal steady-state voltagramm should approximate 60mV for a reversible system (295). $E_{1/2}$ can be determined by the potential of half the steady state current ($i_{ss}$).

*Electrochemical Impedance Spectroscopy*

Direct current (DC) flows in a single direction in response to a uni-polarity potential (i.e. positive and negative potentials do not switch back and forth). Alternating current (AC) flows back and forth as a sinusoid as it moves forward and is generated using an alternator. Simplistically, if you place a circuit between two poles of a magnet as shown in Figure 2.7, a potential difference, or voltage, will be electromagnetically induced between the two coils. This voltage drives current flow. As you rotate the circuit, the voltage across the circuit will change until it reaches the opposite polarity. The resulting sinusoidal voltage waveform generates a complementary sinusoidal or alternating current response. When the frequency is non-zero (as is

the case for AC current), these voltage and current sine waves are typically not in sync or in phase with each other. The degree to which current is shifted in time compared to voltage is termed phase, θ. The θ provides useful information about which component contributes most to total impedance at a given frequency. For example, as the θ approaches -90˚, the circuit is mostly capacitive. As it approaches 0˚, the circuit is mostly resistive.

Electrode kinetics, reaction rate, diffusion, etc are all parameters that hinder the flow of charge in an electrochemical cell and they can be modeled as components of an AC circuit (307). These equivalent circuit models, discussed more below, can be used to describe the behavior of an electrochemical cell. The closer the calculated response of the model is to the measured response, the better the model is said to represent the actual physical processes at the interface (308). The analogous resistors and capacitors (inductors are also included in this category but will not be discussed in detail here) have a given impedance. Impedance (Z) is the opposition to current flow and is a measure of how difficult it is to move charge through a given circuit at a specific frequency when a voltage is applied.

It is formally defined as the ratio of the voltage-time function and the current-time function:

$$\text{Equation 1. } Z = \frac{V(t)}{I(t)} = \frac{V_0 \sin(2\pi f t)}{I_0 \sin(2\pi f + \varphi)}$$

where $V_0$ and $I_o$ are the amplitude of the voltage and current respectively, f is the frequency in degrees, and φ is the phase shift of the current sinusoidal with respect to the voltage sinusoidal (309, 310). A system's impedance can therefore be calculated by measuring the current response after applying a sinusoidal voltage function with a small amplitude, $V_0$ (309). This oscillation amplitude is typically smaller than 10 mV to facilitate a pseudo-linear relationship between current and voltage (311). At larger voltages, the relationship becomes nonlinear and increases the complexity of analysis. Furthermore, higher voltages as seen in amperometric techniques

may damage the biorecognition layer by exerting a force on charged biomolecules like proteins and nucleic acid (312).

Electrochemical impedance spectroscopy (EIS) is a technique that characterizes the electrode-electrolyte interface by sampling the impedance throughout a range of frequencies and creating an impedance "spectrum" (309). The current I(t) at a given frequency may differ from the AC voltage V(t) by both amplitude and phase (Figure 2.8a), which makes the resulting impedance a complex number. Its real component consists of resistance while capacitance and inductance compose the imaginary component. Impedance can thus be described in terms of its magnitude and phase or its real and imaginary components. EIS data can therefore be represented in two different formats. A Nyquist plot (also known as a Cole-Cole plot) plots the imaginary part of the impedance at each frequency against the corresponding real part (Figure 2.8c). A Bode plot plots the phase and absolute impedance |Z| on the y-axes against the log of the frequency of the x-axis (Figure 2.8d). The values of several parameters can be extracted from this graph including the solution resistance, charge transfer resistance, and the double layer capacitance (307). EIS may be used to investigate Faradaic or non-Faradaic systems. Impedance biosensors generally refer to Faradaic systems that measure impedance through a range or even a single frequency, while non-Faradaic impedance measurements are typically used in capacitive biosensors that investigate changes in the double layer capacitance at a single frequency.

EIS data can be fit using a circuit model. For a Faradaic system, the Randles-Ershler equivalent circuit is the most commonly employed circuit model of an electrode-electrolyte interface (313) (Figure 2.9) and is based on the work of Randles (314, 315) and Ershler (316) in 1947. It places the non-Faradaic charging current in parallel with the simultaneous flow of Faradaic current from a redox reaction. As mentioned previously, various electrochemical

processes impede current and are analogous to circuit components like capacitors and resistors (308). The charging current of the double layer is modelled as a capacitor ($C_{DL}$). Likewise, the Faradaic current must overcome both a charge transfer resistance ($R_{ct}$), also known as the polarization resistance ($R_p$), and the Warburg impedance ($Z_W$). $R_{ct}$ represents the resistance of a species to be oxidized or reduced at a given potential (317). Stated another way, $R_{ct}$ is the difficulty of achieving an electron transfer between the electrode and the redox species at the electrode interface. How quickly reactants diffuse to the electrode interface (and how quickly products diffuse away) can affect how much charge transfer occurs (i.e. how much Faradaic current there is). This impedance from mass transport is known as Warburg impedance ($Z_W$). Both the Faradaic and non-Faradaic currents must overcome an electrolyte or solution resistance ($R_s$), which results from the ions' limited ability to conduct electrons (312) and is placed in series with the two parallel currents. These electrochemical processes (and their corresponding circuit components) are influenced by the frequency of the applied sinusoidal potential. At high frequencies, capacitors act as a short circuit (i.e. negligible impedance) causing the current to preferentially flow through that half of the circuit. Thus, the current is only impeded by the in-series solution resistance ($R_s$) as the frequency increases causing $R_s$ to dominate the impedance equation. At low frequencies, capacitors have high impedance and begin to act as an open (broken) circuit as the frequency approaches 0 Hz. Thus, at these low frequencies, the current will predominantly flow through the Faradaic circuit components (including the solution resistance) which offer less impedance (295). In this case, the total impedance is dominated by $Z_W$ because reactants must diffuse farther at low frequencies. At intermediate frequencies, the total circuit impedance has contributions from both the Faradaic and non-Faradaic components

For a non-Faradaic system (i.e. one without redox reactions), the circuit model is very similar to the Randles equivalent circuit. However, the series combination of $Z_W$ and $R_{ct}$ is

instead replaced with a leakage resistance, $R_{leak}$ (312). Ideally, $R_{leak}$ should be infinite for a non-Faradaic system which contains no redox species, causing all current to flow through $C_{DL}$. In practice, a small amount of current may leak across the interface and is thus accounted for in the circuit model.

### *Field Effect Transistor Biosensors*

A field effect transistor (FET) is a semiconductor device with three electrode terminals that controls the current through the device with an electric field. Two of the electrodes, the source and drain, are connected by a semiconductor channel. The gate electrode acts as a control electrode. It is placed near the channel, where it generates an electric field that alters the conducting properties of the channel. Any change in the gate's voltage creates a correspond change in the current flow through the channel. Field effect transistor biosensors (BioFETs) use a biorecognition surface at the gate electrode to control the current (318, 319). When an analyte binds to this surface, it changes the electrical surface charge (i.e. voltage) of the gate electrode which is then detected by the corresponding change in the channel current (320). Electrochemical techniques that measure changes in voltage are termed potentiometry.

## Surface Functionalization and Chemistry

Immobilization of a biorecognition probe to a transducer surface is a fundamental property of biosensors. The transducer surface properties, the properties of the individual probe, and the immobilization method all affect the probe's behavior and orientation at the interface. These behavior profiles are still poorly understood but directly influence biosensor performance including its sensitivity, specificity, and reproducibility. Although approaches to immobilize nucleic acid probes employ similar principles, this discussion will focus on immobilization strategies for protein-based biosensors. Such methods include adsorption, covalent coupling, and affinity-based immobilization (321, 322).

*Adsorption of Biorecognition Probe*

Adsorption is a non-covalent, spontaneous process by which a molecule adheres to a surface through hydrophobic, electrostatic, and/or van der Waals interactions (323). The process is commonly used in molecular biology techniques to immobilize probe molecules or block surfaces. The example that molecular biologists would be most familiar with is the adsorption of protein to a polystyrene plate through mostly hydrophobic interactions for an ELISA assay (324). The adsorption process is affected by many parameters including the protein characteristics (size, charge, rigidity), surface characteristics (surface energy, charge, hydrophobicity, roughness), and the environmental characteristics (bulk protein concentration, temperature, pH, ionic strength, and buffer composition) (325, 326).

The surface and environmental characteristics may affect a protein differently depending on its inherent traits such as rigidity. To interact with a hydrophobic surface, proteins often must undergo conformational changes to expose their hydrophobic core (324). Hard proteins have a more stable molecular structure that does not readily change conformation. Thus, even when adsorbed to a surface, hard proteins tend to maintain their structural integrity. In contrast, soft proteins like IgG or BSA are flexible and easily change conformation (327). As a result, as a soft protein "relaxes" on a surface, the protein spreads out to maximize contact points with the surface and takes on a denatured conformation. Temperature may differentially influence adsorption of hard or soft proteins either kinetically or thermodynamically (328). Kinetically, higher temperature can increase the rate of protein diffusion to the surface by increasing the rate of diffusion. However, mildly high temperatures may also cause partial desorption of hard proteins which maintain structural integrity and thus molecular mobility. In contrast, soft proteins demonstrate resistance to heat-induced desorption because they tend to denature at the surface. Thermodynamically, at temperatures higher than the protein's denaturation temperature,

the adsorption of a hard protein may increase as the protein in solution denatures. The newly exposed hydrophobic surfaces of the denatured protein readily facilitate adsorption to a hydrophobic surface.

Although adsorption does occur via electrostatic interactions between a charged protein and a charged surface, it occurs most readily at the protein's isoelectric point (pI or IEP), which corresponds to the pH where a protein has an overall net neutral charge (329). This is likely due to a reduction in repulsive electrostatic protein-protein interactions. Solutions with higher ionic strength screen proteins from charge interactions and may cause protein aggregation, however the different ions may influence adsorption differently, obscuring a more general trend (330).

Using adsorption to immobilize a probe protein has several advantages. It uses fewer reagents compared to other immobilization methods and maximum surface coverage can be obtained in less than an hour (331). Typically for adsorption protocols, protein concentrations 3-10× larger than the adsorption capacity are sufficient to reach maximal coverage. BSA, for example, has an adsorption capacity of 3 $mg/m^2$ while IgG has a capacity of 2.5 $mg/m^2$ (332). Most protein probes will have capacities within or near this range. Proteins may be displaced from the surface by other proteins (Vroman effect), but at fixed pHs, desorption from a hydrophobic surface occurs so slowly as to be considered irreversible, even after buffer rinses (333, 334). Changes in pH induce conformational changes in the protein that cause it to desorb from the surface (335).

A disadvantage of using adsorption may arise from loss of binding activity from the immobilized protein. While soft proteins like IgG are especially known to denature upon adsorption, there has been disagreement over whether such denaturation reduces binding activity. Some reviews report that conformational changes upon adsorption can enhance activity (325), whereas some studies demonstrate reduced activity (336), and still others show no effect on

activity at all from denaturation (337, 338). These discrepancies may arise from differences in individual protein and/or surface properties and more research is required to elucidate underlying mechanisms.

Multiple studies have also shown that the effects of surface packing negatively affect binding activity (56, 58). One study found increasing binding activity with increasing concentrations of adsorbed antibody until ~1 $mg/m^2$ (337). At greater surface concentrations, the binding activity quickly declined. This effect is likely due to steric hindrance and repulsive protein-protein interactions that inhibit target binding. Because this effect has large implications for sensor sensitivity, it is important optimize the probe concentration adsorbed to the surface. Maximal density does not necessarily correlate to highest sensitivity. The packing density is also influenced by environmental conditions like pH and ionic strength. Conditions that promote charged interactions between adsorbed proteins (e.g. $pH \neq pI$) result in a loosely packed layer whereas conditions that negate these charged interactions (e.g. high ionic strength or $pH = pI$) form densely packed and even multilayers (325, 329).

Because adsorption is a non-specific process it is difficult to control the orientation of the probe at the surface. Essential target binding sites may therefore be inaccessible and reduce the overall sensitivity of the sensor. In the case of an antibody molecule, it can take one of four configurations at the surface: end-on, head-on, side-on, or flat-on. Earlier studies on antibody orientation concluded that antibodies have a preference for a flat-on orientation at the surface (337, 340). However, these conclusions were determined by calculating the thickness of the protein layer and recent research using mass spectrometry and total internal reflection fluorescence indicates that at lower surface concentrations, antibodies instead adopt a side-on configuration that transitions to an end-on configuration as protein-protein interactions increase with increasing concentration (334, 341).

*Covalent Coupling*

Covalent immobilization of protein to a surface uses chemical agents to form a covalent bond between functional groups present at the surface and on the protein. Functionalization groups can be introduced to the surface in various ways depending on the material. Alkanethiol chains (also known as alkylthiols) consist of a terminal sulfur group, a carbon chain of methylene groups, and a head group. The terminal sulfur group allows the alkanethiol to self-assemble on electrode metals like gold, platinum, or copper (342) to form a self-assembled monolayer (SAM) that is stable at a wide range of potentials (0.8 V to -1.4 V) (343). The head group consists of a functionalization group such as a carboxylic acid (COOH), amine ($NH_2$), azide, aldehyde (CHO), or thiol (SH) group that can be used to covalently immobilize a protein. Furthermore, long and short chain alkanethiols can be mixed to control the density of immobilized probe by using the short chain polymer as a spacer (343). Common alkanethiols used in biosensor research include 11-MUA (11-mercaptoundecanoic acid) (344, 345), 3-MPA (3-mercaptopriopionic acid) (346), MCH (mercapto-1-hexanol) (347, 348), MCU (11-mercapto-1-undecanol) (349), and lipoic (thioctic) acid (350, 351). Organosilanes are like alkanethiols in their ability to form functional monolayers on an inorganic surface and comprise of a silicon molecule bound to a carbon spacer chain. The silicon is generally attached to a reactive group that allows the chain to covalently bind to inorganic surfaces such as indium tin oxide (ITO) electrodes (352–354). At the other end lies a functional group that can be used for bioconjugation. For carbon-based electrodes, electropolymerization can be used to form a conductive polymer layer and introduce functional onto the surface (355). Common reagents for this process include poly(pyrrole propionic acid) (pPPA) (355) or other pyrrole derivatives (356), polyaniline (PANI) (357, 358), nafion (359), and polytyramine (360). Alternatively, the carbon surface can be oxidized to form carboxylic acid functional groups (361). Once introduced to the surface, functionalized groups can be used

for either random or oriented immobilization of proteins depending on the composition of the protein.

### *Affinity-based Immobilization*

Affinity tags are commonly used for site-directed immobilization which optimally orients the protein on the surface. Proteins with a histidine-tag (His-tag) at either terminus can be immobilized to conductive polymers like pyrrole (362). The polymer is functionalized with nitrilotriacetic acid (NTA) which indirectly binds the His-tag via a coordinated metal ion. Biotinylated proteins can be immobilized to surfaces that are coated with streptavidin though the biotin is conjugated to amine groups spread randomly throughout the protein and this leads to random orientation. Biotinylated antibodies can be oriented by site specifically conjugating the biotin at the sulfur bridges present in the antibody molecule (363). Lastly, Fc binding proteins such as protein A or protein G are commonly adsorbed or covalently linked to the electrode surface first to bind the Fc fragment of an antibody and orient it in a head-on orientation. Affinity-based methods are used to easily orient a protein on the surface without concerns of denaturation or activity loss that can be associated with adsorption and/or covalent methods. However, these interactions are less stable which could lead to a loss of probe functionalization over time.

### *Blocking*

Nonspecific adsorption of nonspecific target to the transducer surface can interfere with and mask the specific signal of the biorecognition event. Such fouling can also pose a problem for electrochemical assays. As such, it is critical that biosensor design incorporate a mechanism to minimize nonspecific binding. This is typically done with a blocking reagent that binds to the electrode surfaces to fill any pinholes left in the protein and/or SAM monolayer. Bovine serum albumin (BSA) has been used as a standard blocking agent in molecular biology for decades and

is also commonly used to block electrode surfaces (364–366). Although regularly used, research indicates that BSA is a poor blocking agent. Most biosensor studies perform target detection in buffers like PBS or TBST at a neutral pH. However, because BSA has a pI of 4.7, it carries a negative charge at neutral pH, and such a negatively charged surface would facilitate, not prevent nonspecific adsorption. Furthermore, BSA has been shown to interact with antibody and is even suspected to displace up to 10% of specifically adsorbed antibody (334).

Ethanolamine is another commonly used blocking agent (367–369) that consists of a two-carbon chain with an amine group at one end and a hydroxyl group at the other. After covalent probe immobilization, the ethanolamine binds via its amine group to unbound, activated carboxylic (370) or aldehyde groups (371), deactivating and blocking the surface. However, because the hydroxyl group carries a negative charge, a surface blocked with only ethanolamine will carry an overall negative charge that facilitates adsorption. 1-dodecanethiol is an alkanethiol chain that is commonly used to block gold surfaces after probe immobilization (372). Yet, because it is a hydrophobic molecule, it likely is also an imperfect reagent for blocking.

Because adsorption happens most readily at charged or hydrophobic surfaces, merely filling pinholes in the monolayer is not sufficient to prevent nonspecific adsorption. Reagents carefully chosen to design neutral, hydrophilic surface is the most efficient means of blocking the surface of the electrode. Recent zwitterionic approaches have been extremely successful to improve antifouling capacity. A zwitterion, also called a dipolar ion, has both positive and negative chemical groups with a net charge of zero. Such approaches generate a monolayer of zwitterionic polymers or molecules such as carboxybetaine (373), sulfobetaine (373, 374), cysteine (375) or zwitterionic peptides (376, 377). Although zwitterionic approaches demonstrate excellent antifouling capacity, their prohibitive cost inhibits their practical use. Polyethylene glycol (PEG) is a neutral, hydrophilic polymer that has seen biomedical use for

decades and is currently considered the gold-standard in some fields like drug delivery to reduce nonspecific interactions (378). It has received much attention as a blocking reagent for biosensor applications (379–382).

## History of Electrochemical Biosensor Research

A series of scientific milestones in the 19th and 20th centuries paved the way for the start of biosensor research, including the ability to immobilize proteins onto a surface (383). Although the term "biosensor" was not coined until 1977 by Karl Cammann (384), the first biosensor was built in 1962 by Leland C. Clark, Jr. Clark's glucose enzyme electrode was modeled after his oxygen sensor design and measured glucose by the amount of oxygen that was consumed by glucose oxidase (GOx) as it catalyzed the oxidation of glucose. Early research on the "enzyme electrode" (as the first biosensors were called) mainly focused on the quantitation of various oxidase substrates such as glucose (385–388), urea (389–391), creatinine (392), ions (393, 394), etc typically by electrochemically measuring the consumption of oxygen, production of hydrogen peroxide, or changes in pH. Briefly, enzyme was immobilized in a polyacrylamide gel layer that was wrapped around the electrode surface. Substrates can diffuse through the layer to be catalyzed by the enzyme and products (or lack there-of) diffuse towards the electrode where they are detected electrochemically. Both amperometric (386, 395, 396) and potentiometric techniques (389, 397–399) (which measures the corresponding change in charge density and thus transmembrane potential at the interface between the membrane and solution) were commonly employed. The first immunosensor was published in 1975 to detect yeast mannan (400) and was followed in the next four years by similar immunosensors for syphilis antibody (401), human chorionic gonadotropin (HCG) (402, 403), human serum albumin (HSA), and blood type (404). These potentiometric bioaffinity sensors used membrane-bound antigen or antibody to detect complementary analyte with a corresponding change in charge density and

thus transmembrane potential at the interface between the membrane and solution. Immunosensors were also combined with enzymatic signal amplification to create the first amperometric enzyme immunosensor in 1976 (405). In these systems, antibody is immobilized in a gel membrane at the electrode surface. Analyte competes with labeled antigen for antibody binding and the ratio of labeled vs unlabeled binding sites is concentration dependent (406).

Further work on the enzyme electrode sought to combat problems such as costly production or instability of enzyme when electrostatically immobilized. Thus, the first "microbial sensors" from the early 1980's were effectively enzyme electrodes that measured substrates using immobilized microorganisms that produced the required enzyme (407–409). Other problems with the first generation of enzyme electrodes included a limitation to enzymes that could produce electroactive species. Furthermore, the high potentials required to detect these species generated interfering currents from other electroactive physiological species (410).

To mitigate these limitations, second generation biosensors used soluble redox mediators such as ferrocene derivatives to facilitate electron transfer between the enzyme and electrode and decrease the oxidation potential (411–414). These mediated biosensors enabled non-electroactive species to be measured for the first time (410) and also decreased interference from physiological species by reducing the applied potential (415). However, mediated electron transfer was slow and limited the sensitivity of the sensor (415). The absorption of enzyme to the electrode also caused problems with stability, reusability, and reproducibility (416).

To increase sensitivity, research for third generation of biosensors investigated the use of molecular transducers for direct electron transfer. The term molecular transducer was coined by Ghindilis et al to refer to an enzyme that can directly interact with the electrode (417). I.e. these enzymes such as cytochrome c, peroxidase, and ferredoxin (418–424) can catalyze the transfer of an electron directly between a substrate and the electrode without the need for a mediator like

ferrocene. However, because only a small number of enzymes are capable of direct electron transfer, the third generation biosensors were limited in the analytes they could detect.

Polymer films were used for the first time in the 1980's and 90's to immobilize probe protein. Alkanethiols (343, 425), conductive polymers (426, 427), and silanes (428) were all introduced into biosensor research around this time to more effectively control protein immobilization without losing activity or to immobilize redox mediators for direct electron transfer (429). These biosensors demonstrated a high range of limits of detection (LODs) from target concentrations of 400 pg/mL to 12 ng/mL to 1 μg/mL (428, 430, 431). To enhance sensitivity, interdigitated electrodes (IDEs) were introduced in the late 1980's and early 1990's (432, 433). IDE constitute two electrodes with comb-like fingers that are meshed together just μm apart into an array. They increase current signal through a process called redox cycling. During redox cycling, one electrode of the IDE is biased at a cathodic potential and the other is biased at an anodic potential. The species of interest will be reduced at the cathodic and immediately diffuses to the anode where it is oxidized. A single molecule can therefore contribute repeatedly to the current signal, amplifying it (434). Using this method, early reports by Morita et al and Aoki et al reported an improved LOD of ~5 pg/mL of dopamine and ~1.7 pg/mL for catecholamines respectively (433, 435).

The first advancements required for lab on chip (LOC) technology began in the late 1980's and early 1990's with the introduction of flow-injection (FI) systems for biosensor analysis (413, 436, 437). FI analysis uses a peristaltic pump to flow sample over a functionalized electrode. Because FI systems minimize handling and enhance control, they increase reproducibility and reusability. Semiconductor fabrication techniques like CMOS technology (complementary metal-oxide semiconductor) also gained popularity in the 1990's and 2000's to generate microelectrode arrays for biosensing purposes. These microelectrode

arrays had numerous advantages as described by Wittstock (438). Because the array was composed of ultramicroelectrodes (UMEs), edge effects increased mass transport to the electrode through radial diffusion and the small electrode area reduced background capacitive current. The array of UMEs amplified the current signal while maintaining the properties of an UME. The signal could be further enhanced by interdigitating one UME with another to allow for redox cycling. Lastly, microelectrode arrays have large potential for multiplexed analysis. Early arrays consisted of 64 electrodes (439, 440) though recent reports have used 256 electrodes (441) and even high density arrays of 8192 electrodes (442). As biosensing technology became increasingly miniaturized, advancements in microfluidics have allowed flow-injection systems to become miniaturized and are discussed in detail by Henares et al (443).

**Nanotechnology in Biosensor Development**

Since the late 1990's to early 2000's, the use of nanotechnology for biosensor research has seen explosive growth. Nanotechnology involves the study and manipulation of materials that are 1-100 nm in one dimension (e.g. thin films), two dimensions (e.g. nanotubes, nanowires), or all three dimensions (e.g. nanoparticles, quantum dots). Nanomaterials display unique properties that differ from their bulk material and result from the large ratio of surface area to volume as well as quantum size effects that dominate at the nanoscale (444). Surface effects including increased surface stress and elasticity occur because atoms at the surface of a material have fewer binding partners than their bulk counterparts. Repulsion between free electrons forces the material to deform into a more spherical shape with a smaller surface area to volume ratio (compared to other possible configurations such as a cube) to minimize free energy (445). Fewer binding partners at the surface also correlates to fewer stabilizing forces, giving the surface atoms greater elasticity. In addition, the increased proportion of atoms at the surface of the material causes the nanomaterial to become highly reactive and unstable and results in unique

catalytic properties that the bulk material does not possess (444). Quantum size effects occur because free electrons, which freely move through the bulk material, become confined at the nanoscale (446). This phenomenon of quantum confinement results in altered electrical, magnetic, and optical properties of nanomaterials that scale with size and can therefore be controlled by controlling the size of the nanomaterial.

There are currently a wide variety of nanomaterials and nanostructures. The most common nanomaterials include noble metal nanoparticles (NMNPs) (447), carbon nanomaterials (361, 448), metal oxide nanomaterials (449), polymer nanomaterials (450), and porous nanomaterials (451, 452). An exhaustive discussion of nanomaterials is beyond the scope of this text, but commonly used nanoparticles will be briefly introduced below.

*Noble Metal Nanoparticles*

As discussed above, immobilization of protein to the electrode surface can reduce or even inactivate bioactivity of the probe. Because NMNPs are comparable in size to biomolecules and have large surface areas, biomolecules can be readily immobilized to the NMNP surface without denaturing and thus little to no reduction in binding or enzymatic activity; thus, they exhibit high biocompatibility. Typical NMNPs are comprised of gold (AuNPs) (453), silver (AgNPs) (454), platinum (PtNPs) (455), palladium (PdNPs) (456), or alloys of these materials (457). These NMNPs are fabricated by chemically reducing a noble metal salt in an aqueous or organic solvent. AuNPs, for example, are commonly generated by chemically reducing chloroauric acid ($HAuCl_4$) in aqueous sodium citrate (458). However, due to the high surface energy that results from nanoscale surface effects as described above, NMNPs must be prepared in the presence of a stabilizer (e.g. PEG, thiolated protein, etc) that passivates the surface and prevents aggregation (447, 459). These stabilizers can also be used to introduce charge or chemical groups that facilitate biomolecule immobilization. Core-shell NPs that use a noble metal shell to maintain

biocompatibility and a metal or metal oxide core are also commonly reported in the literature (180, 181).

While the properties of NMNPs differ based on the size and makeup of the nanoparticle (444), NMNPs can be used in two general ways to amplify biosensor signal. First, the NMNPs can be functionalized to the electrode surface where their high biocompatibility and large surface area allow higher densities of active probe biomolecules to be immobilized to the surface of the bulk electrode. The NMNPs can be functionalized to the electrode surface via a SAM layer (462), layer-by-layer assembly (463), hybridization with other nanomaterials to form a complex nanostructure (464, 465), or using sol-gel technology (466, 467). Furthermore, most redox enzymes (e.g. horseradish peroxidase, hemoglobin) cannot transfer electrons directly with the bulk electrode surface because the redox center, shielded by the outer protein shell, is too far away for direct electron transfer to the surface. These biosensors must be supplemented with a redox mediator such as ferrocene. Proteins immobilized on NMNPs, however, do not denature and are more dynamic in their spatial arrangement; this could facilitate contact between the nanoparticle and the enzyme redox center (468, 469). Thus, NMNPs can be used for direct electron transfer from an enzymatic signal without the need for a mediator.

Second, NMNPs can also be used as an electrochemical label in which the NP is attached to biomolecule probe and the current from acidic oxidation of the NMNP into ions corresponds to the analyte concentration (447). For example, Zhang et al conjugated bimetallic Cu@Au core-shell NPs to an antibody for an electrochemical immunosensor (470). The current response from electrochemically oxidizing the Cu into $Cu^{2+}$ correlated linearly with target concentration. Chen et al reported a similar sensor measuring the stripping current from the oxidation of $Ag@SiO_2$ core-shell NPs into $Ag^{+}$ ions (471).

## Conclusion

Biosensor research is becoming increasingly sophisticated and draws on knowledge from many scientific and engineering fields including electrical engineering, electrochemistry, material science, surface chemistry, molecular biology, microbiology, protein biochemistry, and more. Subsequent chapters will draw on knowledge from these fields as detailed in this chapter to describe the development of novel electrochemical assay and sensor platforms.

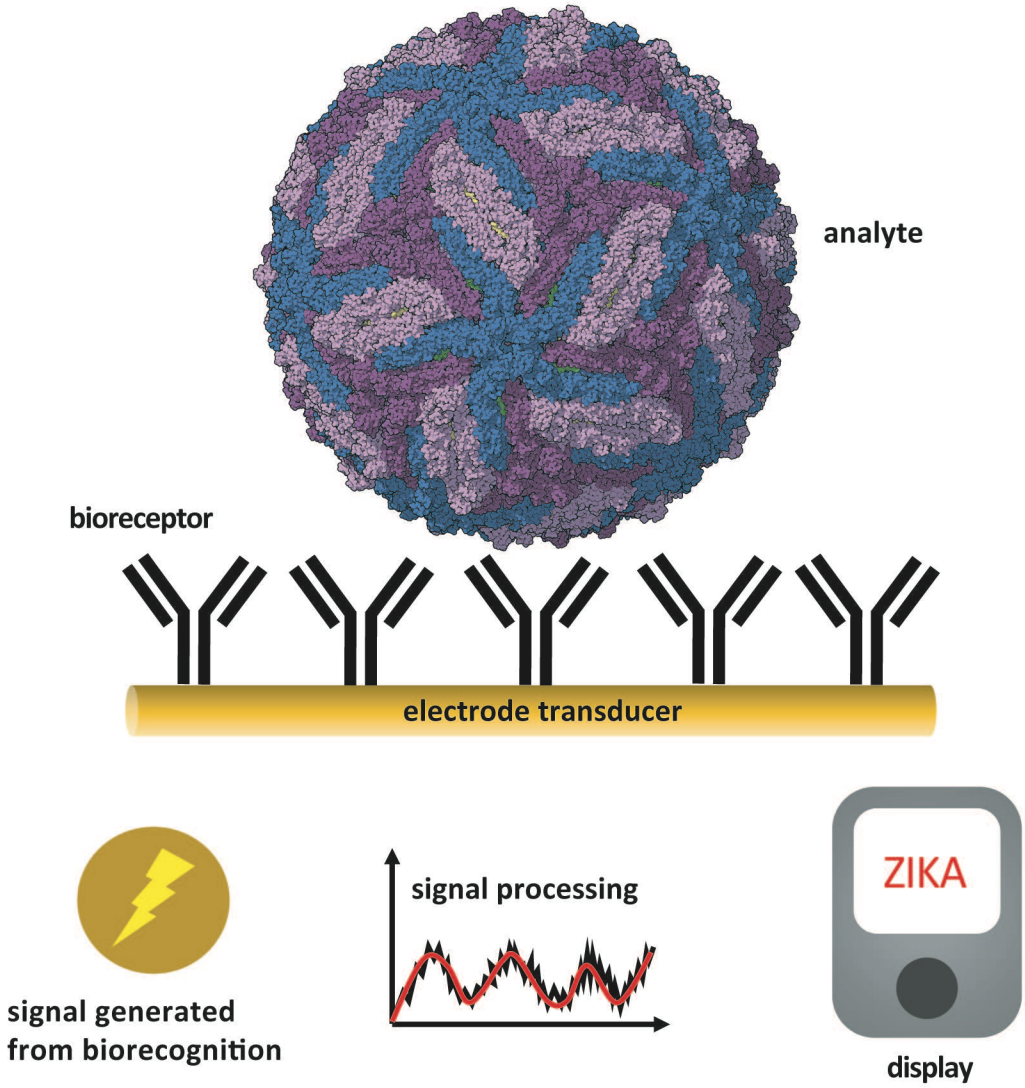


**Figure 2.1 Biosensor.** A transducer converts the signal from a biorecognition event between bioreceptor and analyte into an electrochemical signal that is processed by a signal processor. These results are then shown on the display. Zika virus structure adapted from (15).

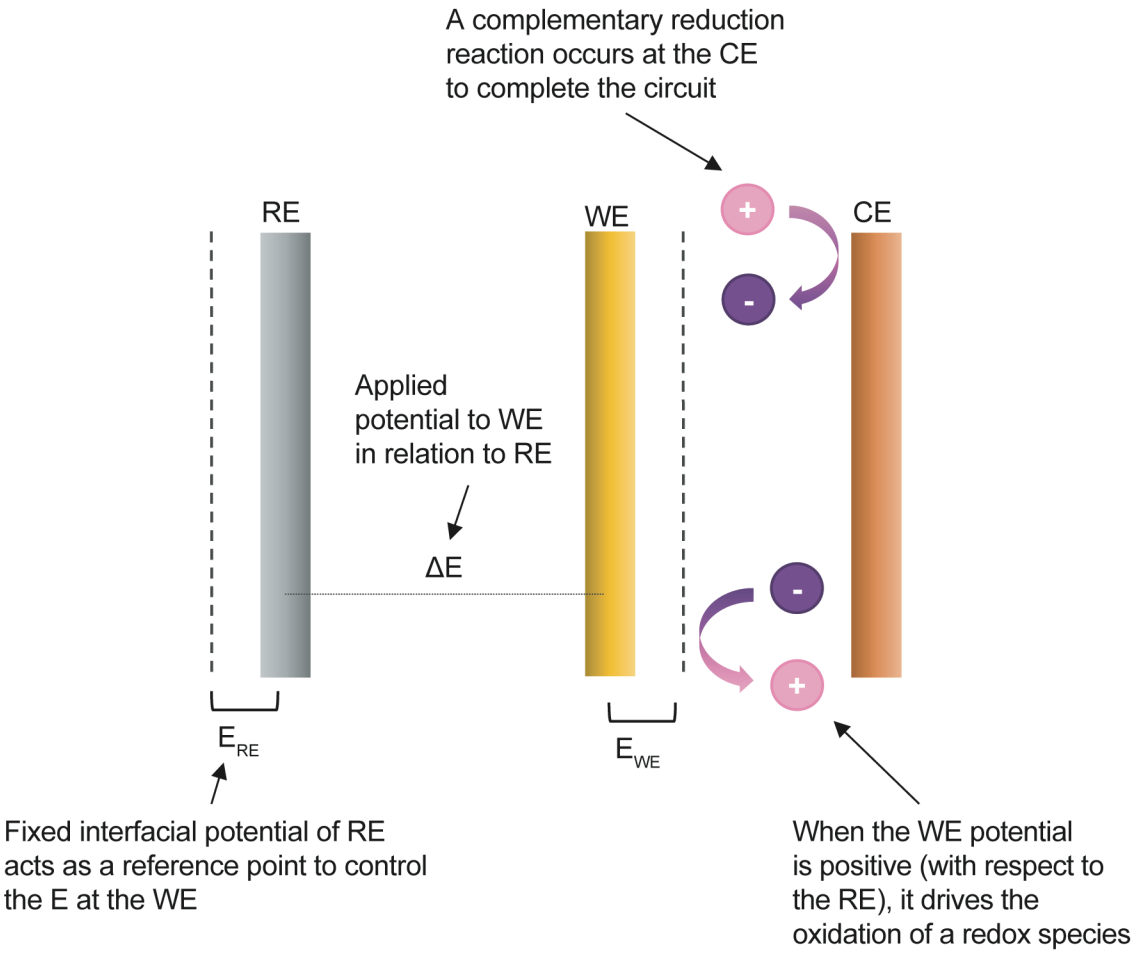


**Figure 2.2 Three electrode system.**

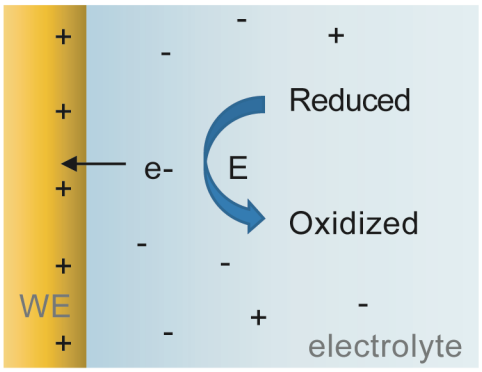


**Figure 2.3 Faradaic current.** Faradaic current is generated as an electron is transferred to or from the working electrode during a reduction or oxidation reaction at a given potential, E.

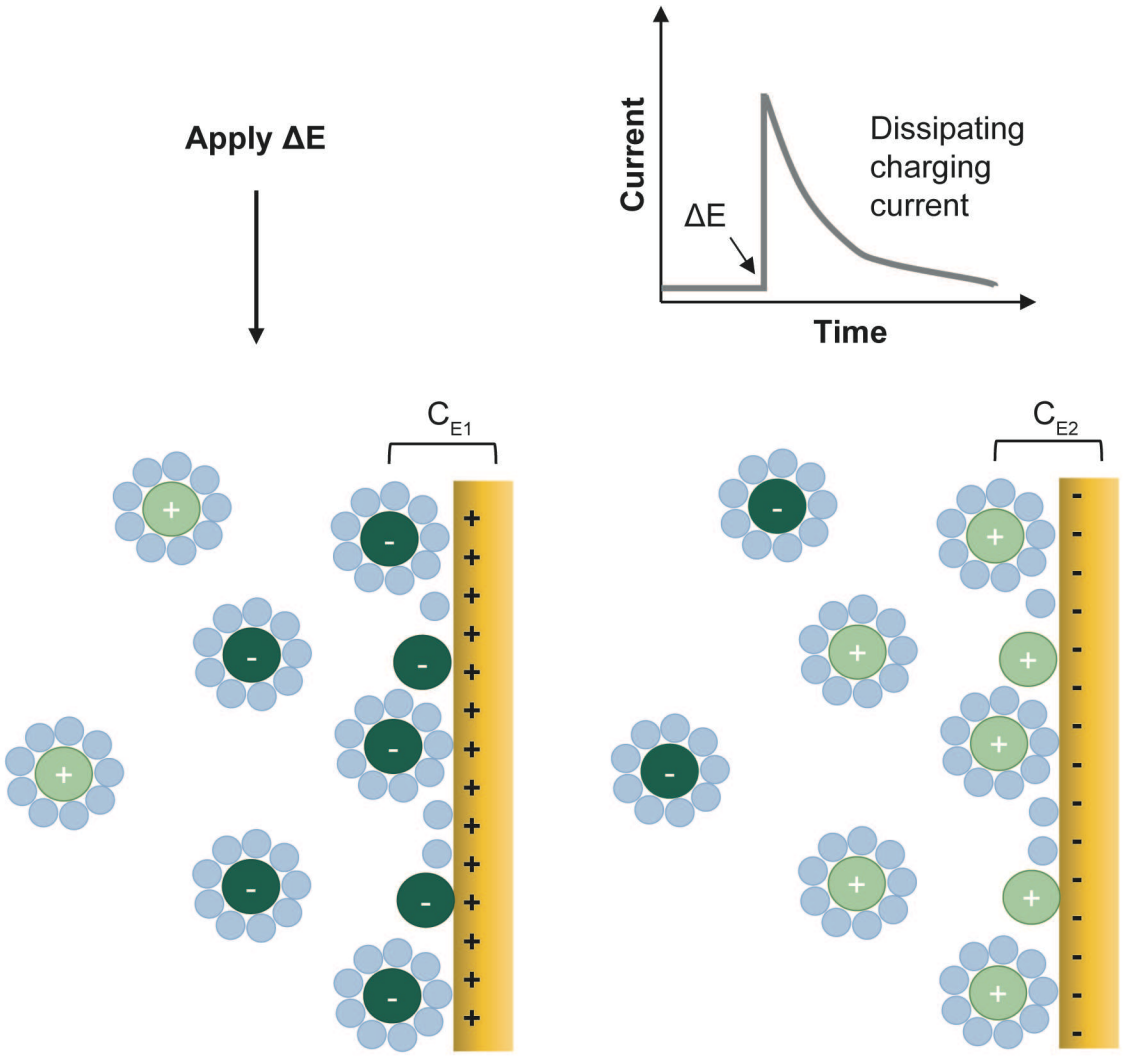


**Figure 2.4 Charging or capacitive current.** At any given potential, charge will accumulate at the electrode surface creating a double layer capacitance ($C_{E1}$). Upon a change in potential (ΔE), the charges will move to re-equilibrate the double layer. As these charges move, a current flows that dissipates over time as the system reaches equilibrium ($C_{E2}$).

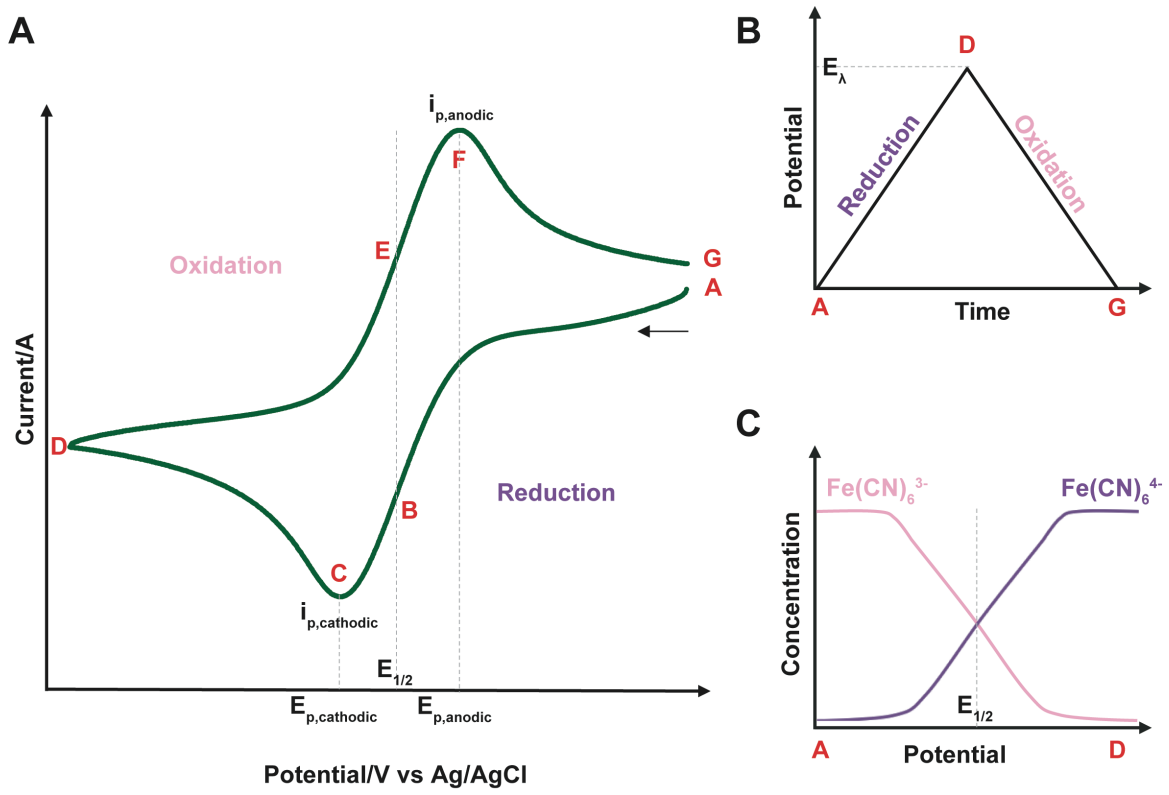


**Figure 2.5 Cyclic voltammetry.** A) Voltagramm of ferricyanide and ferrocyanide analysis. The potential is scanned towards lower potentials starting from point A. At sufficiently low potentials, ferricyanide is reduced to ferrocyanide producing an increase in current signal. The half-wave potential, $E_{1/2}$, is reached at point B where the concentrations of ferricyanide and ferrocyanide become equal. As ferricyanide is depleted at the electrode surface, the current reaches its peak current, $i_{p,cathodic}$, and falls off until the potential reaches the switching potential, $E_\lambda$, at point D. The scan is then reversed in the opposite direction towards higher potentials. At sufficiently high potentials, ferrocyanide will begin to oxidize to ferricyanide. It reaches its $E_{1/2}$ at point E and as ferrocyanide is depleted, the current will again peak at point F and fall off until the final potential at point G. The peak to peak separation ($\Delta E_p$) can be determined by subtracting $E_{p,anodic}$ from $E_{p,cathodic}$. B) Potential scan for cyclic voltammetry. The scan starts at point A and is ramped down to point D, known as the switching potential, $E_\lambda$. The scan is then reversed back. C) Concentration profile of ferricyanide and ferrocyanide during cyclic voltammetry. The scan starts at point A with high concentrations of ferricyanide, which is depleted as it is reduced to ferrocyanide. At $E_\lambda$ (D), high concentrations of ferrocyanide can be oxidized back to ferricyanide. Figure modified from (296).

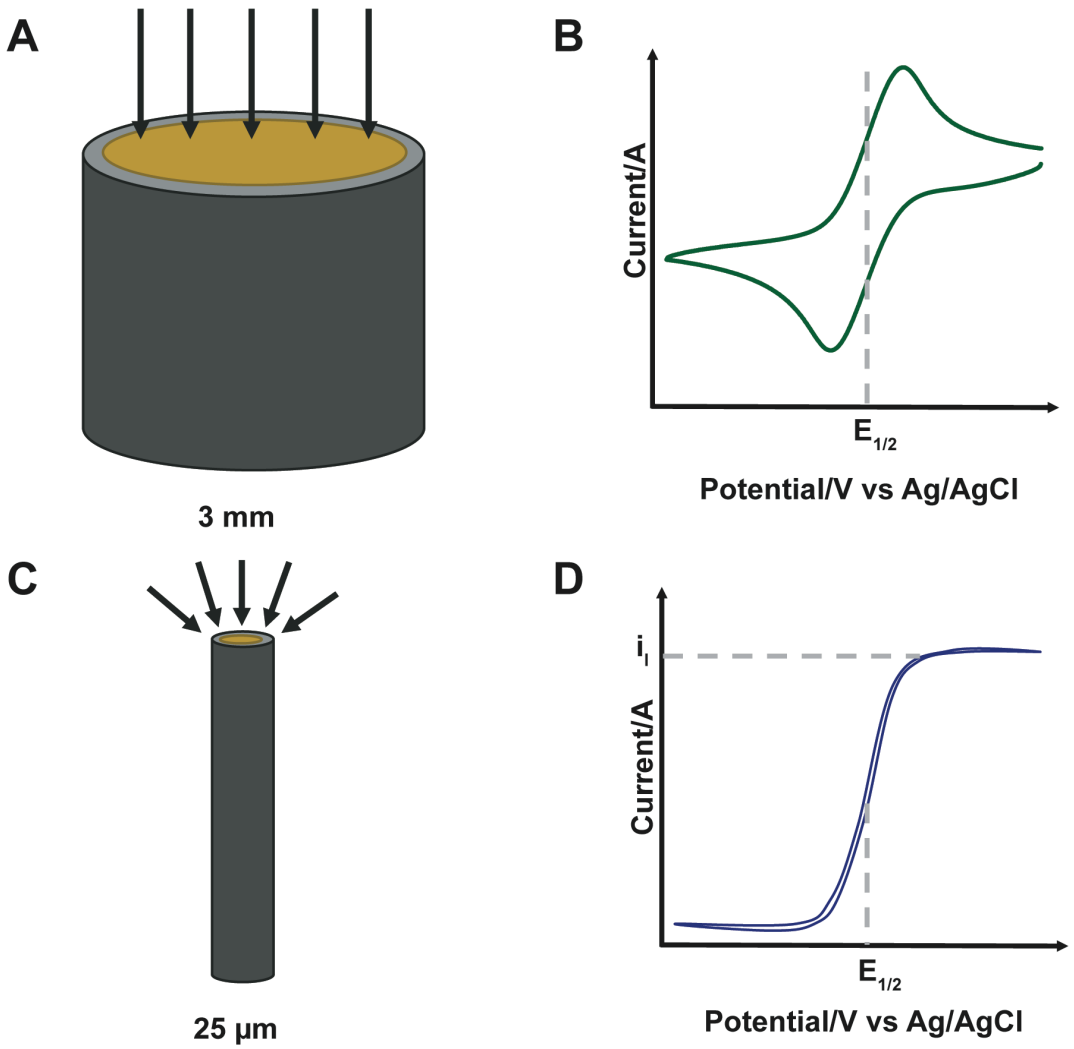


**Figure 2.6 Macroelectrode vs microelectrode behavior.** A) Linear diffusion of species to the macroelectrode surface. B) Duck-shaped voltagramm. Because linear diffusion does not replace species as quickly as they are depleted, the current peaks and then falls off creating the traditional "duck-shaped" voltagramm. C) Radial diffusion of species to the microelectrode surface. D) Steady state voltagramm. Edge effects resulting in radial diffusion increases the rate of mass transport to the electrode surface, replenishing the species at the surface as quickly as they react. In this case, current is no longer limited by mass transport and instead reaches a limiting current, $i_l$, corresponding to the rate of electron transfer. Figure modified from (306, 472, 473).

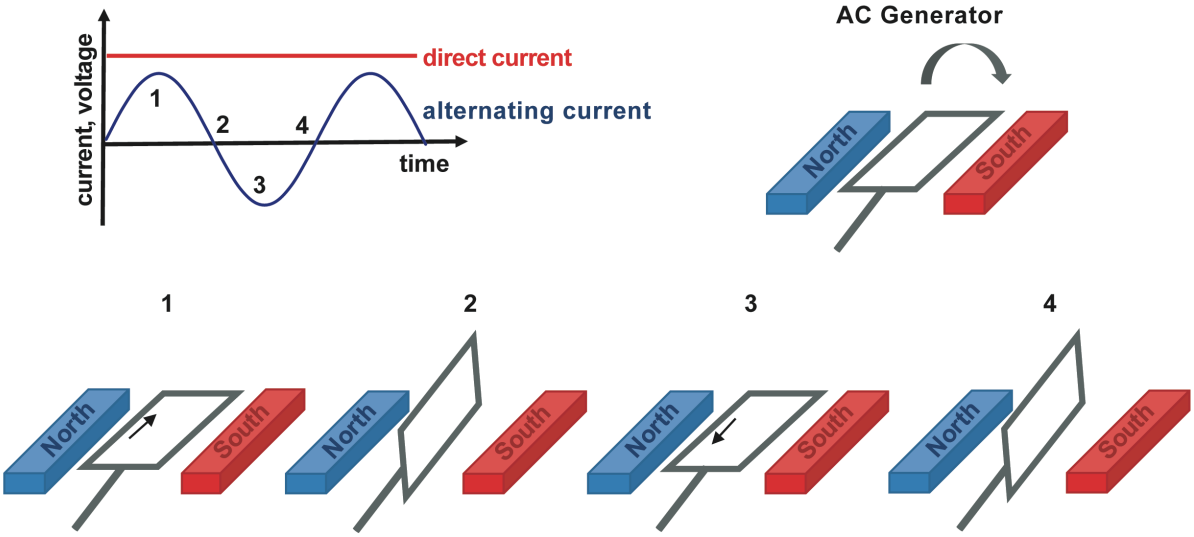


**Figure 2.7 Direct vs alternating current.** DC voltage is static, thus producing a static current signal. AC voltage, however, oscillates back and forth, generating a complementary sinusoidal current response. AC current is generated using an AC generator. By rotating a circuit between two magnetic poles, the voltage across the circuit will continuous change, alternating between two polarities. This voltage generates an alternating current signal. Figure modified from (474, 475).

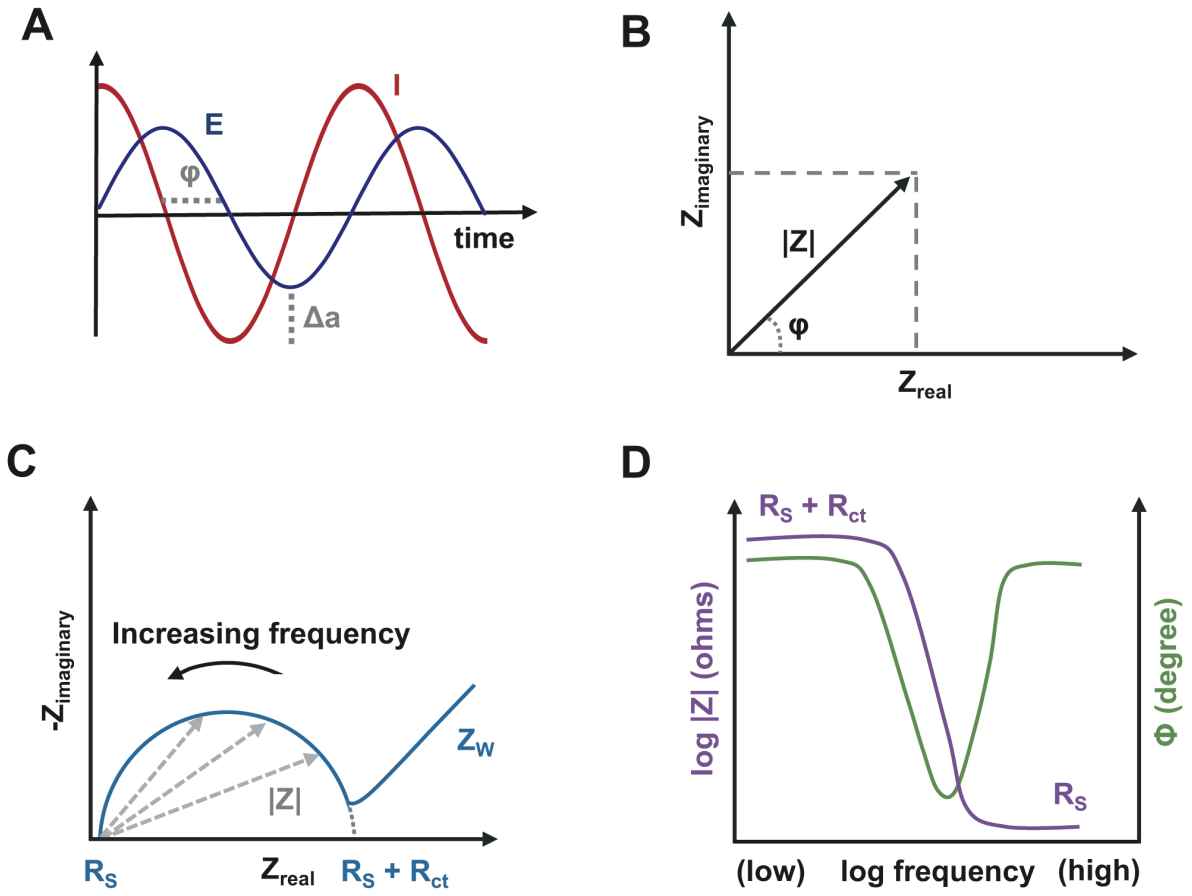


**Figure 2.8 Electrochemical impedance spectroscopy.** A) AC potential (E) and current (I) response. The current and potential signals can be shifted in time by a given phase (φ) and may also differ in amplitude (Δa). B) Impedance, Z, is a complex number with real and imaginary components that can be represented as a vector with an angle (phase, φ) and magnitude, |Z|. C) Nyquist plot. Z is measured through a range of frequencies and imaginary components are plotted against the real components to yield a semicircle shape. At high frequencies, the double layer capacitance acts as a short circuit with only the solution resistance, $R_s$ impeding the current flow. At lower frequencies, the charge transfer resistance dominates, corresponding to the difficulty of oxidizing or reducing a species. At sufficiently low frequencies, the current becomes limited by how quickly species can diffuse to the electrode surface. This impedance due to mass transport is called Warburg impedance, $Z_W$. D) Bode plot. Because frequency is implicit in the Nyquist plot, a Bode plot may be used to explicitly examine the relationship between phase or impedance with frequency. Figure modified from (295, 307).

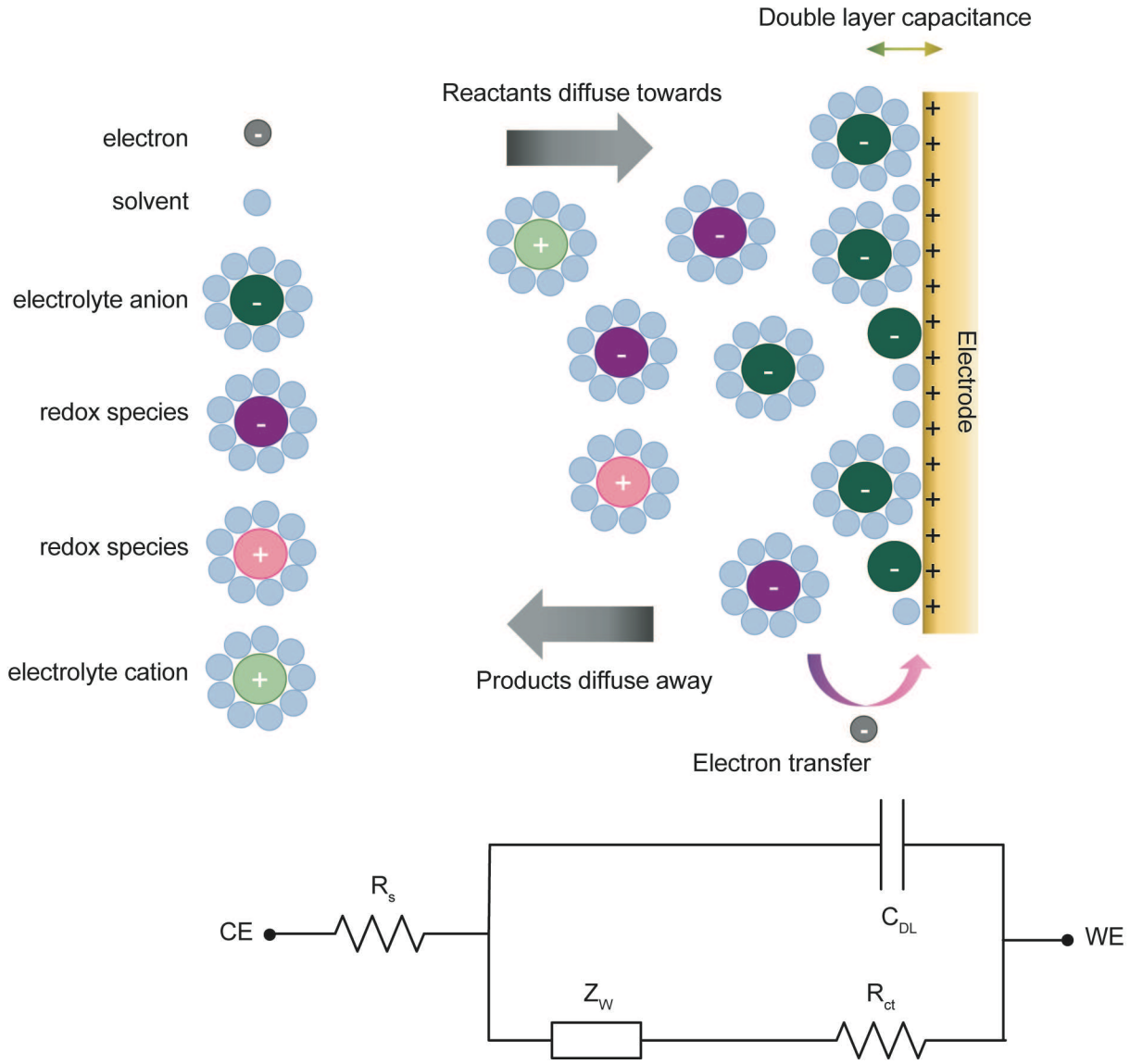


**Figure 2.9 Randle's equivalent circuit.** As the current flows through the system, various phenomena at the electrode surface can be modeled as circuit components. Redox reactions and charging of the double layer capacitance occur simultaneously and are thus placed in a parallel circuit. The redox reaction must overcome impedance related to mass transport of the species to the electrode (Warburg impedance, $Z_W$) as well a charge transfer resistance, $R_{ct}$ which corresponds to the difficulty of oxidizing or reducing a species at a given potential. Both the redox and double layer processes are subject to the solution resistance, $R_s$, which corresponds to how well the electrolyte can conduct electricity and is placed in series with the Faradaic and non-Faradaic components. Figure modified from (476).

# CHAPTER 3 - A NUCLEASE PROTECTION ELISA ASSAY FOR COLORIMETRIC AND ELECTROCHEMICAL DETECTION OF NUCLEIC ACID (477)

## Introduction

Nuclease protection has been an essential tool in molecular biology for over forty years and is an ideal candidate for a simplified nucleic acid detection (NAT) platform. This technique employs an endonuclease such as S1 nuclease (478), mung bean nuclease (479), or RNAse (480) that demonstrates specificity for single-stranded nucleic acids. Traditionally, DNA or RNA that is hybridized to a DNA probe is "protected" from endonuclease digestion and is detected via gel electrophoresis analysis (481). Nuclease protection assays demonstrate high specificity and are effective alternatives for techniques such as Northern blotting and PCR for NAT (482). They were first employed in molecular genetics as a technique to map elements of the genome (483) or quantify messenger RNA transcripts (484, 485) and their traditional use has been extended to investigate drug immunotoxicity (486) and transgenic expression (487). Nuclease protection has also been used to detect endogenous (479, 488) and viral (482, 489) microRNA. More recently, nuclease protection has been integrated with sandwich hybridization assays (SHAs) for colorimetric detection and monitoring of environmental algal species (490–492). Some research has been directed toward clinical use of nuclease protection to detect biomarkers associated with cancer (493–497) or genetic disorders (498) but to date, no work has been done to investigate its potential as an infectious disease diagnostic.

Many viral diseases including Zika fever, influenza, dengue fever, and chikungunya present with general, nonspecific symptoms that encumber differential diagnosis (499). Thus, the Center for Disease Control (CDC) typically recommends NAT on serum, urine, or other biologically-relevant samples to diagnose viral disease during the early stage of infection (260,

500). This is typically done with approved real-time PCR assays which exhibit good specificity and sensitivity – often with limits of detection around $10^3$ genome copy equivalents (GCE) $mL^{-1}$ (261). However, the real-time PCR assay is very technical, requiring design of three sequence-specific probes in conserved regions of the viral genome with expensive fluorescent and quenching tags (261). Many infections like Zika virus infection are associated with medical complications that necessitate monitoring and timely intervention. While gel-based nuclease protection assays have previously served as an effective alternative for PCR in research (482), the lengthiness and technicality of gel analysis limits the traditional assays use as a diagnostic.

To improve the potential of nuclease protection assays as a clinical diagnostic, gel analysis of nuclease protection can be replaced with enzymatic readout. Cai et al developed a nuclease protection sandwich hybridization assay (NPA-SH) in 2006 with an enzyme-mediated signal output (501). Although the assay was subsequently used by other groups for environmental monitoring (490, 492), the NPA-SH format requires three DNA oligo probes: a NPA probe, capture probe, and a signal probe. Designing three separate probes for every target of interest increases the assay complexity and limits its adaptability to other potential analytes.

Here, we report a proof-of-principle nuclease protection-ELISA (NP-ELISA) for the specific and sensitive detection of nucleic acid (Figure 3.1). In contrast to the NPA-SH, the NP-ELISA uses a single oligo capture probe which was designed in this case to have specificity towards a respective Zika (ZIKV) or Kunjin (KUNV) virus sequence. The capture probe is mixed with a nucleic acid target (i) and hybridized products (ii) are immobilized to the bottom of a microtiter plate and are subjected to a digestion reaction with S1 nuclease which degrades single stranded nucleic acid including unbound probe (iii). HRP-conjugated anti-Digoxigenin antibody binds to a digoxigenin molecule bound to the 3' end of the capture probe and facilitates an enzymatic readout (iv). The assay was validated using synthesized target oligos and then

compared for colorimetric, chemiluminescent, and electrochemical detection methods. Although electrochemical detection yielded the best sensitivity, the assay is adaptable to all three formats. The NP-ELISA is a new valuable approach for NAT that uses fewer reagents and inexpensive instrumentation compared to real-time PCR.

## Materials and Methods

### *Materials*

NP-ELISA assays were performed in clear Neutravidin/BSA treated 8-well strips (ThermoScientific Cat# 15128) for absorbance and electrochemical assays and High Sensitivity Streptavidin black 8 well strips (ThermoScientific, Cat#15525) for chemiluminescence assays. S1 nuclease was purchased from Invitrogen (Cat#EN0321). Ultra TMB-ELISA and SuperSignal ELISA Femto Maximum Sensitivity Substrate were purchased from ThermoScientific (Cat#34028 and Cat#37075). HRP-conjugated anti-Digoxigenin antibody was purchased from AbCam (Cat#ab6212). 5× Hybridization buffer was made with final concentrations of 1.5 M NaCl, 5 mM EDTA, and 190 mM HEPES, pH 7.0 (502). Digestion buffer (3 M NaCl, 20 mM Zn acetate, and 600 mM Na acetate, pH 4.5) was used for S1 nuclease digestion (502). Dilution buffer for the nuclease was made according to the manufacturer's protocol. All buffers were made with Millipore Milli-Q water (18 MΩ $cm^{-1}$), filtered with a 0.45 μm filter membrane, and stored at 4˚ C. Oligonucleotide probe and target sequences specific for a section of the envelope protein coding region in Zika (target/probe 1) and West Nile virus Kunjin subtype (target/probe 2) viruses (Genbank Accession # KU501215 and AY274504, respectively) were synthesized by Integrated DNA Technologies. Sequences were as follows:

BG992 (Probe 1): 5' Biotin-TTTGCACCATCCATCTCAGCCTCC-Digoxigenin

BG993 (Target 1): GGAGGCTGAGATGGATGGTGCAAA

BG975 (Probe 2): 5' Biotin-TAGTATGCACTGGTGTCTATCCCT-Digoxigenin

BG1082 (Target 2): AGGGATAGACACCAGTGCATACTA

BG859 (Extended Target 2):

CAGGGATAGACACCAGTGCATACTATGTGATGACTGTCGG

BG 946 (Scrambled Target 2 nonspecific control):

AGCACGTGTCCGTTGTTATTGGAGTACGCACCGAGAAGAA

BG860 (Target 2 90% complementary target):

CAGCGATAGAGACCAGGGCATACTAAGTGATGACTGTCGG

BG861 (Target 2 80% complementary target):

CAGCGAAAGAGACGAGGGCATACAAAGTGTTGACTGTCGG

*Hybridization and Digestion*

A 25 µL solution of 50 fmol probe oligos (BG975 or BG992), 0.5× hybridization buffer, and the indicated target amount were added to a microtube. Probe and target oligos were denatured at 95˚C for 1 minute followed by annealing at 50˚C for 2 minutes. After the annealing step, the hybridized probe:target mixture was transferred to the plate. Prior to use, neutravidin-coated plates were rinsed with 200 µL/well with 1× TBST buffer and incubated for 5 minutes. The digestion reaction mix (final concentrations of 1× S1 digestion buffer and 50U of S1 nuclease) was added to each well and the plate was incubated at 42˚C for 1h. The plate was rinsed five times with 200 µL rinses of 1× TBST and incubated for 5 minutes in between each wash. After rinsing, target detection was performed as described in the following section.

*Absorbance Detection*

Absorbance detection was performed in clear 8-well strips using TMB ELISA substrate after the S1 nuclease digestion step. 100 µL of 1:1000 anti-digoxigenin antibody was added to each well and allowed to incubate for one hour at room temperature. After antibody incubation, wells were again washed five times with 1× TBST buffer. 100 µL of UltraTMB-ELISA was

added to each well. Plates were incubated for 30 minutes at room temperature and then the HRP reaction was quenched with the addition of 100 µL of 2 M $H_2SO_4$. Absorbance at 450 nm was measured using a PerkinElmer VICTOR X5 plate reader. Data was analyzed with Prism GraphPad software. All errors bars indicate standard error of the mean (SEM).

*Chemiluminescence Detection*

Chemiluminescence detection was performed in black 8-well strips using a SuperSignal ELISA Fempto Maximum Sensitivity Substrate. After antibody incubation, wells were washed five times with 1× TBST. 100 µL of substrate was added to each well and allowed to incubate for no longer than five minutes. Total luminescence was measured using a PerkinElmer VICTOR X5 plate reader. Data was analyzed with Prism GraphPad software. All error bars indicate SEM.

*Electrochemical Detection*

Electrochemical assays were performed in clear 8-well strips using a CHI1242B Potentiostat (CH Instruments, Inc, TX). A 25 µm diameter Au disk microelectrode (CH Instruments, Model CHI106) was used as the working electrode. The working electrode was polished with an alumina slurry (0.1 µm diameter), washed with water, then cleaned electrochemically through cycling in 50mM KOH before each use. An Ag/AgCl microelectrode (25µm diameter, eDAQ, Colorado Springs) was used as the reference/counter electrode in a two-electrode setup. After the rinses, 100µL of 1:1000 anti-digoxigenin was added to each well and incubated for 1 hour at room temperature. After antibody incubation, wells were again washed five times with 1× TBST buffer. 100 µL of Ultra TMB-ELISA or 100 µL of 1mM hydroquinone (HQ) with 0.1% $H_2O_2$ were added to each well and incubated for 30 minutes. The oxidation of TMB or HQ was quenched with 10 µL of 8 M $H_2SO_4$. SWV measurements were taken in a range of -0.2 V to 1.4 V for TMB and 0.4 V to -0.4 V for HQ at a frequency of 15 Hz and were

conducted in a CS-3A Cell Stand faradaic cage. SWV curves were averaged and the peaks were integrated from ~0.47 V to ~0.62 V using the automatic peak finding function of the CHI1242B software. The data was then analyzed with Prism GraphPad software. All error bars indicate SEM.

## Results and Discussion

### *Optimization of Nuclease Protection*

Oligo probes were designed with sequence specificity for either ZIKV (Target 1; BG992) or KUNV (Target 2; BG975). To optimize the probe concentration for use in the assay, BG992 and BG975 were titrated out and incubated with anti-digoxigenin HRP-conjugated antibody. The signal response was analyzed with absorbance and the results are presented in Figure 3.2a. As expected, increasing concentrations of probe increased the signal response until the signal saturated at $6\times10^{12}$ molecules $mL^{-1}$. Similar results were obtained for both the ZIKV and the KUNV probes, suggesting that oligo sequence should not affect the detection mechanism. A linear dynamic range of $6\times10^{10}$ - $6\times10^{12}$ molecules $mL^{-1}$ was determined, spanning three orders of magnitude. The probe concentration that gave the highest signal without saturation was $6\times10^{12}$ molecules $mL^{-1}$ and was used for downstream applications.

The effect of S1 nuclease concentration on the absorbance signal was also investigated (Figure 3.2b). The enzyme was serially diluted and allowed to catalyze degradation of $6\times10^{12}$ molecules $mL^{-1}$ (50 fmol) of probe (BG992) bound to the neutravidin plate in S1 digestion buffer for 1 hour at 42˚ C. Maximum signal was retained with increasing amounts of nuclease from 5 μU to 0.5 U. Addition of 5 U of nuclease caused the signal to drop dramatically and 50 U resulted in a complete loss of signal. To ensure complete degradation and removal of unbound nucleic acid, 50 U (5 μL of 10 U/μL) of nuclease was chosen for further experiments.

DNA oligo targets (Target 1 (BG993) or Target 2 (BG1082)) and complementary probes (Probe 1 (BG992) or Probe 2 (BG975)) were designed and synthesized to test target detection by nuclease protection. The targets were hybridized to their respective probe and unbound probe was digested with S1 nuclease. A range of concentrations were then tested to determine the linear dynamic range (LDR) and the limit of detection (LOD). For the absorbance readout, 3,3',5,5'-Tetramethylbenzidine (TMB) was used as a colorimetric substrate for HRP. The results in Figure 3.3a demonstrate a sigmoidal response with a linear dynamic range of $9.64\times10^{10}$ – $1.20\times10^{13}$ molecules $mL^{-1}$. This range is consistent with that obtained for the probe titration. LOD is generally calculated using the linear calibration curve according to ICH standard (503), through

$$\text{LOD} = \frac{3.3\sigma}{m} \quad (3.1)$$

where $\sigma$ is the standard deviation of the blank sample and $m$ is the slope of the regression line. We found, however, that using this method for absorbance detection produced artificially low LODs that did not account for the signal drop-off outside the linear range. The LOD was instead calculated via

$$\text{LOD} = \mu_{\text{blank}} + 3\sigma_{\text{blank}} \quad (3.2)$$

where $\mu_{\text{blank}}$ and $\sigma_{\text{blank}}$ are the mean and standard deviation respectively of a series of blank samples (504). With this method (equation 3.2), the LOD was calculated to be $9.80\times10^{10}$ molecules $mL^{-1}$. To place our results in perspective, the CDC reported an LOD of $2.45\times10^{3}$ genome copy equivalents (GCE) $mL^{-1}$ for their Trioplex real time PCR assay which is used to detect ZIKV, dengue virus, and chikungunya virus (261). Because the LOD for the absorbance readout is several orders higher than comparable clinical assays, it may limit the absorbance assay's applicability to viral diagnostics. However, the absorbance NP-ELISA may still be used for accurate detection of nucleic acid at higher concentrations.

### *NP-ELISA Specificity*

To test the specificity of the NP-ELISA, nuclease protection was attempted with nonspecific target oligos. As shown in Figure 3.3a, when increasing amounts of Target 2 (BG1082) are added to Probe 1 (BG992), no protection was observed. Likewise, when Target 1 (BG993) was added to the Probe 2 (BG975), no protection was observed. This indicates that the nonspecific target is not able to protect the probe and thus the probe oligos are digested by the enzyme in the presence of non-specific targets. To further validate the specificity of the assay, three different nonspecific targets were employed. The targets were scrambled to have 90% (36/40 matched base pairs), 80% (32/40) or 0% complementarity to Probe 2 while maintaining equivalent GC%. They were added to the reaction in 5× excess compared to the probe concentration. The results (Figure 3.4) show that even with high sequence similarity (4 mismatches or 8 mismatches, 90% and 80% complementarity respectively), nonspecific targets provide virtually no protection to the probe oligo from S1 nuclease digestion and do not differ significantly from the negative control (no probe). These data suggest a high specificity that may be further confirmed by testing protection with 1-3 mismatches and agree with the reported use of nuclease protection to detect single nucleotide mutations (505–507). The targets for the specificity assay, including the 100% complementary oligo, were designed to have overhanging sequences. These data also suggest that overhanging target DNA sequences do not have a significant effect on specific target detection.

### *Increasing NP-ELISA Sensitivity through Chemiluminescent Detection*

Because the LOD for NP-ELISA absorbance detection is significantly higher than LODs for clinically used assays like the Trioplex assay (261), chemiluminescent and electrochemical HRP detection schemes were tested to see if the LOD could be significantly improved. Chemiluminescent substrates have been used in place of colorimetric substrates to increase the

sensitivity of ELISAs (508). The assay was tested with SuperSignal ELISA Fempto Maximum Sensitivity Substrate for detection (Figure 3.3b), which yielded a comparable, though slightly smaller dynamic range compared to absorbance ($4.82\times10^{11}$ – $1.20\times10^{13}$ molecules $mL^{-1}$). Because the chemiluminescent substrate did not significantly increase assay sensitivity, no further experiments were performed with the chemiluminescent substrate.

*Electrochemical Characterization of Hydroquinone/Benzoquinone and 3,3',5,5'-Tetramethylbenzidine*

HRP catalyzes the reduction of peroxide into water using a cosubstrate (e.g. TMB) that functions as an electron donor. HRP thus oxidizes TMB in a two-step irreversible process. The first one-electron oxidation of TMB produces a blue-colored product consisting of an equilibrium between the cation free-radical and a charge transfer complex of the precursor diamine and its diimine oxidation product (509, 510). At acidic pHs, the second-electron oxidation product becomes stable, yielding the yellow-colored diamine (509, 511). These two products can be quantified with absorbance at 370nm and 420nm respectively (509). TMB and its oxidized forms are also electrochemically active, generating a faradaic current that can be detected by electrochemical techniques. The concept of a plate-based electrochemical immunoassay was published as early as the 1980s (512), but has not been widely studied and has been overshadowed by immunosensor research. Electrochemical detection typically provides lower LODs, wider dynamic ranges, and better sensitivity compared to absorbance techniques (513). Additionally, interference from turbid or colored samples is not an issue for electrochemical analysis as it is the case spectrophotometric techniques (514). Lastly, the instrumentation for voltammetry is relatively inexpensive (~$2000 USD) when compared to a real time PCR system (~$15,000 USD) or even a plate reader (~$5000 USD) and is easily miniaturized (514).

To see if electrochemistry could increase the NP-ELISA assay's sensitivity, TMB was characterized with cyclic voltammetry as an electrochemical HRP substrate and optimized for square wave voltammetry detection. Square wave voltammetry (SWV) is a pulsing technique known to be both fast and highly sensitive (304). As a differential method, the peak height of a SWV curve is not always proportional to the concentration of the species, so peak area integration was employed to give a more accurate readings (515). Although TMB is the most widely used as an HRP substrate due to its chromogenic properties and is an easily accessible reagent for electrochemical detection, some research has shown an inability to detect TMB using SWV (516). Multiple other molecules can function as an HRP substrate including hydroquinone (HQ), o-phenilendiamine, p-chlorophenol, and more (516). Due to its widespread use in biosensor applications (355, 517–520), HQ was chosen as a second electrochemical substrate to compare against TMB. Like TMB, HQ also undergoes a two-electron oxidation to form its product p-benzoquinone (BQ) via a semiquinone intermediate (521). To determine the optimal electrode material for analysis, cyclic voltammetry (CV) was performed with both enzymatic products (1 mM BQ in 1× PBS, pH 7.4 and ox2-TMB in proprietary citrate buffer + $H_2SO_4$, pH 1) using Au (2 mm diameter) and glassy carbon electrodes (GCE) (3 mm), as well as a Pt electrode (2 mm) to test BQ (Figure 3.5). BQ exhibits one reduction peak at 0.115 V for Au, 0.036 V for GCE, and 0.067 V for Pt and a single oxidation peak at 0.179 V, 0.315 V, and 0.304 V respectively. Peak to peak values ($\Delta E_p$) are shown in Table 1 and are graphed in Figure 3.5b. The $\Delta E_p$ for GCE and Pt are large at 279 mV and 237 mV respectively, indicating a quasi-reversible process /slow electron transfer kinetics. $\Delta E_p$ for Au, however, was close to ideal at 64 mV and suggests that the BQ reduction to HQ is reversible at an Au electrode. The Au working electrode was thus chosen for further HQ-BQ analysis.

Interestingly, the redox behavior of ox2-TMB was different at Au and GCE electrodes. At the Au electrode, ox2-TMB exhibits two reduction peaks at 0.615 V and 0.473 V but only a single oxidation peak at 0.549 V. Conversely for GCE, there is one reduction peak at 0.486 V and one oxidation peak at 0.525 V. The $\Delta E_p$ for GCE was 39 mV, which suggests that the species readily adsorbs to the carbon surface (295).

**Table 1. Peak to peak separation of BQ CV curves**

| Electrode Metal | $\Delta E_p$ (mV) |
|---|---|
| Au | 64 |
| GCE | 279 |
| Pt | 237 |

This was also evidenced by extensive fouling as depicted in Figure 3.6. Although fouling was also noted for both BQ and TMB at the gold electrode, it was less pronounced. To mitigate the effects of fouling, the Au electrode was polished with alumina slurry then washed with Milli Q water in between all measurements and was used for downstream TMB analysis.

Electrochemical characterization of the HRP substrates and products was performed using cyclic voltammetry and the results are shown in Figure 3.7. 1 mM HQ and 1 mM BQ in 1× PBS were tested and compared in Figure 3.7a. HQ exhibited oxidation and reduction peaks at 0.241 V and 0.071 V respectively with a $\Delta E_p$ of 170 mV, which is indicative of a quasireversible process. BQ however, showed oxidation and reduction peaks at 0.179 V and 0.115 V with a $\Delta E_p$ of 64 mV. It is not clear what leads to quasireversible electrochemical behavior for HQ but not BQ. Furthermore, BQ exhibited a second small reduction peak at -0.133 V which could correspond to the semiquinone intermediate and was not observed at the GCE and Pt electrodes.

Next, the electrochemical behavior of TMB was analyzed in a 1-Step TMB-Ultra solution from ThermoScientific (Figure 3.7b). The clear species exhibited two oxidation peaks at 0.606 V and 0.412 V as well as two reduction peaks at 0.439 V and 0.267 V. The blue species (ox1-

TMB) was generated by adding 50µL of 200 pg $mL^{-1}$ anti-Digoxigenin/HRP in 1× PBS to 900µL of clear TMB substrate. It behaved similarly with two oxidation peaks at 0.563 V and 0.384 V and two reduction peaks at 0.418 V and 0.273 V. Because the yellow species (ox2-TMB) is only stable at low pH, it was generated by adding 100µL of 8 M $H_2SO_4$ to the solution and it demonstrated different electrochemical behavior. Likely due to the lower pH, the two reduction peaks were shifted towards higher potentials at 0.615 V and 0.473 V. Only a single oxidation peak was noted at 0.549 V and is likely due to the instability of the TMB intermediate form at low pH.

Due to its speed and sensitivity, square wave voltammetry was used for assay analysis. Initial potential ($E_{initial}$) was optimized for BQ analysis as shown in Figure 3.8a. A small relationship between $E_{initial}$ and peak current ($i_p$) was observed. Starting the scan at higher potentials may convert extra HQ to BQ before being converted back to HQ during reduction. Thus, starting at higher potentials has a small signal amplification effect. Scan frequency was also optimized as shown in Figure 3.8b. Higher frequencies generate a larger signal but may also correspond to higher capacitive background signal. The signal to noise ratios are listed in Table 2 and were largest for 15 Hz (3.05) which was chosen for further analysis.

*Increasing NP-ELISA Sensitivity through Electrochemical Detection*

TMB and HQ were compared in the NP-ELISA for sensitivity and the results are shown in Figure 3.9. A probe titration was performed for electrochemical detection with both TMB and HQ to optimize the probe amount for the electrochemical assay. HQ as a substrate yielded a wider dynamic range ($6.02\times10^5$ – $6.02\times10^{15}$ molecules $mL^{-1}$) compared to the absorbance readout with TMB, but the variability was higher (Figure 3.5d). The probe titration data for TMB (Figure 3.5b) shows a linear dynamic range of 0 – $6\times10^{11}$ molecules $mL^{-1}$, which is several

magnitudes larger than the absorbance readout ($9.64\times10^{10}$ – $1.20\times10^{13}$ molecules $mL^{-1}$), suggesting a much higher sensitivity for electrochemical TMB readout versus absorbance

**Table 3.2. Relationship between frequency and signal to noise ratio for square wave voltammetry**

| Frequency (Hz) | S/N |
|---|---|
| 30 | 2.99 |
| 15 | 3.05 |
| 10 | 3.01 |
| 5 | 2.71 |

readout. At concentrations greater than $6\times10^{13}$ molecules $mL^{-1}$, the oxidized TMB rapidly precipitates out of solution and yields little to no electrochemical signal. However, in the tested range, TMB peaks were sharper and more defined than the HQ peaks (Figure 3.9a and 3.9c respectively). Given its demonstrated superiority as an electrochemical substrate, TMB was chosen over HQ for downstream applications. A probe concentration of $6\times10^{12}$ molecules $mL^{-1}$ (50 fmol) was chosen for electrochemical target detection.

*Sensitivity of Electrochemical Detection*

The sensitivity of the NP-ELISA with TMB-based electrochemical detection was assessed for a DNA oligo target (Figure 3.10). A linear range of 0 - $6\times10^{13}$ molecules $mL^{-1}$ was determined, in agreement with the electrochemical probe titration. While electrochemical detection has a significantly higher sensitivity than absorbance, poor reproducibility at low concentrations may limit the accuracy of the assay. Reproducibility may be improved by using electroactive substrates that mitigate the quasi-reversibility of the TMB reaction and the fouling of the electrode with electrochemical species. The LOD was calculated using the linear calibration line according to the ICH guidelines (503) via Equation 1. The LOD was determined to be $3.72\times10^{3}$ molecules $mL^{-1}$. Reported viral loads range from $10^{3}$-$10^{8}$ GCE $mL^{-1}$ in blood and urine (139). The dynamic range for the NP-ELISA is significantly wider than the reported

clinical range and the calculated LOD is similar to that of the Trioplex assay at $2.45\times10^3$ GCE $mL^{-1}$ (261). By detecting such small amounts of nucleic acid, clinicians may be able to diagnose infection sooner and enable earlier medical intervention for at-risk fetuses.

## Conclusion

In this work, we have described a novel nuclease protection ELISA (NP-ELISA) that has clinical relevance as an alternative to real time RT-PCR. The assay has excellent specificity with highly similar sequences and is compatible with multiple signal visualization modalities. Electrochemical detection can reach an LOD of $3.72\times10^3$ molecules $mL^{-1}$, within a relevant clinical range for nucleic acid detection. Further research is required to address the limitations of this study. Because a synthetic system was used to assess proof-of-concept principles, more work is required to address the functionality of the assay with biological samples. Furthermore, poor reproducibility at low concentrations can obscure the accuracy of electrochemical analysis and may be a result of the quasi-reversible nature of these redox reactions and the propensity of these species to foul the electrode surface. However, potentiostats for electrochemical detection are significantly less expensive and more portable than real time PCR systems, making the assay more accessible for sensing or screening in remote areas. For example, our previous research with microwire electrodes shows that electrochemical detection is easily miniaturized into handheld, disposable paper sensors (522, 523). Our research group is currently working to implement the NP-ELISA on microwires for antibody-less, hand-held detection of nucleic acids.

In addition to its capacity for miniaturization, the NP-ELISA has large potential as a multiplexed assay. For the antibody-based assay, sequence specific probes can be designed with conjugated small molecules other than digoxigenin. Antibodies specific for these small molecules can be conjugated to different enzymes with different electroactive substrates. Because oxidation or reduction of the reaction products would occur at different potentials, one

potential sweep would allow the user to identify each target in a single sample at a different potential. This greatly increases the NP-ELISA's usefulness as a differential diagnostic tool. The data presented here as well as above mentioned future directions suggest that the NP-ELISA is a viable alternative for clinical NAT with potential for direct, multiplexed, and hand-held detection of pathogen nucleic acids.

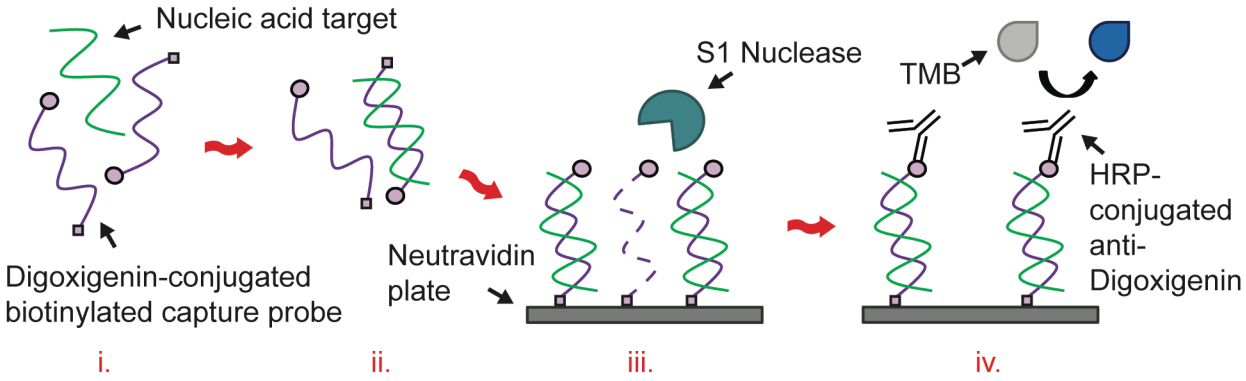


**Figure 3.1. Conceptualization of NP-ELISA.** Oligo capture probes specific for ZIKV (BG992) or KUNV (BG975) are mixed with target nucleic acid (i) and are allowed to hybridize (ii). The hybridized probe is immobilized to a neutravidin plate via a 5' biotin molecule (iii). S1 nuclease degrades any unbound probe, leaving only the hybridized probe behind (iii). An HRP-conjugated antibody binds to the 3' Digoxigenin molecule on the probe and catalyzes the oxidation of TMB to produce a colorimetric or electrochemical signal (iv).

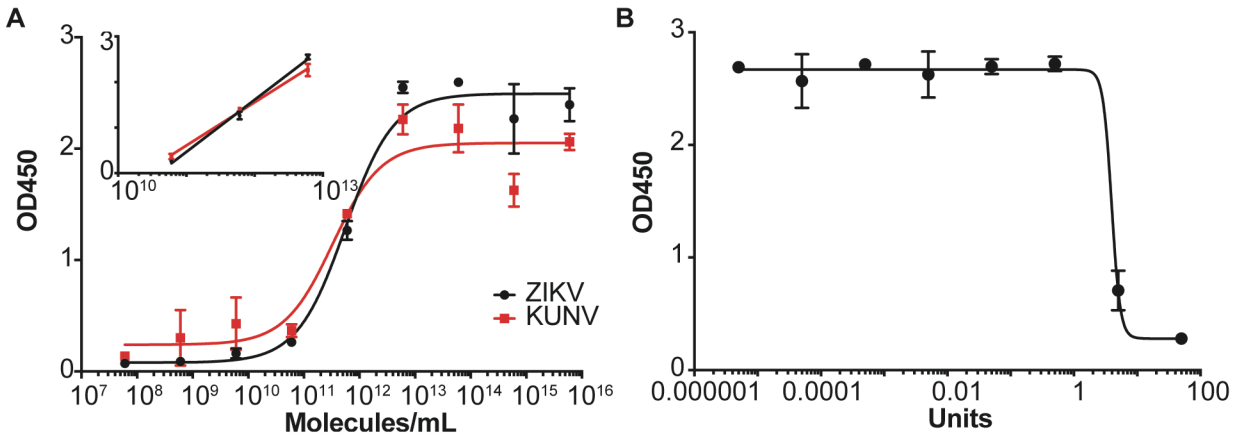


**Figure 3.2. Optimization of nuclease protection.** A) The effect of probe concentration on absorbance signal was examined. A sigmoidal response was observed with a linear range of $6\times10^{10}$- $6\times10^{12}$ molecules $mL^{-1}$. Probe sequence (BG992 vs BG975) had no effect on signal response. B) The effect of S1 nuclease concentration on absorbance signal was investigated.

Dilutions lower than 5U had no effect on the signal. 50U of enzyme caused total loss of signal, indicating complete digestion of the probe (BG992).

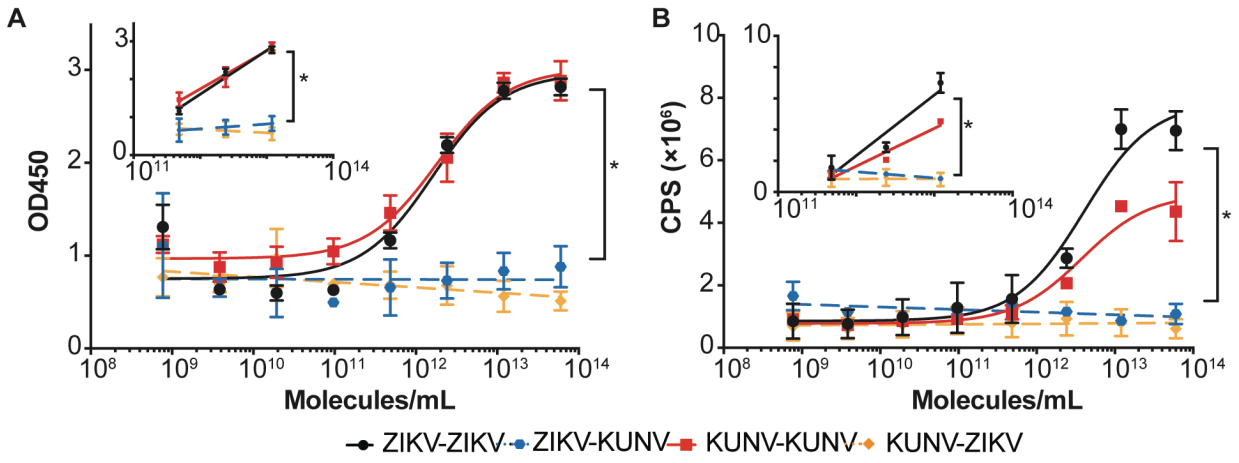


**Figure 3.3**. **Spectrophotometric Detection of Oligo Target.** A) Oligo target was titrated out to determine the effect of target concentration on absorbance signal. A sigmoidal signal response was obtained with a linear dynamic range of $9.64\times10^{10}$ – $1.20\times10^{13}$ molecules $mL^{-1}$. The limit of detection was determined to be $9.80\times10^{10}$ molecules $mL^{-1}$ for absorbance detection. B) A chemiluminescent substrate was used in attempt to increase the sensitivity of spectrophotometric detection. A linear range of was determined to be $4.82\times10^{11}$ – $1.20\times10^{13}$ molecules $mL^{-1}$, which is smaller than the range determined for absorbance detection. Because chemiluminescent detection did not increase sensitivity, no further experiments were done with the substrate.

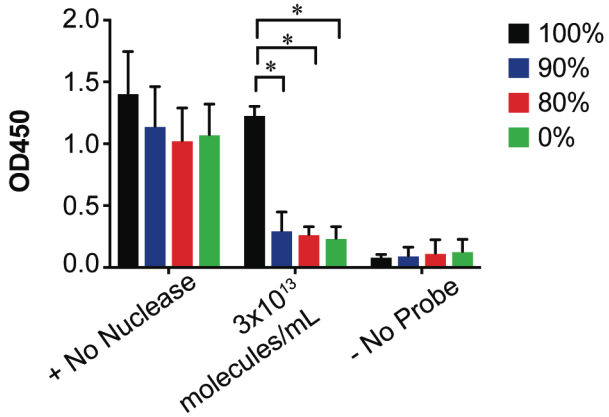


**Figure 3.4**. **Effect of mutations and target length on nuclease protection.** Mutations were added to the target oligos (BG860, BG861, BG946) and tested for capacity for nuclease protection. Even with high complementarity, the signal from mutated targets did not differ significantly from the - control. To test the effect of length on protection, these targets were designed to have overhanging sequences. Signal from the 100% complementary target (BG859)

did not differ significantly from the + control, suggesting that overhangs to not detrimentally affect protection.

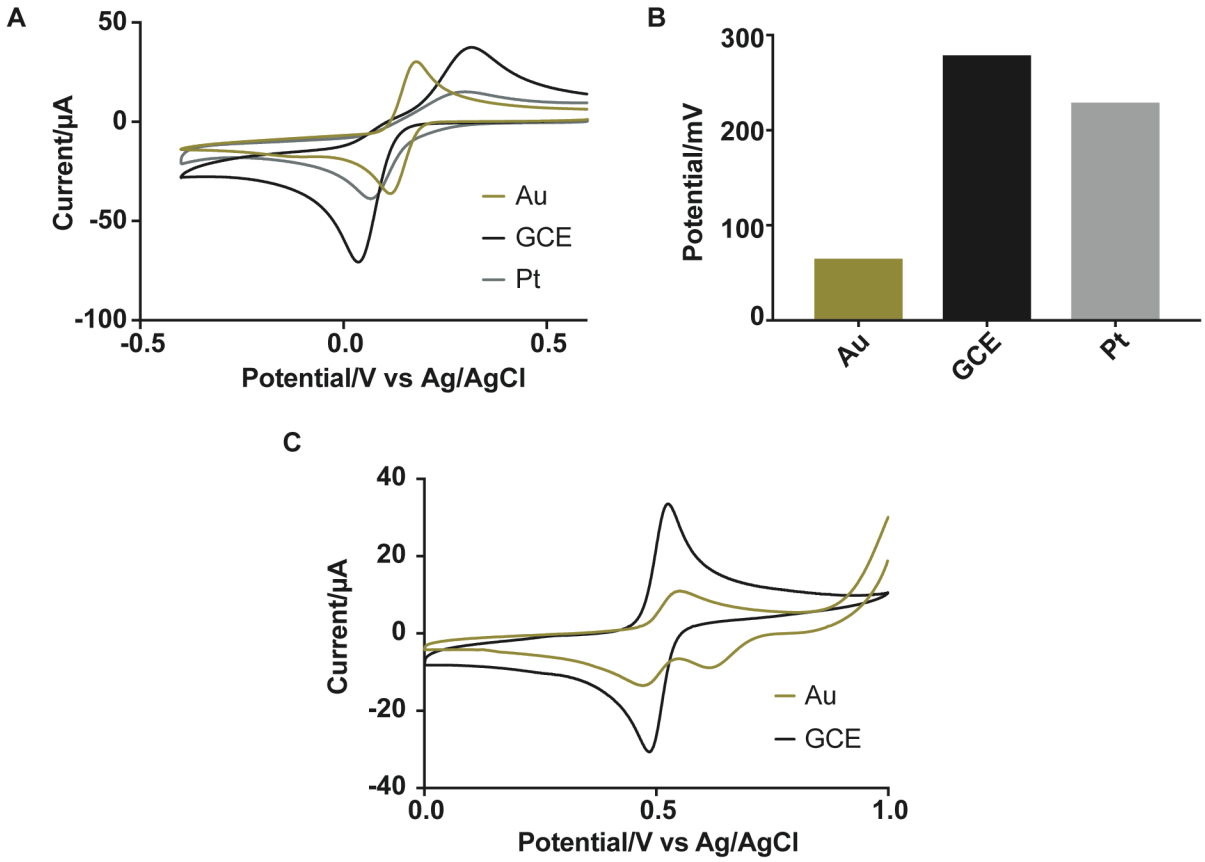


**Figure 3.5**. **Electrode optimization for BQ and TMB analysis.** A) Cyclic voltammetry of 1 mM BQ in 1× PBS (pH 7.4) with Au, GCE, and Pt electrodes. B) $\Delta E_p$ values for BQ CV analysis with Au, GCE, and Pt electrodes. C) Cyclic voltammetry of ox2-TMB in proprietary citrate buffer + $H_2SO_4$ (pH 1) with Au and GCE electrodes.

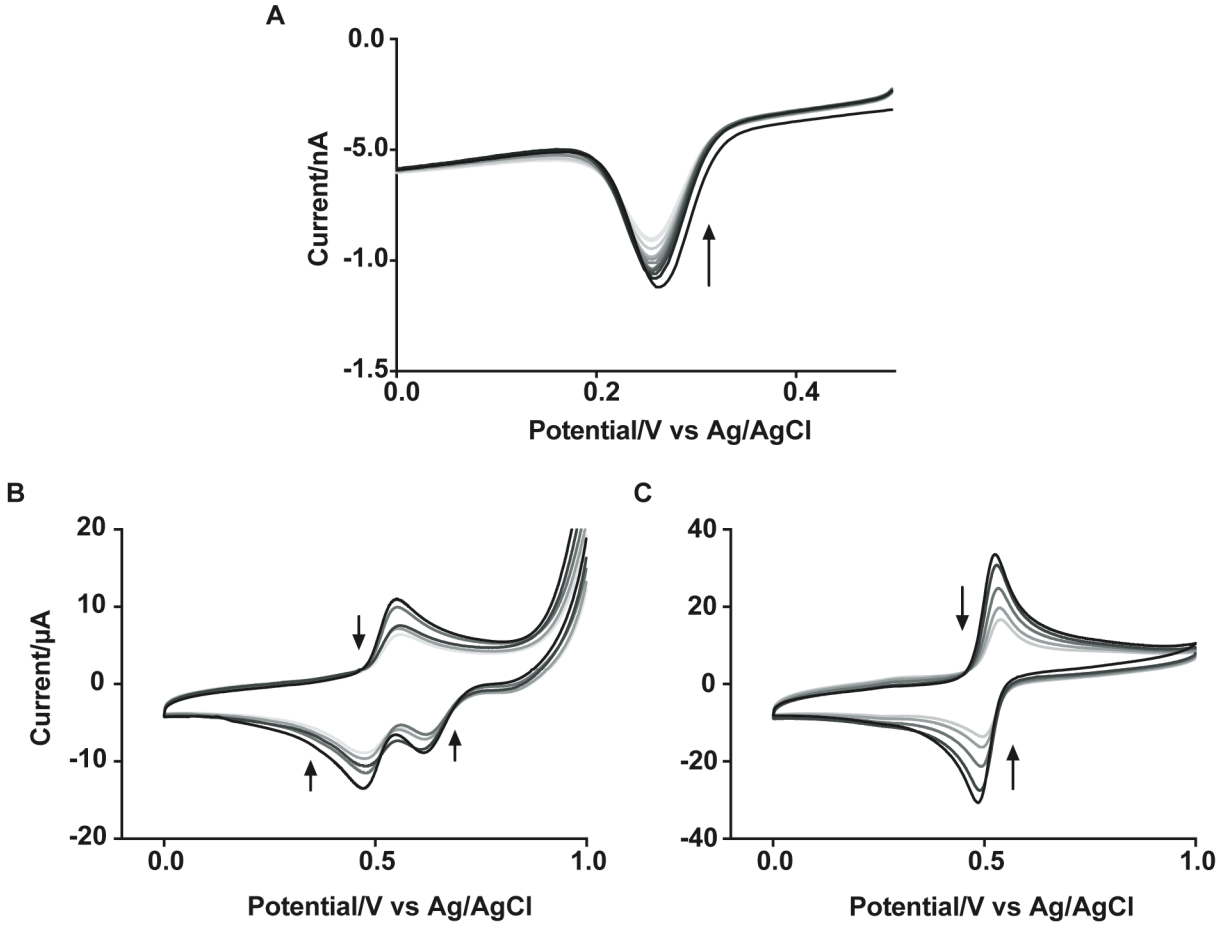


**Figure 3.6**. **Electrode fouling during BQ and TMB analysis.** A) Repeated square wave voltammetry measurements of 1mM BQ in $H_2SO_4$ with Au electrode. B) Repeated cyclic voltammetry measurements of ox2-TMB in proprietary citrate buffer + $H_2SO_4$ (pH 1) with Au electrode. C) Repeated cyclic voltammetry measurements of ox2-TMB in proprietary citrate buffer + $H_2SO_4$ (pH 1) with GCE electrode.

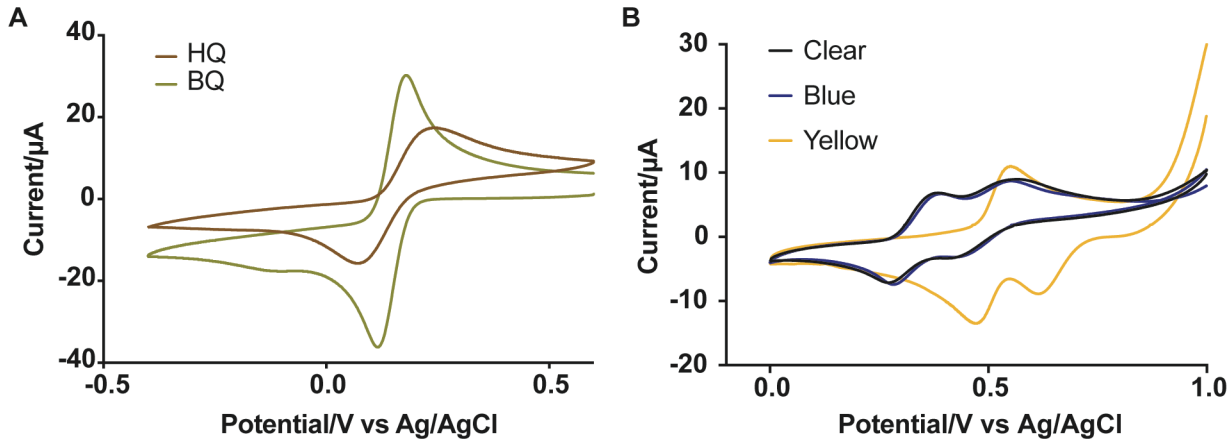


**Figure 3.7**. **Electrochemical characterization of HRP substrates and products.** A) Cyclic voltammetry of 1 mM HQ and 1 mM BQ in 1× PBS. B) Cyclic voltammetry of TMB (clear species) and ox1-TMB (blue species) in proprietary citrate buffer and ox2-TMB (yellow species) in citrate buffer + $H_2SO_4$ (pH 1).

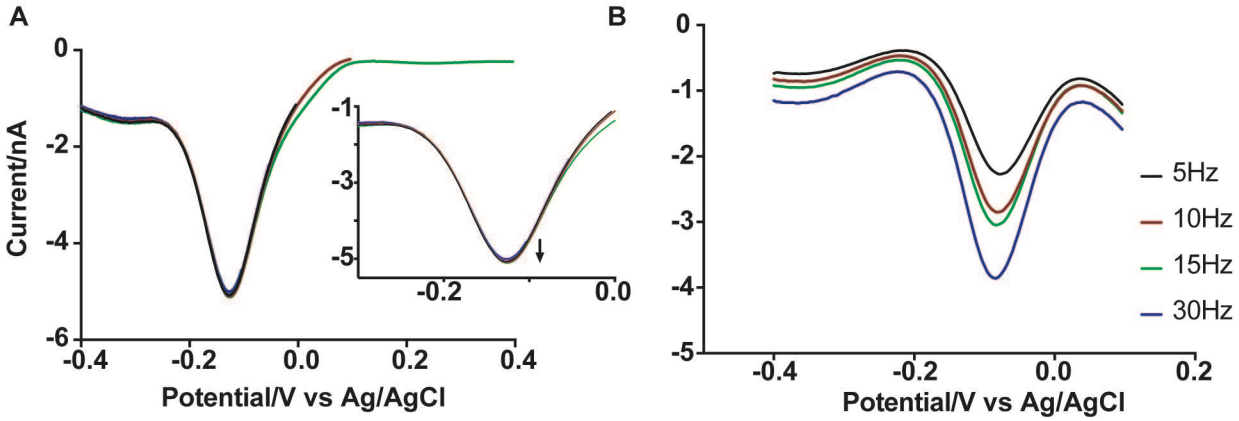


**Figure 3.8**. **Optimization of square wave voltammetry parameters.** A) Relationship between initial potential ($E_{initial}$) and peak current ($i_p$) during square wave voltammetry analysis of 1 mM BQ in 1× PBS. B) Relationship between frequency and current response during square wave voltammetry analysis of 5 mM HQ + 100 µM BQ in 1× PBS.

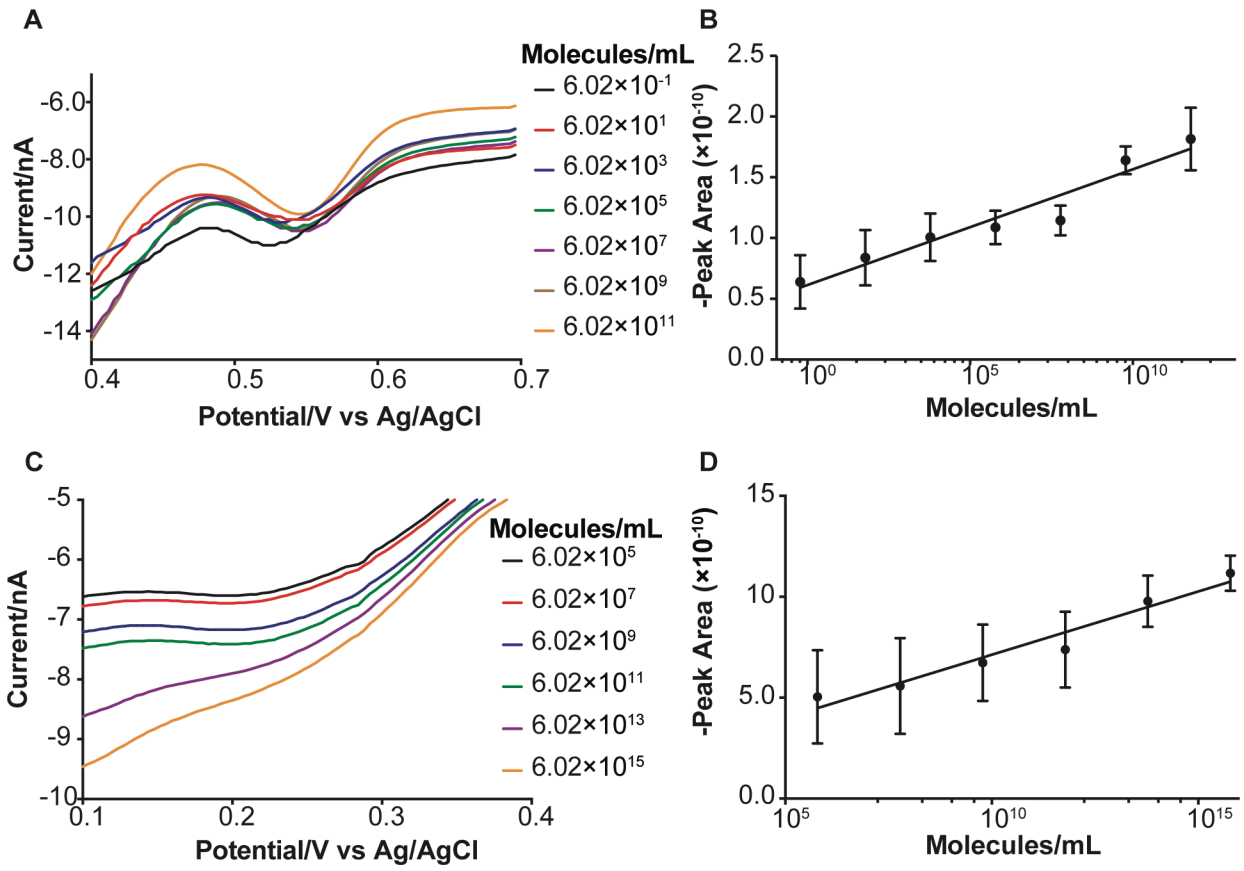


**Figure 3.9**. **Optimization of Electrochemical Detection.** A) Square wave voltammetry results evaluating TMB as an electrochemical substrate for HRP. B) Peaks were integrated and the peak area was plotted to obtain a linear range of $0 – 6\times10^{11}$ molecules $mL^{-1}$ was determined. C) Square wave voltammetry results for hydroquinone as an alternative substrate for electrochemical detection. D) Peak integration was performed and peak areas were plotted. A linear range of $6.02\times10^{5} – 6.02\times10^{15}$ molecules $mL^{-1}$ was obtained.

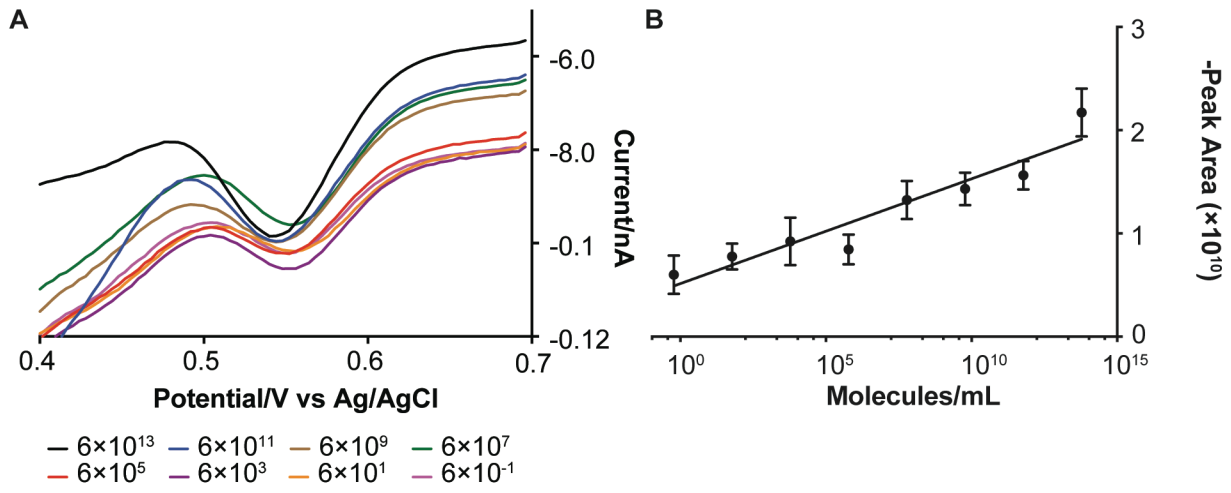


**Figure 3.10**. **Electrochemical Detection of Target Oligo.** A) Square wave voltammetry was used for oligo target detection (BG993). B) The peak area was obtained from 0.45 V to 0.65 V and plotted against the log molecules $mL^{-1}$. A linear curve was obtained from 0 - $6\times10^{13}$ molecules $mL^{-1}$ with an LOD of $3.72\times10^{3}$ molecules $mL^{-1}$.

# CHAPTER 4 - AN ULTRA-SENSITIVE CAPACITIVE MICROWIRE SENSOR FOR PATHOGEN-SPECIFIC ANTIBODY RESPONSES (524)

## Introduction

Detecting and analyzing the humoral antibody response in clinical samples is critical for diagnosis of infectious disease, understanding pathogenesis and immune response kinetics, and vaccine development (525). Current methods for antibody detection include immunoprecipitation (e.g., hemagglutination), immunoblotting, plaque reduction neutralization tests, and immunosorbent assays (526). Among these methods, the enzyme-linked immunosorbent assay (ELISA) is used as the gold standard clinical diagnostic tool for antibody detection (527). However, established detection techniques, including ELISAs, require large instrumentation in centralized laboratories and specialized training to execute and interpret the results (528, 529). These disadvantages limit the use of ELISAs in low-resource settings (528, 530). When standard laboratory tools are not locally accessible, samples must be collected, stored under specific conditions, and sent to reference laboratories, which leads to additional turnaround time. As a result, many cases go undiagnosed and this indicates an urgent need for sensitive and robust assays that can be used at the point of care (POC) to quickly diagnose infection and provide health-care providers with actionable information.

As one branch of electrochemical immunosensors, capacitive biosensors employ direct sample application for label-free detection. Other electrochemical antibody sensors have been developed for serological analysis, but these designs incorporate enzymatic labels (531, 532) or toxic redox couples (277) that increase the complexity and cost of the sensor. Compared to other immunosensors, capacitive biosensors are ideal candidates for sensitive and label-free bioanalysis platforms. Capacitive sensing is based on the underlying theory of the electrical

double layer (533, 534), where the working electrode is conjugated with probe that binds its respective target to increase the thickness of the double layer. Because capacitance is inversely proportional to the length of the double layer, this increase in double layer width produces a corresponding decrease in capacitance (535, 536). Such capacitive signals provide a direct measure of target binding and can be rapidly detected. Based on our previous work using capacitive change to detect DNA (535), the sensitivity of capacitive biosensors is far superior to traditional diagnostic assays (535–538) and is ideal for the detection of low antibody titers found during early stages of infection. Capacitive biosensors are thus an attractive sensing modality that has not yet been fully explored for specific antibody detection.

The goal of this work, done in collaboration with Lei Wang, was to develop a novel POC platform that can specifically detect low levels of antigen-specific antibodies in serum. Due to its clinical relevance, Zika virus (ZIKV) was chosen as a model system to validate the sensing platform. ZIKV is an emerging Flavivirus that is closely related to other mosquito-borne viruses of clinical importance, such as yellow fever, West Nile, and dengue viruses. It has become a major public health concern due to neurological complications in infected adults (136, 167–169) and severe developmental complications for fetuses of infected women (194, 196, 539–541). Therefore, accurate and early diagnosis of ZIKV infection is essential for proper monitoring and medical intervention in these cases.

In this study, we developed a capacitive immunosensor that specifically detects ZIKV antibodies using a sensor modified with ZIKV envelope (E) protein. The sensor presented here directly measures ZIKV-specific polyclonal antibody in mouse serum, with a lower dilution boundary of $1{:}10^{12}$ by day 4 and is ultrasensitive compared to the CDC MAC-ELISA which employs a 1:400 serum dilution over seven days after symptom onset (269). The antibody detection system discriminates between virus specific antibodies with little cross-reactivity,

indicating a high degree of selectivity, and can even differentiate antibody isotypes. This method is distinguished from previous antibody detection methods not only in the platform, but also by its superior sensitivity and specificity.

## Material and Methods

### *Study Design*

The purpose of this study was to build a sensitive capacitive biosensor for the specific detection of ZIKV antibody. The working microwire surface was functionalized with E protein from either ZIKV (ZIKV E) or Chikungunya virus (CHIKV E). The microwire sensor was then validated using pre-immune and immune mouse serum collected 4, 7, 14, and 21 days post ZIKV immunization which tested positive for ZIKV IgG by Western blotting and subsequently used to isotype Day 4 and 21 mouse sera for IgM and IgG antibody. Three experimental replicates were performed for each serum sample. Control samples and experimental sample replicates are indicated in the text and figure legends.

### *Materials*

Potassium hydroxide (KOH), iron (III) chloride hexahydrate ($FeCl_3 \cdot 6H_2O$), 30% hydrogen peroxide ($H_2O_2$), and absolute ethanol were purchased from Fisher Scientific (Fairlawn, NJ). High-purity silver ink was purchased from SPI Supplies (West Chester, PA). 11-Mercaptoundecanoic acid (MUA) was purchased from Santa Cruz Biotechnology (Dallas, TX). 3-Mercapto-1-propanol (MPOH) was purchased from Tokyo Chemical Industry Co., Ltd. (Portland, OR). N-Hydroxysuccinimide (NHS) and 1-Ethyl-3-(3-dimethylaminopropyl)-carbodiimide (EDC) were purchased from Acros Organics (Geel, Belgium). Ethanolamine, Tween-20, and 2-(N-morpholino) ethanesulfonic acid (MES) was purchased from Sigma-Aldrich (St. Louis, MO). Phosphate buffered saline (1× PBS: 137 mM NaCl, 2.7 mM KCl, 10 mM $Na_2HPO_4$ and 1.8 mM $KH_2PO_4$, pH 7.4) was purchased from Hyclone (Logan, UT). All reagents

were used as received without further purification. All stock solutions were prepared using ultrapure water (18 MΩ cm) purified with the Nanopure System (Kirkland, WA). Wires of 99.99% pure gold (25 μm) and silver (25 μm) were purchased from California Fine Wire Company (Grover Beach, CA) and used as the working and reference electrode materials, respectively.

Recombinant ZIKV E and recombinant CHIKV E were purchased from MyBioSource, Inc. (San Diego, CA) and stored at –20°C until use. Nunc Maxisorp 96 well plates (Cat# 44-2404-21) and 1-Step Ultra TMB-ELISA were purchased from Thermo Scientific. HRP-conjugated anti-mouse IgG (ab97023) and IgM (ab97230) were purchased from AbCam. ZIKV immune mouse serum was generated after DNA immunization of mice with ZIKV virus-like particle expression plasmids modeled from previous work (542). Details for the construction of the immunization plasmids, immunization, and serum collection are described by Wang et al (524).

*Surface functionalization of the working electrode*

A 25 μm diameter Au microwire was used as the working electrode. To prepare the surface of the electrode, the Au microwire was immersed in a 20 mL solution of 50 mM KOH and 25% $H_2O_2$ for 10 min (543), and thoroughly rinsed in Milli-Q water to remove residual reagent. The Au microwire was then plasma cleaned for 2 min in an $O_2$ Plasma Etch PE-25 (Plasma Etch, Carson City, NV, USA) at a pressure of 200 mTorr and with 150 W applied to the RF coil. An alkanethiol self-assembling monolayer (SAM) layer formation reaction was performed immediately after plasma cleaning. A 10 mM mixed solution consisting of a 1:1 ratio of 3-MPOH (3-Mercapto-1-propanol) to 11-MUA (11-Mercaptoundecanoic acid) was prepared in the absolute ethanol. The gold microwires were immersed in the mixed solution for 48 hours

without light at room temperature and then rinsed three times with deionized water to remove residual reagent.

The MUA carboxyl groups on the SAM were immediately activated for antigen coupling using NHS/EDC bioconjugation. The SAM modified gold microwires were incubated in 20 mL of 20 mM EDC and NHS in 0.1 M MES (2-(N-morpholino) ethanesulfonic acid) (pH 6.0) buffer for 30 min and then rinsed with 20 mL 0.1 M MES buffer. A solution of 8 μg/mL antigen (ZIKV E or CHIKV E) was incubated on the activated MUA surface for 2 hrs. After antigen incubation, the surface was incubated in 0.1 M ethanolamine in 1× PBS solution for 30 min to passivate unbound, activated MUA. The wire was rinsed with 1× PBS, incubated for 10 min, then rinsed three times with 30 μL of 0.1× PBS buffer before baseline measurements.

*Fabrication of the microwire chip*

The capacitive sensor was constructed using a glass substrate with a polydimethylsiloxane (PDMS) layer 1 mm in height, and two metal microwires. To make the PDMS layer, PDMS prepolymer [RTV 615 A and B (10:1, w/w)] was mixed, degassed, then poured onto a flat silicon wafer to yield a 1 mm-thick fluidic layer (544). The PDMS layer was baked for 30 min at 80°C, then peeled from the silicon wafer. A biopsy punch (Technical Innovations, FL, Inc. USA) was used to create 6 mm diameter wells, then both the PDMS and glass substrate were exposed to oxygen plasma (Plasma Etch, NV, USA) for 1 min and bonded together. Ag/AgCl and Au microwires were then spaced in parallel 1 mm apart across the well. A two-electrode system was employed using Au and Ag/AgCl microwires as the working and reference electrodes, respectively, each with a surface area of $4.7\times10^{-3}$ $cm^2$. Ag/AgCl reference electrodes were made by dipping silver Ag wire in 50 mM iron (III) chloride for 50 s, forming a silver chloride layer on the surface. Silver paint was applied to wire ends to create touchpads that could be connected to the capacitance reader.

*Capacitance readout*

Capacitance measurement data were collected using an Instek LCR-821 benchtop LCR meter (New Taipei City, Taiwan) with a PC interface for data acquisition. Because double layer capacitance is a non-faradaic signal, a 0 V DC bias voltage was applied. A 20 mV root mean square (RMS) AC voltage was applied to the sensors at a frequency of 20 Hz. All capacitance readouts were recorded in parallel mode in 30 µL of 0.1×PBST and 60 data points were collected per reading. A lab-made faradic cage was used to remove electrical interference during readout. Capacitance data was analyzed using Matlab (Math-works) and statistical tests were performed using R (www.r-project.org). Only p values less than 0.05 were considered statistically significant.

*Mouse serum analysis*

Clarified mouse sera were diluted $1{:}10^6$ and $1{:}10^{12}$ in 30 µL 1× PBST buffer and incubated on microwire chips for 5 min at room temperature. Following incubation, electrodes were rinsed three times with 30 µL 1× PBST buffer and three times with 30 µL 0.1× PBST buffer. To determine the isotype of anti-ZIKV antibodies in the mouse sera the microwire sensor was first immersed in 30 µL of mouse serum diluted $1{:}10^6$ in 1× PBST for 5 min at room temperature. Antibodies specific for each isotype were then incubated for 5 min at dilutions of $1{:}10^6$ and $1{:}10^{12}$ in 30 µL 1× PBST buffer. Following incubation, electrodes were rinsed three times with 30 µL 1× PBST buffer and three times with 0.1× PBST buffer prior to capacitance reading.

*ELISA analysis of anti-Zika IgM and IgG levels in mouse sera*

An ELISA assay was used to determine the relative amounts of IgM and IgG in the Mouse 3, 4, and 6 Day 4 and Day 21 serum samples. Briefly, 100 µL of 10 µg/mL ZIKV E protein diluted in PBS (pH 7.4) was added to each well of a Nunc Maxisorp 96 well plate and

incubated at 4˚C overnight. Excess antigen was discarded, and the wells were washed three times with 0.05% PBST (pH 7.4). 300µL of fresh blocking buffer (4% milk powder in PBS) was then incubated in each well for 1 hour at room temperature. Afterwards, the wells were washed six times with 0.05% PBST. 100 µL of mouse serum was then incubated for 1 hour at room temperature at dilutions of 1:100, 1:500, and 1:2500. 10 µg/mL of 4G2 antibody was used as a positive control. The wells were washed again six times with 300µL of 0.05% PBST and 100 µL of 1:3000 HRP-conjugated anti-mouse IgG or IgM was incubated for 1 hour at room temperature. The plate was washed six times with 300 µL 0.05% PBST then again twice with 300 µL of PBS to eliminate residual detergent. 100 µL of TMB-ELISA substrate was incubated for 30 minutes at room temperature and quenched with 100 µL of $H_2SO_4$. Absorbance was measured at 450 nm.

## Results and Discussion

*Sensor design and working principles.*

The label-free capacitive immunosensor introduced here uses microwire electrodes for sensitive and rapid detection of antibodies produced during the host immune response to vaccination, in this case antibodies against ZIKV. The device is made of low-cost, easily accessible materials. A glass slide is used as the base substrate with a biocompatible polydimethylsiloxane (PDMS) well for sample application. Au and Ag/AgCl microwires (working and reference electrodes respectively) are immobilized across the PDMS well (Figure 4.1a) and 30 µL of liquid sample is added to the well and incubated for 5 min. Measurements can then be taken in as quickly as one minute. Microelectrode wires, compared to other electrode fabrication methods like ink printing, paste, and sputter-coated electrodes, demonstrate increased mass transport rates due to radial diffusion (545, 546). This increases the current density and consequently improves sensitivity and enhances detection limits (547). In addition, microwire

electrodes hold additional benefits of simple fabrication without expensive equipment, ease of surface chemical modification, and availability in different pure and alloyed compositions (522).

Randle's equivalent circuit is commonly employed in biosensor research to model the electrode-electrolyte interface of a Faradaic system (410). However, our sensor has been designed as a non-Faradaic system to measure capacitive charging currents only. With no offset voltage applied to the electrode, off-target electrochemical reactions or charge transfer at the interface should be minimal. AC electrokinetic microflows have been known to affect capacitive charging currents, but these effects typically begin to occur at a peak-to-peak amplitude of 1-2 V and do not become prominent until 6-15 V (548, 549). The influence of microflows at the 20 mV oscillation voltage used here is negligible. Thus, to model the charging current at the interface, we place $C_{DL}$ in parallel with a leakage resistance, $R_{Leak}$. $C_{DL}$ in turn can be modeled as the total capacitance, $C_{tot}$, of several capacitors in series, as visualized in Figure 4.1b. The first component constitutes the insulating SAM layer on the electrode surface, $C_{SAM}$. The second, $C_{Ag}$, includes the anchoring groups and the recognition element (antigen), which is followed by the concentration-dependent antibody layer, $C_{Ab}$.

Based on this model, the specific binding of antibody to antigen results in a change in the total capacitance, $C_{tot}$. $C_{SAM}$ is generally large and constant and its contribution to the $C_{tot}$ may therefore be ignored. The sensitivity of the sensor is predominately determined by the relative capacitance between antigen and antibody. In this case, use of a large analyte like antibody increases the sensitivity of our sensor by creating a proportionally larger increase in double layer width compared to smaller analytes like antigens (550).

*Detection of anti-ZIKV antibodies during an immunization time-course.*

To explore the performance of the capacitive immunosensor in a complex matrix with various interfering species, we tested if ZIKV-specific polyclonal antibodies could be detected in

mouse serum. Ten CD1 mice were administered with a DNA vaccine for ZIKV and serum samples were collected before vaccination (pre-immune samples), and 4, 7, 14 and 21 days after vaccination. To confirm a Day 21 anti-ZIKV immune response, the samples were first tested for IgG antibody using strip Western blots and ZIKV-infected Vero cell lysates as the antigen (data not shown). Of the 10 vaccinated mice, two with strong anti-Zika IgG antibody responses (mice 3 and 4) and one with a weak anti-Zika IgG antibody response (mouse 6) were chosen for further analysis. Mouse 3, 4, and 6 samples were tested with the ZIKV E functionalized sensor. To determine suitable dilutions of the mouse serum samples for the platform, the pre-immune and Day 4 mouse sera were tested with a wide range of concentrations ($1{:}10^{18}$ to $1{:}10^{3}$ dilutions in 1× PBST). As shown in Figure 4.2, the average -ΔC obtained from the Day 4 serum increases along with increased concentration and the pre-immune sera conversely shows no significant change in the average -ΔC across the dilution range. There is no significant difference between pre-immune and Day 4 serum at dilutions lower than $1{:}10^{12}$. All dilutions at and above $1{:}10^{12}$ show statistically significant differences with p-values less than 0.05. These results indicate that this platform can differentiate vaccinated from non-vaccinated mouse serum at ultra-dilute concentrations as low as $1{:}10^{12}$ and as few as four days after vaccination. This is comparable to the early acute phase of infection before or concurrent with disease symptomology (551). Subsequently, this assay can extend the window of antibody detection into the early acute phase of infection which currently diagnosed by nucleic acid testing (NAT) (259).

Based on the results in Figure 4.2, two dilutions of the mouse serum, $1{:}10^{6}$ and $1{:}10^{12}$ were chosen to characterize Day 4, 7, 14 and 21 mouse sera. Each of the three biological replicates was tested and averaged. Every biological replicate is the average of three technical replicates. The $-\Delta C$ for each post-vaccination sample was compared to the pre-immune sample as shown in Figure 4.3. At a $1{:}10^{12}$ dilution, the -ΔC increases with each time point after

vaccination and saturates around Day 14. The lower $-\Delta C$ for Day 14 can be attributed to its smaller sample size as there was no serum collected for mouse 6 on this day. Although results are similar for the $1{:}10^6$ dilution compared to the $1{:}10^{12}$ dilution, it is notable that the -ΔC for this dilution saturates as early as Day 4 after immunization. Because the $1{:}10^6$ dilution is significantly more concentrated, this is not unexpected. More importantly, this capacitive immunosensor can detect target antibodies at extremely low concentrations as early as four days and through 21 days post-vaccination.

Reliably analyzing serum at dilutions of $1{:}10^{12}$, these results suggest that our sensor has a sensitivity that is far superior to other platforms (277, 344) and this increased sensitivity enables us to detect an antibody response four days earlier compared to established serological methods (552). It is unclear what the underlying mechanism is that gives rise to such extreme signal changes at low concentrations, but the reported dynamic range was highly reproducible. It is well established that proteins randomly orient themselves when immobilized to a surface (553) so that binding regions of many probes may not be accessible and leave a portion of the surface as inert. This may cause the active functionalized surface area to be much smaller than the total surface area. Therefore, while antibody in ultra-dilute sera may bind to only a small fraction of the total surface area, the proportion of the active surface area that is bound may be significantly larger and may contribute to large percentage changes in capacitance. However, even though significant advances have been made in the understanding of the interfacial region, thermodynamic models of functionalized surfaces fail when more complex charge distributions are considered (554). Further research is needed to elucidate what is happening at the interface of functionalized surfaces to understand the high sensitivity of our sensing system.

Our sensor also requires less sample volume than comparable ELISAs (30 μL of $1{:}10^{12}$ vs 50-100 μL of 1:400 diluted sample (269)), which preserves precious serum sample and

reduces reagent waste. Furthermore, whereas the CDC ZIKV MAC-ELISA needs 12+ hours to obtain results from sample application, our sensor can produce results in under ten minutes. This could result in faster diagnostics needed to determine a timely and effective therapeutic intervention.

*Specificity tests with mouse sera.*

To further characterize the specificity of the sensor, we examined whether anti-ZIKV serum had any cross-reactivity with CHIKV sensors. CHIKV E antigen was conjugated to the microwire as a control probe to test two dilutions ($1{:}10^{12}$ and $1{:}10^{6}$) of the pre-immune and ZIKV-vaccinated Day 21 mouse serum. Figure 4.4 compares the $-\Delta C$ results obtained with specific ZIKV E probe and control CHIKV E probe. The y-axis marks the difference in $-\Delta C$ between Day 21 and pre-immune samples, and the x-axis denotes the two probes used. As shown in Figure 4.4a, the $-\Delta C$ between Day 21 and pre-immune mouse serum using ZIKV E probe is approximately 9 nF at the $1{:}10^{12}$ dilution, suggesting that ZIKV antibody concentrations increase significantly after 21 days post vaccination. In comparison, the CHIKV E sensor shows almost no change (~0 nF), 21 days post ZIKV vaccination, indicating that only specific binding occurred. A small increase in capacitance may be attributed to small amounts of nonspecific adsorption. There is a statistically significant difference between the ZIKV E and CHIKV E functionalized sensors. Similar results are observed for a $1{:}10^{6}$ dilution (Figure 4.4b.)

These results demonstrate satisfactory reproducibility and further validate the excellent specificity and sensitivity of this platform in a complex physiological matrix. Therefore, our sensor may be useful for direct detection of antigen-specific antibodies in serum and other potential types of biological sample.

*Isotyping of antibodies in mouse serum samples.*

Antibody isotyping is a diagnostic component required to separate acute from past infections. To characterize whether our wire sensor platform can be used to determine the isotypes present in a serum sample, wire sensors were functionalized with ZIKV E protein and saturated with antibody using a $1{:}10^6$ dilution of serum from Day 4 or Day 21. Anti-mouse IgM or IgG was applied to the sensor and the results are compared in Figure 4.5. As expected from published flavivirus antibody kinetics (500) and the corresponding ELISA data (Figure 4.6), Day 4 IgM levels were higher than IgG. It was somewhat surprising that the sensor detected constant levels of IgM between Day 4 and Day 21 given that the ELISA showed an increase from Day 4 to Day 21. This may be explained by saturation of the sensor. A recent report, however, indicates that anti-ZIKV IgM levels drop off 8-16 days after symptom onset (552). The discrepancy between our ELISA data and theirs may be due to our use of the immunodominant E protein instead of NS1 as antigen or it could be related to differences in host species. Antibody kinetics for dengue virus indicate that IgM can be detected for over 90 days (500), suggesting that a higher titer for Day 21 is reasonable.

The sensor results also show an increase in IgG levels from Day 4 to Day 21, which agrees with the ELISA data. However, higher levels of IgG than IgM do conflict somewhat with the ELISA results, which show slightly higher IgM for both days. Because the IgM is significantly larger than IgG, it is possible that steric hindrance causes the IgM sensor to saturate faster than the IgG sensor leading to a narrower dynamic range. As a smaller molecule, more IgG may be able to bind to the wire surface and produce a larger signal. Cabral-Miranda et al. recently published an immunosensor for ZIKV antibody with isotyping capacity that was able to detect a $10^6$ to $10^7$ dilutions of serum (277). However, the reported design has decreased sensitivity compared to our system and it also incorporates a toxic redox couple that limits its

point of care use. Without using labels or redox couples, our sensor can distinguish antibody isotypes from a complex serum matrix containing a mixture of isotypes. These results enhance the applicability of the sensor for point of care diagnostic purposes and even for research purposes.

## Conclusion

Although diagnosis of infectious diseases like ZIKV require laboratory confirmation, current methodologies are limited to use by specialized diagnostic laboratories. Recent outbreaks like that of Ebola virus and ZIKV indicate a growing need for simple, sensitive, and selective diagnostics amenable to a point of care setting. The ultra-sensitive capacitance sensor introduced in this study represents a simple and robust platform for pathogen-specific antibody detection in serum. Within minutes and without using labels or redox couples, our sensor can detect anti-ZIKV antibodies during an immunization time course and distinguish antibody isotypes from a complex serum matrix containing a mixture of isotypes. Furthermore, this sensor design can be easily integrated with microfluidics and handheld measuring devices to make it suitable for field work and point of care testing. Our research team is currently working to integrate this immunosensor platform into our previously developed paper-based analytical device (555). Continued development of this novel platform technology can greatly increase the capacity of public health agencies worldwide to assess drug or vaccine efficacy and to monitor emerging infectious diseases of global importance in future.

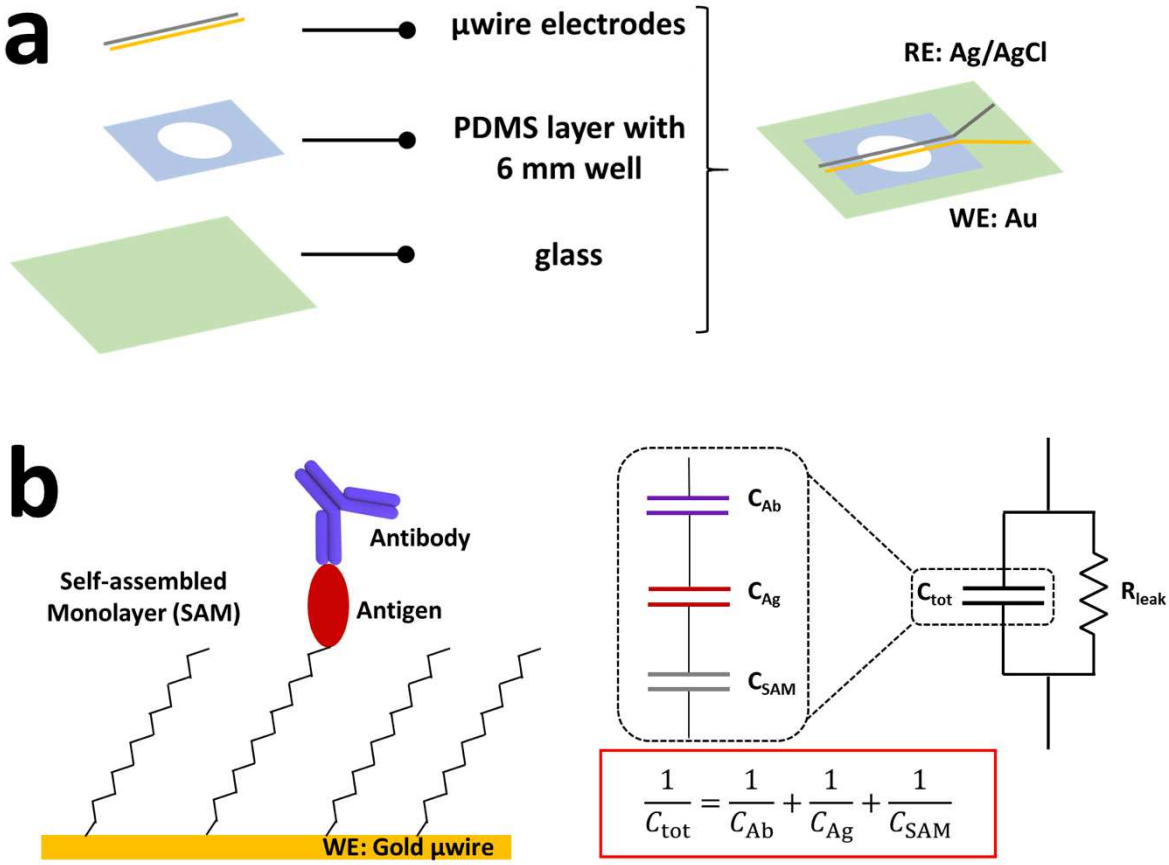


**Figure 4.1. Schematic of capacitive immunosensor design and working principles.** A) Device layers and resulting immunosensor shown from the top. RE: reference electrode, WE: working electrode. B) Working electrode (Au microwire) surface chemistry and functionalized layers, with the corresponding equivalent circuit and total capacitance equation. Double layer capacitance, $\boldsymbol{C_{DL}}$, is placed in parallel with a leakage resistance, $\boldsymbol{R_{Leak}}$. $\boldsymbol{C_{DL}}$ represents the total capacitance, $\boldsymbol{C_{tot}}$, of the individual capacitance contribution from each surface layer.

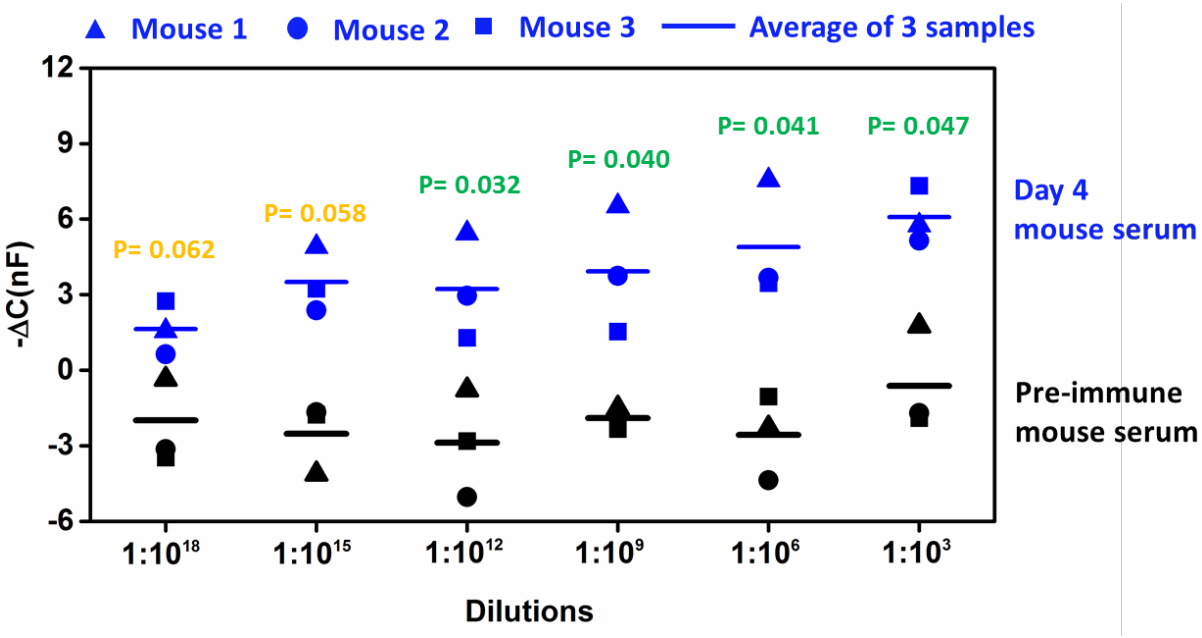


**Figure 4.2. Capacitive responses of pre-immune and Day 4 after ZIKV infected mouse serums at a wide range of dilutions from 1:10$^{18}$ to 1:10$^{3}$ dilutions in 1x PBST buffer** ($n$ = 3 at each dilution).

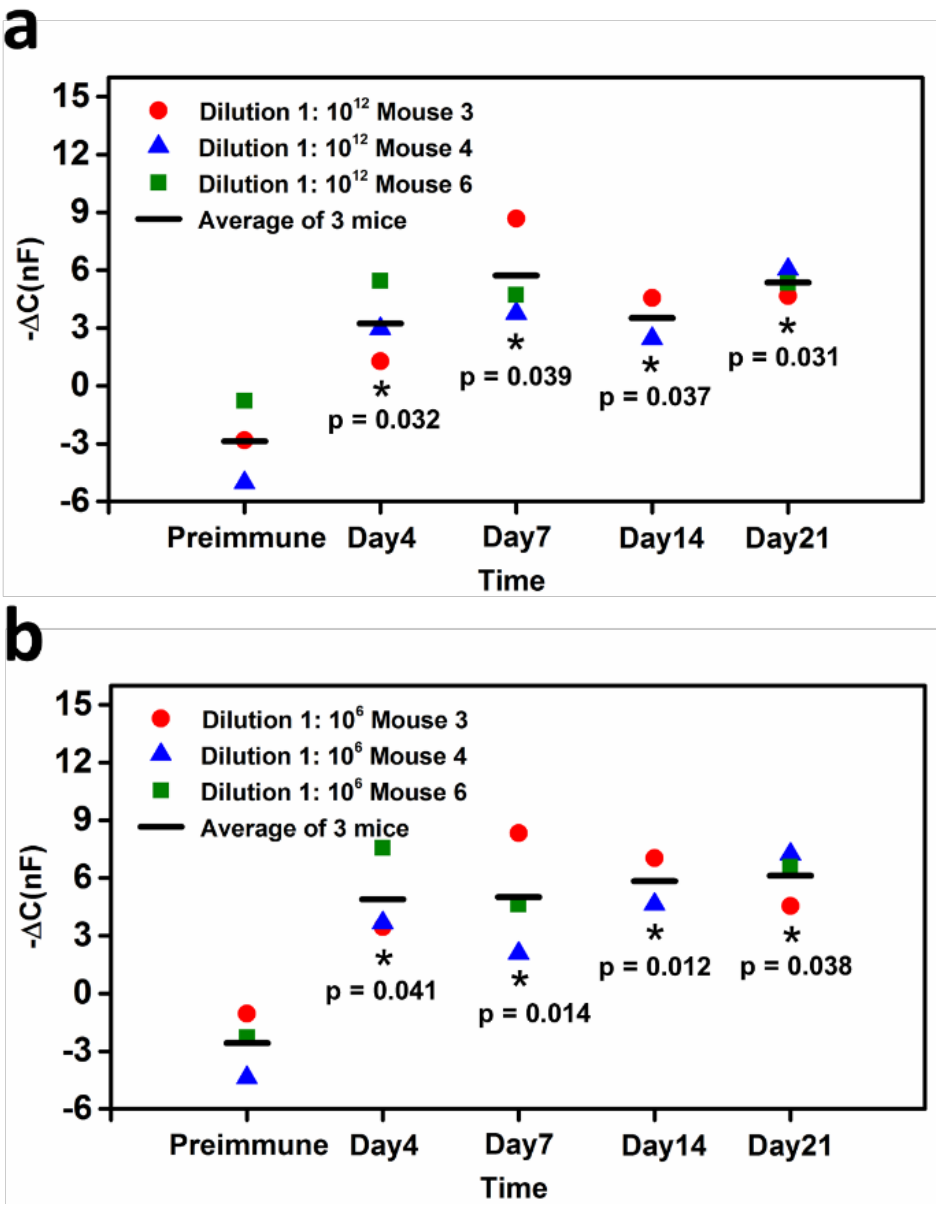


**Figure 4.3. Immune response kinetics for mouse serum samples.** Capacitive response to mouse serum at different time points pre- and-post vaccination with ZIKV. A) Mouse serum tested at a $1{:}10^{12}$ dilution in 1× PBST buffer. B) Mouse serum tested at a $1{:}10^{6}$ dilution in 1× PBST buffer. Three biological samples (n = 3, mean ± STD) for each time point were tested except for Day 14 (n = 2, mean ± STD). Each biological sample shown is the average of three technique replicates. A paired t-test was carried out between pre- and post- vaccination with ZIKV samples. * paired t-test: $p < 0.05$.
6.

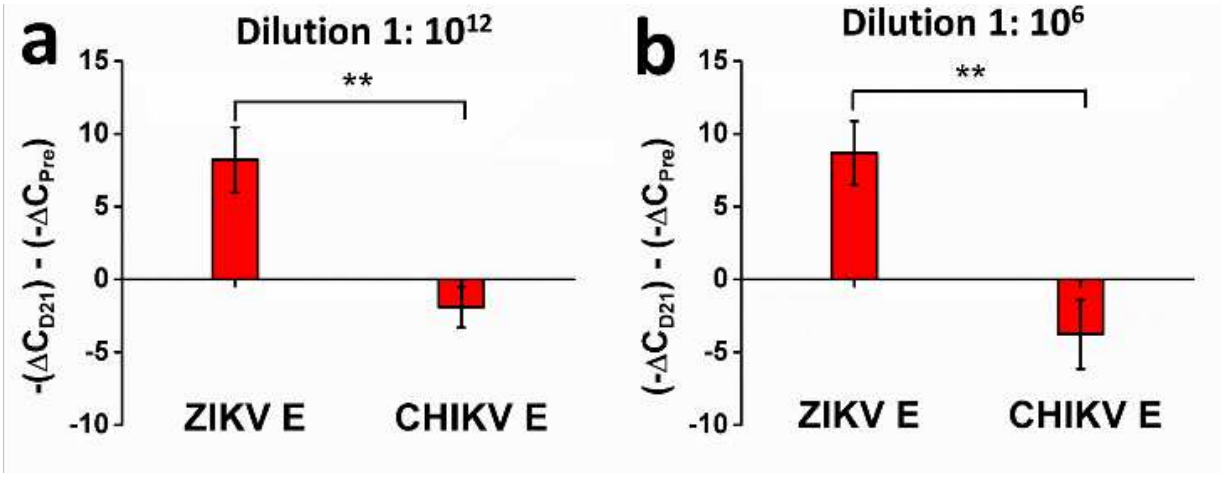


**Figure 4.4. Specificity tests with samples of mouse sera.** A) The difference between the negative capacitance change for Day 21 and pre-immune mouse serum samples at a 1:$10^{12}$ dilution in 1× PBST buffer are compared for ZIKV E and CHIKV E recognition antigens (n = 3 at each concentration, mean ± STD). B) The difference between the negative capacitance for Day 21 and pre-immune mouse serum samples at a 1:$10^{6}$ dilution in 1× PBST buffer are compared for ZIKV E and CHIKV E recognition antigens (n = 3 at each concentration, mean ± STD). ** paired t-test: $p < 0.01$.

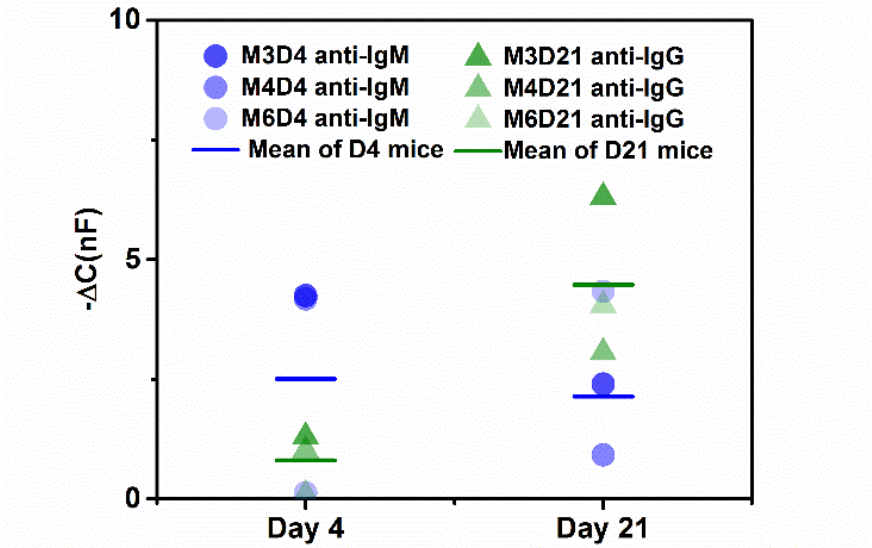


**Figure 4.5. Isotyping of antibodies in samples of mouse sera.** Capacitive response of antibody isotypes in mouse serum at day 4 and 21 with ZIKV. Mouse serum was used at a 1:$10^{6}$ dilution in 1× PBST buffer to saturate the surface for isotype detection. Three biological samples (n = 3, mean ± STD) for each time point were tested. Each biological sample shown is the average of three technical replicates.

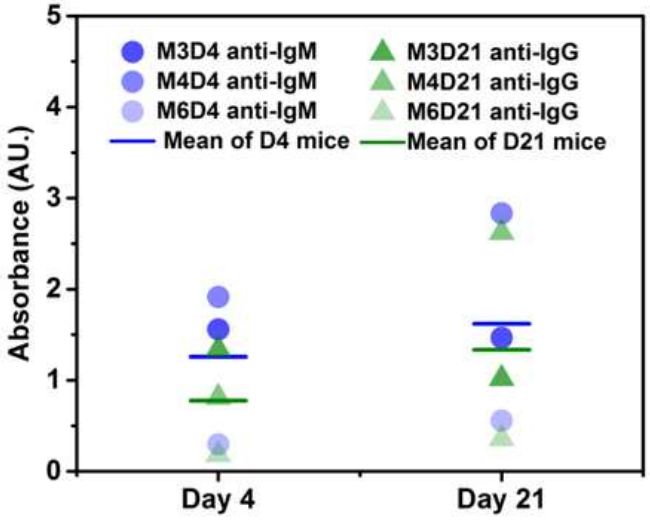


**Figure 4.6. ELISA analysis of anti-Zika IgM and IgG levels in Mice 3, 4, and 6.**

# CHAPTER 5 - DESIGN AND OPTIMIZATION OF ELECTRODE SURFACE CHEMISTRY FOR A NOVEL ELECTRODE ARRAY SENSOR (556)

## Introduction

Antigen-capture enzyme immunosorbent assays (EIAs) and immunohistochemistry can be used for direct flavivirus detection (557), however, these techniques lack sensitivity, are time and labor intensive, and must be performed in specialized laboratories by trained personnel. Electrochemical biosensors have several advantages including high sensitivity, portability, simplicity, and cost-effectiveness that make them attractive for viral diagnosis. However, only a small portion of biosensor research has been devoted to investigating direct detection of virus particles.

Most sensors report clinically relevant limits of detection (LOD) ranging from 0.12 plaque forming units per mililiter (PFU/mL) (558) to 167 PFU/mL (559) using electrochemical impedance spectroscopy (EIS) or voltammetric techniques like cyclic voltammetry (CV), linear sweep voltammetry (LSV), and differential pulse voltammetry (DPV). While these sensors demonstrate good sensitivity and specificity, the electrodes are designed as individual chips that must be independently handled. As such, these sensors lack potential for high-throughput. In this work, done in collaboration with Lang Yang, a novel array biosensor was designed that allows multiple electrodes to be simultaneously functionalized and handled. The electrode array consists of two rows of 12 gold electrode pairs in a sun/moon configuration, each with an area of 0.5 $mm^2$ per electrode (Figure 5.1). The electrode array was used to develop an impedance sensor for detection of Zika virus (ZIKV) particles which was chosen due to its clinical relevance as an emerging pathogen. Briefly, 4G2 antibody was immobilized to a mixed self-assembling monolayer (SAM) composed of short and long chain alkanethiols on the gold surface. EIS measurements were then taken for a virus concentration range of 10 to 11,110 focus forming

units (FFU) and the percent delta change of charge transfer resistance (%$\Delta R_{ct}$) was plotted as a linear line with an LOD of 22.4 FFU (S/N = 3).

**Table 5.1 Reported limits of detection for direct virus particle sensing**

| LOD (PFU/mL) | Analyte | Technique | Year | Reference |
|---|---|---|---|---|
| 0.12 | Dengue (DENV) | EIS | 2017 | (558) |
| 0.23 | DENV2 | EIS | 2013 | (560) |
| 0.5 | Influenza (H1N1) | amperometry | 2017 | (561) |
| 1 | DENV2 | DPV | 2012 | (562) |
| 1 | DENV2 | EIS | 2012 | (563) |
| 1 | H1N1 | LSV | 2014 | (564) |
| 8 | Fowel adenovirus (FAdV) | CV | 2018 | (565) |
| 10 particles | West Nile Virus | EIS | 2018 | (523) |
| 22 FFU | ZIKV | EIS | 2018 | This work |
| 113 | H1N1 | DPV | 2017 | (566) |
| 167 | Japanese encephalitis virus (JEV) | EIS | 2016 | (559) |

## Materials and Methods

### *Materials*

Phosphate buffered saline (1× PBS: 137 mM NaCl, 2.7 mM KCl, 10 mM $Na_2HPO_4$ and 1.8 mM $KH_2PO_4$, pH 7.4) was purchased from Hyclone (Logan, UT). 11-Mercaptoundecanoic acid (MUA) was purchased from Santa Cruz Biotechnology (Dallas, TX) and 3-Mercapto-1-propanol (MPOH) was purchased from Tokyo Chemical Industry Co., Ltd. (Portland, OR). Potassium hydroxide (KOH), 30% hydrogen peroxide ($H_2O_2$), and reagent alcohol were obtained from Fisher Scientific (Fairlawn, NJ). N-Hydroxysuccinimide (NHS) and 1-Ethyl-3-(3-dimethylaminopropyl)-carbodiimide (EDC) were obtained from Acros Organics (Geel, Belgium). Ethanolamine, Tween-20, and 2-(N-morpholino) ethanesulfonic acid (MES) were purchased from Sigma-Aldrich (St. Louis, MO). Potassium ferricyanide (CAS # 13746-66-2) and Potassium ferrocyanide (CAS# 14459-95-1) were also purchased from Sigma-Aldrich. Tris-base (CAS# 77-86) was purchased from Sigma and citric acid (CAS# 5949-29-1) and sodium phosphate monobasic monohydrate (CAS# 10049-21-5) were purchased from Fisher Scientific.

SylGuard 184 Silicon Elastomer and Curing Agent were purchased from Dow. Stock solutions were prepared using ultrapure water (18 MΩ cm).

4G2 mouse B cell hybridomas (D1-4G2-4-15) were purchased from ATCC and stored at -80˚C until use. Recombinant ZIKV E and recombinant CHIKV E were purchased from MyBioSource, Inc. (San Diego, CA) and stored at –20°C until use. HRP-conjugated anti-mouse IgG (ab97023) was purchased from AbCam while Nunc Maxisorp 96 well plates (Cat# 44-2404-21), 1-Step Ultra TMB-ELISA, and 1-Step Ultra TMB-Blotting were obtained from ThermoScientific. Dulbecco's Modified Eagle Medium (DMEM) was purchased from Life Technologies and supplemented with 10% fetal bovine serum (FBS), 25 mM HEPES (CAS# 7365-45-9 Sigma), 1× L-glutamine, and 1× Penicillin/Streptomycin to make complete DMEM (cDMEM). All reagents were used as received without further purification.

*Electrode fabrication*

Gold electrode arrays were fabricated using photolithography. Briefly, 1×3 inch glass slides were rinsed successively with acetone, isopropyl alcohol (IPA), and nanopure water then dried with $N_2$ gas and baked at 135˚C to evaporate residual moisture. The glass slide was then spin-coated with S-1813 photoresist at 3000 rpm for 30 seconds. Once coated, the slide was baked at 135˚C for 1 minute. A photomask was placed on the slide which was then exposed to ultraviolet light for 6 seconds and developed in S-1813 developer for 1 minute. Development was quenched by rinsing with nanopure water and the slide was then dried with $N_2$ gas. The developed slide was then cleaned by immersion in 1 M HCl for 1 minute, rinsed with nanopure water, and dried with $N_2$ gas. Metal deposition was then performed to coat the slide first with a 10 nm Cr adhesion layer then a 150 nm Au layer to generate the electrode. Lift off was performed by immersing the metal-coated slide in acetone to remove excess metal, leaving

behind the electrode array which was then rinsed with acetone, IPA, and nanopore water and dried with $N_2$ gas.

*PDMS fabrication*

SylGuard Elastomer base and curing agent were mixed (10:1 ratio w/w), degassed, and poured onto a silicon wafer to produce a 3 mm thick PDMS layer. A biopsy punch (Technical Innovations, FL, Inc. USA) was used to generate 3.5 mm diameter wells. Both the PDMS and electrode array were plasma cleaned in an $O_2$ Plasma Etch PE-25 (Plasma Etch, Carson City, NV, USA) at 200 mTorr pressure and application of 150 W to the RF coil for 5 minutes, then bonded together.

*Surface functionalization of the electrodes*

Electrodes were cleaned by immersing the array into 20 mL 50 mM KOH/25% $H_2O_2$. The array was then rinsed in 20 mL nanopure water and dried with $N_2$ gas. After PDMS bonding, the array was plasma cleaned for 5 minutes in an $O_2$ Plasma Etch PE-25 (Plasma Etch, Carson City, NV, USA) at 200 mTorr pressure and application of 150 W to the RF coil. Immediately after plasma cleaning, the array was immersed in a 20 mL solution of 9 mM MUA/9 mM MPOH in reagent alcohol. The array was then rinsed in 20 mL reagent alcohol and immersed in 100 mM NHS/100 mM EDC in 0.1 M MES, 0.5 M NaCl, pH 5.0 for 30 minutes to activate the surface and subsequently rinsed with 20 mL 0.1 M MES, 0.5 M NaCl, pH 5.0. 10 µL of 2.55 mg/mL 4G2 antibody was added to each electrode and incubated for 2 hours for bioconjugation. Each electrode was rinsed twice with 10 µL 1 M ethanolamine in PBS and then incubated with 10 µL 1 M ethanolamine for 30 minutes. The electrodes were then rinsed three times with 10 µL PBS and incubated 1 hour with 10 µL 2.5 mg/mL BSA in PBS. Afterwards, they were rinsed five times with 10 µL PBS and incubated with 10 µL clarified ZIKV or SINV for 30 minutes. The electrodes were rinsed five times again with 10 µL PBS.

*Electrochemical measurements*

Capacitance measurements were performed in 10 µL of 0.1× PBST using an Instek LCR-6200 (New Taipei City, Taiwan) in parallel mode. 0 V DC bias was applied to the electrode and 20 mV root mean square voltage ($V_{rms}$) was applied at a frequency of 20 Hz.

Electrochemical impedance spectroscopy (EIS) measurements were performed in 10 µL of 5 mM $K_3Fe(CN)_6$/5 mM $K_4Fe(CN)_6$ in PBS using a ZIVE SP1 potentiostat (WonATech Co, Ltd. Seoul, South Korea). To equilibrate the electrochemical system, the sequence was started with 30 seconds of amperometry at 0 V then transitioned immediately to EIS at 0 V DC bias and 10 mV $V_{rms}$. The frequency was scanned from 800 kHz to 1 Hz.

*ELISA characterization*

To validate 4G2 antibody, 100 µL of ZIKV was added to a Nunc Maxisorp 96 well plate and incubated overnight at 4˚C. The wells were rinsed three times with 200 µL 0.05% PBST and 300 µL of blocking buffer (4% milk in PBS) was incubated for 1 hour at room temperature. The wells were then rinsed six times with 200 µL 0.05% PBST and 100 µL of 8 µg/mL 4G2 antibody in blocking buffer was incubated for 1 hour at room temperature. Then they were again rinsed six times and 100 µL goat anti mouse/HRP secondary antibody (1:3000 in blocking buffer) was incubated for 1 hour at room temperature. The wells were rinsed six times with 200 µL 0.05% PBST then twice with 200 µL PBS to remove detergent. 100 µL of 1-Step Ultra TMB-ELISA was added to the wells and incubated for 30 minutes before quenching with 100 µL 2 M $H_2SO_4$. Absorbance was measured at 450 nm using a PerkinElmer VICTOR X5 plate reader.

*4G2 Production and Purification*

4G2 hybridomas were thawed on ice and added directly to 10 mL of chilled cDMEM. The cells were then centrifuged at 1500 rpm for 5 minutes at 4˚C. The media was aspirated off and the cells were transferred to a T-75 flask with 10 mL cDMEM and incubated at 37˚C for two

days before expansion into five T-150 flasks with 20 mL cDMEM. The cells were grown to 80% density and the media was replaced with Hybrimax serum-free media and incubated at 37˚C for four days. The cells were centrifuged at 1500 rpm for 5 minutes at 4˚C and the supernatant was pulled off, filtered with a 0.45 µm membrane, and stored at 4˚C until purification. 4G2 antibody was loaded onto a Protein A column in 20 mM sodium phosphate (monobasic monohydrate), pH 7 with an AKTA Pure FPLC. The antibody was eluted using 0.1 M citric acid, pH 3 and fractionated directly into a fraction plate containing 100 µL 1 M Tris-base, pH 7.4 neutralization buffer. Antibody-containing fractions were collected, pooled, and dialyzed overnight into PBS buffer with 20% glycerol. The dialyzed antibody was then concentrated, quantified using a Nanodrop 2000c, validated with an ELISA, and stored at -20˚C until use.

*Virus Production and Quantitation*

Vero cells were grown to 70% confluency and infected with ZIKV or SINV at an MOI of 0.1 for 72 hours at 37˚C. The cells were then centrifuged at 1500 rpm for 5 minutes and the supernatant was drawn off and stored at -80˚C until use.

The virus was quantified with a focus forming assay (FFA). Briefly, Vero cells were plated at 100,000 cells/well and incubated overnight at 37˚C. Virus was diluted with 2% FBS cDMEM into a 1:10 serial dilution series, added to the cells, and incubated 1 hour at 37˚C. An agarose overlay was added to the plate and the cells were incubated for 48 hours at 37˚C. 500 µL of formaldehyde was added to each well and the agar overlay was removed. The cell monolayer was gently rinsed three times with 500 µL PBS. The cells were then incubated with Perm Wash Buffer (0.3% Tween 20, 0.1% BSA in PBS) for 5 minutes and 500 µL of 500 ng/mL 4G2 antibody (diluted with Perm Wash Buffer) was added to the cells and incubated overnight at 4˚C. The cell monolayer was gently rinsed three times with 500 µL of ELISA wash buffer (0.5% Tween20 in PBS) and 500 µL of goat anti-mouse/HRP secondary antibody (1:5000 in Perm

Wash Buffer) was added and incubated 2 hours at room temperature. The cells were gently rinsed three times with 500 µL ELISA wash buffer and 150 µL of 1-Step TMB Ultra Blotting Solution was added to the wells. Development was quenched by rinsing four times with 500 µL nanopore water. The titer of focus forming units per mL (FFU/mL) was calculated using the formula below:

$$\frac{\#\ of\ focus\ formations}{Dilution \times\ Volume}$$

The virus was clarified by diluting 1 mL of stock virus with PBS and adding to a 300k Vivaspin column. The column was centrifuged at 1500 rpm for 3-4 minutes. The solution was mixed, filled again to 15 mL and centrifuged once more. This was repeated 2-3 times until the solution was clear. The virus solution was then resuspended at 1 mL with PBS and applied directly to the functionalized electrodes.

## Results and Discussion

### *Sensor principles*

Significant advancements have been made in biosensor research in terms of sensitivity and specificity. However, many sensor designs are still lacking in throughput and compatibility with portable, handheld instruments. The goal of this work is to use existing principles of electrode surface functionalization to validate a novel electrode array design for direct virus particle sensing. The array, shown in Figure 5.1a, is fabricated by photolithography and metal deposition to create a 2×12 array of Au electrode pairs and the capacity to independently treat 24 electrodes simultaneously enhances throughput. Furthermore, probe antibodies may be immobilized to individual electrodes by fabricating and bonding a set of PDMS wells to the glass substrate surface as shown in Figure 5.1b.

The circuit model shown in Figure 5.1c describes the electrochemical behavior at the surface of the electrode pair. Because the two electrodes have different geometries, they each

contribute an independent $R_{ct}$ and double layer capacitance ($C_{dl}$) which are separated by the solution resistance ($R_s$). $R_{ct}$ is the most sensitive parameter for characterizing the electrode-electrolyte interface and, ignoring the Warburg impedance ($Z_W$), the total charge transfer resistance $R_{ct,\,total}$ can be extracted by calculating $R_{ct1}$ and $R_{ct2}$ from the transfer function below.

$$Z(\omega) = Z' + jZ''$$

$$= R_s + \frac{R_{ct1}}{1 + \omega^2 R_{ct1}^2 C_{dl1}^2} - \frac{j\omega R_{ct1}^2 C_{dl1}^2}{1 + \omega^2 R_{ct1}^2 C_{dl1}^2} + \frac{R_{ct2}}{1 + \omega^2 R_{ct2}^2 C_{dl2}^2} - \frac{j\omega R_{ct2}^2 C_{dl2}}{1 + \omega^2 R_{ct2}^2 C_{dl2}^2}$$

As the mass at the electrode surface increasingly passivates the surface during target binding (Figure 5.2), charge transfer becomes more difficult resulting in larger $R_{ct}$ values.

*Sensor characterization*

To characterize adsorption of protein to the electrode surface, the electrodes were functionalized with either MCU, thiolated oligos, or left bare (Figure 5.3a). It is well established that protein readily adsorbs to a gold surface through hydrophobic interactions and effectively blocks the surface. Thus, as expected, addition of 15 µL of 5 µg/mL of ZIKV E protein (75 ng) to the bare electrode drops the capacitance signal. Interestingly, the DNA-functionalized surface demonstrated no change in capacitance indicating that protein did not adsorb to a surface passivated with DNA. Also surprising was an observed increase in capacitance as protein adsorbs to an alkanethiol SAM.

Surface functionalization is critical for sensor performance. Incomplete blocking may amplify background and nonspecific signals, reducing specificity, and too much or little biorecognition probe may negatively impact sensitivity. Furthermore, the presence of debris on the electrode surface may hinder the functionalization process and reduce performance. It is therefore critical to rigorously clean electrodes before use. A cleaning protocol was adopted from (523) and optimized for the array sensor. The array was immersed in a solution of KOH and 25% $H_2O_2$ for ten-minute intervals and EIS was performed to characterize the charge

transfer. As shown in Figure 5.3b, 20 minutes in cleaning solution largely decreased impedance which continued to drop after subsequent intervals until the signal plateaued at 40 minutes. To ensure complete surface cleanliness, an immersion time of 45 minutes was chosen for downstream applications.

The surface of the sensor was characterized by EIS after each step in the fabrication process (Figure 5.3c and 5.3d). The sensor was first modified with a mixed SAM layer of MUA and MPOH adapted from Mihailescu et al 2015 (567). MUA is a long chain alkanethiol with ten carbons while MPOH is a short chain alkanethiol with three carbons. By mixing these long and short chain alkanethiols in defined ratios (e.g. 1:1 in this work), the bioreceptor density can be controlled to reduce steric hindrance and optimize target binding (343). After SAM modification, the $R_{ct}$ dramatically increased which is attributed to the passivation of the electrode surface. 4G2 probe antibody was then immobilized via the carboxyl headgroups of MUA by NHS/EDC bioconjugation which surprisingly decreased $R_{ct}$. This effect may due to electrostatic repulsion of charge from negatively charged carboxyl groups of MUA which greatly enhance $R_{ct}$. Therefore, once antibody is conjugated to the head groups, the negative charge is neutralized and the contribution towards impedance from electrostatic repulsion is lost.

After probe immobilization, remaining unconjugated headgroups were deactivated with ethanolamine, causing the $R_{ct}$ to increase once again and the surface was then blocked by adsorption of BSA which further increased $R_{ct}$ again. Subsequent passivation layer (SAM, 4G2 probe, ethanolamine deactivation, and BSA blocking) have a characteristic $R_{ct}$ pattern, which has been readily characterized and repeated.

*Sensor optimization and specificity*

As a model system, recombinant ZIKV E and chikungunya (CHIKV) E were chosen for specific and nonspecific targets respectively. Target analysis was done using both EIS and

capacitance readout at 20 Hz (Figure 5.4). EIS yielded no significant change in impedance signal and capacitance readout showed a small change in capacitance that did not differ significantly between ZIKV and CHIKV E targets. Because larger analytes produce proportionally larger changes in double layer width and therefore capacitance, the microwire sensor described and validated in Chapter 4 was used to determine whether ZIKV E (53 kDa) and CHIKV E (38 kDa) are too small to create a measurable change in double layer width. The results in Figure 5.5a show a small (< 8%), statistically significant change in capacitance for 300 pg of ZIKV E applied to the sensor. However, flavivirus and alphavirus E protein generally does not exist in soluble form in clinical samples, but rather in context with the virus particle. Therefore, because capacitance readout for E protein lacked sensitivity and because soluble E protein is not a realistic target, infectious virus particles were used for capacitive target analysis. The results in Figure 5.6a show that surprisingly, no significant signal change was obtained for target virus. Capacitive measurements were then taken to validate the probe functionalization but still showed no change in signal that should be associated with bioreceptor immobilization (Figure 5.6b). In an attempt to increase sensitivity, the electrode pair was shorted together to increase surface area and a commercial Ag/AgCl reference microelectrode (25 μm diameter) was used. However, while the raw values shown in Figure 5.6c differed between the external Ag/AgCl and internal Au references, no significant increase in signal change was noted using the Ag/AgCl. As one last confirmation that capacitance readout lacked sensitivity for this platform, the difference in capacitance was compared between a bare and SAM-functionalized electrode (Figure 5.6d). A small increase in capacitance was noted upon alkanethiol binding, but these results did not compare well to other data which indicate a prominent change in surface blocking and electrostatic repulsion when the electrode is passivated with an alkanethiol SAM (Figure 5.3).

EIS is a technique well-known for its sensitivity (523) and was therefore used to investigate the sensor specificity using virus particles. Clarified virus particle analysis was first compared to a PBS negative control which showed a large nonspecific buffer signal. After ruling out buffer contamination, it was hypothesized that extended incubations at room temperature could destabilize and denature the 4G2 antibody probe causing it to spread out and maximize contact points on the electrode surface (327). The relaxed antibody could more effectively passivate the surface, resulting in a large jump in impedance. In contrast, target binding may stabilize the antibody conformation through protein-protein interactions and prevent denaturation. In this case, target binding would also increase impedance, but gaps in the passivation layer would allow reagents to penetrate the passivation layer and yield a smaller impedance compared to denatured protein. To mitigate possible denaturation effects, sensor fabrication was done at 4˚C and target analysis was again compared to a PBS negative control. However, as shown in Figure 5.7a, refrigeration did not decrease the nonspecific signal enough for target detection. Although it remains unclear why PBS buffer incubations increase impedance, the sensor is still able to differentiate between SINV and ZIKV particles. ZIKV (12,200 FFU) was compared to an excess of SINV particles (267,000 FFU) (n = 6). Figure 5.7b shows that the impedance signal is significantly larger for ZIKV compared to SINV which indicates that the sensor demonstrates good specificity and can distinguish between similar targets.

*Concentration dependent sensing of ZIKV*

The sensor response was investigated using EIS for virus concentrations ranging from 10 FFU to 11,110 FFU. Increasing concentrations were added consecutively to an electrode and $\%\Delta R_{ct}$ was calculated to normalize the response from variations between electrodes (523) and plotted against the log of the additive virus amount (n = 4). As can be seen in Figure 5.8, the

array sensor response is linear for all tested concentrations ($R^2 = 0.9843$) and though there is background signal from the negative PBS control, the slope for subsequent PBS incubations is significantly different from the calibration curve ($p = 0.0001$). The LOD (S/N = 3) was calculated to be 22.4 FFU and was determined using the equation below

$$\mathrm{LOD} = \mu_{blank} + 3\sigma_{blank}$$

where σ is the standard deviation of the mean blank signal and μ is the average blank signal. This LOD compares well to other reported sensors and to reported viral loads of 80 PFU/mL of ZIKV in saliva (568), making it a viable alternative to immunohistochemistry and antigen-capture EIAs for direct virus detection.

## Conclusion

We describe here a novel array biosensor used for direct impedance sensing of ZIKV particles. The sensor demonstrated good specificity when tested against nonspecific SINV and had a clinically relevant LOD of 22.4 FFU. The sensor can be further improved by investigating fabrication methods to increase probe protein stability and additional work is needed to integrate the array with microfluidics which would automate sample handling. Future research is also needed to investigate biosensor storage and reusability, however, this array sensor is an important step towards direct and high-throughput sensitive and specific virus detection at the point-of-care. By providing a platform for further development, point-of-care diagnostics will enable physicians to diagnose patients quickly without expensive sample shipment and technical assays. Reduced turnaround times enable physicians to medically intervene sooner and mitigate possible sequelae.

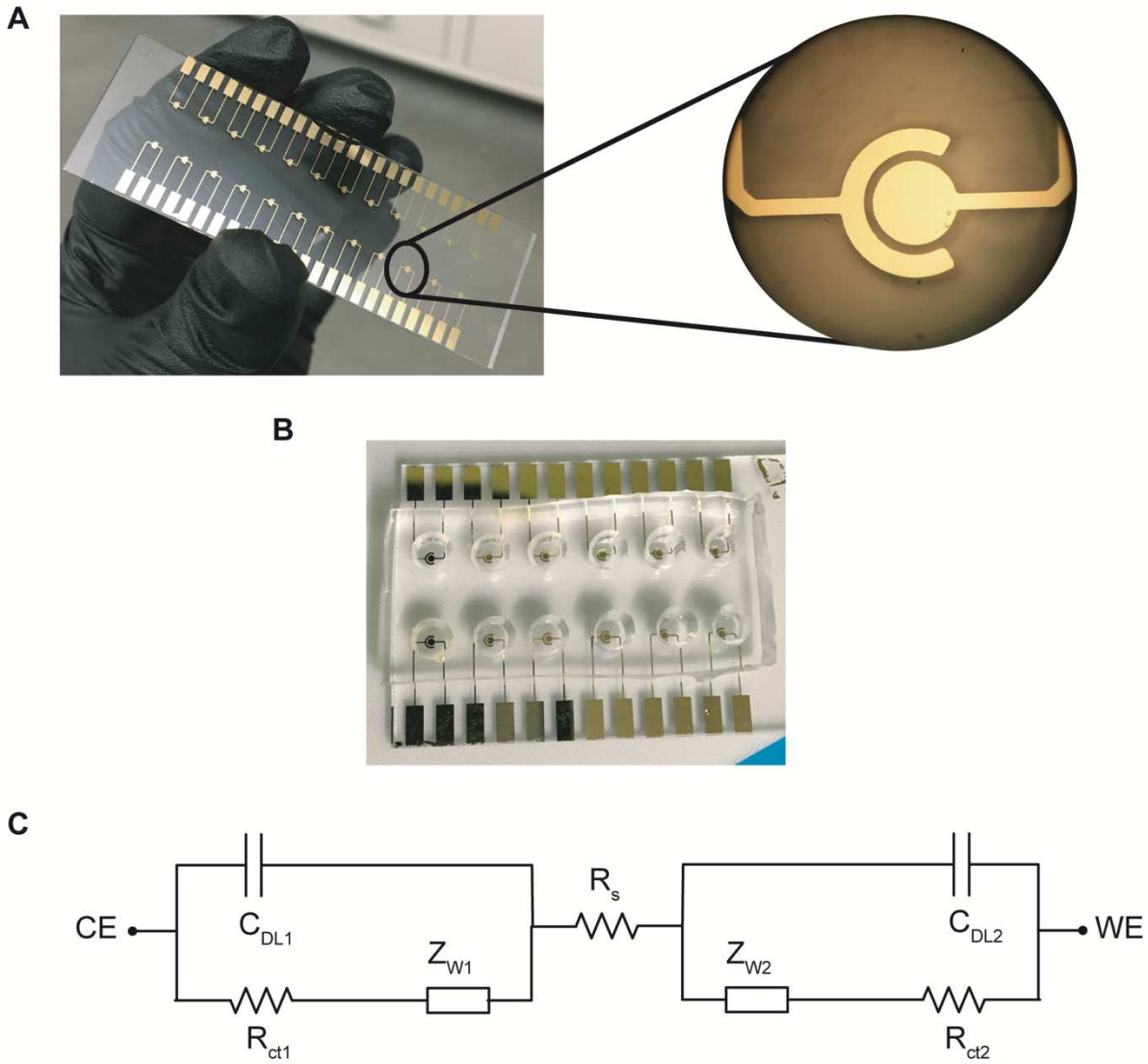


**Figure 5.1. Array sensor design and circuit model.** A) 2 × 12 electrode array with 24 pairs of electrodes in a sun/moon configuration. B) PDMS wells bonded to the array for individual electrode treatment. C) Circuit model for the sun/moon electrode pair. Although the electrodes have the same area, their different geometries lead them to contribute differentially to the charge transfer resistance, $R_{ct}$. The surface is therefore best modeled by two asymmetric Randles circuits between the working electrode (WE) and counter electrode (CE) separated by a solution resistance, $R_s$.

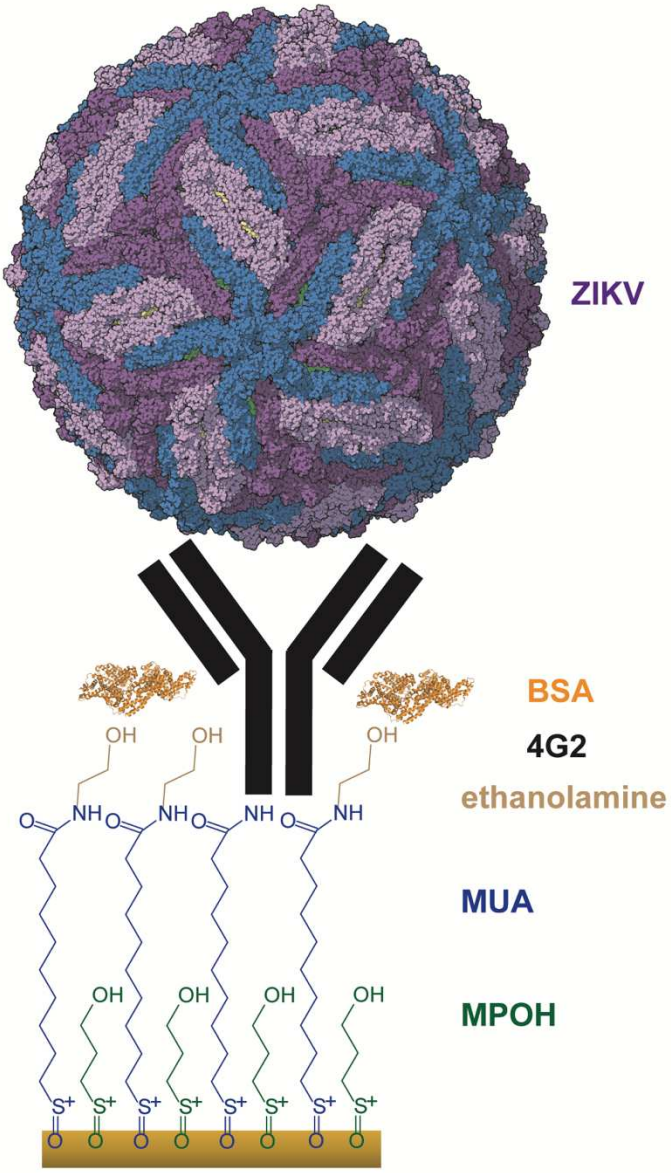


**Figure 5.2. Electrode surface functionalization and target detection.** The gold electrode is modified with a mixed SAM of long (MUA) and short (MPOH) chain alkanethiols at an equal ratio. The carboxylic head groups of the MUA are functionalized with 4G2 antibody via NHS/EDC chemistry and remaining head groups are deactivated with ethanolamine. Bovine serum albumin (BSA) is adsorbed to the surface to block nonspecific binding. ZIKV structure adapted from (15) and BSA structure adapted from (569).

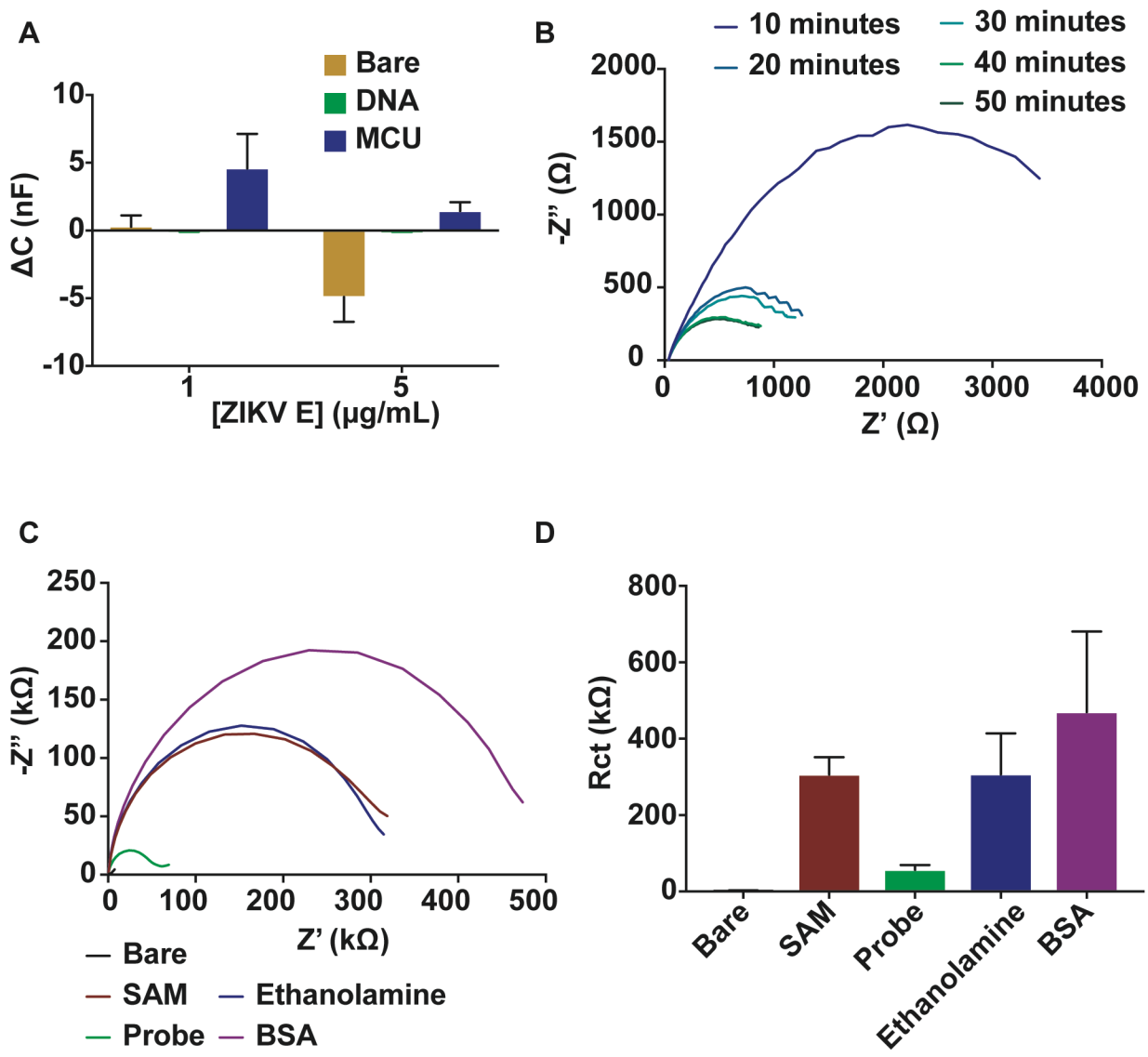


**Figure 5.3. Characterization of the electrode surface.** A) Adsorption of recombinant ZIKV E protein on the bare, DNA-passivated, and MCU passivated surface. B) Optimization of electrode cleaning. C) EIS characterization of step-wise electrode functionalization. D) Charge transfer resistance, $R_{ct}$, for step-wise electrode functionalization. (mean + SEM)

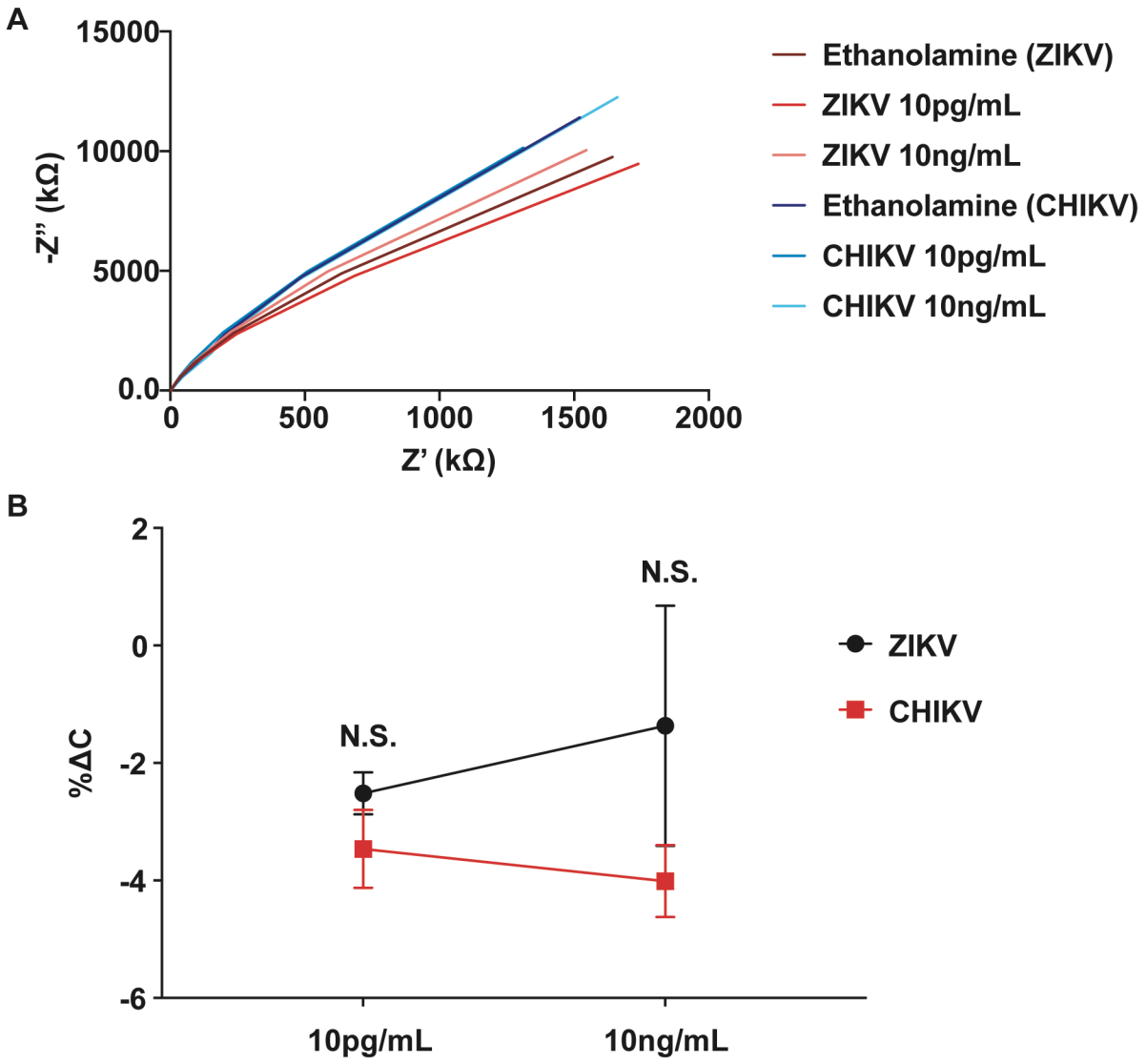


**Figure 5.4. Specificity testing with recombinant ZIKV and CHIKV E protein.** A) EIS testing of ZIKV (specific) and CHIKV (nonspecific) E protein from an ethanolamine-passivated electrode baseline. B) Percent capacitance change from ZIKV (specific) and CHIKV (nonspecific) E protein target. (mean ± SEM)

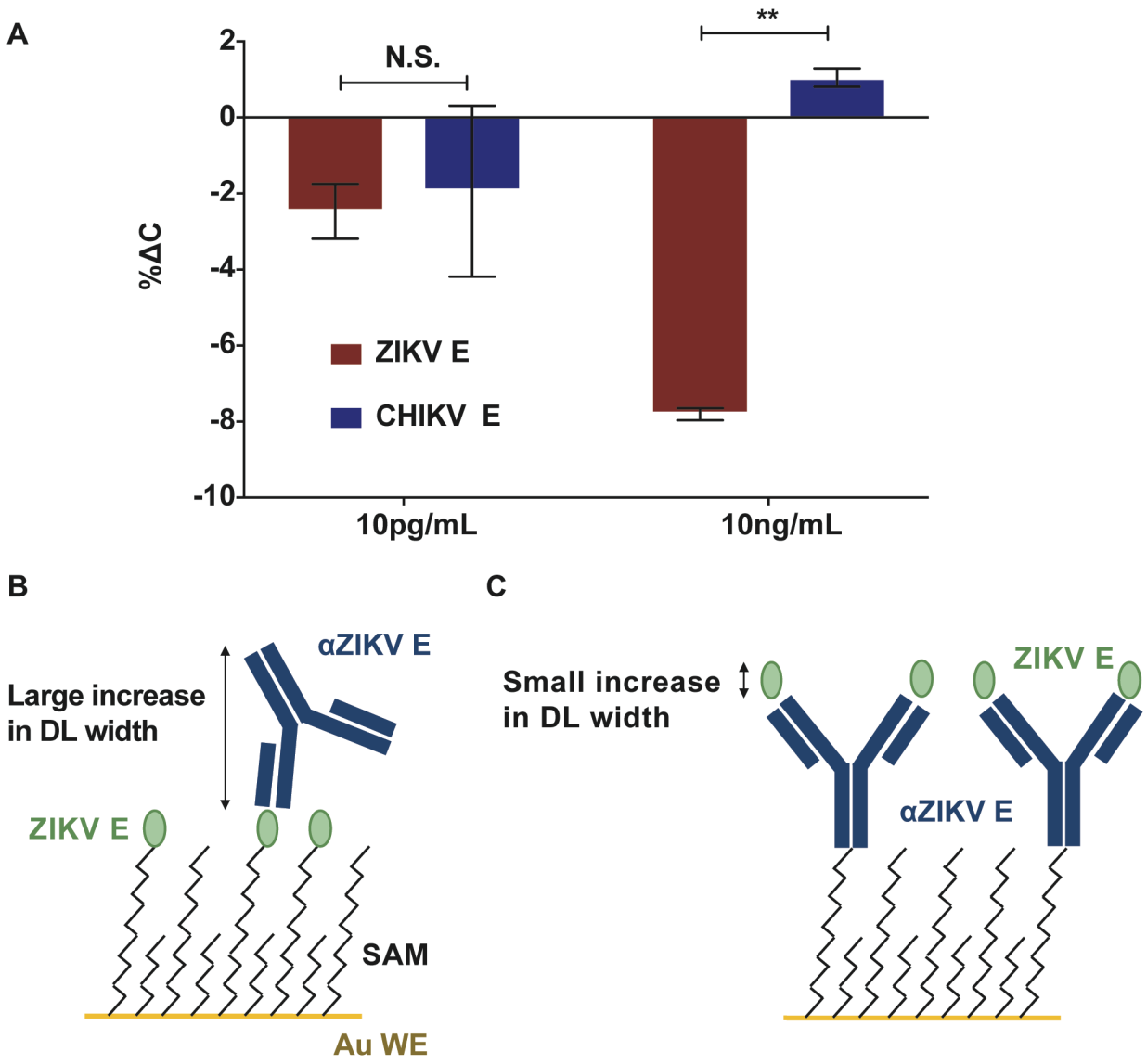


**Figure 5.5. Wire sensor analysis of recombinant ZIKV and CHIKV E protein.** A) Percent capacitance change for ZIKV and CHIKV E target protein (mean ± SEM). B) Double layer length associated with a large analyte (αZIKV E) and a small analyte (ZIKV E).

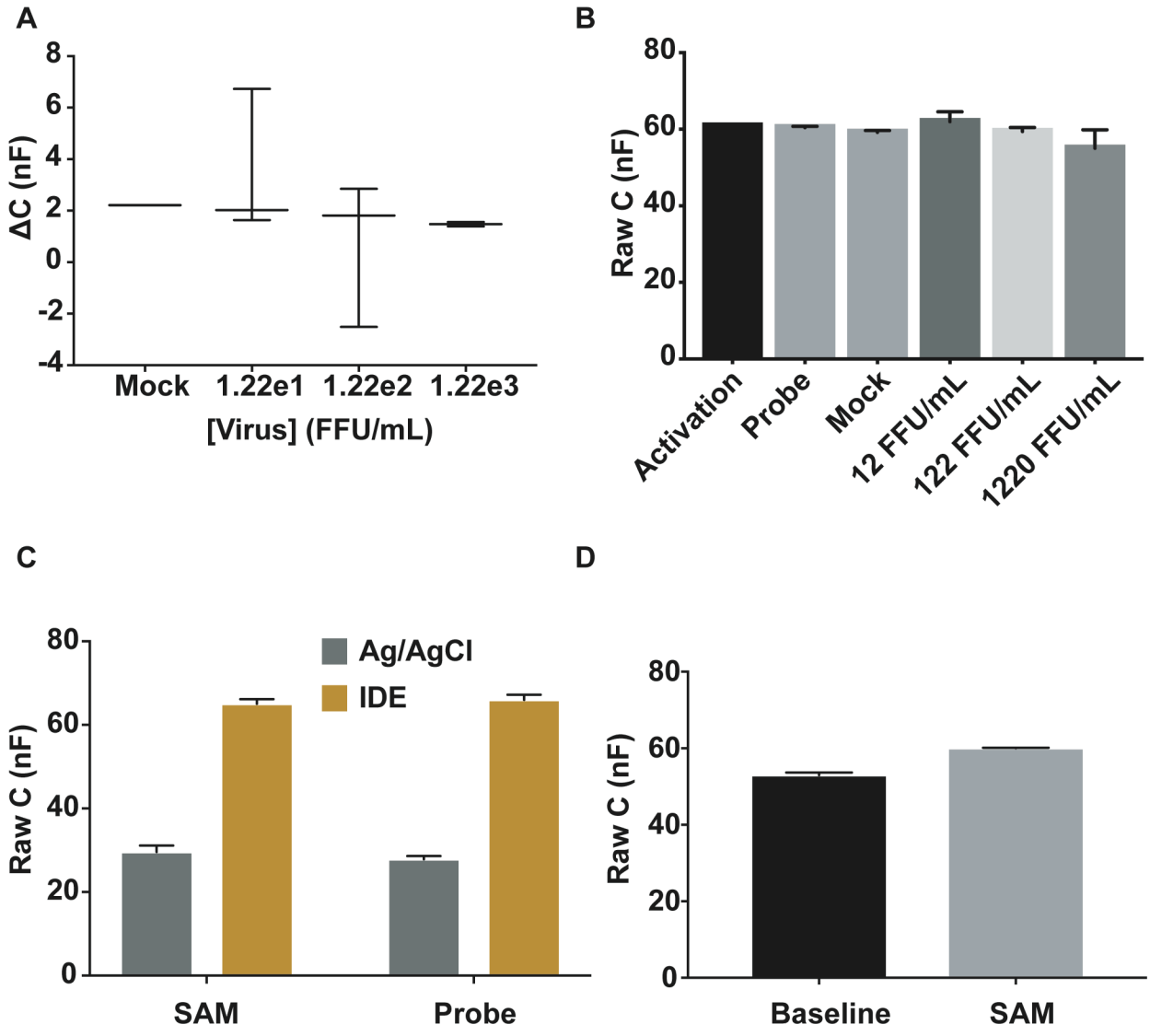


**Figure 5.6. Capacitance measurements for ZIKV particle detection and electrode characterization.** A). Capacitance response for ZIKV concentrations ranging from 12 FFU/mL – 1220 FFU/mL compared to a mock sample. B) Investigation of capacitive response to 4G2 probe immobilization compared to mock and virus samples. C) Comparison of capacitive response to SAM and 4G2 probe functionalization with the array electrode pair and an external Ag/AgCl reference electrode. D) Capacitive response of bare and SAM-functionalized electrodes. (mean ± SEM)

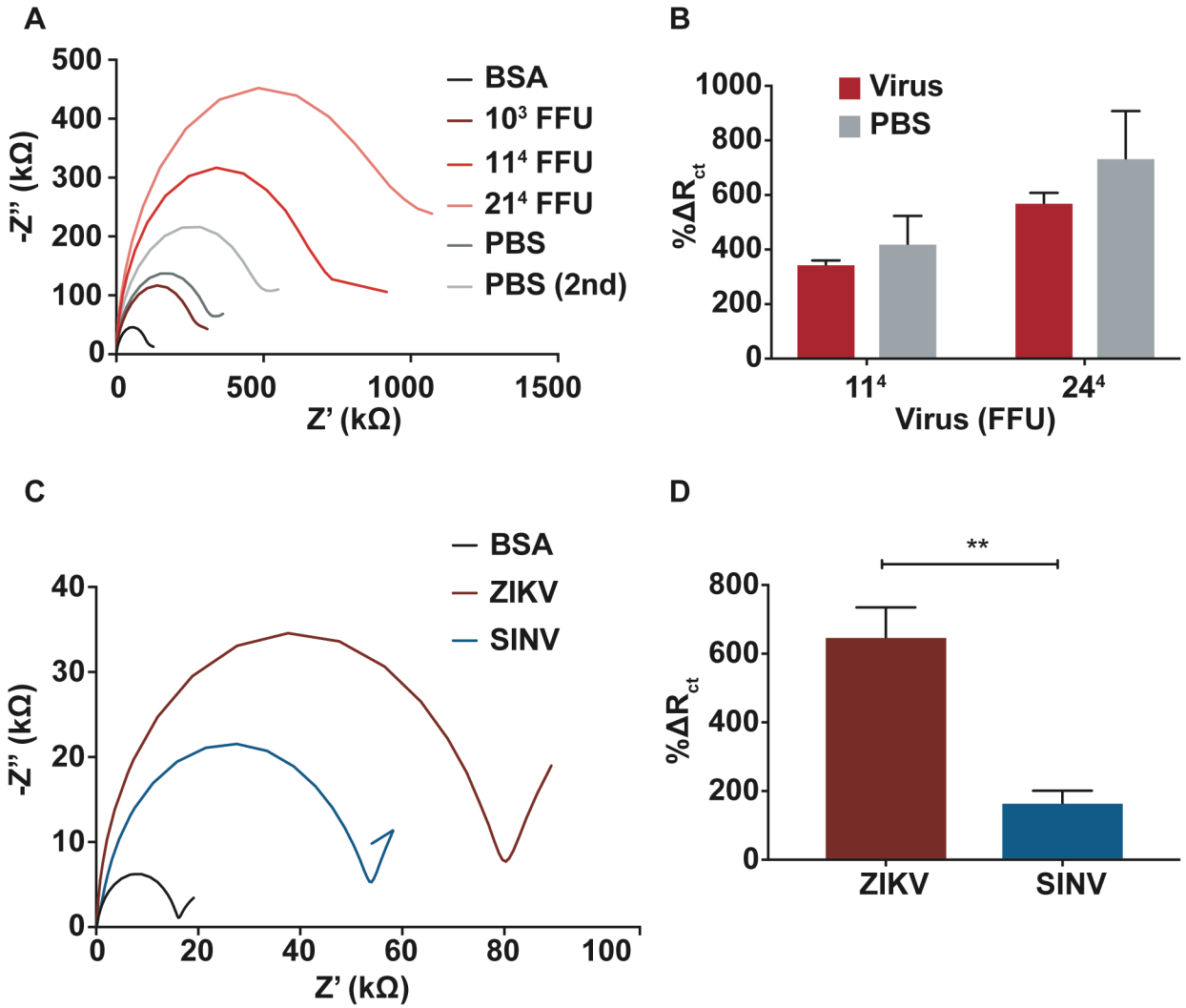


**Figure 5.7. Background noise and specificity.** A) EIS target and buffer control responses after refrigerated fabrication and target incubations. B) $\%\Delta R_{ct}$ response for virus and buffer control. C) EIS response comparing ZIKV (12,200 FFU) with an excess of SINV negative control (267,000 FFU). D) $\%\Delta R_{ct}$ response for ZIKV compared to an excess of SINV negative control. (n = 6, mean ± SEM, p = 0.01)

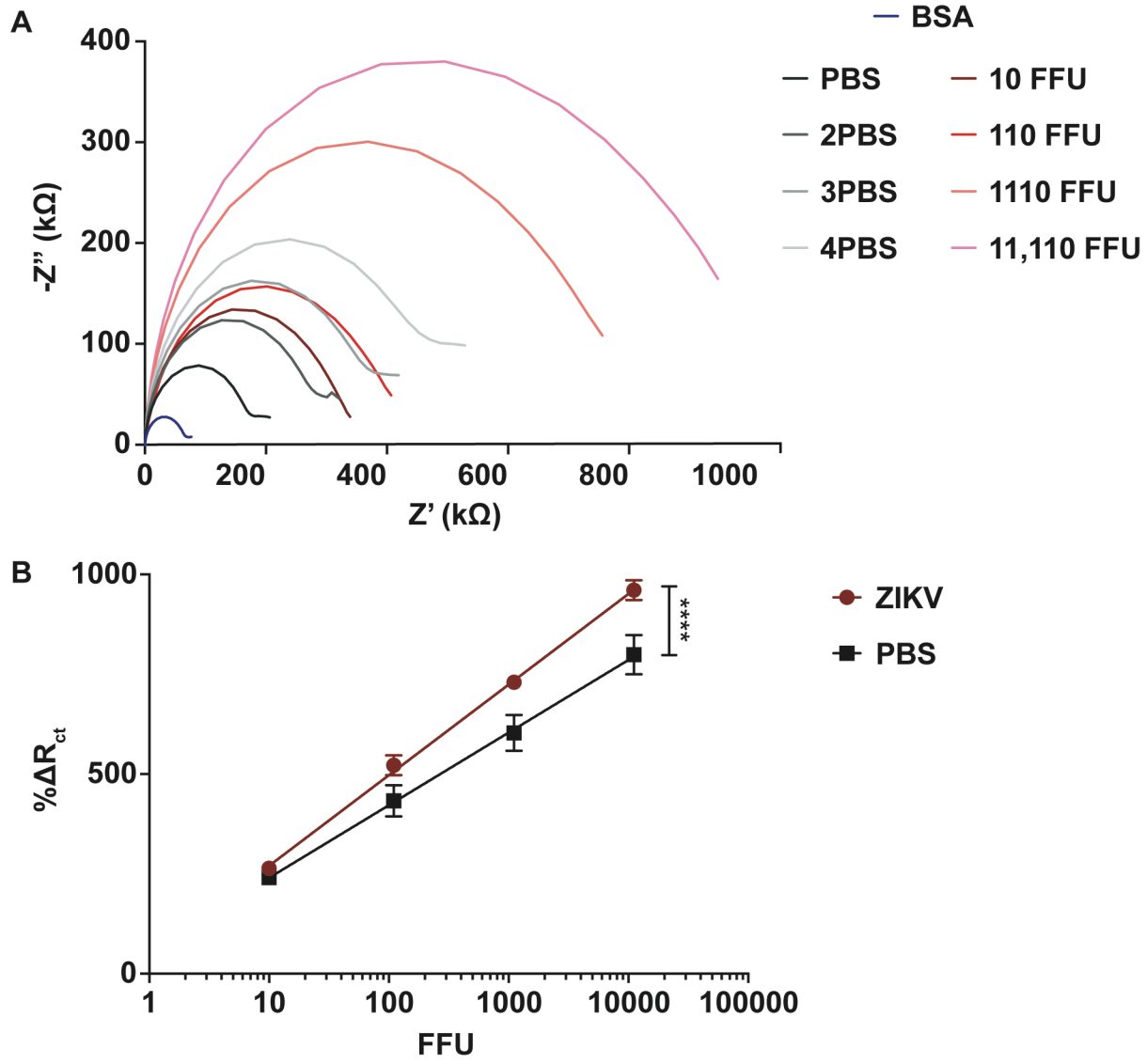


**Figure 5.8. Calibration of the array sensor.** A) Nyquist plots for the EIS response of subsequent ZIKV incubations (10 – 11,110 FFU) compared to subsequent PBS negative control incubations. B) Linear response of $\%\Delta R_{ct}$ against the logarithmic concentration of ZIKV (or PBS negative control). The slopes of the specific and background lines are significantly different (n = 4 technical replicates, mean ± SEM, p = 0.0001).

# CHAPTER 6 - CONCLUSION

## Summary

ZIKV is an emerging arbovirus that caused over 64,000 confirmed cases of ZIKV fever during the 2015-2016 Brazilian outbreak alone (148). While the majority of cases are asymptomatic or manifest with a mild febrile illness, 1% of patients develop severe neurological complications including Guillan Barré syndrome, transverse myelitis, encephalitis, etc (162). Furthermore, the incidence of microcephaly and other birth defects is four to nine fold higher in infants exposed to ZIKV in the womb (212). In order to properly monitor patients for complications and intervene rapidly when necessary, timely and accurate diagnosis is crucial for disease outcome. Accurate diagnostics are also essential for disease surveillance which facilitates timely intervention for outbreaks. Current diagnostic techniques like nucleic acid testing by real time PCR and serological testing by ELISA and PRNT are reliable and sensitive but are slow, costly, and must be executed is specialized laboratories with bulky equipment. There is a large need for new tools that reduce labor, cost, and time. Electrochemical sensors demonstrate excellent sensitivity and are easily miniaturized, making them an attractive platform for point-of-care diagnostics. In this work, we have described three new electrochemical platforms for ZIKV diagnosis for nucleic acid testing, serological analysis, and virus detection.

The NP-ELISA described in Chapter 3 builds upon reported enzymatic assays (501) and simplifies the platform to reduce cost and labor while maintaining sensitivity comparable to commercial assays. Chapter 4 discusses a novel microwire sensor that is simpler in design, faster, and significantly increases sensitivity compared to ELISAs and other reported sensors (277, 344). Although electrochemical biosensors out-perform ELISAs in miniaturization and portability, they often lack throughput. A novel electrode array is described in Chapter 5 that adds throughput for the direct detection of virus particles. These advancements expand the

boundaries and possibilities of assay development and contribute innovations that can be readily integrated in mainstream biosensor research.

## Future Directions

While the platforms described here offer innovations to the field of electrochemical biosensors, they each have limitations that need to be addressed as well as potential for further development. The NP-ELISA was validated using a synthetic DNA oligo model target and more work needs to be done to investigate the assay's capacity to detect viral RNA. Current gold standard diagnostics use an intermediate step to indirectly detect RNA, which increases reagent and instrumentation costs as well as labor. The ability to directly detect RNA would negate the need for these extra steps and reduce cost, labor, time, and assay complexity. This reduces turnaround time, providing health care providers with the information they need for proper patient care earlier, which would reduce sequelae and improve disease outcome. However, nuclease protection has traditionally been used to detect mRNA and microRNA. Because RNA-RNA hybrids are thermodynamically more stable than RNA-DNA hybrids (570), extensive secondary structure throughout the ZIKV RNA genome may preferentially fold back onto itself rather than hybridizing with the oligo and inhibit its ability to successfully protect the probe from degradation. Hybridization conditions need to be carefully optimized to mitigate the inhibitory effects of secondary structure. Once optimized, research employing traditional nuclease protection assays indicates that the assay tolerates partially degraded RNA, whereas other molecular techniques like PCR and LAMP assays do not. As long as the region complementary to the probe is intact, hybridization and protection may occur properly. This has large impact for point-of-care use as proper sample storage is not always feasible in the field and samples may rapidly degrade. Additionally, the electrochemical assay can be easily integrated into handheld, disposable paper sensors for point-of-care use which have already been developed by our group

(522, 523). The assay can also be developed as a multiplexed sensor by employing multiple antibody-small molecule pairs with different enzymatic substrates that undergo oxidation and reduction at distinguishable potentials. Multiplexed analysis enables health care providers to test patients with general, nonspecific symptomology for multiple pathogens simultaneously and dramatically reduce time for diagnosis.

The microwire sensor demonstrates extreme sensitivity that enables antibody detection four days earlier and with less sample volume compared to gold standard assays. The underlying mechanism for the sensor's sensitivity is currently unknown, and further work needs to be done to understand the interfacial interactions and electrochemistry. Such studies may include characterization of the amount, behavior, and orientation of ZIKV E protein at the electrode surface and surface plasmon resonance studies to investigate the interaction of ZIKV E with its antibody on the electrode. In addition, the microwire sensor currently uses a glass substrate, but can also be developed as a paper microwire sensor for point-of-care applications. During the process of integrating the wire sensor with paper microfluidics, challenges will need to be addressed such as long-term probe protein stability as well reagent dehydration for storage and shipping, and rehydration for use. However, incorporating a paper substrate increases ease of handling and allows for incorporation of microfluidics that automate sample processing – all of which increase efficiency and reduce cost, labor, and time for diagnosis.

Lastly, the array sensor increases throughput and enables multiple electrodes to be handled simultaneously. As such, the sensor has large capacity for multiplexed analysis by functionalizing different electrodes with probes for various pathogens, and such developments will also require intricate microfluidics to control and automate sample application. As described previously, an automated, multiplexed sensor enables differential diagnosis to be completed faster and easier without expensive shipment of environmentally-sensitive clinical

samples to a specialized diagnostic laboratory. Several challenges still remain to be addressed for the array sensor, primarily involving the background signal from buffer. Although contamination has been ruled out, it is still unclear what mechanisms give rise to increasing background signals which do not occur in the presence of specific or nonspecific virus. While the surface can be modified with better antifouling agents to further reduce nonspecific signal, it may be beneficial to probe the surface using approaches like microscopy, x-ray reflectometry, or isothermal titration calorimetry to investigate the behavior of the passivation layers. Once optimized, the array sensor exhibits great potential for point-of-care applications. Together, these three platforms represent crucial steps in the development of tenable commercial point-of-care diagnostics in terms of multiplexing capacity, direct detection, sensitivity, and throughput.

REFERENCES


1. Westaway EG, Brinton MA, Gaidamovich SYa, Horzinek MC, Igarashi A, Kääriäinen L, Lvov DK, Porterfield JS, Russell PK, Trent DW. 1985. Flaviviridae. Intervirology 24:183–92.
2. Knipe DM, Howley PM. 2013. Fields Virology, 6th ed. Lippincott Williams &Wilkins, Philadelphia.
3. Mukhopadhyay S, Kuhn RJ, Rossmann MG. 2005. A structural perspective of the Flavivirus life cycle. Nat Rev Microbiol 3:13–22.
4. Calisher CH, Karabatsos N, Dalrymple JM, Shope RE, Porterfield JS, Westaway EG, Brandt WE. 1989. Antigenic relationships between flaviviruses as determined by cross-neutralization tests with polyclonal antisera. J Gen Virol 70:37–43.
5. SMITHBURN KC. 1954. Antigenic relationships among certain arthropod-borne viruses as revealed by neutralization tests. J Immunol 72:376–88.
6. Kuno G, Chang GJ, Tsuchiya KR, Karabatsos N, Cropp CB. 1998. Phylogeny of the genus Flavivirus. J Virol 72:73–83.
7. Barba-Spaeth G, Dejnirattisai W, Rouvinski A, Vaney M-C, Medits I, Sharma A, Simon-Lorière E, Sakuntabhai A, Cao-Lormeau V-M, Haouz A, England P, Stiasny K, Mongkolsapaya J, Heinz FX, Screaton GR, Rey FA. 2016. Structural basis of potent Zika-dengue virus antibody cross-neutralization. Nature 536:48–53.
8. Lanciotti RS, Lambert AJ, Holodniy M, Saavedra S, del Carmen Castillo Signor L. 2016. Phylogeny of Zika Virus in Western Hemisphere , 2015. Emerg Infect Dis 22:DOI: 10.3201/eid2205.160065.
9. Kutsuna S, Kato Y, Takasaki T, Moi ML, Kotaki A, Uemeru H, Matono T, Fujiya Y,

Mawatari M, Takeshita N, Hayamawa S, Kanagawa S, Ohmagari N. 2014. Two cases of Zika fever imported from French Polynesia to Japan, December 2013 to Jauary 2014. Eurosurveillance 19:pii: 20683.

10. Zammarchi L, Stella G, Mantella A, Bartolozzi D, Tappe D, Günther S, Oestereich L, Cadar D, Muñoz-Fontela C, Bartoloni A, Schmidt-Chanasit J. 2015. Zika virus infections imported to Italy: Clinical, immunological and virological findings, and public health implications. J Clin Virol 63:32–35.
11. Zammarchi L, Tappe D, Fortuna C, Remoli ME, Günther S, Venturi G, Bartoloni A. 2015. Zika virus infection in a traveller returning to Europe from Brazil , March 2015. Euro Surveil 20:pii=21153.
12. Karimi O, Goorhuis A, Schinkel J, Codrington J, Vreden SGS, Vermaat JS, Stijnis C, Grobusch MP. 2016. Thrombocytopenia and subcutaneous bleedings in a patient with Zika virus infection. Lancet 6736:18–19.
13. Zhong Y Bin, Liu XQ, Deng YC, Xu PH, Zhong GR, Zhang W. 2016. First Case of Laboratory - confirmed Zika Virus Infection Imported into China 129:2013–2014.
14. Dupont-Rouzeyrol M, O'Connor O, Calvez E, Daurès M, John M, Grangeon J-P, Gourinat A-C. 2015. Co-infection with Zika and Dengue Viruses in 2 Patients, New Caledonia, 2014. Emerg Infect Dis 21:381–382.
15. Sirohi D, Chen Z, Sun L, Klose T, Pierson TC, Rossmann MG, Kuhn RJ. 2016. The 3.8 Å resolution cryo-EM structure of Zika virus. Science (80- ) 5316:1–7.
16. Faye O, Freire CCM, Iamarino A, Faye O, de Oliveira JVC, Diallo M, Zanotto PMA, Sall AA. 2014. Molecular Evolution of Zika Virus during Its Emergence in the 20th Century. PLoS Negl Trop Dis 8:e2636.
17. Zhang Y, Zhang W, Ogata S, Clements D, Strauss JH, Baker TS, Kuhn RJ, Rossmann

MG. 2004. Conformational Changes of the Flavivirus E Glycoprotein. Structure 12:1607–1618.

18. Hasan SS, Sevvana M, Kuhn RJ, Rossmann MG. 2018. Structural biology of Zika virus and other flaviviruses. Nat Struct Mol Biol 25:13–20.

19. Rey FA, Heinz FX, Mandl C, Kunz C, Harrison SC. 1995. The envelope glycoprotein from tick-borne encephalitis virus at 2 Å resolution. Nature 375:291–298.

20. Mandl CW, Allison SL, Holzmann H, Meixner T, Heinz FX. 2000. Attenuation of Tick-Borne Encephalitis Virus by Structure-Based Site-Specific Mutagenesis of a Putative Flavivirus Receptor Binding Site. J Virol 74:9601–9609.

21. Zhang W, Chipman PR, Corver J, Johnson PR, Zhang Y, Mukhopadhyay S, Baker TS, Strauss JH, Rossmann MG, Kuhn RJ. 2003. Visualization of membrane protein domains by cryo-electron microscopy of dengue virus. Nat Struct Biol 10:907–12.

22. Dejnirattisai W, Jumnainsong A, Onsirisakul N, Fitton P, Vasanawathana S, Limpitikul W, Puttikhunt C, Edwards C, Duangchinda T, Supasa S, Chawansuntati K, Malasit P, Mongkolsapaya J, Screaton G. 2010. Cross-Reacting Antibodies Enhance Dengue Virus Infection in Humans. Science (80- ) 328:745–748.

23. Beltramello M, Williams KL, Simmons CP, MacAgno A, Simonelli L, Quyen NTH, Sukupolvi-Petty S, Navarro-Sanchez E, Young PR, De Silva AM, Rey FA, Varani L, Whitehead SS, Diamond MS, Harris E, Lanzavecchia A, Sallusto F. 2010. The human immune response to dengue virus is dominated by highly cross-reactive antibodies endowed with neutralizing and enhancing activity. Cell Host Microbe 8:271–283.

24. Lai C-Y, Tsai W-Y, Lin S-R, Kao C-L, Hu H-P, King C-C, Wu H-C, Chang G-J, Wang W-K. 2008. Antibodies to Envelope Glycoprotein of Dengue Virus during the Natural Course of Infection Are Predominantly Cross-Reactive and Recognize Epitopes

Containing Highly Conserved Residues at the Fusion Loop of Domain II. J Virol 82:6631–6643.

25. Jarmer J, Zlatkovic J, Tsouchnikas G, Vratskikh O, Strauss J, Aberle JH, Chmelik V, Kundi M, Stiasny K, Heinz FX. 2014. Variation of the Specificity of the Human Antibody Responses after Tick-Borne Encephalitis Virus Infection and Vaccination. J Virol 88:13845–13857.

26. Oliphant T, Nybakken GE, Austin SK, Xu Q, Bramson J, Loeb M, Throsby M, Fremont DH, Pierson TC, Diamond MS. 2007. Induction of Epitope-Specific Neutralizing Antibodies against West Nile Virus. J Virol 81:11828–11839.

27. Nadugala MN, Jeewandara C, Malavige GN, Premaratne PH, Goonasekara CL. 2017. Natural antibody responses to the capsid protein in sera of Dengue infected patients from Sri Lanka. PLoS One 12:1–15.

28. Chung KM, Nybakken GE, Thompson BS, Engle MJ, Marri A, Fremont DH, Diamond MS. 2006. Antibodies against West Nile Virus Nonstructural Protein NS1 Prevent Lethal Infection through Fc γ Receptor-Dependent and -Independent Mechanisms Antibodies against West Nile Virus Nonstructural Protein NS1 Prevent Lethal Infection through Fc ∕∕ Receptor-D. J Virol 80:1340–1351.

29. Dai L, Wang Q, Qi J, Shi Y, Yan J, Gao GF. 2016. Molecular basis of antibody-mediated neutralization and protection against flavivirus. IUBMB Life 783–791.

30. Heinz FX, Stiasny K. 2017. The Antigenic Structure of Zika Virus and Its Relation to Other Flaviviruses: Implications for Infection and Immunoprophylaxis. Microbiol Mol Biol Rev 81:e00055-16.

31. Stettler K, Beltramello M, Espinosa DA, Graham V, Cassotta A, Bianchi S, Vanzetta F, Minola A, Jaconi S, Mele F, Foglierini M, Pedotti M, Simonelli L, Dowall S, Atkinson B,

Percivalle E, Simmons CP, Varani L, Blum J, Baldanti F, Cameroni E, Hewson R, Harris E, Lanzavecchia A, Sallusto F, Corti D. 2016. Specificity, cross-reactivity and function of antibodies elicited by Zika virus infection. Science (80- ) 8505.

32. Stiasny K, Kiermayr S, Holzmann H, Heinz FX. 2006. Cryptic Properties of a Cluster of Dominant Flavivirus Cross-Reactive Antigenic Sites. J Virol 80:9557–9568.

33. Paul LM, Carlin ER, Jenkins MM, Tan AL, Barcellona CM, Nicholson CO, Michael SF, Isern S. 2016. Dengue virus antibodies enhance Zika virus infection. Clin Transl Immunol 5:e117.

34. Rodenhuis-Zybert I a., Moesker B, da Silva Voorham JM, van der Ende-Metselaar H, Diamond MS, Wilschut J, Smit JM. 2011. A Fusion-Loop Antibody Enhances the Infectious Properties of Immature Flavivirus Particles. J Virol 85:11800–11808.

35. Göertz GP, Abbo SR, Fros JJ, Pijlman GP. 2017. Functional RNA during Zika virus infection. Virus Res 1–13.

36. Ng WC, Soto-Acosta R, Bradrick SS, Garcia-Blanco MA, Ooi EE. 2017. The 5′ and 3′ untranslated regions of the flaviviral genome. Viruses 9:1–14.

37. Filomatori C V., Lodeiro MF, Alvarez DE, Samsa MM, Pietrasanta L, Gamarnik A V. 2006. A 5′ RNA element promotes dengue virus RNA synthesis on a circular genome. Genes Dev 20:2238–2249.

38. Yu L, Nomaguchi M, Padmanabhan R, Markoff L. 2008. Specific requirements for elements of the 5’ and 3’ terminal regions in flavivirus RNA synthesis and viral replication. Virology 374:170–85.

39. Khromykh A a, Meka H, Guyatt KJ, Westaway EG. 2001. Essential Role of Cyclization Sequences in Flavivirus RNA Replication Essential Role of Cyclization Sequences in Flavivirus RNA Replication †. J Virol 75:6719–6728.

40. Alvarez DE, Lodeiro MF, Ludueña SJ, Lía I, Gamarnik A V, Lodeiro F, Luduen SJ. 2005. Long-Range RNA-RNA Interactions Circularize the Dengue Virus Genome Long-Range RNA-RNA Interactions Circularize the Dengue Virus Genome. J Virol 79:6631–6643.

41. Hahn CS, Hahn YS, Rice CM, Lee E, Dalgarno L, Strauss EG, Strauss JH. 1987. Conserved elements in the 3′ untranslated region of flavivirus RNAs and potential cyclization sequences. J Mol Biol 198:33–41.

42. Akiyama BM, Laurence HM, Massey AR, Costantino DA, Xie X, Yang Y, Shi PY, Nix JC, Beckham JD, Kieft JS. 2016. Zika virus produces noncoding RNAs using a multi-pseudoknot structure that confounds a cellular exonuclease. Science (80- ) 354:1148–1152.

43. Moon SL, Anderson JR, Kumagai Y, Wilusz CJ, Akira S, Khromykh AA, Wilusz J. 2012. A noncoding RNA produced by arthropod-borne flaviviruses inhibits the cellular exoribonuclease XRN1 and alters host mRNA stability. RNA 18:2029–40.

44. Manzano M, Reichert ED, Polo S, Falgout B, Kasprzak W, Shapiro BA, Padmanabhan R. 2011. Identification of cis-acting elements in the 3′-untranslated region of the dengue virus type 2 RNA that modulate translation and replication. J Biol Chem 286:22521–22534.

45. Yu L, Markoff L. 2005. The topology of bulges in the long stem of the flavivirus 3’ stem-loop is a major determinant of RNA replication competence. J Virol 79:2309–24.

46. Zhang L. 2010. Glycosaminoglycan (GAG) biosynthesis and GAG-binding proteinsProgress in Molecular Biology and Translational Science, 1st ed. Elsevier Inc.

47. Chen Y, Maguire T, Hileman RE, Fromm JR, Esko JD, Linhardt RJ, Marks RM. 1997. Dengue virus infectivity depends on envelope protein binding to target cell heparan sulfate. Nat Med 3:866–871.

48. Kim SY, Zhao J, Liu X, Fraser K, Lin L, Zhang X, Zhang F, Dordick JS, Linhardt RJ. 2017. Interaction of Zika Virus Envelope Protein with Glycosaminoglycans. Biochemistry 56:1151–1162.

49. Perera-Lecoin M, Meertens L, Carnec X, Amara A. 2013. Flavivirus entry receptors: An update. Viruses 6:69–88.

50. Bermejo-Jambrina M, Eder J, Helgers LC, Hertoghs N, Nijmeijer BM, Stunnenberg M, Geijtenbeek TBH. 2018. C-type lectin receptors in antiviral immunity and viral escape. Front Immunol 9:1–12.

51. Wang P, Hu K, Luo S, Zhang M, Deng X, Li C, Jin W, Hu B, He S, Li M, Du T, Xiao G, Zhang B, Liu Y, Hu Q. 2016. DC-SIGN as an attachment factor mediates Japanese encephalitis virus infection of human dendritic cells via interaction with a single high-mannose residue of viral E glycoprotein. Virology 488:108–119.

52. Shimojima M, Takenouchi A, Shimoda H, Kimura N, Maeda K. 2014. Distinct usage of three C-type lectins by Japanese encephalitis virus: DC-SIGN, DC-SIGNR, and LSECtin. Arch Virol 159:2023–2031.

53. Phanthanawiboon S, A-nuegoonpipat A, Panngarm N, Limkittikul K, Ikuta K, Anantapreecha S, Kurosu T. 2014. Isolation and propagation of Dengue virus in Vero and BHK-21 cells expressing human DC-SIGN stably. J Virol Methods 209:55–61.

54. Richter MKS, Da Silva Voorham JM, Torres Pedraza S, Hoornweg TE, Van De Pol DPI, Rodenhuis-Zybert IA, Wilschut J, Smit JM. 2014. Immature dengue virus is infectious in human immature dendritic cells via interaction with the receptor molecule DC-SIGN. PLoS One 9.

55. Davis CW, Nguyen H-Y, Hanna SL, Sánchez MD, Doms RW, Pierson TC. 2006. West Nile virus discriminates between DC-SIGN and DC-SIGNR for cellular attachment and

infection. J Virol 80:1290–301.

56. Pokidysheva E, Zhang Y, Battisti AJ, Bator-Kelly CM, Chipman PR, Xiao C, Gregorio GG, Hendrickson WA, Kuhn RJ, Rossmann MG. 2006. Cryo-EM reconstruction of dengue virus in complex with the carbohydrate recognition domain of DC-SIGN. Cell 124:485–493.

57. Navarro-Sanchez E, Altmeyer R, Amara A, Schwartz O, Fieschi F, Virelizier JL, Arenzana-Seisdedos F, Desprès P. 2003. Dendritic-cell-specific ICAM3-grabbing non-integrin is essential for the productive infection of human dendritic cells by mosquito-cell-derived dengue viruses. EMBO Rep 4:723–728.

58. Miller JL, deWet BJM, Martinez-Pomares L, Radcliffe CM, Dwek RA, Rudd PM, Gordon S. 2008. The Mannose Receptor Mediates Dengue Virus Infection of Macrophages. PLoS Pathog 4:e17.

59. Lo YL, Liou GG, Lyu JH, Hsiao M, Hsu TL, Wong CH. 2016. Dengue virus infection is through a cooperative interaction between a mannose receptor and CLEC5A on macrophage as a multivalent hetero-complex. PLoS One 11:1–13.

60. Cheng G, Cox J, Wang P, Krishnan MN, Dai J, Qian F, Anderson JF, Fikrig E. 2010. A C-type lectin collaborates with a CD45 phosphatase homolog to facilitate West Nile virus infection of mosquitoes. Cell 142:714–25.

61. Liu K, Qian Y, Jung Y, Zhou B, Cao R, Shen T, Shao D, Wei J, Ma Z, Chen P, Zhu H, Qiu Y. 2017. mosGCTL-7, a C-Type Lectin Protein, Mediates Japanese Encephalitis Virus Infection in Mosquitoes. J Virol 91:1–18.

62. Liu P, Ridilla M, Patel P, Betts L, Gallichotte E, Shahidi L, Thompson NL, Jacobson K. 2017. Beyond attachment: Roles of DC-SIGN in dengue virus infection. Traffic 18:218–231.

63. Maruri-Avidal L, Weisberg AS, Moss B. 2013. Direct Formation of Vaccinia Viral Membranes from the Endoplasmic Reticulum in the Absence of the Newly Characterized L2-Interacting A30.5 Protein. J Virol 87:12313–12326.

64. Amara A, Mercer J. 2015. Viral apoptotic mimicry. Nat Rev Microbiol 13:461–469.

65. Santiago C, Ballesteros A, Martínez-Muñoz L, Mellado M, Kaplan GG, Freeman GJ, Casasnovas JM. 2007. Structures of T cell immunoglobulin mucin protein 4 show a metal-Ion-dependent ligand binding site where phosphatidylserine binds. Immunity 27:941–51.

66. Richard AS, Zhang A, Park S-J, Farzan M, Zong M, Choe H. 2015. Virion-associated phosphatidylethanolamine promotes TIM1-mediated infection by Ebola, dengue, and West Nile viruses. Proc Natl Acad Sci 112:14682–14687.

67. Jemielity S, Wang JJ, Chan YK, Ahmed AA, Li W, Monahan S, Bu X, Farzan M, Freeman GJ, Umetsu DT, DeKruyff RH, Choe H. 2013. TIM-family Proteins Promote Infection of Multiple Enveloped Viruses through Virion-associated Phosphatidylserine. PLoS Pathog 9.

68. Meertens L, Carnec X, Lecoin MP, Ramdasi R, Guivel-Benhassine F, Lew E, Lemke G, Schwartz O, Amara A. 2012. The TIM and TAM Families of Phosphatidylserine Receptors Mediate Dengue Virus Entry. Cell Host Microbe 12:544–557.

69. Dejarnac O, Hafirassou ML, Chazal M, Versapuech M, Gaillard J, Perera-Lecoin M, Umana-Diaz C, Bonnet-Madin L, Carnec X, Tinevez JY, Delaugerre C, Schwartz O, Roingeard P, Jouvenet N, Berlioz-Torrent C, Meertens L, Amara A. 2018. TIM-1 Ubiquitination Mediates Dengue Virus Entry. Cell Rep 1779–1793.

70. Sasaki T, Knyazev PG, Clout NJ, Cheburkin Y, Göhring W, Ullrich A, Timpl R, Hohenester E. 2006. Structural basis for Gas6-Axl signalling. EMBO J 25:80–87.

71. Stitt TN, Conn G, Gore M, Lai C, Bruno J, Radziejewski C, Mattsson K, Fisher J, Gies

DR, Jones PF. 1995. The anticoagulation factor protein S and its relative, Gas6, are ligands for the Tyro 3/Axl family of receptor tyrosine kinases. Cell 80:661–670.

72. Liu S, DeLalio LJ, Isakson BE, Wang TT. 2016. AXL-Mediated Productive Infection of Human Endothelial Cells by Zika Virus. Circ Res 119:1183–1189.

73. Richard AS, Shim B-S, Kwon Y-C, Zhang R, Otsuka Y, Schmitt K, Berri F, Diamond MS, Choe H. 2017. AXL-dependent infection of human fetal endothelial cells distinguishes Zika virus from other pathogenic flaviviruses. Proc Natl Acad Sci 114:2024–2029.

74. Wang ZY, Wang Z, Zhen Z Da, Feng KH, Guo J, Gao N, Fan DY, Han DS, Wang PG, An J. 2017. Axl is not an indispensable factor for zika virus infection in mice. J Gen Virol 98:2061–2068.

75. Persaud M, Martinez-Lopez A, Buffone C, Porcelli SA, Diaz-Griffero F. 2018. Infection by Zika viruses requires the transmembrane protein AXL, endocytosis and low pH. Virology 518:301–312.

76. Nowakowski TJ, Pollen AA, Lullo E Di, Kriegstein AR, Francisco S, Francisco S, Francisco S, Francisco S. 2017. Expression Analysis Highlights AXL as a Candidate Zika Virus Entry Receptor in Human Stem Cells. Cell Stem Cell 18:591–596.

77. Hastings AK, Yockey LJ, Jagger BW, Hwang J, Uraki R, Gaitsch HF, Parnell LA, Cao B, Mysorekar IU, Rothlin C V, Fikrig E, Diamond MS, Iwasaki A. 2017. TAM Receptors Are Not Required for Zika Virus Infection in Mice. Cell Rep 19:558–568.

78. Sirohi D, Kuhn RJ. 2017. Zika Virus Structure, Maturation, and Receptors. J Infect Dis 216:S935–S944.

79. Fibriansah G, Ng T-S, Kostyuchenko VA, Lee J, Lee S, Wang J, Lok S-M. 2013. Structural Changes in Dengue Virus When Exposed to a Temperature of 37 C. J Virol

87:7585–7592.

80. Fibriansah G, Lok SM. 2016. The development of therapeutic antibodies against dengue virus. Antiviral Res 128:7–19.

81. Stiasny K, Allison SL, Marchler-Bauer a, Kunz C, Heinz FX. 1996. Structural requirements for low-pH-induced rearrangements in the envelope glycoprotein of tick-borne encephalitis virus. J Virol 70:8142–8147.

82. Allison SL, Schalich J, Stiasny K, Mandl CW, Kunz C, Heinz FX. 1995. Oligomeric rearrangement of tick-borne encephalitis virus envelope proteins induced by an acidic pH. J Virol 69:695–700.

83. Modis Y, Ogata S, Clements D, Harrison SC. 2004. Structure of the dengue virus envelope protein after membrane fusion. Nature 427:313–319.

84. Bressanelli S, Stiasny K, Allison SL, Stura EA, Duquerroy S, Lescar J, Heinz FX, Rey FA. 2004. Structure of a flavivirus envelope glycoprotein in its low-pH-induced membrane fusion conformation. EMBO J 23:728–738.

85. Byk LA, Iglesias NG, De Maio FA, Gebhard LG, Rossi M, Gamarnik A V. 2016. Dengue Virus Genome Uncoating Requires Ubiquitination. MBio 7:1–10.

86. Garcia-Blanco MA, Vasudevan SG, Bradrick SS, Nicchitta C. 2016. Flavivirus RNA transactions from viral entry to genome replication. Antiviral Res 134:244–249.

87. Chiu W, Kinney RM, Dreher TW. 2005. Control of Translation by the 5′- and 3′-Terminal Regions of the Dengue Virus Genome. J Virol 79:8303–8315.

88. Clyde K, Harris E. 2006. RNA secondary structure in the coding region of dengue virus type 2 directs translation start codon selection and is required for viral replication RNA secondary structure in the coding region of dengue virus Type 2 Directs Translation Start Codon Selecti. J Virol 80:2170–2182.

89. Miller S, Kastner S, Krijnse-Locker J, Bühler S, Bartenschlager R. 2007. The non-structural protein 4A of dengue virus is an integral membrane protein inducing membrane alterations in a 2K-regulated manner. J Biol Chem 282:8873–8882.

90. Vidotto A, Morais ATS, Ribeiro MR, Pacca CC, Terzian ACB, Gil LHVG, Mohana-Borges R, Gallay P, Nogueira ML. 2017. Systems Biology Reveals NS4B-Cyclophilin A Interaction: A New Target to Inhibit YFV Replication. J Proteome Res 16:1542–1555.

91. Rastogi M, Sharma N, Singh SK. 2016. Flavivirus NS1: a multifaceted enigmatic viral protein. Virol J 13:131.

92. Klema VJ, Padmanabhan R, Choi KH. 2015. Flaviviral replication complex: Coordination between RNA synthesis and 5'-RNA capping. Viruses 7:4640–4656.

93. You, Shihyun and Padmanabhan R. 1999. A Novel in Vitro Replication System for Dengue Virus. J Biol Chem 274:33714–33722.

94. Calmels C, Ventura M, Aknin C, Métifiot M, Andreola ML. 2017. De novo RNA synthesis catalyzed by the Zika Virus RNA polymerase domain. Sci Rep 7:1–9.

95. Westaway EG, Mackenzie JM, Khromykh A a. 2003. Kunjin RNA replication and applications of Kunjin replicons. Adv Virus Res 59:99–140.

96. Saeedi BJ, Geiss BJ. 2012. Regulation of flavivirus RNA synthesis and capping. Wiley Interdiscip Rev RNA 4:723–35.

97. Issur M, Geiss BJ, Bougie I, Picard-Jean F, Despins S, Mayette J, Hobdey SE, Bisaillon M. 2009. The flavivirus NS5 protein is a true RNA guanylyltransferase that catalyzes a two-step reaction to form the RNA cap structure. Rna 15:2340–2350.

98. Gokhale NS, McIntyre ABR, McFadden MJ, Roder AE, Kennedy EM, Gandara JA, Hopcraft SE, Quicke KM, Vazquez C, Willer J, Ilkayeva OR, Law BA, Holley CL, Garcia-Blanco MA, Evans MJ, Suthar MS, Bradrick SS, Mason CE, Horner SM. 2016.

N6-Methyladenosine in Flaviviridae Viral RNA Genomes Regulates Infection. Cell Host Microbe 20:654–665.

99. Lichinchi G, Zhao BS, Wu Y, Lu Z, Qin Y, He C, Rana TM. 2016. Dynamics of Human and Viral RNA Methylation during Zika Virus Infection. Cell Host Microbe 20:666–673.

100. Lorenz IC, Allison SL, Heinz FX, Helenius A. 2002. Folding and dimerization of tick-borne encephalitis virus envelope proteins prM and E in the endoplasmic reticulum. J Virol 76:5480–91.

101. Kiermayr S, Kofler RM, Mandl CW, Heinz FX, Messner P. 2004. Isolation of Capsid Protein Dimers from the Tick-Borne Encephalitis Flavivirus and In Vitro Assembly of Capsid-Like Particles Isolation of Capsid Protein Dimers from the Tick-Borne Encephalitis Flavivirus and In Vitro Assembly of Capsid-Like Particles. J Virol 78:8078–8084.

102. Yu I-M, Holdaway HA, Chipman PR, Kuhn RJ, Rossmann MG, Chen J. 2009. Association of the pr Peptides with Dengue Virus at Acidic pH Blocks Membrane Fusion. J Virol 83:12101–12107.

103. DICK GWA, KITCHEN SF, HADDOW AJ. 1952. Zika virus. I. Isolations and serological specificity. Trans R Soc Trop Med Hyg 46:509–20.

104. DICK GWA. 1952. Zika virus. II. Pathogenicity and physical properties. Trans R Soc Trop Med Hyg 46:521–34.

105. Smithburn KC. 1952. Neutralizing antibodies against certain recently isolated viruses in the sera of human beings residing in East Africa. J Immunol 69:223–234.

106. DICK GW. 1953. Epidemiological notes on some viruses isolated in Uganda; Yellow fever, Rift Valley fever, Bwamba fever, West Nile, Mengo, Semliki forest, Bunyamwera, Ntaya, Uganda S and Zika viruses. Trans R Soc Trop Med Hyg 47:13–48.

107. SMITHBURN KC, KERR JA, GATNE PB. 1954. Neutralizing antibodies against certain viruses in the sera of residents of India. J Immunol 72:248–57.

108. SMITHBURN KC. 1954. Neutralizing antibodies against arthropod-borne viruses in the sera of long-time residents of Malaya and Borneo. Am J Hyg 59:157–63.

109. HAMMON WM, SCHRACK WD, SATHER GE. 1958. Serological survey for a arthropod-borne virus infections in the Philippines. Am J Trop Med Hyg 7:323–328.

110. Macnamara FN. 1954. Zika virus: a report on three cases of human infection during an epidemic of jaundice in Nigeria. Trans R Soc Trop Med Hyg.

111. Simpson DIH. 1964. Zika Virus Infection in Man. Trans R Soc trop Med Hyg,.

112. Wikan N, Smith DR. 2017. First published report of Zika virus infection in people: Simpson, not MacNamara. Lancet Infect Dis 17:15–17.

113. Boorman JP, Draper CC. 1968. Isolations of arboviruses in the Lagos area of Nigeria, and a survey of antibodies to them in man and animals. Trans R Soc Trop Med Hyg 62:269–77.

114. Bearcroft WG. 1956. Zika virus infection experimentally induced in a human volunteer. Trans R Soc Trop Med Hyg 50:442–8.

115. Zhu Z, Chan JF-W, Tee K-M, Choi GK-Y, Lau SK-P, Woo PC-Y, Tse H, Yuen K-Y. 2016. Comparative genomic analysis of pre-epidemic and epidemic Zika virus strains for virological factors potentially associated with the rapidly expanding epidemic. Emerg Microbes Infect 5:e22.

116. Weinbren M., Williams M. 1958. Zika virus: Further isolations in the zika area, and some studies on the strains isolated. Trans R Soc Trop Med Hyg.

117. HADDOW AJ, WILLIAMS MC, WOODALL JP, SIMPSON DI, GOMA LK. 1964. Twelve Isolations of Zika Virus From Aedes (Stegomyia) Africanus (Theobald) Taken in

and Above a Uganda Forest. Bull World Health Organ 31:57–69.

118. Marchette NJ, Garcia R, Rudnick A. 1969. Isolation of Zika virus from *Aedes aegypti* mosquitoes in Malaysia. Am J Trop Med Hyg 18:411–5.

119. Pond WL. 1963. Arthropod-borne virus antibodies in sera from residents of South-East Asia. Trans R Soc Trop Med Hyg 57:364–371.

120. Filipe a. R, Martins CM V, Rocha H. 1973. Laboratory infection with Zika virus after vaccination against yellow fever. Arch fur die gesamte Virusforschungr 43:315–319.

121. Alera MT, Hermann L, Tac-An IA, Klungthong C, Rutvisuttinunt W, Manasatienkij W, Villa D, Thaisomboonsuk B, Velasco JM, Chinnawirotpisan P, Lago CB, Roque VG, Macareo LR, Srikiatkhachorn A, Fernandez S, Yoon I-K. 2015. Zika virus infection, Philippines, 2012. Emerg Infect Dis 21:722–4.

122. Fagbami AH. 1979. Zika virus infections in Nigeria: virological and seroepidemiological investigations in Oyo State. J Hyg (Lond) 83:213–219.

123. Adekolu-John EO, Fagbami AH. 1983. Arthropod-borne virus antibodies in sera of residents of Kainji Lake Basin, Nigeria 1980. Trans R Soc Trop Med Hyg.

124. Olson JG, Ksiazek TG. 1981. Zika virus, a cause of fever in Central Java, Indonesia. Trans R Soc Trop Med Hyg.

125. Olson J, Ksiazek T, Gubler D, Lubis S, Simanjuntak G, Lee V, Nalim S, Juslis K, See R. 1983. A survey for arboviral antibodies in sera of humans and animals in Lombok, Republic of Indonesia. Ann Trop Med Parasitol.

126. Rodhain F, Gonzalez JP, Mercier E, Helynck B, Larouze B, Hannoun C. 1989. Arbovirus infections and viral haemorrhagic fevers in Uganda: A serological survey in Karamoja district, 1984. Trans R Soc Trop Med Hyg.

127. Darwish MA, Hoogstraal H, Roberts TJ, Ahmed IP, Omar F. 1983. A sero-

epidemiological survey for certain arboviruses (Togaviridae) in Pakistan. Trans R Soc Trop Med Hyg.

128. Moore DL. 1975. Arthropod-borne viral infections of man in Nigeria, 1964-1970. Ann Trop Med Parasitol 69:49–64.

129. Duffy MR, Chen T-H, Hancock WT, Powers AM, Kool JL, Lanciotti RS, Pretrick M, Marfel M, Holzbauer S, Dubray C, Guillaumot L, Griggs A, Bel M, Lambert AJ, Laven J, Kosoy O, Panella A, Biggerstaff BJ, Fischer M, Hayes EB. 2009. Zika virus outbreak on Yap Island, Federated States of Micronesia. N Engl J Med 360:2536–2543.

130. Heang V, Yasuda CY, Sovann L, Haddow AD, da Rosa APT, Tesh RB, Kasper MR. 2012. Zika virus infection, Cambodia, 2010. Emerg Infect Dis 18:349–351.

131. Grard G, Caron M, Mombo IM, Nkoghe D, Mboui Ondo S, Jiolle D, Fontenille D, Paupy C, Leroy EM. 2014. Zika Virus in Gabon (Central Africa) - 2007: A New Threat from Aedes albopictus? PLoS Negl Trop Dis 8:1–6.

132. Kwong JC, Druce JD, Leder K. 2013. Zika virus infection acquired during brief travel to Indonesia. Am J Trop Med Hyg 89:516–517.

133. Foy BD, Kobylinski KC, Foy JLC, Blitvich BJ, da Rosa AT, Haddow AD, Lanciotti RS, Tesh RB. 2011. Probable Non-Vector-borne Transmission of Zika Virus, Colorado, USA. Emerg Infect Dis 17:880–882.

134. Cao-Lormeau VM, Roche C, Teissier A, Robin E, Berry AL, Mallet HP, Sall AA, Musso D. 2014. Zika virus, French Polynesia, South Pacific, 2013. Emerg Infect Dis 20:1085–1086.

135. Cauchemez S, Besnard M, Bompard P, Dub T, Guillemette-Artur P, Eyrolle-Guignot D, Salje H, Van Kerkhove MD, Abadie V, Garel C, Fontanet A, Mallet H-P. 2016. Association between Zika virus and microcephaly in French Polynesia, 2013-15: a

retrospective study. Lancet (London, England) 6736:1–8.

136. Oehler E, Watrin L, Larre P, Leparc-Goffart I, Lastere S, Valour F, Baudouin L, Mallet H, Musso D, Ghawche F. 2014. Zika virus infection complicated by Guillain-Barre syndrome--case report, French Polynesia, December 2013. Euro Surveill 19:7–9.

137. Israeli E, Agmon-Levin N, Blank M, Chapman J, Shoenfeld Y. 2012. Guillain-Barre syndrome-a classical autoimmune disease triggered by infection or vaccination. Clin Rev Allergy Immunol 42:121–130.

138. Butler D. 2016. Zika virus: Brazil's surge in small-headed babies questioned by report. Nature 530:13–4.

139. Musso D, Gubler DJ. 2016. Zika Virus. Clin Microbiol Rev 29:487–524.

140. World Health Organization. 2014. Pacific syndromic surveillance report. Western Pacific Region.

141. Promed-mail. 2014. Zika virus—Pacific (07): Chile (Easter Island), French Polynesia. ProMED-mail archive no. 20140309.2322907.

142. Promed-mail. 2015. Zika virus—Pacific Vanuatu. ProMED-mail archive no. 20150501.3334549.

143. ECDC. 2015. Zika virus infection outbreak, Brazil and the Pacific region. 25 May 2015. Rapid Risk Assess http://ecdc.europa.eu/en/publications/Publications.

144. ECDC EC for DP and C. 2015. Rapid risk assessment: Zika virus epidemic in the Americas: potential association with microcephaly and Guillain-Barré syndrome, 10 December 2015. Ecdc 1–14.

145. Campos GS, Bandeira AC, Sardi SI. 2015. Zika Virus Outbreak, Bahia, Brazil. Emerg Infect Dis 21:doi: 10.3201/eid2110.150847.

146. Zanluca C, Melo VCA de, Mosimann ALP, Santos GIV dos, Santos CND dos, Luz K.

2015. First report of autochthonous transmission of Zika virus in Brazil. Mem Inst Oswaldo Cruz 110:569–572.

147. Musso D. 2015. Zika Virus Transmission from French Polynesia to Brazil. Emerg Infect Dis 21:1887.

148. Hygino XLC, Jr C, Nascimento XOJM, Lopes XFPPL, Silva XIRF. 2018. Neuroimaging Findings of Zika Virus – Associated Neurologic Complications in Adults.

149. Kleber de Oliveira W, Cortez-Escalante J, De Oliveira WTGH, do Carmo GMI, Henriques CMP, Coelho GE, Araújo de França GV. 2016. Increase in Reported Prevalence of Microcephaly in Infants Born to Women Living in Areas with Confirmed Zika Virus Transmission During the First Trimester of Pregnancy — Brazil, 2015. MMWR Morb Mortal Wkly Rep 65:242–247.

150. Pan American Health Organization, World Health Organization. 2015. Neurological syndrome, congenital malformations, and Zika virus infection. Implications for public health in the Americas.

151. McCarthy M. 2016. WHO sets out 56m Zika virus response plan. Bmj 352:i1042.

152. Camacho E, Paternina-Gomez M, Blanco PJ, Osorio PE, Aliota MT. 2016. Detection of Autochthonous Zika Virus Transmission in Sincelejo, Colombia. Emerg Infect Dis 22:DOI: 10.3201/eid2205.160023.

153. Arzusa-Ortega L, Polo A, Pérez-Tatis G, López-García H, Parra E, Pardo-Herrera LC, Rico-Turca AM, Villamil-Gómez W, Rodríguez-Morales AJ. 2016. Fatal Zika Virus Infection in Girl with Sickle Cell Disease, Colombia. Emerg Infect Dis J 22:2014–2016.

154. Thomas DL, Sharp TM, Torres J, Armstrong PA, Munoz-Jordan J, Ryff KR, Martinez-Quiñones A, Arias-Berríos J, Mayshack M, Garayalde GJ, Saavedra S, Luciano CA, Valencia-Prado M, Waterman S, Rivera-García B. 2016. Local Transmission of Zika

Virus - Puerto Rico, November 23, 2015-January 28, 2016. MMWR Morb Mortal Wkly Rep 65:154–158.

155. Korhonen EM, Huhtamo E, Smura T, Kallio-Kokko H, Raassina M, Vapalahti O. 2016. Zika virus infection in a traveller returning from the Maldives, June 2015. Euro Surveill Bull Eur sur les Mal Transm = Eur Commun Dis Bull 21:5–8.

156. Perkasa A, Yudhaputri F, Haryanto S, Hayati RF, Ma'roef CN, Antonjaya U, Yohan B, Myint KSA, Ledermann JP, Rosenberg R, Powers AM, Sasmono RT. 2016. Isolation of Zika Virus from Febrile Patient, Indonesia. Emerg Infect Dis 22.

157. GeurtsvanKessel CH, Islam Z, Islam MB, Kamga S, Papri N, van de Vijver DAMC, Reusken C, Mogling R, Heikema AP, Jahan I, Pradel FK, Pavlicek RL, Mohammad QD, Koopmans MPG, Jacobs BC, Endtz HP. 2018. Zika virus and Guillain–Barré syndrome in Bangladesh. Ann Clin Transl Neurol 5:606–615.

158. Umapathi T, Kam Y-W, Ohnmar O, Ng BCJ, Ng Y, Premikha M, Leo Y-S, Ng LFP. 2018. The 2016 Singapore ZIKV outbreak did not cause a surge in Guillain-Barré syndrome. J Peripher Nerv Syst 197–201.

159. Sassetti M, Zé-Zé L, Franco J, Cunha J da, Gomes A, Tomé A, Alves M-J. 2018. First case of confirmed congenital Zika syndrome in continental Africa. Trans R Soc Trop Med Hyg 1–5.

160. World Health Organization. 2016. Fifth meeting of the emergency committee under the international health regulations (2005) regarding microcephaly , other neurological disorders and Zika virus. World Heal Organ http://www.who.int/mediacentre/news/statements/201.

161. Sharp TM, Muñoz-Jordán J, Perez-Padilla J, Bello-Pagán MI, Rivera A, Pastula DM, Salinas JL, Martínez Mendez JH, Méndez M, Powers AM, Waterman S, Rivera-García B.

2016. Zika Virus Infection Associated with Severe Thrombocytopenia. Clin Infect Dis ciw476.

162. Anaya JM, Rodríguez Y, Monsalve DM, Vega D, Ojeda E, González-Bravo D, Rodríguez-Jiménez M, Pinto-Díaz CA, Chaparro P, Gunturiz ML, Ansari AA, Gershwin ME, Molano-González N, Ramírez-Santana C, Acosta-Ampudia Y. 2017. A comprehensive analysis and immunobiology of autoimmune neurological syndromes during the Zika virus outbreak in Cúcuta, Colombia. J Autoimmun 77:123–138.

163. del Carpio-Orantes L, Peniche Moguel KG, Sánchez Díaz JS, Pola-Ramirez M del R, Mata Miranda M del P, García-Méndez S, Perfecto-Arroyo MA, Solís-Sánchez I, Trujillo-Ortega BM, González-Flores EE. 2018. Síndrome de Guillain-Barré asociado a zika; análisis de la cohorte delegacional en la región Veracruz norte durante 2016-2017. Neurología xx:2017–2019.

164. Brasil P, Sequeira PC, Freitas AD, Zogbi HE, Calvet GA, de Souza RV, Siqueira AM, de Mendonca MCL, Nogueira RMR, de Filippis AMB, Solomon T. 2016. Guillain-Barré syndrome associated with Zika virus infection. Lancet IN PRESS:1482.

165. Mancera-Páez O, Román GC, Pardo-Turriago R, Rodríguez Y, Anaya JM. 2018. Concurrent Guillain-Barré syndrome, transverse myelitis and encephalitis post-Zika: A case report and review of the pathogenic role of multiple arboviral immunity. J Neurol Sci 395:47–53.

166. Neri VC, Xavier MF, Barros PO, Bento CM, Marignier R, Alvarenga RP. 2018. Case Report: Acute Transverse Myelitis after Zika Virus Infection. Am J Trop Med Hyg 00:tpmd170938.

167. Mécharles S, Herrmann C, Poullain P, Tran T, Deschamps N, Mathon G, Landais A, Breurec S. 2016. Case Report Acute myelitis due to Zika virus infection. Lancet 8:6736.

168. Carteaux G, Maquart M, Bedet A, Contou D, Brugières P, Fourati S, Cleret de Langavant L, de Broucker T, Brun-Buisson C, Leparc-Goffart I, Mekontso Dessap A. 2016. Zika Virus Associated with Meningoencephalitis. N Engl J Med 1386–1388.

169. Soares CN, Brasil P, Medialdea R, Msc C, Sequeira P, Bispo De Filippis A, Borges VA, Theophilo F, Ellul MA, Tom M, Frcp S. 2016. Fatal encephalitis associated with Zika Virus infection in an adult. J Clin Virol 83:63–65.

170. Vieira MA da C e. S, Castro AA de S, Henriques DF, da Silva EVP, Tavares FN, Martins LC, Guimarães LM, Monteiro TAF, Azevedo R do S da S, Cruz ACR, Vasconcelos PF da C. 2018. Encephalitis associated with Zika virus infection and reactivation of the varicella-zoster virus in a Brazilian child. Rev Soc Bras Med Trop 51:390–392.

171. Zaidi MB, De Moraes CG, Petitto M, Yepez JB, Sakuntabhai A, Simon-Loriere E, Prot M, Ruffie C, Kim SS, Allikmets R, Terwilliger JD, Lee JH, Maestre GE. 2018. Non-congenital severe ocular complications of Zika virus infection. JMM Case Reports 5:4–6.

172. de Azevedo MB, Coutinho MSC, da Silva MA, Arduini DB, Lima JDV, Monteiro R, Mendes BNB, Lemos MCF, Noronha CP, Saraceni V. 2018. Neurologic manifestations in emerging arboviral diseases in Rio de Janeiro city, Brazil, 2015-2016. Rev Soc Bras Med Trop 51:347–351.

173. Acosta-Ampudia Y, Monsalve DM, Castillo-Medina LF, Rodríguez Y, Pacheco Y, Halstead S, Willison HJ, Anaya J-M, Ramírez-Santana C. 2018. Autoimmune Neurological Conditions Associated With Zika Virus Infection. Front Mol Neurosci 11.

174. Anaya J-M, Ramirez-Santana C, Salgado-Castaneda I, Chang C, Ansari A, Gershwin ME. 2016. Zika virus and neurologic autoimmunity: the putative role of gangliosides. BMC Med 14:49.

175. Willison HJ, Jacobs BC, van Doorn PA. 2016. Guillain-Barré syndrome. Lancet 388:717–

727.

176. Dirlikov E, Major CG, Medina NA, Lugo-Robles R, Matos D, Muñoz-Jordan JL, Colon-Sanchez C, Garcia M, Olivero-Segarra M, Malave G, Rodríguez-Vega GM, Thomas DL, Waterman SH, Sejvar JJ, Luciano CA, Sharp TM, Rivera-García B. 2018. Clinical Features of Guillain-Barré Syndrome With vs Without Zika Virus Infection, Puerto Rico, 2016. JAMA Neurol 30345:1–10.

177. López-Vèrges S, Pachar MR, Araúz D, Suárez JA, Moreno B, Gundacker ND, Araúz AB, Suárez M. 2018. Zika Virus–Associated Cerebellitis with Complete Clinical Recovery. Am J Trop Med Hyg 00:1–3.

178. Sips GJ, Wilschut J, Smit JM. 2012. Neuroinvasive flavivirus infections. Rev Med Virol 22:69–87.

179. Liou ML, Hsu CY. 1998. Japanese encephalitis virus is transported across the cerebral blood vessels by endocytosis in mouse brain. Cell Tissue Res 293:389–394.

180. Samuel MA, Wang H, Siddharthan V, Morrey JD, Diamond MS. 2007. Axonal transport mediates West Nile virus entry into the central nervous system and induces acute flaccid paralysis. Proc Natl Acad Sci 104:17140–17145.

181. Das S, Laxminarayana SV, Chandra N, Ravi V, Desai A. 2009. Heat shock protein 70 on Neuro2a cells is a putative receptor for Japanese encephalitis virus. Virology 385:47–57.

182. Chu JJH, Ng ML. 2003. Characterization of a 105-kDa plasma membrane associated glycoprotein that is involved in West Nile virus binding and infection. Virology 312:458–469.

183. Tang H, Hammack C, Ogden SC, Jin P. 2016. Zika Virus Infects Human Cortical Neural Progenitors and Attenuates Their Growth Brief Report Zika Virus Infects Human Cortical Neural Progenitors and Attenuates Their Growth. Stem Cell 1–4.

184. Dang J, Tiwari SK, Lichinchi G, Qin Y, Patil VS, Eroshkin AM, Rana TM. 2016. Zika Virus Depletes Neural Progenitors in Human Cerebral Organoids through Activation of the Innate Immune Receptor TLR3. Cell Stem Cell 1–8.

185. Li H, Saucedo-Cuevas L, Regla-Nava JA, Chai G, Sheets N, Tang W, Terskikh A V., Shresta S, Gleeson JG. 2016. Zika Virus Infects Neural Progenitors in the Adult Mouse Brain and Alters Proliferation. Cell Stem Cell 19:593–598.

186. Garcez PP, Loiola EC, Madeiro da Costa R, Higa LM, Trindade P, Delvecchio R, Nascimento JM, Brindeiro R, Tanuri A, Rehen SK. 2016. Zika virus impairs growth in human neurospheres and brain organoids. Science (80- ) 352:816–818.

187. Cugola FR, Fernandes IR, Russo FB, Freitas BC, Dias JLM, Guimarães KP, Benazzato C, Almeida N, Pignatari GC, Romero S, Polonio CM, Cunha I, Freitas CL, Brandão WN, Rossato C, Andrade DG, Faria D de P, Garcez AT, Buchpigel CA, Braconi CT, Mendes E, Sall AA, Zanotto PM de A, Peron JPS, Muotri AR, Beltrão-Braga PCB. 2016. The Brazilian Zika virus strain causes birth defects in experimental models. Nature 534:1–15.

188. Paul AM, Acharya D, Neupane B, Thompson EA, Gonzalez-Fernandez G, Copeland KM, Garrett M, Liu H, Lopez ME, de Cruz M, Flynt A, Liao J, Guo Y-L, Gonzalez-Fernandez F, Vig PJS, Bai F. 2018. Congenital Zika Virus Infection in Immunocompetent Mice Causes Postnatal Growth Impediment and Neurobehavioral Deficits. Front Microbiol 9:1–12.

189. Sánchez-San Martín C, Li T, Bouquet J, Streithorst J, Yu G, Paranjpe A, Chiu CY. 2018. Differentiation enhances Zika virus infection of neuronal brain cells. Sci Rep 8:14543.

190. Osuna CE, Lim SY, Deleage C, Griffin BD, Stein D, Schroeder LT, Omange R, Best K, Luo M, Hraber PT, Andersen-Elyard H, Ojeda EFC, Huang S, Vanlandingham DL, Higgs S, Perelson AS, Estes JD, Safronetz D, Lewis MG, Whitney JB. 2016. Zika viral

dynamics and shedding in rhesus and cynomolgus macaques. Nat Med 22:1448–1455.

191. Pardigon N. 2017. Pathophysiological mechanisms of Flavivirus infection of the central nervous system. Transfus Clin Biol 24:96–100.

192. Brito CAA, Henriques-Souza A, Soares CRP, Castanha PMS, Machado LC, Pereira MR, Sobral MCM, Lucena-Araujo AR, Wallau GL, Franca RFO. 2018. Persistent detection of Zika virus RNA from an infant with severe microcephaly - a case report. BMC Infect Dis 18:1–9.

193. Wongsurawat T, Athipanyasilp N, Jenjaroenpun P, Jun S-R, Kaewnapan B, Wassenaar TM, Leelahakorn N, Angkasekwinai N, Kantakamalakul W, Ussery DW, Sutthent R, Nookaew I, Horthongkham N. 2018. Case of Microcephaly after Congenital Infection with Asian Lineage Zika Virus, Thailand. Emerg Infect Dis 24:2–5.

194. Mlakar J, Korva M, Tul N, Popović M, Poljšak-Prijatelj M, Mraz J, Kolenc M, Resman Rus K, Vesnaver Vipotnik T, Fabjan Vodušek V, Vizjak A, Pižem J, Petrovec M, Avšič Županc T. 2016. Zika Virus Associated with Microcephaly. N Engl J Med 160210140106006.

195. Peloggia A, Ali M, Nanda K, Bahamondes L. 2018. Zika virus exposure in pregnancy and its association with newborn visual anomalies and hearing loss. Int J Gynecol Obstet 1–5.

196. Ventura LO, Ventura C V, Lawrence L, van der Linden V, van der Linden A, Gois AL, Cavalcanti MM, Barros EA, Dias NC, Berrocal AM, Miller MT. 2017. Visual impairment in children with congenital Zika syndrome. J Am Assoc Pediatr Ophthalmol Strabismus.

197. Ventura C V, Maia M, Ventura B V, Linden V Van Der, Araújo EB, Ramos RC, Rocha MAW, Carvalho MDCG, Belfort R, Ventura LO. 2016. Ophthalmological findings in infants with microcephaly and presumable intra-uterus Zika virus infection. Arq Bras Oftalmol 79:1–3.

198. de Paula Freitas B, de Oliveira Dias JR, Prazeres J, Sacramento GA, Ko AI, Maia M, Belfort R. 2016. Ocular Findings in Infants With Microcephaly Associated With Presumed Zika Virus Congenital Infection in Salvador, Brazil. JAMA Ophthalmol 1–19.

199. Silva AF da. 2018. Differential diagnosis of pathological intracranial calcifications in patients with microcephaly related to congenital Zika virus infection. Radiol Bras 51:270–271.

200. Yasri S, Wiwanitkit V. 2018. Femur-Sparing Pattern of Fetal Growth After Maternal Zika Virus Infection. Am J Obstet Gynecol 2018.

201. Walker CL, Merriam AA, Ohuma EO, Dighe MK, Gale M, Rajagopal L, Papageorghiou AT, Gyamfi-Bannerman C, Adams Waldorf KM. 2018. Femur-sparing pattern of abnormal fetal growth in pregnant women from New York City after maternal Zika virus infection. Am J Obstet Gynecol 219:187.e1-187.e20.

202. O'Driscoll M, Jeggo PA. 2008. The role of the DNA damage response pathways in brain development and microcephaly: Insight from human disorders. DNA Repair (Amst) 7:1039–1050.

203. Devhare P, Meyer K, Steele R, Ray RB, Ray R. 2017. Zika virus infection dysregulates human neural stem cell growth and inhibits differentiation into neuroprogenitor cells. Cell Death Dis 8:1–8.

204. Liang Q, Luo Z, Zeng J, Chen W, Foo S-S, Lee S-A, Ge J, Wang S, Goldman SA, Zlokovic B V, Zhao Z, Jung JU. 2016. Zika Virus NS4A and NS4B Proteins Deregulate Akt-mTOR Signaling in Human Fetal Neural Stem Cells to Inhibit Neurogenesis and Induce Autophagy. Cell Stem Cell 19:663–671.

205. Peng H, Liu B, Yves TD, He Y, Wang S, Tang H, Ren H, Zhao P, Qi Z, Qin Z. 2018. Zika virus induces autophagy in human umbilical vein endothelial cells. Viruses 10.

206. Li C, Xu D, Ye Q, Hong S, Jiang Y, Liu X, Zhang N, Shi L, Qin C-F, Xu Z. 2016. Zika Virus Disrupts Neural Progenitor Development and Leads to Microcephaly in Mice. Cell Stem Cell 1–7.

207. Li C, Wang Q, Jiang Y, Ye Q, Xu D, Gao F, Xu JW, Wang R, Zhu X, Shi L, Yu L, Zhang F, Guo W, Zhang L, Qin CF, Xu Z. 2018. Disruption of glial cell development by Zika virus contributes to severe microcephalic newborn mice. Cell Discov 4:1–12.

208. Martinot AJ, Abbink P, Afacan O, Prohl AK, Bronson R, Hecht JL, Borducchi EN, Larocca RA, Peterson RL, Rinaldi W, Ferguson M, Didier PJ, Weiss D, Lewis MG, De La Barrera RA, Yang E, Warfield SK, Barouch DH. 2018. Fetal Neuropathology in Zika Virus-Infected Pregnant Female Rhesus Monkeys. Cell 173:1111–1122.e10.

209. Coffey LL, Keesler RI, Pesavento PA, Woolard K, Singapuri A, Watanabe J, Cruzen C, Christe KL, Usachenko J, Yee J, Heng VA, Bliss-Moreau E, Reader JR, Von Morgenland W, Gibbons AM, Jackson K, Ardeshir A, Heimsath H, Permar S, Senthamaraikannan P, Presicce P, Kallapur SG, Linnen JM, Gao K, Orr R, MacGill T, McClure M, McFarland R, Morrison JH, Van Rompay KKA. 2018. Intraamniotic Zika virus inoculation of pregnant rhesus macaques produces fetal neurologic disease. Nat Commun 9:1–12.

210. Seferovic M, Martín CSS, Tardif SD, Rutherford J, Castro ECC, Li T, Hodara VL, Parodi LM, Giavedoni L, Layne-Colon D, Tamhankar M, Yagi S, Martyn C, Reyes K, Suter MA, Aagaard KM, Chiu CY, Patterson JL. 2018. Experimental Zika Virus Infection in the Pregnant Common Marmoset Induces Spontaneous Fetal Loss and Neurodevelopmental Abnormalities. Sci Rep 8:1–15.

211. Adams Waldorf KM, Stencel-Baerenwald JE, Kapur RP, Studholme C, Boldenow E, Vornhagen J, Baldessari A, Dighe MK, Thiel J, Merillat S, Armistead B, Tisoncik-Go J, Green RR, Davis MA, Dewey EC, Fairgrieve MR, Gatenby JC, Richards T, Garden GA,

Diamond MS, Juul SE, Grant RF, Kuller L, Shaw DWW, Ogle J, Gough GM, Lee W, English C, Hevner RF, Dobyns WB, Gale M, Rajagopal L. 2016. Fetal brain lesions after subcutaneous inoculation of Zika virus in a pregnant nonhuman primate. Nat Med 1–6.

212. Campos MC, Dombrowski JG, Phelan J, Marinho CRF, Hibberd M, Clark TG, Campino S. 2018. Zika might not be acting alone: Using an ecological study approach to investigate potential co-acting risk factors for an unusual pattern of microcephaly in Brazil. PLoS One 13:e0201452.

213. Hoffman DC, Duran-Reynals F. 1930. The Mechanism of Enhancement of Infections by Testicle Extract. Science 72:508.

214. Hawkes RA. 1964. Enhancement of the Infectivity of Arboviruses by Specific Antisera Produced in Domestic Fowls. Aust J Exp Biol Med Sci 42:464-482.

215. Hawkes R., Lafferty K. 1967. The enhancement of virus infectivity by antibody. Virology 33:250–261.

216. Russell PK, Udomsakdi S, Halstead SB. 1967. Antibody response in dengue and dengue hemorrhagic fever. Jpn J Med Sci Biol 20 Suppl:103–8.

217. Halstead SB. 1979. In vivo enhancement of dengue virus infection in rhesus monkeys by passively transferred antibody. J Infect Dis 140:527–33.

218. Halstead SB, O'Rourke EJ. 1977. Dengue viruses and mononuclear phagocytes. I. Infection enhancement by non-neutralizing antibody. J Exp Med 146:201–17.

219. Halstead SB, O'Rourke EJ, Allison AC. 1977. Dengue viruses and mononuclear phagocytes. II. Identity of blood and tissue leukocytes supporting in vitro infection. J Exp Med 146:218–29.

220. Peiris JS, Porterfield JS. 1979. Antibody-mediated enhancement of Flavivirus replication in macrophage-like cell lines. Nature 282:509-511.

221. Halstead SB, Porterfield JS, O'Rourke EJ. 1980. Enhancement of dengue virus infection in monocytes by flavivirus antisera. Am J Trop Med Hyg 29:638–642.

222. Brandt WE, McCown JM, Gentry MK, Russell PK. 1982. Infection enhancement of dengue type 2 virus in the U-937 human monocyte cell line by antibodies to flavivirus cross-reactive determinants. Infect Immun 36:1036–1041.

223. Halstead SB, Venkateshan CN, Gentry MK, Larsen LK. 1984. Heterogeneity of infection enhancement of dengue 2 strains by monoclonal antibodies. J Immunol 132:1529–32.

224. Morens DM, Halstead SB, Marchette NJ. 1987. Profiles of antibody-dependent enhancement of dengue virus type 2 infection. Microb Pathog 3:231–7.

225. Halstead SB. 1970. Observations related to pathogenesis of dengue hemorrhagic fever: Hypotheses and discussion. Yale J Biol Med 42:350–362.

226. World Health Organization. 1973. Pathogenetic mechanisms in dengue haemorrhagic fever: report of an international collaborative study. Bull World Heal Organ 48:117–133.

227. Lei H-Y, Yeh T-M, Liu H-S, Lin Y-S, Chen S-H, Liu C-C. 2001. Immunopathogenesis of dengue virus infection. J Biomed Sci 8:377–388.

228. Fazekas de St Groth, Webster RG. 1966. Disquisitions of Original Antigenic Sin. I. Evidence in man. J Exp Med 124:331–45.

229. Stephenson JR. 2005. Understanding dengue pathogenesis: Implications for vaccine design. Bull World Health Organ 83:308–314.

230. Kontny U, Kurane I, Ennis FA. 1988. Gamma interferon augments Fc gamma receptor-mediated dengue virus infection of human monocytic cells. J Virol 62:3928–3933.

231. Littaua R, Kurane I, Ennis FA. 1990. Human IgG Fc receptor II mediates antibody-dependent enhancement of dengue virus infection. J Immunol 144:3183–6.

232. Moi ML, Lim CK, Chua KB, Takasaki T, Kurane I. 2012. Dengue virus infection-

enhancing activity in serum samples with neutralizing activity as determined by using FcγR-expressing cells. PLoS Negl Trop Dis 6.

233. Sun P, Bauza K, Pal S, Liang Z, Wu S jue, Beckett C, Burgess T, Porter K. 2011. Infection and activation of human peripheral blood monocytes by dengue viruses through the mechanism of antibody-dependent enhancement. Virology 421:245–252.

234. Van Der Schaar HM, Rust MJ, Chen, Van Der Ende-Metselaar H, Wilschut J, Zhuang X, Smit JM. 2008. Dissecting the cell entry pathway of dengue virus by single-particle tracking in living cells. PLoS Pathog 4:e1000244.

235. Krishnan MN, Sukumaran B, Pal U, Agaisse H, Murray JL, Hodge TW, Fikrig E. 2007. Rab 5 is required for the cellular entry of dengue and West Nile viruses. J Virol 81:4881–5.

236. Flipse J, Wilschut J, Smit JM. 2013. Molecular mechanisms involved in antibody-dependent enhancement of dengue virus infection in humans. Traffic 14:25–35.

237. Costa V V., Fagundes CT, Valadão DF, Ávila T V., Cisalpino D, Rocha RF, Ribeiro LS, Ascenção FR, Kangussu LM, Junior CMQ, Astigarraga RG, Gouveia FL, Silva TA, Bonaventura D, De Almeida Sampaio D, Leite ACL, Teixeira MM, Souza DG. 2014. Subversion of early innate antiviral responses during antibody-dependent enhancement of Dengue virus infection induces severe disease in immunocompetent mice. Med Microbiol Immunol 203:231–250.

238. Halstead SB. 2015. Pathogenesis of Dengue: Dawn of a New Era. F1000Research 28:1385–7.

239. Smit JM, Moesker B, Rodenhuis-Zybert I, Wilschut J. 2011. Flavivirus cell entry and membrane fusion. Viruses 3:160–171.

240. Zaitseva E, Yang ST, Melikov K, Pourmal S, Chernomordik L V. 2010. Dengue virus

ensures its fusion in late endosomes using compartment-specific lipids. PLoS Pathog 6:e1001131.

241. Huang X, Yue Y, Li D, Zhao Y, Qiu L, Chen J, Pan Y, Xi J, Wang X, Sun Q, Li Q. 2016. Antibody-dependent enhancement of dengue virus infection inhibits RLR-mediated Type-I IFN-independent signalling through upregulation of cellular autophagy. Sci Rep 6:22303.

242. Halstead SB, Mahalingam S, Marovich MA, Ubol S, Mosser DM. 2010. Intrinsic antibody-dependent enhancement of microbial infection in macrophages: disease regulation by immune complexes. Lancet Infect Dis 10:712–722.

243. Green S, Vaughn DW, Kalayanarooj S, Nimmannitya S, Suntayakorn S, Nisalak A, Rothman AL, Ennis FA. 1999. Elevated plasma interleukin-10 levels in acute dengue correlate with disease severity. J Med Virol 59:329–34.

244. Bethell DB, Flobbe K, Cao XT, Day NP, Pham TP, Buurman WA, Cardosa MJ, White NJ, Kwiatkowski D. 1998. Pathophysiologic and prognostic role of cytokines in dengue hemorrhagic fever. J Infect Dis 177:778–82.

245. Ubol S, Phuklia W, Kalayanarooj S, Modhiran N. 2010. Mechanisms of immune evasion induced by a complex of dengue virus and preexisting enhancing antibodies. J Infect Dis 201:923–935.

246. Chareonsirisuthigul T, Kalayanarooj S, Ubol S. 2007. Dengue virus (DENV) antibody-dependent enhancement of infection upregulates the production of anti-inflammatory cytokines, but suppresses anti-DENV free radical and pro-inflammatory cytokine production, in THP-1 cells. J Gen Virol 88:365–375.

247. Pal T, Dutta SK, Mandal S, Saha B, Tripathi A. 2014. Differential clinical symptoms among acute phase Indian patients revealed significant association with dengue viral load

and serum IFN-gamma level. J Clin Virol 61:365–370.

248. Mangada MM, Rothman AL. 2005. Altered cytokine responses of dengue-specific CD4+ T cells to heterologous serotypes. J Immunol 175:2676–83.

249. K G, S H, K O, T K, K A, K M, K K, H Y. 2012. Dengue Hemorrhagic Fever in an adult traveler returning to Japan. Intern Med 51:1779–1782.

250. Soni H, Gandhi V, Varma S, Kaur D, Epelbaum O. 2015. A 47-year-old returning traveler with shock. Chest 147:e8–e12.

251. Woon YL, Hor CP, Hussin N, Zakaria A, Goh PP, Cheah WK. 2016. A Two-Year Review on Epidemiology and Clinical Characteristics of Dengue Deaths in Malaysia, 2013-2014. PLoS Negl Trop Dis 10:e0004575.

252. De Madrid AT, Porterfield JS. 1974. The flaviviruses (group B arboviruses): a cross-neutralization study. J Gen Virol 23:91–6.

253. Fagbami A, Halstead SB, Marchette N, Larsen K. 1988. Heterologous flavivirus infection-enhancing antibodies in sera of Nigerians. Am J Trop Med Hyg 38:205–207.

254. Dejnirattisai W, Supasa P, Wongwiwat W, Rouvinski A, Barba-Spaeth G, Duangchinda T, Sakuntabhai A, Cao-Lormeau VM, Malasit P, Rey FA, Mongkolsapaya J, Screaton GR. 2016. Dengue virus sero-cross-reactivity drives antibody-dependent enhancement of infection with zika virus. Nat Immunol 17:1102–1108.

255. Priyamvada L, Quicke KM, Hudson WH, Onlamoon N, Sewatanon J, Edupuganti S, Pattanapanyasat K, Chokephaibulkit K, Mulligan MJ, Wilson PC, Ahmed R, Suthar MS, Wrammert J. 2016. Human antibody responses after dengue virus infection are highly cross-reactive to Zika virus. Proc Natl Acad Sci U S A 113:7852-7857.

256. Barba-Spaeth G, Dejnirattisai W, Rouvinski A, Vaney M-C, Medits I, Sharma A, Simon-Lorière E, Sakuntabhai A, Cao-Lormeau V-M, Haouz A, England P, Stiasny K,

Mongkolsapaya J, Heinz FX, Screaton GR, Rey FA. 2016. Structural basis of potent Zika–dengue virus antibody cross-neutralization. Nature 1–23.

257. Stettler K, Beltramello M, Espinosa DA, Graham V, Cassotta A, Bianchi S, Vanzetta F, Minola A, Jaconi S, Mele F, Foglierini M, Pedotti M, Simonelli L, Dowall S, Atkinson B, Percivalle E, Simmons CP, Varani L, Blum J, Baldanti F, Cameroni E, Hewson R, Harris E, Lanzavecchia A, Sallusto F, Corti D. 2016. Specificity, cross-reactivity, and function of antibodies elicited by Zika virus infection. Science 353:823–826.

258. Robinson N, Mayorquin Galvan EE, Zavala Trujillo IG, Zavala-Cerna MG. 2018. Congenital Zika syndrome: Pitfalls in the placental barrier. Rev Med Virol 1–7.

259. Nicolini AM, McCracken KE, Yoon J-Y. 2017. Future developments in biosensors for field-ready Zika virus diagnostics. J Biol Eng 11:7.

260. Centers for Disease Control and Prevention. 2017. Diagnostic Tests for Zika Virus Zika virus.

261. Centers for Disease Control and Prevention. 2017. Trioplex Real-Time RT-PCR Assay Instructions for Use.

262. Samy AM, Thomas SM, Wahed AA El, Cohoon KP, Townsend Peterson A. 2016. Mapping the global geographic potential of Zika virus spread. Mem Inst Oswaldo Cruz 111:559–560.

263. Attaway DF, Waters NM, Geraghty EM, Jacobsen KH. 2017. Zika virus: Endemic and epidemic ranges of Aedes mosquito transmission. J Infect Public Health 10:120–123.

264. Gootenberg JS, Abudayyeh OO, Lee JW, Essletzbichler P, Dy AJ, Joung J, Verdine V, Donghia N, Daringer NM, Freije CA, Myhrvold C, Bhattacharyya RP, Livny J, Regev A, Koonin E V, Hung DT, Sabeti PC, Collins JJ, Zhang F. 2017. Nucleic acid detection with CRISPR-Cas13a/C2c2. Science 356:438–442.

265. Myhrvold C, Freije CA, Gootenberg JS, Abudayyeh OO, Metsky HC, Kellner MJ, Barnes KG, Chak B, Yozwiak NL, MacInnis BL, Zhang F, Sabeti PC, Durbin AF, Gehrke L, Bosch I, Tan AL, Paul LM, Isern S, Michael SF, Parham LA, Garcia KF, Lorenzana I, Mondini A, Nogueira ML. 2018. Field-deployable viral diagnostics using CRISPR-Cas13. Science 448:444–448.

266. Castro T, Sabalza M, Barber C, Abrams W, Da Costa AC, De Pádua Milagres FA, Braz-Silva PH, Malamud D, Gallottini M. 2018. Rapid diagnosis of Zika virus through saliva and urine by Loop-mediated isothermal amplification (LAMP). J Oral Microbiol 10:1510712.

267. Guo X-G, Zhou Y-Z, Li Q, Wang W, Wen J-Z, Zheng L, Wang Q. 2018. Rapid and reliable diagnostic method to detect Zika virus by real-time fluorescence reverse transcription loop-mediated isothermal amplification. AMB Express 8:60.

268. Calvert AE, Biggerstaff BJ, Tanner NA, Lauterbach M, Lanciotti RS. 2017. Rapid colorimetric detection of Zika virus from serum and urine specimens by reverse transcription loop-mediated isothermal amplification (RT-LAMP). PLoS One 12:1–16.

269. CDC. 2016. Zika MAC-ELISA For Use Under an Emergency Use.

270. Wesson DM, Lorenzana I, Buekens P, Alger J, Ward MJ, García J, Lopez W, Berrueta M, García K, Cafferata ML, Parham L, Bock H, Ciganda A. 2018. Zika Virus and the World Health Organization Criteria for Determining Recent Infection Using Plaque Reduction Neutralization Testing. Am J Trop Med Hyg 99:doi: 10.4269/ajtmh.18-0237.

271. Safronetz D, Sloan A, Stein DR, Mendoza E, Barairo N, Ranadheera C, Scharikow L, Holloway K, Robinson A, Traykova-Andonova M, Makowski K, Dimitrova K, Giles E, Hiebert J, Mogk R, Beddome S, Drebot M. 2017. Evaluation of 5 Commercially Available Zika Virus Immunoassays. Emerg Infect Dis 23:3–8.

272. Balmaseda A, Zambrana JV, Collado D, Garcia N, Saborío S, Elizondo D, Mercado JC, Gonzalez K, Cerpas C, Nuñez A, Corti D, Waggoner JJ, Kuan G, Burger-Calderon R, Harris E. 2018. Comparison of four serological methods and two RT-PCR assays for diagnosis and surveillance of Zika. J Clin Microbiol 56:JCM.01785-17.

273. Felix AC, Souza NCS, Figueiredo WM, Costa AA, Inenami M, da Silva RM, Levi JE, Pannuti CS, Romano CM. 2017. Cross reactivity of commercial anti-dengue immunoassays in patients with acute Zika virus infection. J Med Virol 10–12.

274. De Ory F, Sánchez-Seco MP, Vázquez A, Montero MD, Sulleiro E, Martínez MJ, Matas L, Merino FJ, Sáez E, Salud BR, Pérez MR, Cilla CG, Dorado JC, Cabrera J, Gil-González MD, Galán JC, Zufiaurre MNG, Goyanes MJ, Campelo C, Alberdi MB, Fernández BC, Carretero RC, Valle MTD, Roblas RF, Bermejo IG, Cía JIG, Betancor AH, Mestanza ICL, Alfaro LR, Fedele G, Pedrero LAA, Ruesca RB, Buendía B, Praetorius AG, Porto MH, Hernández AH, Garcés ML, López AIL, Cordero PM, Pérez RM, Esteban LM, Germán FJR, García MR, Suárez PDC, Hernando CG, López MA, Andrés NA, Zaragozi FJA, Muñoz EB, Martínez XC, Nieto AC, Navalpotro D, Martín AE, Margüello MG, Real SH, Bugui MJL, Alfaro EM, Luque JCS, Maestre MM, Míguezsantiyán A, Rivilla AP, Ruiz MP, Vigas IP, Fernández CR, Arroyo RS, Flórez MRS, Daporta MT, Romero EDV, Rello SR, Escudero MJR, Salva F, Sanz JC, Minguito T, Molero F, De LaFuente JM, Herrera L, Balfagón P, Hernández ML, Murillo MÁ, Perea MC. 2018. Comparative evaluation of indirect immunofluorescence and NS-1-based ELISA to determine zika virus-specific IgM. Viruses 10:1–9.

275. Wong SJ, Furuya A, Zou J, Xie X, Dupuis AP, Kramer LD, Shi PY. 2017. A Multiplex Microsphere Immunoassay for Zika Virus Diagnosis. EBioMedicine 16:136–140.

276. Koishi AC, Suzukawa AA, Zanluca C, Camacho DE, Comach G, Duarte dos Santos CN.

2018. Development and evaluation of a novel high-throughput image-based fluorescent neutralization test for detection of Zika virus infection. PLoS Negl Trop Dis 12:1–15.

277. Cabral-Miranda G, Cardoso AR, Ferreira LCS, Sales MGF, Bachmann MF. 2018. Biosensor-based selective detection of Zika virus specific antibodies in infected individuals. Biosens Bioelectron 113:101–107.

278. Afsahi S, Lerner MB, Goldstein JM, Lee J, Tang X, Bagarozzi DA, Pan D, Locascio L, Walker A, Barron F, Goldsmith BR. 2018. Novel graphene-based biosensor for early detection of Zika virus infection. Biosens Bioelectron 100:85–88.

279. Draz MS, Venkataramani M, Lakshminarayanan H, Saygili E, Moazeni M, Vasan A, Li Y, Sun X, Hua S, Yu XG, Shafiee H. 2018. Nanoparticle-enhanced electrical detection of Zika virus on paper microchips. Nanoscale 10:11841-11849.

280. Filer JE, Henry CS, Geiss BJ. Electrochemical Biosensors and Assays: An Introduction for Biologists. Prep.

281. Thevenot DR, Tóth K, Durst RA, Wilson GS. 1999. Electrochemical Biosensors: Recommended Definitions and Classification. Pure Appl Chem 71:2333–2348.

282. Karunakaran C, Rajkumar R, Bhargava K. 2015. Introduction to Biosensors. Biosens Bioelectron 1–68.

283. 2014. linear range, p. 3558. *In* IUPAC Compendium of Chemical Terminology. IUPAC, Research Triagle Park, NC.

284. 2014. sensitivityin metrology and analytical chemistry, A, p. 5606. *In* IUPAC Compendium of Chemical Terminology. IUPAC, Research Triagle Park, NC.

285. IUPAC. 1992. Limit of Detection in Analysis. IUPAC Compend Chem Terminol 148.

286. 1995. Reproducibility. IUPAC Compend Chem Terminol 1699:5305.

287. Rocchitta G, Spanu A, Babudieri S, Latte G, Madeddu G, Galleri G, Nuvoli S, Bagella P,

Demartis MI, Fiore V, Manetti R, Serra PA. 2016. Enzyme biosensors for biomedical applications: Strategies for safeguarding analytical performances in biological fluids. Sensors (Switzerland) 16.

288. Wen W, Yan X, Zhu C, Du D, Lin Y. 2017. Recent Advances in Electrochemical Immunosensors. Anal Chem 89:138–156.

289. Du Y, Dong S. 2017. Nucleic acid biosensors: Recent advances and perspectives. Anal Chem 89:189–215.

290. Seo H Bin, Gu MB. 2017. Aptamer-based sandwich-type biosensors. J Biol Eng 11:11.

291. Zhou T, Han H, Liu P, Xiong J, Tian F, Li X. 2017. Microbial Fuels Cell-Based Biosensor for Toxicity Detection: A Review. Sensors 17:2230.

292. Hammond JL, Formisano N, Estrela P, Carrara S, Tkac J. 2016. Electrochemical biosensors and nanobiosensors. Essays Biochem 60:69–80.

293. Damborsky P, vitel J, Katrlik J. 2016. Optical biosensors. Essays Biochem 60:91–100.

294. Fogel R, Limson J, Seshia AA. 2016. Acoustic biosensors. Essays Biochem 60:101–110.

295. Bard AJ, Faulkner LR. 2001. Electrochemical methods: fundamentals and applications, 2nd ed. John Wiley & Sons, Inc., New York.

296. Elgrishi N, Rountree KJ, McCarthy BD, Rountree ES, Eisenhart TT, Dempsey JL. 2018. A Practical Beginner's Guide to Cyclic Voltammetry. J Chem Educ 95:197–206.

297. Trasatti S. 1990. The "absolute" electrode potential-the end of the story. Electrochim Acta 35:269–271.

298. Harvey D. Potential. Anal Sci Digit Libr http://www.asdlib.org/onlineArticles/ecourseware/Kelly_Potentiometry/PDF-1-Potential.pdf

299. Harvey D. Reference and Auxiliary Electrodes. Anal Sci Digit

Libr http://www.asdlib.org/onlineArticles/ecourseware/Kelly_Potentiometry/PDF-15-Ref&AuxElec.pdf

300. Trasatti S. 1986. The Absolute Electrode Potential : An Explanatory Note. Pure Appl Chem 58:955–966.

301. Bagotsky VS. 2005. Fundamentals of Electrochemistry. John Wiley & Sons, Inc., Hoboken, NJ, USA.

302. Bond AM, Compton RG, Fiedler DA, Inzelt G, Kahlert H, Komorsky-Lovric S, Lohse H, Lovric M, Marken F, Neudeck A, Retter U, Scholz F, Stojek Z. 2010. Electroanalytical Methods, 2nd ed. Springer Berlin Heidelberg, Berlin, Heidelberg.

303. Zoski CG. 1986. Charging current discrimination in analytical voltammetry. J Chem Educ 63:910.

304. Osteryoung JG, Osteryoung RA. 1985. Square Wave Voltammetry. Anal Chem 57:101A–110A.

305. Harvey D. Working Electrodes. Anal Sci Digit Libr http://www.asdlib.org/onlineArticles/ecourseware/Kelly_Potentiometry/PDF-16-WorkingElec.pdf

306. Heinze J. 1993. Ultramicroelectrodes in Electrochemistry. Angew Chemie Int Ed English 32:1268–1288.

307. Princeton Applied Research. 2015. Basics of Electrochemical Impedance Spectroscopy. Princet Appl Res.

308. Yuan X-Z, Song C, Wang H, Zhang J. 2010. Electrochemical Impedance Spectroscopy in PEM Fuel Cells: Fundamentals and ApplicationsElectrochemical Impedance Spectroscopy in PEM Fuel Cells Fundamentals and Applications.

309. Pänke O, Balkenhohl T, Kafka J, Schäfer D, Lisdat F. 2008. Impedance spectroscopy and

biosensing. Adv Biochem Eng Biotechnol 109:195–237.

310. Gamry Instruments. 2017. Basics of Electrochemical Impedance Spectroscopy.

311. Barbero G, Alexe-Ionescu AL, Lelidis I. 2005. Significance of small voltage in impedance spectroscopy measurements on electrolytic cells. J Appl Phys 98.

312. Daniels JS, Pourmand N. 2007. Label-free impedance biosensors: Opportunities and challenges. Electroanalysis 19:1239–1257.

313. Bahadir EB, Sezgintürk MK. 2016. A review on impedimetric biosensors. Artif Cells, Nanomedicine Biotechnol 44:248–262.

314. Randles JEB. 1947. Kinetics of rapid electrode reactions. Discuss Faraday Soc 1:11.

315. Geddes L a. 1997. Historical evolution of circuit models for the electrode-electrolyte interface. Ann Biomed Eng 25:1–14.

316. Ershler B. 1947. Investigation of electrode reactions by the method of charging-curves and with the aid of alternating currents. Discuss Faraday Soc 1:269–271.

317. Toshev Y, Mandova V, Boshkov N, Stoychev D, Petrov P, Tsvetkova N, Raichevski G, Tsvetanov C, Gabev A, Velev R, Kostadinov K. 2006. Protective coating of zinc and zinc alloys for industrial applications4M 2006 - Second International Conference on Multi-Material Micro Manufacture. Woodhead Publishing Limited.

318. Lee CS, Kyu Kim S, Kim M. 2009. Ion-sensitive field-effect transistor for biological sensing. Sensors 9:7111–7131.

319. Grieshaber D, MacKenzie R, Vörös J, Reimhult E. 2008. Electrochemical biosensors - Sensor principles and architectures. Sensors 8:1400–1458.

320. Schöning MJ, Poghossian A. 2006. Bio FEDs (Field-Effect Devices): State-of-the-art and new directions. Electroanalysis 18:1893–1900.

321. Faccio G. 2018. From protein features to sensing surfaces. Sensors (Switzerland) 18.

322. Sharma S, Byrne H, O'Kennedy RJ. 2016. Antibodies and antibody-derived analytical biosensors. Essays Biochem 60:9–18.

323. Bhakta SA, Evans E, Benavidez TE, Garcia CD. 2015. Protein adsorption onto nanomaterials for the development of biosensors and analytical devices: A review. Anal Chim Acta 872:7–25.

324. Butler JE. 2000. Solid Supports in Enzyme-Linked Immunosorbent Assay and Other Solid-Phase Immunoassays. Methods 22:4–23.

325. Rabe M, Verdes D, Seeger S. 2011. Understanding protein adsorption phenomena at solid surfaces. Adv Colloid Interface Sci 162:87–106.

326. Benavidez TE, Torrente D, Marucho M, Garcia CD. 2015. Adsorption of soft and hard proteins onto OTCEs under the influence of an external electric field. Langmuir 31:2455–2462.

327. Norde W, Lyklema J. 2012. Interfacial behaviour of proteins, with special reference to immunoglobulins. A physicochemical study. Adv Colloid Interface Sci 179–182:5–13.

328. Kiesel I, Paulus M, Nase J, Tiemeyer S, Sternemann C, Rüster K, Wirkert FJ, Mende K, Büning T, Tolan M. 2014. Temperature-driven adsorption and desorption of proteins at solid-liquid interfaces. Langmuir 30:2077–2083.

329. Demanèche S, Chapel JP, Monrozier LJ, Quiquampoix H. 2009. Dissimilar pH-dependent adsorption features of bovine serum albumin and α-chymotrypsin on mica probed by AFM. Colloids Surfaces B Biointerfaces 70:226–231.

330. Norde W. 1986. Adsorption of proteins from solution at the solid-liquid interface. Adv Colloid Interface Sci 25:267–340.

331. Nejadnik MR, Deepak FL, Garcia CD. 2011. Adsorption of Glucose Oxidase to 3-D Scaffolds of Carbon Nanotubes: Analytical Applications. Electroanalysis 23:1462–1469.

332. Hermanson G. 2008. Bioconjugate Techniques, 2nd ed. Elsevier Inc.

333. Latour RA. 2015. The Langmuir isotherm: A commonly applied but misleading approach for the analysis of protein adsorption behavior. J Biomed Mater Res - Part A 103:949–958.

334. Wiseman ME, Frank CW. 2012. Antibody adsorption and orientation on hydrophobic surfaces. Langmuir 28:1765–1774.

335. P. Baghci and S. M. Birnbaum. 1981. Effect of pH on the Adsorption of Immunoglobulin G on Anionic Poly ( vinyltoluene ) Model Latex Particles. J Colloid Interface Sci 83:460–478.

336. Felsovalyi F, Patel T, Mangiagalli P, Kumar SK, Banta S. 2012. Effect of thermal stability on protein adsorption to silica using homologous aldo-keto reductases. Protein Sci 21:1113–1125.

337. Xu H, Lu JR, Williams DE. 2006. Effect of surface packing density of interfacially adsorbed monoclonal antibody on the binding of hormonal antigen human chorionic gonadotrophin. J Phys Chem B 110:1907–1914.

338. Sassolas A, Blum LJ, Leca-Bouvier BD. 2012. Immobilization strategies to develop enzymatic biosensors. Biotechnol Adv 30:489–511.

339. Vareiro MMLM, Liu J, Knoll W, Zak K, Williams D, Jenkins ATA. 2005. Surface plasmon fluorescence measurements of human chorionic gonadotrophin: Role of antibody orientation in obtaining enhanced sensitivity and limit of detection. Anal Chem 77:2426–2431.

340. Xu H, Zhao X, Grant C, Lu JR, Williams DE, Penfold J. 2006. Orientation of a monoclonal antibody adsorbed at the solid/solution interface: A combined study using atomic force microscopy and neutron reflectivity. Langmuir 22:6313–6320.

341. Couston RG, Skoda MW, Uddin S, van der Walle CF. 2012. Adsorption behavior of a human monoclonal antibody at hydrophilic and hydrophobic surfaces. MAbs 5:126–39.

342. Th. Wink, S. J. van Zuilen a. B and WPVB. 1997. Self-assembled Monolayers for Biosensors. Analyst, 122:43R–50R.

343. Gooding JJJ, Hibbert DBB. 1999. The application of alkanethiol self-assembled monolayers to enzyme electrodes. TRAC-Trends Aanal Chem 18:525–533.

344. Cecchetto J, Fernandes FCB, Lopes R, Bueno PR. 2017. The capacitive sensing of NS1 Flavivirus biomarker. Biosens Bioelectron 87:949–956.

345. Soares AC, Soares JC, Shimizu FM, Rodrigues V da C, Awan IT, Melendez ME, Piazzetta MH de O, Gobbi AL, Reis RM, Fregnani JHTG, Carvalho AL, Oliveira Jr. ON. 2018. A simple architecture with self-assembled monolayers to build immunosensors for detecting the pancreatic cancer biomarker CA19-9. Analyst.

346. Yagati AK, Lee MH, Min J. 2018. Electrochemical immunosensor for highly sensitive and quantitative detection of tumor necrosis factor-α in human serum. Bioelectrochemistry 122:93–102.

347. Singh NK, Arya SK, Estrela P, Goswami P. 2018. Capacitive malaria aptasensor using Plasmodium falciparum glutamate dehydrogenase as target antigen in undiluted human serum. Biosens Bioelectron 117:246–252.

348. Amani J, Maleki M, Khoshroo A, Sobhani-Nasab A, Rahimi-Nasrabadi M. 2018. An electrochemical immunosensor based on poly p-phenylenediamine and graphene nanocomposite for detection of neuron-specific enolase via electrochemically amplified detection. Anal Biochem 548:53–59.

349. Fernandes FCB, Santos A, Martins DC, Góes MS, Bueno PR. 2014. Comparing label free electrochemical impedimetric and capacitive biosensing architectures. Biosens

Bioelectron 57:96–102.

350. Teeparuksapun K, Hedström M, Kanatharana P, Thavarungkul P, Mattiasson B. 2012. Capacitive immunosensor for the detection of host cell proteins. J Biotechnol 157:207–213.

351. Labib M, Hedström M, Amin M, Mattiasson B. 2009. A capacitive biosensor for detection of staphylococcal enterotoxin B. Anal Bioanal Chem 393:1539–1544.

352. Demirbakan B, Sezgintürk MK. 2017. A sensitive and disposable indium tin oxide based electrochemical immunosensor for label-free detection of MAGE-1. Talanta 169:163–169.

353. Aydın EB, Aydın M, Sezgintürk MK. 2017. A highly sensitive immunosensor based on ITO thin films covered by a new semi-conductive conjugated polymer for the determination of TNFα in human saliva and serum samples. Biosens Bioelectron 97:169–176.

354. Bahadır EB, Sezgintürk MK. 2016. Label-free, ITO-based immunosensor for the detection of a cancer biomarker: Receptor for Activated C Kinase 1. Analyst 141:5618–5626.

355. Martínez-García G, Sánchez-Tirado E, González-Cortés A, Yáñez-Sedeño P, Pingarrón JM. 2018. Amperometric immunoassay for the obesity biomarker amylin using a screen printed carbon electrode functionalized with an electropolymerized carboxylated polypyrrole. Microchim Acta 185:323.

356. Wajs E, Fernández N, Fragoso A. 2016. Supramolecular biosensors based on electropolymerised pyrrole-cyclodextrin modified surfaces for antibody detection. Analyst 141:3274–3279.

357. Teixeira SR, Lloyd C, Yao S, Andrea Salvatore Gazze, Whitaker IS, Francis L, Conlan RS, Azzopardi E. 2016. Polyaniline-graphene based α-amylase biosensor with a linear dynamic range in excess of 6 orders of magnitude. Biosens Bioelectron 85:395–402.

358. Betty C a. 2009. Highly sensitive capacitive immunosensor based on porous silicon-polyaniline structure: Bias dependence on specificity. Biosens Bioelectron 25:338–343.

359. Gerhardt GA, Oke AF, Nagy G, Moghaddam B, Adams RN. 1984. Nafion-coated electrodes with high selectivity for CNS electrochemistry. Brain Res 290:390–395.

360. Niyomdecha S, Limbut W, Numnuam A, Kanatharana P, Charlermroj R, Karoonuthaisiri N, Thavarungkul P. 2018. Phage-based capacitive biosensor for Salmonella detection. Talanta 188:658–664.

361. Gupta S, Murthy CN, Prabha CR. 2018. Recent advances in carbon nanotube based electrochemical biosensors. Int J Biol Macromol 108:687–703.

362. Ley C, Holtmann D, Mangold KM, Schrader J. 2011. Immobilization of histidine-tagged proteins on electrodes. Colloids Surfaces B Biointerfaces 88:539–551.

363. Jung Y, Jeong JY, Chung BH. 2008. Recent advances in immobilization methods of antibodies on solid supports. Analyst 133:697–701.

364. Damiati S, Peacock M, Leonhardt S, Damiati L, Baghdadi MA, Becker H, Kodzius R, Schuster B. 2018. Embedded disposable functionalized electrochemical biosensor with a 3D-printed flow cell for detection of hepatic oval cells (HOCs). Genes (Basel) 9.

365. Zeng Y, Bao J, Zhao Y, Huo D, Chen M, Yang M, Fa H, Hou C. 2018. A sensitive label-free electrochemical immunosensor for detection of cytokeratin 19 fragment antigen 21-1 based on 3D graphene with gold nanopaticle modified electrode. Talanta 178:122–128.

366. Li F, Li Y, Feng J, Dong Y, Wang P, Chen L, Chen Z, Liu H, Wei Q. 2017. Ultrasensitive amperometric immunosensor for PSA detection based on Cu2O@CeO2-Au nanocomposites as integrated triple signal amplification strategy. Biosens Bioelectron 87:630–637.

367. Zhou L, Mao H, Wu C, Tang L, Wu Z, Sun H, Zhang H, Zhou H, Jia C, Jin Q, Chen X,

Zhao J. 2017. Label-free graphene biosensor targeting cancer molecules based on non-covalent modification. Biosens Bioelectron 87:701–707.

368. Sánchez-Tirado E, Martínez-García G, González-Cortés A, Yáñez-Sedeño P, Pingarrón JM. 2017. Electrochemical immunosensor for sensitive determination of transforming growth factor (TGF) - β1 in urine. Biosens Bioelectron 88:9–14.

369. Gu X, She Z, Ma T, Tian S, Kraatz HB. 2018. Electrochemical detection of carcinoembryonic antigen. Biosens Bioelectron 102:610–616.

370. Labib M, Hedström M, Amin M, Mattiasson B. 2009. A capacitive immunosensor for detection of cholera toxin. Anal Chim Acta 634:255–261.

371. Wongkittisuksa B, Limsakul C, Kanatharana P, Limbut W, Asawatreratanakul P, Dawan S, Loyprasert S, Thavarungkul P. 2011. Development and application of a real-time capacitive sensor. Biosens Bioelectron 26:2466–2472.

372. Ertürk G, Hedström M, Tümer MA, Denizli A, Mattiasson B. 2015. Real-time prostate-specific antigen detection with prostate-specific antigen imprinted capacitive biosensors. Anal Chim Acta 891:120–129.

373. Wang Y-S, Yau S, Chau L-K, Mohamed A, Huang C-J. 2018. Functional Biointerfaces Based on Mixed Zwitterionic Self-Assembled Monolayers for Biosensing Applications. Langmuir acs.langmuir.8b01779.

374. Knowles BR, Yang D, Wagner P, MacLaughlin S, Higgins MJ, Molino PJ. 2018. Zwitterion Functionalized Silica Nanoparticle Coatings: The Effect of Particle Size on Protein, Bacteria, and Fungal Spore Adhesion. Langmuir acs.langmuir.8b01550.

375. Lin P, Chuang T-L, Chen PZ, Lin C-W, Gu FX. 2018. Low-Fouling Characteristics of Ultrathin Zwitterionic Cysteine SAMs. Langmuir acs.langmuir.8b01525.

376. Cheung DL, Lau KHA. 2018. Atomistic Study of Zwitterionic Peptoid Antifouling

Brushes. Langmuir acs.langmuir.8b01939.

377. Wang Y, Cui M, Jiao M, Luo X. 2018. Antifouling and ultrasensitive biosensing interface based on self-assembled peptide and aptamer on macroporous gold for electrochemical detection of immunoglobulin E in serum. Anal Bioanal Chem.

378. Knop K, Hoogenboom R, Fischer D, Schubert US. 2010. Poly(ethylene glycol) in drug delivery: Pros and cons as well as potential alternatives. Angew Chemie - Int Ed 49:6288–6308.

379. Liu B, Huang PJJ, Zhang X, Wang F, Pautler R, Ip ACF, Liu J. 2013. Parts-per-million of polyethylene glycol as a non-interfering blocking agent for homogeneous biosensor development. Anal Chem 85:10045–10050.

380. Ahmad NM, Abdullah J, Yusof NA, Ab Rashid AH, Rahman SA, Hasan MR. 2016. Amperometric biosensor based on zirconium oxide/polyethylene glycol/tyrosinase composite film for the detection of phenolic compounds. Biosensors 6.

381. Song J, Dailey J, Li H, Jang H-J, Zhang P, Wang JT-H, Everett AD, Katz HE. 2017. Extended Solution Gate OFET-Based Biosensor for Label-Free Glial Fibrillary Acidic Protein Detection with Polyethylene Glycol-Containing Bioreceptor Layer. Adv Funct Mater 27:1606506.

382. Hui N, Sun X, Niu S, Luo X. 2017. PEGylated polyaniline nanofibers: Antifouling and conducting biomaterial for electrochemical DNA sensing. ACS Appl Mater Interfaces 9:2914–2923.

383. Borgmann S, Schulte A, Neugebauer S, Schuhmann W. 2011. Advances in Electrochemical Science and Engineering. John Wiley & Sons, Inc.

384. Cammann K. 1977. Bio-sensors based on ion-selective electrodes. Fresenius' Zeitschrift für Anal Chemie 287:1–9.

385. Guilbault GG, Lubrano GJ. 1972. Enzyme electrode for glucose. Anal Chim Acta 60:254–6.

386. Guilbault GG, Lubrano GJ. 1973. An enzyme electrode for the amperometric determination of glucose. Anal Chim Acta 64:439–455.

387. Nanjo M, Guilbault GG. 1974. Enzyme electrode for I-amino acids and glucose. Anal Chim Acta 73:367–373.

388. Mell LD, Maloy JT. 1976. Amperometric Response Enhancement of the Immobilized Glucose Oxidase Enzyme Electrode. Anal Chem 48:1597–1601.

389. Guilbault GG, Montalvo JG. 1969. A Urea-Specific Enzyme Electrode. J Am Chem Soc 91:2164–2165.

390. Guilbault GG, Tarp M. 1974. A specific enzyme electrode for urea. Anal Chim Acta 73:355–65.

391. Johansson G, Ögren L. 1976. An enzyme reactor electrode for urea determinations. Anal Chim Acta 84:23–29.

392. Meyerhoff M, Rechnitz GA. 1976. An activated enzyme electrode for creatinine. Anal Chim Acta 85:277–285.

393. Kiang CH, Kuan SS, Guilbault GG. 1975. A novel enzyme electrode method for the determination of nitrite based on nitrite reductase. Anal Chim Acta 80:209–14.

394. Cserfalvi T, Guilbault GG. 1976. An enzyme electrode based on immobilized arylsulfatase for the selective assay of sulfate ion. Anal Chim Acta 84:259–70.

395. Nanjo M, Guilbault GG. 1974. Enzyme Electrode Sensing Oxygen for Uric Acid in Serum and Urine. Anal Chem 46:1769–1772.

396. Nanjo M, Guilbault GG. 1975. Amperometric determination of alcohols, aldehydes and carboxylic acids with an immobilized alcohol oxidase enzyme electrode. Anal Chim Acta

75:169–80.

397. Nagy G, von Storp LH, Guilbault GG. 1973. Enzyme electrode for glucose based on an iodide membrane sensor. Anal Chim Acta 66:443–55.

398. Booker HE, Haslam JL. 1974. Immobilized enzyme electrode for the determination of arginase. Anal Chem 46:1054–1060.

399. Kawashima T, Rechnitz GA. 1976. Potentiometric enzyme electrode for uric acid. Anal Chim Acta 83:9–17.

400. Janata J. 1975. Immunoelectrode. J Am Chem Soc 97:2914–2916.

401. Aizawa M, Kato S, Suzuki S. 1977. Immunoresponsive Membrane I. Membrane Potential Change Associated with an Immunochemical Reaction Between Membrane-Bound Antigen and Free Antibody. J Memb Sci 2:125–132.

402. Yamamoto N, Nagasawa Y, Sawai M, Sudo T, Tsubomura H. 1978. Potentiometric investigations of antigen-antibody and enzyme-enzyme inhibitor reactions using chemically modified metal electrodes. J Immunol Methods 22:309–317.

403. Aizawa M, Morioka A, Suzuki S, Nagamura Y. 1979. Enzyme immunosenser. Ill. Amperometric determination of human cherienic gonadotropin by membrane-bound antibody. Anal Biochem 94:22–28.

404. Aizawa M, Kato S, Suzuki S. 1980. Electrochemical typing of blood using affinity membranes. J Memb Sci 7:1–10.

405. Aizawa M. 1987. Immunosensors. Philos Trans R Soc Lond B Biol Sci 316:121–34.

406. Aizawa M, Morioka A, Suzuki S. 1980. An enzyme immunosensor for the electrochemical determination of the tumor antigen α-fetoprotein. Anal Chim Acta 115:61–67.

407. Karube I, Suzuki S, Okada T, Hikuma M. 1980. Microbial sensors for volatile

compounds. Biochimie 62:567–73.

408. Okada T, Karube I, Suzuki S. 1983. NO2 Sensor which uses immobilized nitrite oxidizing bacteria. Biotechnol Bioeng 25:1641–1651.

409. Hikuma M, Obana H, Yasuda T, Karube I, Suzuki S. 1980. A potentiometric microbial sensor based on immobilized escherichia coli for glutamic acid. Anal Chim Acta 116:61–67.

410. Marks RS. 2013. Electrochemical Biosensors. Taylor & Francis Group, LLC, Boca Raton, FL.

411. Kulys JJ, Čénas NK. 1983. Oxidation of glucose oxidase from Penicillium vitale by one- and two-electron acceptors. Biochim Biophys Acta (BBA)/Protein Struct Mol 744:57–63.

412. Cass AEG, Davis G, Francis GD, Hill HAO, Aston WJ, Higgins IJ, Plotkin E V., Scott LDL, Turner APF. 1984. Ferrocene-mediated enzyme electrode for amperometric determination of glucose. Anal Chem 56:667–671.

413. Moody GJ, Sanghera GS, Thomas JDR. 1987. Chemically lmmobilised Bi-enzyme Electrodes in the Redox Mediated Mode for the Flow Injection Analysis of Glucose and Hypoxanthine. Analyst 112:65–70.

414. Aoki K, Morita M, Niwa O, Tabei H. 1988. Quantitative analysis of reversible diffusion-controlled currents of redox soluble species at interdigitated array electrodes under steady-state conditions. J Electroanal Chem Interfacial Electrochem 256:269–282.

415. Zhang W, Li G. 2004. Third-generation biosensors based on the direct electron transfer of proteins. Anal Sci 20:603–609.

416. Hall EAH. 1988. Recent Progress in Biosensor Development. Int J Biochem 20:357–362.

417. Ghindilis AL, Atanasov P, Wilkins E. 1997. Enzyme-Catalyzed Direct Electron Transfer: Fundamentals and Analytical Applications. Electroanalysis 9:661–674.

418. Eddowes MJ, Hill HAO. 1977. Novel method for the investigation of the electrochemistry of metalloproteins:cytochrome c. J Chem Soc Chem Commun 21:771–772.

419. Kuznetsov BA, Mestechkina N., Shumakovich GP. 1977. Electrochemical Behavior of Proteins Containing Coenzyme Groups and Metals. Bioelectrochemistry Bioenerg 4:1–17.

420. Bogdanovskaya VA, Tarasevich MR, Hintsche R, Scheller F. 1988. Electrochemical transformations of proteins adsorbed at carbon electrodes. Bioelectrochemistry Bioenerg 19:581–584.

421. Razumas VJ, Gudavičius A V., Kulys JJ. 1983. Redox conversion of peroxidase on surface-modified gold electrode. J Electroanal Chem Interfacial Electrochem 151:311–315.

422. Razumas VJ, Gudavičius A V., Kulys JJ. 1986. Kinetics of peroxidase redox conversion on viologen-modified gold electrodes. J Electroanal Chem Interfacial Electrochem 198:81–87.

423. Armstrong FA, George SJ, Thomson AJ, Yates MG. 1988. Direct electrochemistry in the characterisation of redox proteins: Novel properties of Azotobacter 7Fe ferredoxin. FEBS Lett 234:107–110.

424. Frew JE, Hill HAO. 1988. Direct and Indirect Electron-Transfer between Electrodes and Redox Proteins. Eur J Biochem 172:261–269.

425. Turner AP. 1994. Biosensors. Curr Opin Biotechnol 5:49–53.

426. Foulds NC, Lowe CR. 1986. Enzyme Entrapment in Electrically Conducting Polymers. J Chem Soc Faraday Trans 1 1:1259–1264.

427. Umaña M, Waller J. 1986. Protein-Modified Electrodes. The Glucose Oxidase/Polypyrrole System. Anal Chem 58:2979–2983.

428. DeSilva MS, Zhang Y, Hesketh PJ, Maclay GJ, Gendel SM, Stetter JR. 1995. Impedance

based sensing of the specific binding reaction between Staphylococcus enterotoxin B and its antibody on an ultra-thin platinum film. Biosens Bioelectron 10:675–682.

429. Foulds NC, Lowe CR. 1988. Immobilization of Glucose Oxidase in Ferrocene-Modified Pyrrole Polymers. Anal Chem 60:2473–2478.

430. Mirsky VM, Riepl M, Wolfbeis OS. 1997. Capacitative monitoring of protein immobilisation and antibody antigen interactions on monomolecular alkylthiol films on gold electrodes. Biosens Bioelectron 12:977.

431. Yao T, Rechnitz GA. 1988. Amperometric enzyme-immunosensor based on ferrocene-mediated amplification. Biosensors 3:307–12.

432. Sanderson DG, Anderson LB. 1985. Filar Electrodes: Steady-State Currents and Spectroelectrochemistry at Twin Interdigitated Electrodes. Anal Chem 57:2388–2393.

433. Morita M, Niwa O, Horiuchi T. 1997. Interdigitated array microelectrodes as electrochemical sensors. Electrochim Acta 42:3177–3183.

434. Goluch ED, Wolfrum B, Singh PS, Zevenbergen MAG, Lemay SG. 2009. Redox cycling in nanofluidic channels using interdigitated electrodes. Anal Bioanal Chem 394:447–456.

435. Aoki A, Matsue T, Uchida I. 1990. Electrochemical Response at Microarray Electrodes in Flowing Streams and Determination of Catecholamines. Anal Chem 62:2206–2210.

436. Yao T, Satomura M, Wasa T. 1992. Amperometric flow-injection method for determination of biogenic diamines and hypoxanthine by combined use of immobilized enzyme reactors and a peroxidase electrode. Anal Chim Acta 261:161–165.

437. Watanabe E, Endo H, Hayashi T, Toyama K. 1986. Simultaneous determination of hypoxanthine and inosine with an enzyme sensor. Biosensors 2:235–244.

438. Wittstock G. 2002. Sensor arrays and array sensors. Anal Bioanal Chem 372:16–7.

439. Connolly P, Clark P, Curtis ASG, Dow JAT, Wilkinson CDW. 1990. An Extracellular

microelectrode Array for monitoring electrogenic cells in culture. Biosens Bioelectron 5:223–234.

440. Lee H, Liu Y, Ham D, Westervelt RM. 2007. Integrated cell manipulation system--CMOS/microfluidic hybrid. Lab Chip 7:331–337.

441. Couniot N, Francis LA, Flandre D. 2015. A 16 x 16 CMOS Capacitive Biosensor Array Towards Detection of Single Bacterial Cell. IEEE Trans Biomed Circuits Syst 1–1.

442. Wydallis JB, Feeny RM, Wilson W, Kern T, Chen T, Tobet S, Reynolds MM, Henry CS. 2015. Spatiotemporal norepinephrine mapping using a high-density CMOS microelectrode array. Lab Chip 15:4075–4082.

443. Henares TG, Mizutani F, Hisamoto H. 2008. Current development in microfluidic immunosensing chip. Anal Chim Acta 611:17–30.

444. Guisbiers G, Mejía-Rosales S, Leonard Deepak F. 2012. Nanomaterial properties: Size and shape dependencies. J Nanomater 2012:2012–2014.

445. Cammarata RC. 1994. Surface and interface stress effects in thin films. Prog Surf Sci 46:1–38.

446. Balaguru RJB, Jeyaprakash BG. Quantum size effect , electrical conductivity and Quantum transport. Electr Electron Eng - Semicond Nanodevices.

447. Wang J. 2012. Electrochemical biosensing based on noble metal nanoparticles. Microchim Acta 177:245–270.

448. Suvarnaphaet P, Pechprasarn S. 2017. Graphene-based materials for biosensors: A review. Sensors (Switzerland) 17.

449. Liu N, Yi H, Lin Y, Zheng H, Zheng X, Lin D, Dai H. 2018. Combined electrochemiluminescent and electrochemical immunoassay for interleukin 6 based on the use of TiO2 mesocrystal nanoarchitectures. Microchim Acta 185:277.

450. Naseri M, Fotouhi L, Ehsani A. 2018. Recent Progress in the Development of Conducting Polymer-Based Nanocomposites for Electrochemical Biosensors Applications: A Mini-Review. Chem Rec 18:599–618.

451. Kazemi SH, Ghodsi E, Abdollahi S, Nadri S. 2016. Porous graphene oxide nanostructure as an excellent scaffold for label-free electrochemical biosensor: Detection of cardiac troponin I. Mater Sci Eng C 69:447–452.

452. Bhattarai J, Neupane D, Nepal B, Mikhaylov V, Demchenko A, Stine K. 2018. Preparation, Modification, Characterization, and Biosensing Application of Nanoporous Gold Using Electrochemical Techniques. Nanomaterials 8:171.

453. López-Marzo AM, Hoyos-De-La-Torre R, Baldrich E. 2018. NaNO3/NaCl Oxidant and Polyethylene Glycol (PEG) Capped Gold Nanoparticles (AuNPs) as a Novel Green Route for AuNPs Detection in Electrochemical Biosensors. Anal Chem 90:4010–4018.

454. Huang J, Xie Z, Xie Z, Luo S, Xie L, Huang L, Fan Q, Zhang Y, Wang S, Zeng T. 2016. Silver nanoparticles coated graphene electrochemical sensor for the ultrasensitive analysis of avian influenza virus H7. Anal Chim Acta 913:121–127.

455. Charoenkitamorn K, Tue PT, Kawai K, Chailapakul O, Takamura Y. 2018. Electrochemical immunoassay using open circuit potential detection labeled by platinum nanoparticles. Sensors (Switzerland) 18.

456. Aghajari R, Azadbakht A. 2018. Amplified detection of streptomycin using aptamer-conjugated palladium nanoparticles decorated on chitosan-carbon nanotube. Anal Biochem 547:57–65.

457. Wang R, Liu WD, Wang AJ, Xue Y, Wu L, Feng JJ. 2018. A new label-free electrochemical immunosensor based on dendritic core-shell AuPd@Au nanocrystals for highly sensitive detection of prostate specific antigen. Biosens Bioelectron 99:458–463.

458. Guo S, Wang E. 2007. Synthesis and electrochemical applications of gold nanoparticles. Anal Chim Acta 598:181–192.

459. Meets B. 2001. Biotechnology Meets Materials Science. Mater Sci 40:4128–4158.

460. Gajjala RKR, Palathedath SK. 2018. Cu@Pd core-shell nanostructures for highly sensitive and selective amperometric analysis of histamine. Biosens Bioelectron 102:242–246.

461. Zhuo Y, Yuan PX, Yuan R, Chai YQ, Hong CL. 2009. Bienzyme functionalized three-layer composite magnetic nanoparticles for electrochemical immunosensors. Biomaterials 30:2284–2290.

462. Zhao J, Bradbury CR, Huclova S, Potapova I, Carrara M, Fermín DJ. 2005. Nanoparticle-mediated electron transfer across ultrathin self-assembled films. J Phys Chem B 109:22985–22994.

463. Zhao W, Xu JJ, Chen HY. 2006. Electrochemical biosensors based on layer-by-layer assemblies. Electroanalysis 18:1737–1748.

464. Holzinger M, Le Goff A, Cosnier S. 2017. Synergetic effects of combined nanomaterials for biosensing applications. Sensors (Switzerland) 17.

465. Zhang S, Geryak R, Geldmeier J, Kim S, Tsukruk V V. 2017. Synthesis, Assembly, and Applications of Hybrid Nanostructures for Biosensing. Chem Rev 117:12942–13038.

466. Caruso RA, Antonietti M. 2001. Sol-gel nanocoating: An approach to the preparation of structured materials. Chem Mater 13:3272–3282.

467. Toledano R, Mandler D. 2010. Electrochemical codeposition of thin gold nanoparticles/sol-gel nanocomposite films. Chem Mater 22:3943–3951.

468. Gu HY, Yu AM, Chen HY. 2001. Direct electron transfer and characterization of hemoglobin immobilized on a Au colloid-cysteamine-modified gold electrode. J Electroanal Chem 516:119–126.

469. Zhao J, Henkens RW, Stonehuerner J, O'Daly JP, Crumbliss AL. 1992. Direct electron transfer at horseradish peroxidase-colloidal gold modified electrodes. J Electroanal Chem 327:109–119.

470. Zhang X, Geng P, Liu H, Teng Y, Liu Y, Wang Q, Zhang W, Jin L, Jiang L. 2009. Development of an electrochemical immunoassay for rapid detection of E. coli using anodic stripping voltammetry based on Cu@Au nanoparticles as antibody labels. Biosens Bioelectron 24:2155–2159.

471. Chen GZ, Yin ZZ, Lou JF. 2014. Electrochemical immunoassay of escherichia coli O157:H7 using Ag@SiO 2 nanoparticles as labels. J Anal Methods Chem 2014.

472. Harvey D. Cyclic Voltammetry With A Microelectrode. Anal Sci Digit Libr http://www.asdlib.org/onlineArticles/elabware/kuwanaEC_lab/PDF-20-Experiment2.pdf

473. Wightman RM. 1981. Microvoltammetric Electrodes. Anal Chem 53:1125A–1134A.

474. Bestbier A. 2016. Design and build a rotating LED display. http://doi.org/10.13140/RG.2.2.21937.38247

475. Kurtzman T. 2018. Electronics 101 - AC vs DC. SonaLabs Electron.

476. Chang B-Y, Park S-M. 2010. Electrochemical Impedance Spectroscopy. Annu Rev Anal Chem 3:207–229.

477. Filer JE, Channon RB, Henry CS, Geiss BJ. A Nuclease Protection ELISA Assay for Colorimetric and Electrochemical Detection of Nucleic Acid. Submitted.

478. Eyler E. 2013. Explanatory Chapter: Nuclease Protection Assays, p. 89–97. *In* Methods in Enzymology, 1st ed. Elsevier Inc.

479. Hou S-Y, Hsiao Y-L, Lin M-S, Yen C-C, Chang C-S. 2012. MicroRNA detection using lateral flow nucleic acid strips with gold nanoparticles. Talanta 99:375–379.

480. Roberts RA, Sabalos CM, LeBlanc ML, Martel RR, Frutiger YM, Unger JM, Botros IW, Rounseville MP, Seligmann BE, Miller TP, Grogan TM, Rimsza LM. 2007. Quantitative nuclease protection assay in paraffin-embedded tissue replicates prognostic microarray gene expression in diffuse large-B-cell lymphoma. Lab Investig 87:979–997.

481. Smith DR. 1993. S1 Nuclease Protection Mapping, p. 363–372. *In* Transgenesis Techniques. Humana Press, New Jersey.

482. John M, Pfeffer S. 2011. Detection of Viral microRNA with S1 Nuclease Protection Assay, p. 173–182. *In* Methods in molecular biology (Clifton, N.J.).

483. Cammas FM, Clark AJL. 1996. S1 Nuclease Protection Assay Using Streptavidin Dynabeads-Purified Single-Stranded DNA. Anal Biochem 236:182–184.

484. Berk AJ, Sharp PA. 1977. Sizing and mapping of early adenovirus mRNAs by gel electrophoresis of S1 endonuclease-digested hybrids. Cell 12:721–732.

485. Goldrick M, Kessler D. 2003. RNA Analysis by Nuclease ProtectionCurrent Protocols in Neuroscience. John Wiley & Sons, Inc., Hoboken, NJ, USA.

486. Fichorova RN, Mendonca K, Yamamoto HS, Murray R, Chandra N, Doncel GF. 2015. A quantitative multiplex nuclease protection assay reveals immunotoxicity gene expression profiles in the rabbit model for vaginal drug safety evaluation. Toxicol Appl Pharmacol 285:198–206.

487. Irwin MH, Pinkert CA. 2014. Analysis of Transgene Expression, p. 543–564. *In* Transgenic Animal Technology. Elsevier.

488. John M, Constien R, Akinc A, Goldberg M, Moon Y, Spranger M, Hadwiger P, Soutschek J, Vornlocher H, Manoharan M, Stoffel M, Langer R, Anderson DG, Horton JD, Koteliansky V, Bumcrot D. 2007. Effective RNAi-mediated gene silencing without interruption of the endogenous microRNA pathway. Nature 449:745–747.

489. Dolken L, Perot J, Cognat V, Alioua A, John M, Soutschek J, Ruzsics Z, Koszinowski U, Voinnet O, Pfeffer S. 2007. Mouse Cytomegalovirus MicroRNAs Dominate the Cellular Small RNA Profile during Lytic Infection and Show Features of Posttranscriptional Regulation. J Virol 81:13771–13782.

490. Zhen Y, Mi T, Yu Z. 2009. Detection of several harmful algal species by sandwich hybridization integrated with a nuclease protection assay. Harmful Algae 8:651–657.

491. Zhu X, Zhen Y, Mi T, Yu Z. 2012. Detection of Prorocentrum minimum (Pavillard) Schiller with an Electrochemiluminescence–Molecular Probe Assay. Mar Biotechnol 14:502–511.

492. Suh S-S, Park M, Hwang J, Kil E-J, Lee S, Lee T-K. 2016. Detection of the dinoflagellate, Cochlodinium polykrikoides, that forms algal blooms using sandwich hybridization integrated with nuclease protection assay. Biotechnol Lett 38:57–63.

493. Tanner B, Friedberg T, Mitze M, Beck T, Oesch F, Knapstein P-G. 1992. C-erbB-2-oncogene expression in breast carcinoma: Analysis by S1 nuclease protection assay and immunohistochemistry in relation to clinical parameters. Gynecol Oncol 47:228–233.

494. Sun L, Irudayaraj J. 2009. PCR-Free Quantification of Multiple Splice Variants in a Cancer Gene by Surface-Enhanced Raman Spectroscopy. J Phys Chem B 113:14021–14025.

495. Bose D, Jayaraj G, Suryawanshi H, Agarwala P, Pore SK, Banerjee R, Maiti S. 2012. The Tuberculosis Drug Streptomycin as a Potential Cancer Therapeutic: Inhibition of miR-21 Function by Directly Targeting Its Precursor. Angew Chemie Int Ed 51:1019–1023.

496. Pilato B, De Summa S, Danza K, Papadimitriou S, Zaccagna P, Paradiso A, Tommasi S. 2012. DHPLC/SURVEYOR Nuclease: A Sensitive, Rapid and Affordable Method to Analyze BRCA1 and BRCA2 Mutations in Breast Cancer Families. Mol Biotechnol 52:8–

15.

497. Thakur BK, Zhang H, Becker A, Matei I, Huang Y, Costa-Silva B, Zheng Y, Hoshino A, Brazier H, Xiang J, Williams C, Rodriguez-Barrueco R, Silva JM, Zhang W, Hearn S, Elemento O, Paknejad N, Manova-Todorova K, Welte K, Bromberg J, Peinado H, Lyden D. 2014. Double-stranded DNA in exosomes: a novel biomarker in cancer detection. Cell Res 24:766–769.

498. Bannwarth S, Procaccio V, Paquis-Flucklinger V. 2005. Surveyor™ Nuclease: A new strategy for a rapid identification of heteroplasmic mitochondrial DNA mutations in patients with respiratory chain defects. Hum Mutat 25:575–582.

499. Goeijenbier M, Slobbe L, van der Eijk A, de Mendonça Melo M, Koopmans MPG, Reusken CBEM. 2016. Zika virus and the current outbreak: an overview. Neth J Med 74:104–9.

500. Centers for Disease Control and Prevention. 2017. Laboratory Guidance and Diagnostic Testing.

501. Cai Q, Li R, Zhen Y, Mi T, Yu Z. 2006. Detection of two Prorocentrum species using sandwich hybridization integrated with nuclease protection assay. Harmful Algae 5:300–309.

502. Zhou J, Rossi JJ, (Ed.) RPVR. 2011. Antiviral RNAiMethods in Molecular Biology. Humana Press, Totowa, NJ.

503. ICH Experiment Working Group. 2005. Validation of Analytical Procedures : Text and MethodologyInternational Conference on Harmonization.

504. Miller JN, Miller JC. 2010. Statistics and Chemometrics for Analytical ChemistryTechnometrics, 6th ed. Pearson Education Limited.

505. Oleykowski C a, Bronson Mullins CR, Godwin a K, Yeung a T. 1998. Mutation

detection using a novel plant endonuclease. Nucleic Acids Res 26:4597–4602.

506. Till BJ. 2004. Mismatch cleavage by single-strand specific nucleases. Nucleic Acids Res 32:2632–2641.

507. Tadele Z. 2016. Mutagenesis and TILLING to Dissect Gene Function in Plants. Curr Genomics 17:499–508.

508. Holec-Gąsior L, Ferra B, Czechowska J, Serdiuk IE, Krzymiński K. 2018. A novel chemiluminescent immunoassay based on original acridinium ester labels as better solution for diagnosis of human toxoplasmosis than conventional ELISA test. Diagn Microbiol Infect Dis 91:13–19.

509. Muhammad N, Dworeck T, Fioroni M, Schwaneberg U. 2011. Engineering of the E. coli Outer Membrane Protein FhuA to overcome the Hydrophobic Mismatch in Thick Polymeric Membranes. J Nanobiotechnology 9:8.

510. Busa LSA, Komatsu T, Mohammadi S, Maeki M, Ishida A, Tani H, Tokeshi M. 2016. 3,3’,5,5’-Tetramethylbenzidine Oxidation on Paper Devices for Horseradish Peroxidase-based Assays. Anal Sci 32:815–818.

511. Josephy PD, Eling T, Mason RP. 1982. The horseradish peroxidase-catalyzed oxidation of 3,5,3’,5’-tetramethylbenzidine. Free radical and charge-transfer complex intermediates. J Biol Chem 257:3669–75.

512. Heineman WR, Halsall HB. 1985. Strategies for electrochemical immunoassay. Anal Chem 57:1321A–1331A.

513. Sha H, Bai Y, Li S, Wang X, Yin Y. 2014. Comparison between electrochemical ELISA and spectrophotometric ELISA for the detection of dentine sialophosphoprotein for root resorption. Am J Orthod Dentofac Orthop 145:36–40.

514. Martínez-Mancera FD, García-López P, Hernández-López JL. 2015. Pre-clinical

validation study of a miniaturized electrochemical immunoassay based on square wave voltammetry for early detection of carcinoembryonic antigen in human serum. Clin Chim Acta 444:199–205.

515. Monk PMS. 2008. Fundamentals of Electro-Analytical Chemistry. John Wiley & Sons, Inc.

516. Kergaravat S V., Pividori MI, Hernandez SR. 2012. Evaluation of seven cosubstrates in the quantification of horseradish peroxidase enzyme by square wave voltammetry. Talanta 88:468–476.

517. Hong W, Lee S, Cho Y. 2016. Dual-responsive immunosensor that combines colorimetric recognition and electrochemical response for ultrasensitive detection of cancer biomarkers. Biosens Bioelectron 86:920–926.

518. Wang H, Rong Q, Ma Z. 2016. Polyhydroquinone-graphene composite as new redox species for sensitive electrochemical detection of cytokeratins antigen 21-1. Nat Publ Gr 1–6.

519. Giannetto M, Bianchi MV, Mattarozzi M, Careri M. 2017. Competitive amperometric immunosensor for determination of p53 protein in urine with carbon nanotubes/gold nanoparticles screen-printed electrodes: A potential rapid and noninvasive screening tool for early diagnosis of urinary tract carcinoma. Anal Chim Acta 991:133–141.

520. Sánchez-Tirado E, Martínez-García G, González-Cortés A, Yáñez-Sedeño P, Pingarrón JM. 2016. Electrochemical immunosensor for sensitive determination of transforming growth factor (TGF) - β1 in urine. Biosens Bioelectron 1–6.

521. Akai N, Kawai A, Shibuya K. 2011. Water assisted photo-oxidation from hydroquinone to p-benzoquinone in a solid Ne matrix. J Photochem Photobiol A Chem 223:182–188.

522. Adkins JA, Henry CS. 2015. Electrochemical detection in paper-based analytical devices

using microwire electrodes. Anal Chim Acta 891:247–254.

523. Channon RB, Yang Y, Feibelman KM, Geiss BJ, Dandy DS, Henry CS. 2018. Development of an Electrochemical Paper-Based Analytical Device for Trace Detection of Virus Particles. Anal Chem 90:7777–7783.

524. Wang L, Filer J, Lorenz MM, Henry CS, Dandy DS, Geiss BJ. 2018. An Ultra-Sensitive Capacitve Microwire Sensor for Pathogen-Specific Serum Antibody Responses. Under Rev 1–27.

525. Burbelo PD, Ching KH, Bush ER, Han BL, Iadarola MJ. 2010. Antibody-profiling technologies for studying humoral responses to infectious agents. Expert Rev Vaccines 9:567–578.

526. Parnham MJ, Nijkamp FP. 2005. Principles of Immnunopharmacology.

527. Crowther JR. 2008. The ELISA Guidebook Series Editor.

528. Baden LR, Petersen LR, Jamieson DJ, Powers AM, Honein MA. 2016. Zika Virus. N Engl J Med 374:1552-1563.

529. Rabe IB, Staples JE, Villanueva J, Hummel KB, Johnson JA, Rose L, Hills S, Wasley A, Fischer M, Powers AM. 2016. Interim Guidance for Interpretation of Zika Virus Antibody Test Results. MMWR Morb Mortal Wkly Rep 65:543–546.

530. Yager P, Domingo GJ, Gerdes J. 2008. Point-of-Care Diagnostics for Global Health. Annu Rev Biomed Eng 10:107–144.

531. Prado IC, Chino META, dos Santos AL, Souza ALA, Pinho LG, Lemos ERS, De-Simone SG. 2018. Development of an electrochemical immunosensor for the diagnostic testing of spotted fever using synthetic peptides. Biosens Bioelectron 100:115–121.

532. Adornetto G, Fabiani L, Volpe G, De Stefano A, Martini S, Nenna R, Lucantoni F, Bonamico M, Tiberti C, Moscone D. 2015. An electrochemical immunoassay for the

screening of celiac disease in saliva samples. Anal Bioanal Chem 407:7189–7196.

533. Berggren C, Bjarnason B, Johansson G. 2001. Capacitive biosensors. Electroanalysis 13:173–180.

534. Ertürk G, Mattiasson B. 2017. Capacitive biosensors and molecularly imprinted electrodes. Sensors (Switzerland) 17:1–21.

535. Wang L, Veselinovic M, Yang L, Geiss BJ, Dandy DS, Chen T. 2016. A sensitive DNA capacitive biosensor using interdigitated electrodes. Biosens Bioelectron 87:646–653.

536. Teeparuksapun K, Hedström M, Wong EY, Tang S, Hewlett IK, Mattiasson B. 2010. Ultrasensitive detection of HIV-1 p24 antigen using nanofunctionalized surfaces in a capacitive immunosensor. Anal Chem 82:8406–11.

537. Mattiasson B, Hedström M. 2016. Capacitive biosensors for ultra-sensitive assays. TrAC - Trends Anal Chem 79:233–238.

538. Loyprasert S, Hedström M, Thavarungkul P, Kanatharana P, Mattiasson B. 2010. Sub-attomolar detection of cholera toxin using a label-free capacitive immunosensor. Biosens Bioelectron 25:1977–1983.

539. Leal MC, Muniz LF, Ferreira TSA, Santos CM, Almeida LC, Linden V Van Der, Ramos RCF, Rodrigues LC, Caldas Neto SS. 2016. Hearing Loss in Infants with Microcephaly and Evidence of Congenital Zika Virus Infection — Brazil , November 2015 – May 2016. MMWR Morb Mortal Wkly Rep 65:2015–2017.

540. van der Eijk AA, van Genderen PJ, Verdijk RM, Reusken CB, Mögling R, van Kampen JJA, Widagdo W, Aron GI, GeurtsvanKessel CH, Pas SD, Raj VS, Haagmans BL, Koopmans MPG. 2016. Miscarriage Associated with Zika Virus Infection. N Engl J Med 1386–1388.

541. Ventura C V, Maia M, Bravo-Filho V, Góis AL, Belfort R. 2016. Zika virus in Brazil and

macular atrophy in a child with microcephaly. Lancet 387:228.

542. Pierson TC, Sánchez MD, Puffer BA, Ahmed AA, Geiss BJ, Valentine LE, Altamura LA, Diamond MS, Doms RW. 2006. A rapid and quantitative assay for measuring antibody-mediated neutralization of West Nile virus infection. Virology 346:53–65.

543. Fischer LM, Tenje M, Heiskanen AR, Masuda N, Castillo J, Bentien A, Émneus J, Jakobsen MH, Boisen A. 2009. Gold cleaning methods for electrochemical detection applications. Microelectron Eng 86:1282–1285.

544. Wang L, Liu W, Wang Y, Wang J, Tu Q, Liu R, Wang J. 2013. Construction of oxygen and chemical concentration gradients in a single microfluidic device for studying tumor cell-drug interactions in a dynamic hypoxia microenvironment. Lab Chip 13:695–705.

545. Aoki K. 1993. Theory of ultramicroelectrodes. Electroanalysis 5:627–639.

546. Liu Y, Vickers JA, Henry CS. 2004. Simple and Sensitive Electrode Design for Microchip Electrophoresis/Electrochemistry. Anal Chem 76:1513–1517.

547. Salaün P, Van Den Berg CMG. 2006. Voltammetric detection of mercury and copper in seawater using a gold microwire electrode. Anal Chem 78:5052–5060.

548. Yang K, Wu J. 2008. Investigation of microflow reversal by ac electrokinetics in orthogonal electrodes for micropump design. Biomicrofluidics 2:1–8.

549. Wu J. 2006. Biased AC electro-osmosis for on-chip bioparticle processing. IEEE Trans Nanotechnol 5:84–88.

550. Suni II. 2008. Impedance methods for electrochemical sensors using nanomaterials. Trends Anal Chem 27:604–611.

551. Bullard-Feibelman KM, Govero J, Zhu Z, Salazar V, Veselinovic M, Diamond MS, Geiss BJ. 2017. The FDA-approved drug sofosbuvir inhibits Zika virus infection. Antiviral Res 137:134–140.

552. Jeong YE, Cha GW, Cho JE, Lee EJ, Jee Y, Lee WJ. 2017. Viral and serological kinetics in Zika virus-infected patients in South Korea. Virol J 14:4–9.

553. Wu P, Castner DG, Grainger DW. 2008. Diagnostic devices as biomaterials: a review of nucleic acid and protein microarray surface performance issues. J Biomater Sci Polym Ed 19:725–753.

554. Watkins HM, Ricci F, Plaxco KW. 2018. Experimental Measurement of Surface Charge Effects on the Stability of a Surface-Bound Biopolymer. Langmuir acs.langmuir.8b01004.

555. Channon RB, Yang Y, Feibelman KM, Geiss BJ, Dandy DS, Henry CS. 2018. Development of an Electrochemical Paper-Based Analytical Device for Trace Detection of Virus Particles. Anal Chem 90:7777–7783.

556. Yang L, Filer JE, Geiss BJ, Chen T. Design and Validation of a Handheld Potentiostat Prototype. Prep.

557. Nisalek A. 2015. Laboratory diagnosis of dengue virus infections. Southeast Asian J Trop Med Public Heal 46:55–76.

558. Navakul K, Warakulwit C, Yenchitsomanus P thai, Panya A, Lieberzeit PA, Sangma C. 2017. A novel method for dengue virus detection and antibody screening using a graphene-polymer based electrochemical biosensor. Nanomedicine Nanotechnology, Biol Med 13:549–557.

559. Eng XG, Hang FZ, Ao QG, Ei YL. 2016. Sensitive Impedimetric Immunoassay of Japanese Encephalitis Virus Based on Enzyme Biocatalyzed Precipitation on a Gold Nanoparticle-modified Screen-printed Carbon Electrode. Anal Sci 32:1105–1109.

560. Peh AEK, Li SFY. 2013. Dengue virus detection using impedance measured across nanoporous aluminamembrane. Biosens Bioelectron 42:391–396.

561. Singh R, Hong S, Jang J. 2017. Label-free Detection of Influenza Viruses using a Reduced

Graphene Oxide-based Electrochemical Immunosensor Integrated with a Microfluidic Platform. Sci Rep 7:1–11.

562. Cheng MS, Ho JS, Tan CH, Wong JPS, Ng LC, Toh CS. 2012. Development of an electrochemical membrane-based nanobiosensor for ultrasensitive detection of dengue virus. Anal Chim Acta 725:74–80.

563. Nguyen BTT, Peh AEK, Chee CYL, Fink K, Chow VTK, Ng MML, Toh CS. 2012. Electrochemical impedance spectroscopy characterization of nanoporous alumina dengue virus biosensor. Bioelectrochemistry 88:15–21.

564. Singh R, Sharma A, Hong S, Jang J. 2014. Electrical immunosensor based on dielectrophoretically-deposited carbon nanotubes for detection of influenza virus H1N1. Analyst 139:5415–5421.

565. Ahmed SR, Mogus J, Chand R, Nagy E, Neethirajan S. 2018. Optoelectronic fowl adenovirus detection based on local electric field enhancement on graphene quantum dots and gold nanobundle hybrid. Biosens Bioelectron 103:45–53.

566. Devarakonda S, Singh R, Bhardwaj J, Jang J. 2017. Cost-effective and handmade paper-based immunosensing device for electrochemical detection of influenza virus. Sensors (Switzerland) 17.

567. Mihailescu C-M, Stan D, Iosub R, Moldovan C, Savin M. 2015. A Sensitive capacitive immunosensor for direct detection of human heart fatty acid-binding protein (h-FABP). Talanta 132:37–43.

568. Bonaldo MC, Ribeiro IP, Lima NS, Dos Santos AAC, Menezes LSR, da Cruz SOD, de Mello IS, Furtado ND, de Moura EE, Damasceno L, da Silva KAB, de Castro MG, Gerber AL, de Almeida LGP, Lourenço-de-Oliveira R, Vasconcelos ATR, Brasil P. 2016. Isolation of Infective Zika Virus from Urine and Saliva of Patients in Brazil. PLoS Negl

Trop Dis 10:e0004816.

569. Majorek KA, Porebski PJ, Dayal A, Zimmerman MD, Jablonska K, Stewart AJ, Chruszcz M, Minor W. 2012. Structural and immunologic characterization of bovine, horse, and rabbit serum albumins. Mol Immunol 52:174–182.

570. Lesnik EA, Freier SM. 1995. Relative Thermodynamic Stability of DNA, RNA, and DNA:RNA Hybrid Duplexes: Relationship with Base Composition and Structure. Biochemistry 34:10807–10815.

571. Richards FM. 1958. On the Enzymatic Activity of Subtilisin-Modified Ribonuclease. Proc Natl Acad Sci U S A 44:162–6.

572. Ullmann A, Perrin D, Jacob F, Monod J. 1965. Identification par complémentation in vitro et purification d'un segment peptidique de la β-galactosidase d'Escherichia coli. J Mol Biol 12:918–923.

573. Ullmann A, Jacob F, Monod J. 1967. Characterization by in vitro complementation of a peptide corresponding to an operator-proximal segment of the β-galactosidase structural gene of Escherichia coli. J Mol Biol 24:339–343.

574. Ikeda Y, Kumagai H, Okazaki H, Fujishiro M, Motozawa Y, Nomura S, Takeda N, Toko H, Takimoto E, Akazawa H, Morita H, Suzuki JI, Yamazaki T, Komuro I, Yanagisawa M. 2015. Monitoring β-arrestin recruitment via β-lactamase enzyme fragment complementation: Purification of peptide E as a low-affinity ligand for mammalian bombesin receptors. PLoS One 10:1–14.

575. Yu F, Alesand V, Nygren P-Å. 2018. Site-Specific Photoconjugation of Beta-Lactamase Fragments to Monoclonal Antibodies Enables Sensitive Analyte Detection via Split-Enzyme Complementation. Biotechnol J 13:1700688.

576. Rajaee M, Ow DW. 2017. A new location to split Cre recombinase for protein fragment

complementation. Plant Biotechnol J 15:1420–1428.

577. Casanova E, Lemberger T, Fehsenfeld S, Mantamadiotis T, Schütz G. 2003. α complementation in the Cre recombinase enzyme. Genesis 37:25–29.

578. Ohmuro-Matsuyama Y, Ueda H. 2018. Homogeneous Noncompetitive Luminescent Immunodetection of Small Molecules by Ternary Protein Fragment Complementation. Anal Chem 90:3001–3004.

579. Cheng AN, Lo Y-K, Lin Y-S, Tang T-K, Hsu C-H, Hsu JTA, Lee AY-L. 2018. Identification of Novel Cdc7 Kinase Inhibitors as Anti-Cancer Agents that Target the Interaction with Dbf4 by the Fragment Complementation and Drug Repositioning Approach. EBioMedicine 36:241–251.

580. Kolkhof P, Werthebach M, van de Venn A, Poschmann G, Chen L, Welte M, Stühler K, Beller M. 2017. A Luciferase-fragment Complementation Assay to Detect Lipid Droplet-associated Protein-Protein Interactions. Mol Cell Proteomics 16:329–345.

581. Jacobson RH, Zhang XJ, DuBose RF, Matthews BW. 1994. Three-dimensional structure of beta-galactosidase from E. coli. Nature 369:761–6.

582. Welply JK, Fowler A V., Zabin I. 1981. β-Galactosidase alpha-Complementation. J Biol Chem 256:6804–6810.

583. Martinez E, Bartolomé B, de la Cruz F. 1988. pACYC184-derived cloning vectors containing the multiple cloning site and lacZα reporter gene of pUC8/9 and pUC18/19 plasmids. Gene 68:159–162.

584. Cronan JE, Narasimhan ML, Rawlings M. 1988. Insertional restoration of β-galactosidase α-complementation (white-to-blue colony screening) facilitates assembly of synthetic genes. Gene 70:161–170.

585. Haima P, Venema G. 1990. An improved β-galactosidase α-complementation system for

molecular cloning in Bacillus subtilis. Gene 93:41–47.

586. Lin J, Vogt VM. 2000. Functional alpha-fragment of beta-galactosidase can be expressed from the mobile group I intron PpLSU3 embedded in yeast pre-ribosomal RNA derived from the chromosomal rDNA locus. Nucleic Acids Res 28:1428–1438.

587. Luo W, Miao J, Feng Z, Lu R, Sun X, Zhang B, Ding W, Lu Y, Wang Y, Chi X, Ge Y. 2018. Construction of a β-galactosidase-gene-based fusion is convenient for screening candidate genes involved in regulation of pyrrolnitrin biosynthesis in Pseudomonas chlororaphis G05. J Gen Appl Microbiol.

588. Holland AU, Munk C, Lucero GR, Nguyen LD, Landau NR. 2004. α-Complementation assay for HIV envelope glycoprotein-mediated fusion. Virology 319:343–352.

589. Karniely S, Rayzner A, Sass E, Pines O. 2006. α-Complementation as a probe for dual localization of mitochondrial proteins. Exp Cell Res 312:3835–3846.

590. Fang L, Landau NR. 2007. Analysis of Vif-induced APOBEC3G degradation using an α-complementation assay. Virology 359:162–169.

591. Fung P, Peng K, Kobel P, Dotimas H, Kauffman L, Olson K, Eglen RM. 2006. A Homogeneous Cell-Based Assay to Measure Nuclear Translocation Using β-Galactosidase Enzyme Fragment Complementation. Assay Drug Dev Technol 4:263–272.

592. Naqvi T, Lim A, Rouhani R, Singh R, Eglen RM. 2004. β Galactosidase Enzyme Fragment Complementation As a High-Throughput Screening Protease Technology. J Biomol Screen 9:398–408.

593. Broome AM, Bhavsar N, Ramamurthy G, Newton G, Basilion JP. 2010. Expanding the utility of β-galactosidase complementation: Piece by piece. Mol Pharm 7:60–74.

594. So PPL, Chen C Di, Abraham CR. 2011. Detection of amyloid-β protein precursor homo-interactions using beta-galactosidase enzyme fragment complementation. J Alzheimer's

Dis 26:647–655.

595. Charter NW, Horecka J, Loh C-Y, Doan A, Wehrman T, Olson KR. 2015. Rapid, Antibody-Free Detection of Recombinant Proteins on Blots Using Enzyme Fragment Complementation, p. 51–62. *In* Kurien, BT, Scofield, RH (eds.), Detection of Blotted Proteins.

596. Hardjasa A, Ling M, Ma K, Yu H. 2010. Investigating the Effects of DMSO on PCR Fidelity Using a Restriction Digest-Based Method. J Exp Microbiol Immunol 14:161–164.

597. Manibalan K, Mani V, Huang C-H, Huang S-T, Chang P-C. 2015. A new electrochemical substrate for rapid and sensitive in vivo monitoring of β-galactosidase gene expressions. Analyst 140:6040–6046.

# APPENDIX A - CHARACTERIZATION OF ENGINEERED β-GALACTOSIDASE ENZYME FOR PROTEIN FRAGMENT COMPLEMENTATION

## Introduction

Protein fragment complementation assays (PCAs), also known as enzyme fragment complementation (EFC), are based on the idea assembling fragments of an enzyme to reconstitute a functional protein. This phenomenon was first reported in 1958 for ribonuclease (571) and again in 1965 for β-galactosidase (β-gal) (572, 573). While PCAs have now been developed for enzymes such as β-lactamase (574, 575), Cre recombinase (576, 577), and luciferase (578–580), β-galactosidase remains the predominant enzyme used.

β-gal is an enzyme encoded by the *lacZ* gene in E.coli which hydrolyzes the glycosidic bonds of β-galactosides like lactose to yield monosaccharides. It is a tetrameric protein with four identical monomers of 1023 amino acids, each of which are comprised of five subdomains (581). The enzyme can be broken into two fragments called the ω and α fragments. ω fragments, like the M15 or M112 mutants, have a small N-terminal deletion 10-30 amino acids in length (582). Because these mutants exist as dimers, the deletion likely disrupts tetramer formation. α fragments, such as the CNBr2 fragment are the result of termination mutations that produce a small peptide in the N-terminal region which complements the deletion in ω fragments (582). Complementation of α and ω fragments (termed α-complementation) was first employed in molecular cloning to screen plasmid-transformed colonies, a technique called "blue/white screening" (583–585). It has also been employed in mutational analysis (586, 587) and has been used to investigate protein-protein interactions for *in vitro* (588), *in vivo* (589–591), and drug discovery analysis (592). More recently, α-complementation of β-gal was used for diagnostic purposes (593–595), but these *in vivo* and Western blot analyses are too complex and laborious for regular clinical use. Furthermore, while the use of two distinct fragments is useful for

investigating the interaction of two proteins which can be individually conjugated, it complicates diagnostic assays in which a singular analyte is of interest. In this work, we have designed and characterized a novel β-gal mutant with a single mutation that splits the enzyme into two identical, reconstitutable fragments for PCA analysis. Although this research may be incorporated into a biosensor design at a later time, it does not describe a novel electrochemical sensor and has thus been incorporated as an appendix.

## Materials and Methods

### *Materials*

All primers were ordered from Integrated DNA Technologies and resuspended at 1 μg/mL in water. β-gal plasmid (pSF-OXB20-COOH-TEV-BetaGal-6His, catalog number OG3011) was purchased from Oxford Genetics. X-gal (5-Bromo-4-chloro-3-indoxyl-beta-D-galactopyranoside) was purchased from Gold Biotechnology (Cat# X4281C) and diluted according to the manufacturer protocol. PFU Turbo DNA Polymerase was purchased from Agilent (Cat#600250-52). dNTP solution (Cat#NO447S) and DpnI (Cat#R0176S) were purchased from New England BioLabs. Kanamycin monosulfate was purchased from Fisher BioReagents (Cat#BP906-5), imidazole was purchased from Spectrum (CAS 288-32-4). Dimethyl sulfoxide (DMSO) (Cat# 472301-500ML), Trizma hydrochloride (Tris-HCl, Cat# T5941-500G), and glycerol (Cat# G7893-500ML) were purchased from Sigma-Aldrich. NaCl was purchased from Fisher Chemical (Cat# S271-3). HisPur Ni-NTA Superflow Agarose beads were purchased from ThermoScientific (Prod# 25215). A His-Trap HP 5mL column (Cat# GE29-0510-21) was used for affinity purification and a HiLoad Superdex gel filtration column (Cat# 28-9892-35) was used for size exclusion purification on an AKTA Pure FPLC (GE Healthcare). An Applied Biosystems 2720 Thermocycler was used for mutagenesis and a PerkinElmer Victor X5 2030 Multilabel Reader was used for absorbance measurements. A

NanoDrop 2000c spectrophometer (ThermoScientific) was used for spectrophotometric quantification of protein.

*Site Directed Mutagenesis*

Primers were designed to introduce five independent mutations into the β-gal enzyme and are listed in Table 5.1. Each primer was designed to be 21-34 base pairs (bp) in length and have a GC clamp at both ends. A 50 µL reaction mix with final concentrations of 1× PFU Buffer, 2.5 ng/mL forward (F) primer, 2.5 ng/mL reverse (R) primer, X dNTPs, 50 ng of β-gal plasmid (pBG612R), 20× DMSO, and 2.5 U PFU Turbo. Polymerase chain reaction (PCR) was then performed in a thermocycler with the following conditions:

1. 95˚C for 2 minutes
2. 95˚C for 50 seconds
3. 55˚C for 1 minute
4. 68˚C for 8 minutes
5. Repeat 18× steps 2-4
6. 68˚C for 5 minutes

1µL of DpnI restriction enzyme, which digests methylated DNA, was added directly to the PCR product to remove original, unmutated plasmid and incubated for one hour at 37˚C. 1 µL of the digested product was then transformed directly in Dh5α cells and plated on kanamycin plates with 200 µg/mL X-gal substrate. The plates were incubated overnight at 37˚C and colonies selected for analysis were amplified in a 5 mL overnight culture after which mutant plasmids were isolated and purified by miniprep and sent for sequencing analysis at Genewiz using the primers listed in Table A2.

*Protein Purification and Characterization*

To purify wild type (WT) and mutant β-gal enzyme, plasmid was transformed into Dh5α cells and amplified with either a 50 mL or 750 mL culture for batch prep or FPLC protein purification. As the plasmid has a constitutive promoter, no induction step was necessary.

For batch prep purification, 50 mL cultures were centrifuged at 3700 rpm for 20 minutes. The bacterial pellet was resuspended in 10 mL low imidazole buffer (LIB – 50 mM Tris, 400 mM NaCl, 10 mM imidazole, 5% glycerol) and the sample was sonicated ten times for thirty seconds with one minute in between each sonication. The lysate was then centrifuged at 10,000 rpm for 30 minutes at 4˚C. 100 µL of nickel agarose beads were washed with 5 mL LIB and clarified lysate was added to the beads and tumbled overnight at 4˚C. The beads were then centrifuged at 1000 rpm for five minutes, resuspended in 2 mL LIB, and added to a spin column. A lab-made vacuum was used to pull the sample through the spin column and the column was washed three times with 1 mL LIB. 50 µL of 1:1 LIB:HIB (high imidazole buffer – 50 mM Tris, 400 mM NaCl, 500 mM imidazole, 5% glycerol) was added to the column to elute the protein which was quantified using a Nanodrop 2000c.

For FPLC protein purification, 750 mL bacterial cultures were grown overnight at 37˚C and centrifuged at 5000 rpm for 20 minutes and the pellet was resuspended with LIB. The pellet was then microfluidized and clarified and purified with a Ni column and gel filtration (GF) column using an AKTA Pure FPLC.

PAGE analysis was used to validate the purification. Enzymatic assays were used to characterize the enzymatic activity of WT and mutant β-gal enzymes. Diluted protein and X-gal substrate was combined as indicated and absorbance was measured at 595 nm.

**Table A1. Quick Change Mutagenesis Primers**

| Mutation | Identification Number | Sequence |
|---|---|---|
| R13A (F) | BG998 | 5'CCCGTCGTTTTACAAGCTCGTGACTGGGAAAACC |
| R13A (R) | BG999 | 5'GGTTTTCCCAGTCAGCTTGTAAAACGACGGG |
| D15A (F) | BG1000 | 5'CGTTTTACAACGTCGTGCCTGGGAAAACCCTGGC |
| D15A (R) | BG1001 | 5'GCCAGGGTTTTCCCAGGCACGACGTTGTAAAACG |
| S477A (F) | BG1009 | 5'GGATCAAAGCTGTCGATCCTTCC |
| S477A (R) | BG1010 | 5'GGAAGGATCGACAGCTTTGATCC |
| R473A (F) | BG1011 | 5'GCTCTATGCCTGGATCAAATCTGTCG |
| R473A (R) | BG1012 | 5'CGACAGATTTGATCCAGGCATACAGC |
| R431A (F) | BG1013 | 5'CGATGATCCGGCCTGGCTACC |
| R431A (R) | BG1014 | 5'GGTAGCCAGGCCGGATCATCG |

**Table A2. β-galactosidase Sequencing Primers**

| Plasmid Location (bp) | Identification Number | Sequence |
|---|---|---|
| 251-272 | BG1004 | 5'GCTTGCTCTAGCCAGCTATGG |
| 998-1020 | BG1005 | 5'CGTTTGTTCCCACGGAGAATCC |
| 1759-1781 | BG1006 | 5'GGTCATGGATGAGCAGACGATGG |
| 2605-2626 | BG1007 | 5'CGATAACGAACTCCTGCATTGG |
| 3391-3413 | BG1008 | 5'CCTTACTGCCGCCTGTTTTGACC |

## Results and Discussion

Several polar or charge-charge interactions hold the two dimers of the β-gal tetramer together. By mutating the amino acids involved in these interactions, the interaction is broken and the connections are no longer strong enough to hold the dimers together in solution. However, by tethering the mutant dimers to a surface in close proximity with one another, they may be able to re-associate and reconstitute enzymatic activity. These mutant dimers can then be conjugated to single chain antibody fragments or DNA oligo probes which will bind to a diagnostic marker such as a virus particle or genome and tether the dimers in close enough proximity to produce an enzymatic signal corresponding to target concentration.

The positively charged arginine (R) 13 interacting with negatively charged aspartic acid (D) 15 was chosen for preliminary mutagenesis analysis. Both amino acids were independently

mutated to a hydrophobic alanine to break the charge-charge interaction. Because DMSO is commonly used in PCR to relieve secondary structure and supercoiling of the plasmid template (596), the mutagenesis was compared with and without DMSO. Dh5α cells were transformed with the mutagenesis product and grown on plates infused with X-gal, a lactose analog that is cleaved by β-gal to produce a blue product. Three colony phenotypes were expected based on the effect of the enzyme mutation: blue colonies are expected to have no effect on activity from the mutation, light blue colonies are expected to have attenuated activity, and white colonies are expected to have killed activity as a result of the mutation. Initial mutagenesis results as shown in Figure A1a demonstrated zero to low yield for both mutations with little observed difference with DMSO. Both the R13A and D15A mutagenesis reactions with DMSO yielded a singular blue colony. The D15A (-) DMSO reaction did not yield any colonies while the R13A (-) DMSO yield four colonies, half blue and half white. A white colony (R13A_W) was chosen for batch prep purification and enzymatic characterization. Briefly, a 10 µL reaction with 1 mg/mL X-gal and either 0.5 mg/mL R13A_W or 1.1 mg/mL WT protein was incubated for 30 minutes. The qualitative analysis depicted in Figure A1c shows that, as expected from a white colony, the R13A_W mutant did not exhibit any enzymatic activity compared to the WT. To test if enzyme activity could be reconstituted, the 10 µL reaction was combined with 10 µL of washed Ni beads. However, as shown in Figure A1c, no blue product was produced indicating that the enzyme could not be reconstituted.

The mutagenesis was repeated and demonstrated higher yield for the R13A mutant with and without DMSO (Figure A2). Two blue colonies and the single white colony were selected from the R13A (+) DMSO plate and sent for sequencing analysis. Sequencing results indicated that all three plasmids possessed the R13A mutation, but the white colony had additional nonspecific mutations that killed enzymatic activity. Because the other two plasmids yielded

blue phenotypes with full activity, it is likely that the disrupted interaction was not sufficient to break the connection between the dimers.

Three other dimer interactions were identified including the interaction between serine (S) 477 and D469, R473 and threonine (T) 494, and R431 and R26 (which is part of the protein backbone). The mutagenesis was again compared with and without DMSO which produced similar yield. 10 colonies with B, LB, and W phenotypes as circled in Figure A3a and listed in Table A3 were selected for preliminary sequencing analysis. Of the 10 plasmids, only two had successful mutagenesis and these plasmids were sent for full sequencing analysis which unfortunately revealed an extra nonspecific mutation. The mutagenesis was repeated without DMSO and B and W colonies (circled in Figure A5b) were selected from each plate for sequencing analysis. As shown in Table A4, only three plasmids, R473A_W, R473A_B, and S477A_B, had the correct mutation without additional nonspecific mutations. After transformation into Dh5α cells, both R473A _B and S477A_B exhibited B phenotypes as expected while R473A_W exhibited LB phenotype (Figure A3c). Protein was purified by batch prep and a 100 µL reaction of 1 mg/mL X-gal and 5× stock protein (which ranged 71 – 143 µg/mL) was incubated for 15 minutes for enzymatic analysis as shown in Figure A4.

**Table A3. Mutagenesis and sequencing results for R473A, R431A, and S477A mutants**

| Mutation | Phenotype | Plate (+/- DMSO) | Sequencing Analysis |
|---|---|---|---|
| R473A | W | (-) | Nonspecific mutations |
| R473A | B | (-) | No mutation |
| R473A | LB | (+) | Nonspecific mutations |
| R431A | W | (-) | Nonspecific mutations |
| R431A | LB | (-) | Successful |
| R431A | W | (+) | Nonspecific mutations |
| R431A | B | (+) | No mutation |
| S477A | W | (-) | Nonspecific mutations |
| S477A | B | (-) | No mutation |
| S477A | LB | (+) | Successful |

**Table A4. Repeated mutagenesis and sequencing results for R473A, R431A, and S477A mutations**

| Mutation | Phenotype | Sequencing Analysis |
|---|---|---|
| R473A | W | Successful |
| R473A | B | Successful |
| R431A | W | Nonspecific mutations |
| R431A | B | Nonspecific mutations |
| S477A | W | Nonspecific mutations |
| S477A | B | Successful |

The R473A_B mutant showed strong activity compared to the other mutants which had almost no enzymatic activity. Based on the gel analysis in Figure A4c, it is unsurprising that R473A_W had no activity, as it does not appear to be expressed. It is interesting, however, that the S477A_B mutant had no activity in solution. Gel analysis and spectrophotometry results confirm that there was double the amount (143 μg/mL vs 71 μg/mL) of S477A_B in the stock solution. The discrepancy between the B phenotype and no activity in solution could be explained by reconstitution of otherwise attenuated enzyme activity at sufficiently high intracellular concentrations. Because S477A_B was highly expressed, had a B phenotype in bacterial culture, but did not exhibit activity in solution, it was concluded that this mutant exhibited desirable properties for a protein complementation assay.

A larger protein prep was prepared by affinity column and gel filtration. As shown in Figure A5a, the larger WT protein (~540 kDa) comes off the GF column in a single large peak. If the tetramer connections are disrupted in the S477A_B, the protein will likely exist in the smaller (~270 kDa) dimeric form). This is evidenced by the GF trace in Figure A5b, which shows a second peak after the void volume corresponding to the mutant protein. To examine the relationship between enzymatic activity and concentration, S477A_B was serially diluted and combined with X-gal substrate. As shown in Figure A7a, the enzyme does not exhibit activity until it has reached a final concentration of 0.6 μg/mL. To test if the mutant could be used for protein complementation, 60 ng/mL of His-tagged protein was combined with a serial dilution of

Ni beads and a strong linear response was obtained (Figure A7b). These data indicate that the S477A_B mutant can be used for protein complementation-based detection of target biomolecules such as virus particles or viral nucleic acid.

## Conclusion

β-galactosidase has been used for decades in protein fragment complementation assays to characterize protein-protein interactions, facilitate drug discovery, and screen bacterial colonies for successful plasmid transformation. These assays use α-complementation of the larger ω fragment with the small α peptide fragment. However, two distinct fragments complicate analysis when only one analyte is being studied for diagnostic purposes. In this study, we have introduced a singular mutation to change a polar serine into a hydrophobic alanine which splits the enzyme into two identical fragments. These identical fragments may then be attached to single chain antibodies or DNA oligos which bind to large analytes such as virus particles or viral nucleic acid. The β-gal fragment-conjugated probes (antibody or oligo) bind to their analyte and are therefore tethered in close proximity to one another and allows close fragments to associate with one another and reconstitute activity. The ability of the S477A mutant to reconstitute activity was confirmed use Ni beads as a proof of concept. Furthermore, β-gal substrates like 4-Methoxyphenyl-β-galactopyranoside (4-MPGal) which yield electrochemical reporters like 4-methoxy phenol (4-MP) can be used for electrochemical determination of analyte (597). Compared to absorbance-based methods, electrochemical detection has better sensitivity and it is easily miniaturized into handheld devices for lab-on-chip or paper-based biosensors (513, 514).

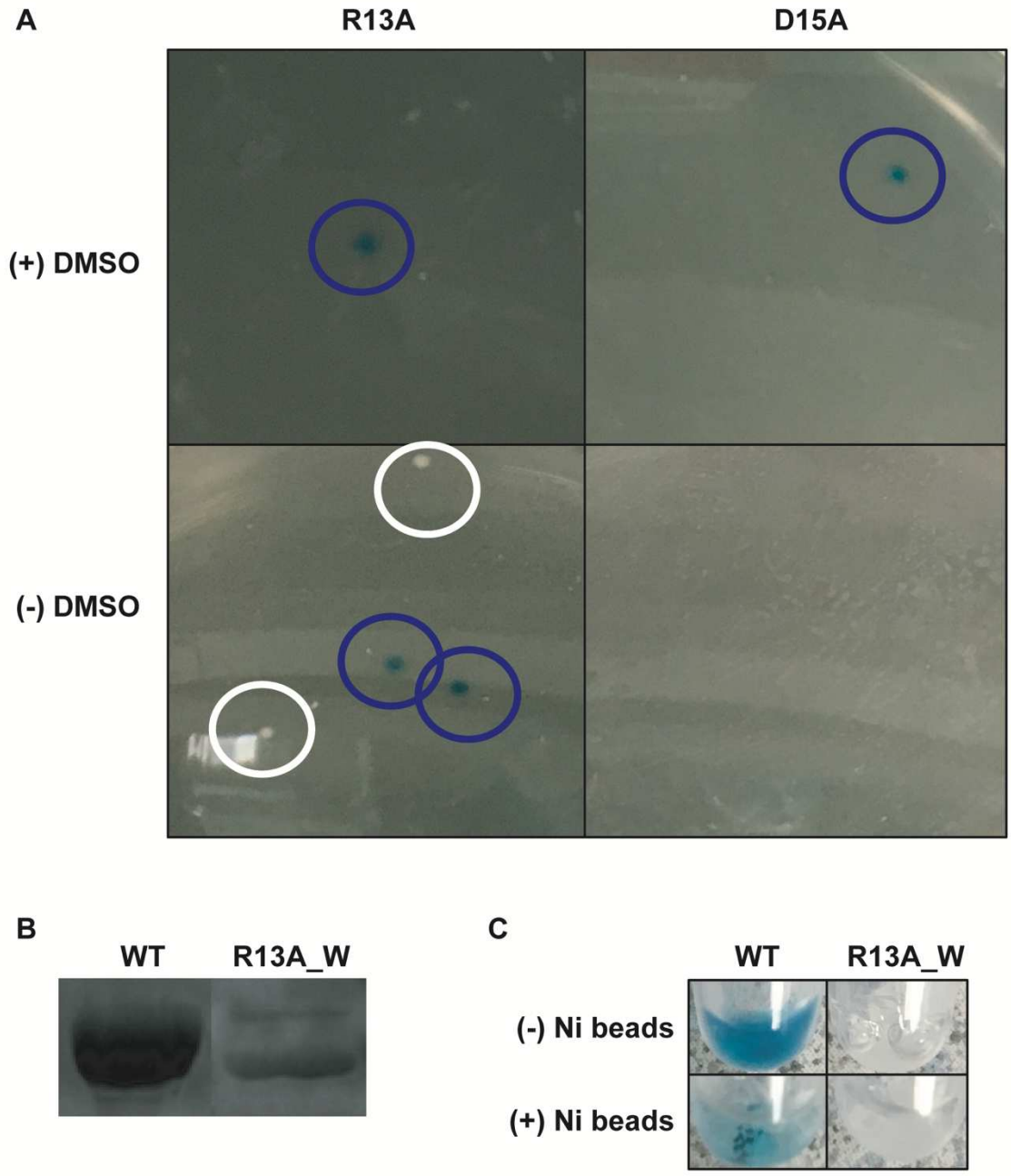


**Figure A1. Characterization of R13A and D15A mutants.** A) Mutagenesis yield was compared with and without DMSO for both R13A and D15A mutants. B) A white colony (R13A_W) was batch purified and validated with PAGE analysis. C) The R13A_W mutant was tested for enzymatic activity and compared with the WT protein. Capacity for reconstitution of mutant activity was tested by combining the enzyme with Ni beads.

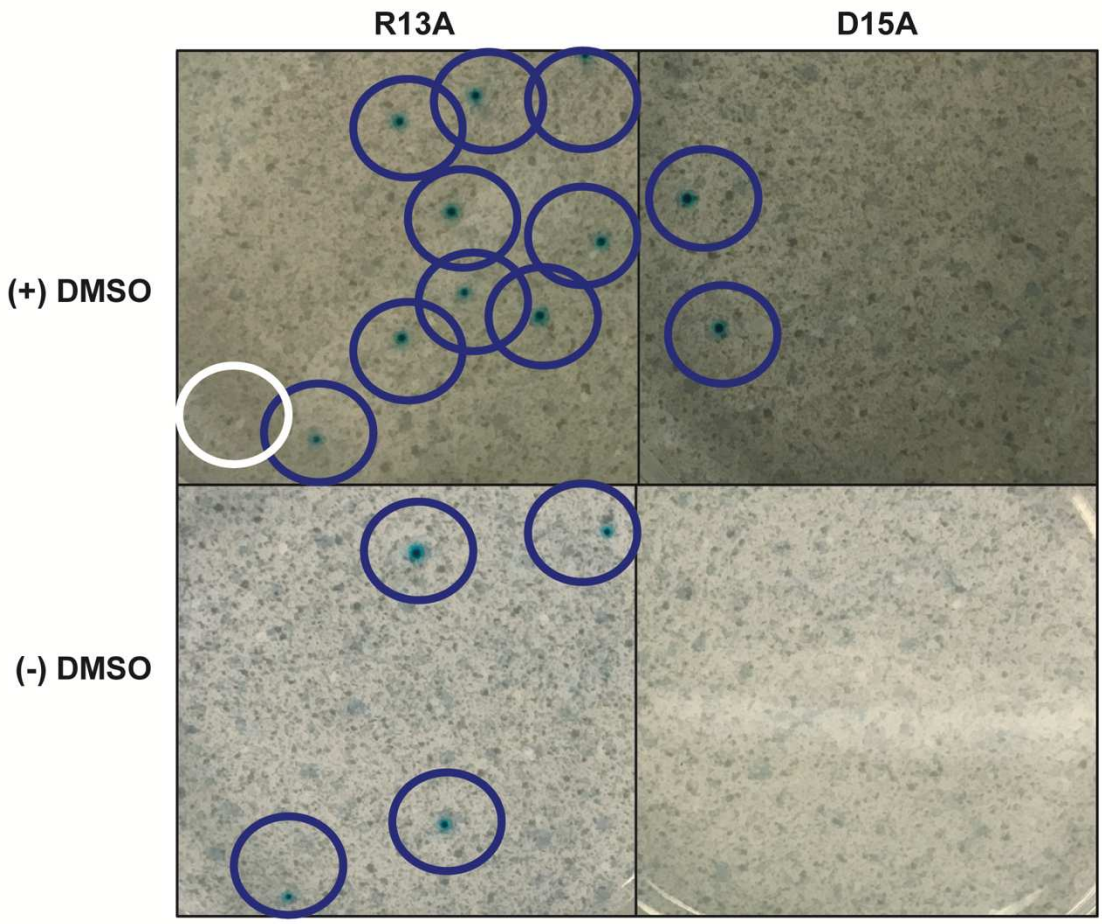


**Figure A2. Repeat of R13A and D15A mutagenesis.** Two blue colonies and the single white colony were selected from the R13A (+) DMSO plate and sent for sequencing analysis which indicated that all three plasmids possessed the R13A mutation, but the white colony had additional nonspecific mutations that killed enzymatic activity.

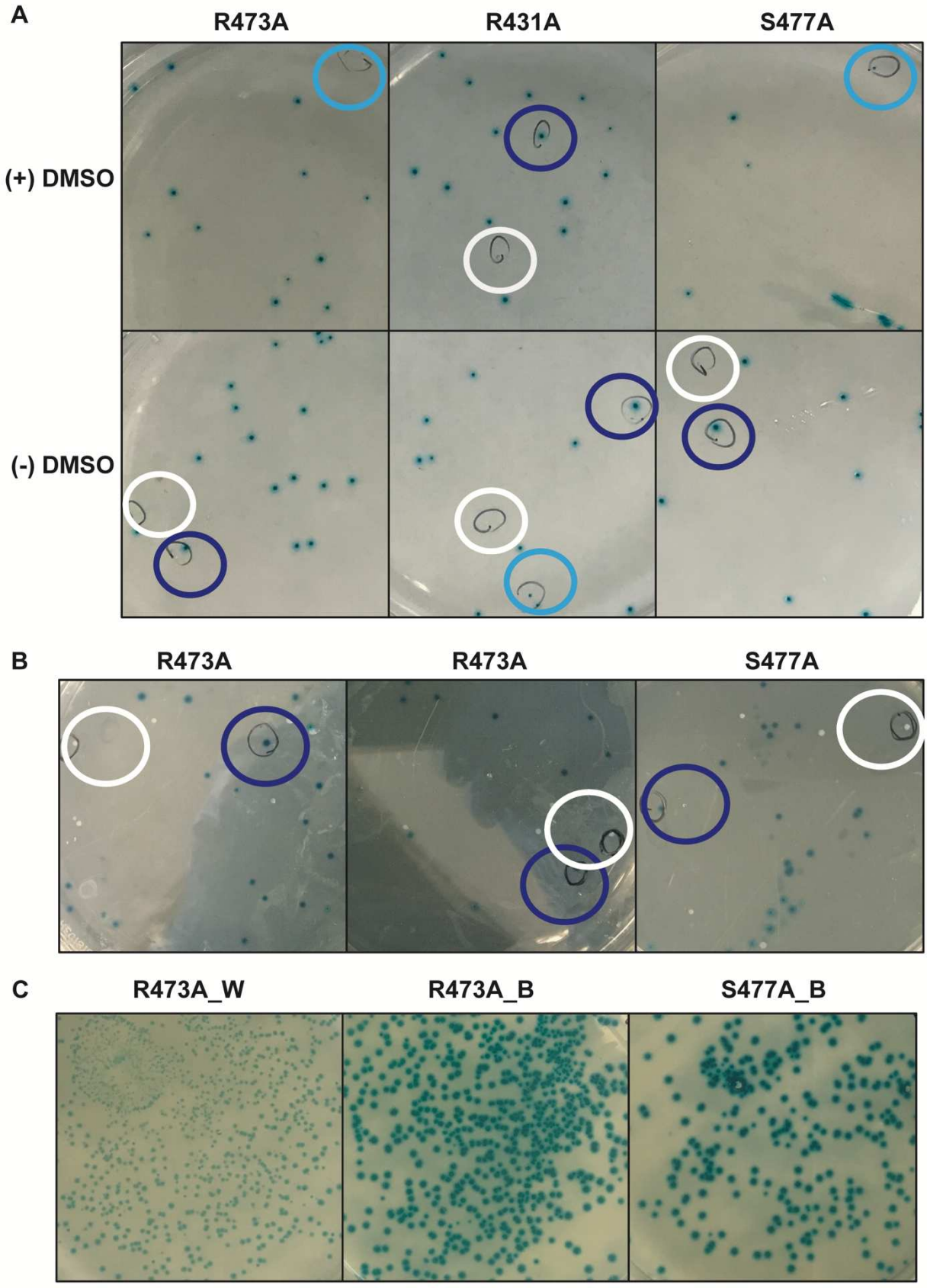
A
R473A
R431A
S477A
(+) DMSO
(-) DMSO
B
R473A
R473A
S477A
C
R473A_W
R473A_B
S477A_B

**Figure A3. Selection of R473A, R431A, and S447A mutants.** A) Ten colonies were selected for sequencing analysis which indicated unsuccessful or nonspecific mutations in all cases. B) The mutagenesis was repeated and B and W colonies were selected for each mutant and sent for sequencing. C) Three colonies demonstrated successful mutation incorporation and these plasmids were isolated and retransformed into bacteria. Surprisingly, R473A_W demonstrated a LB phenotype while R473A_B and S477A_B had B phenotypes as expected.

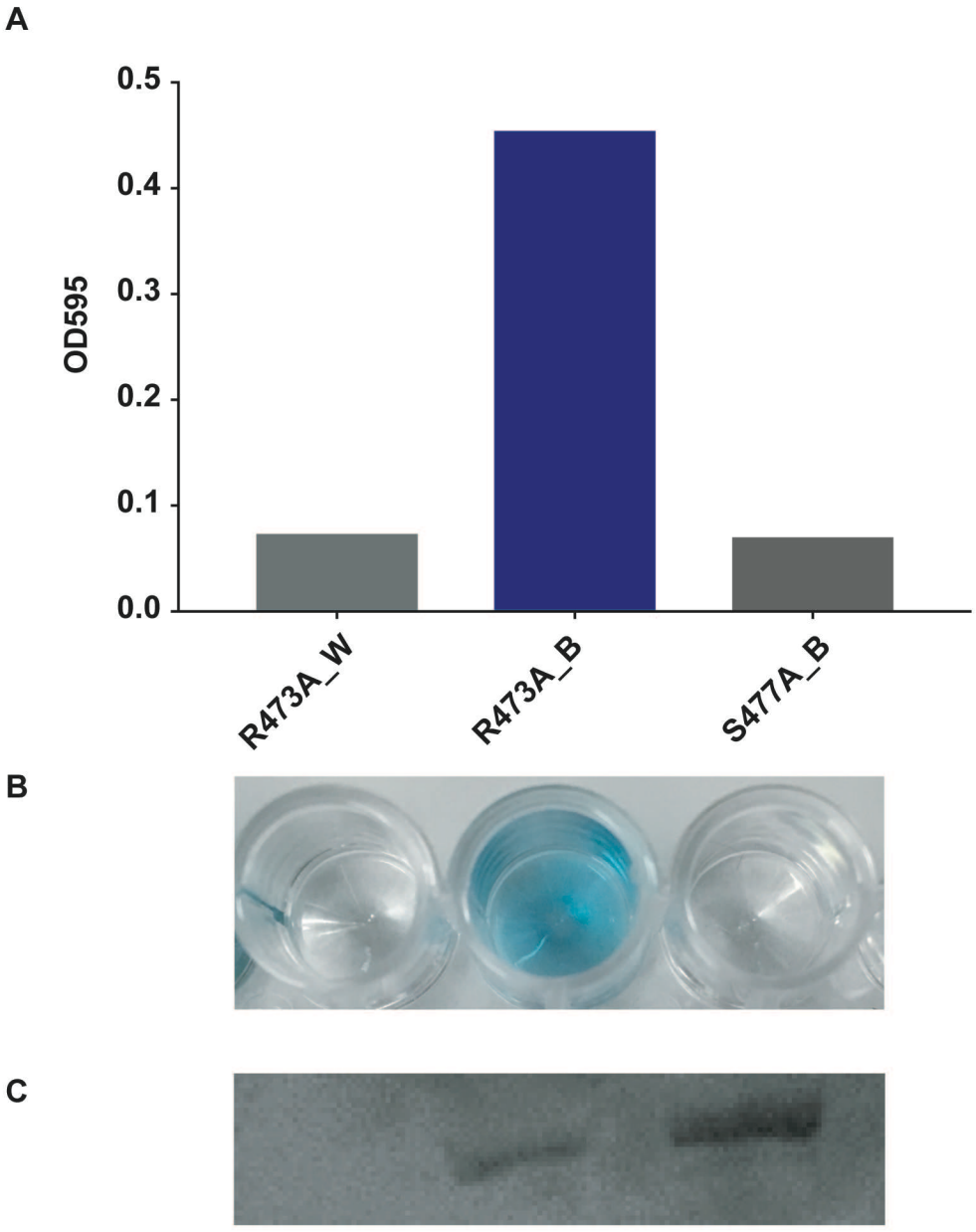


**Figure A4. Characterization of selected mutants.** A-B) Absorbance and colorimetric analysis of mutant β-gal activity. C) PAGE validation of purified mutant protein.

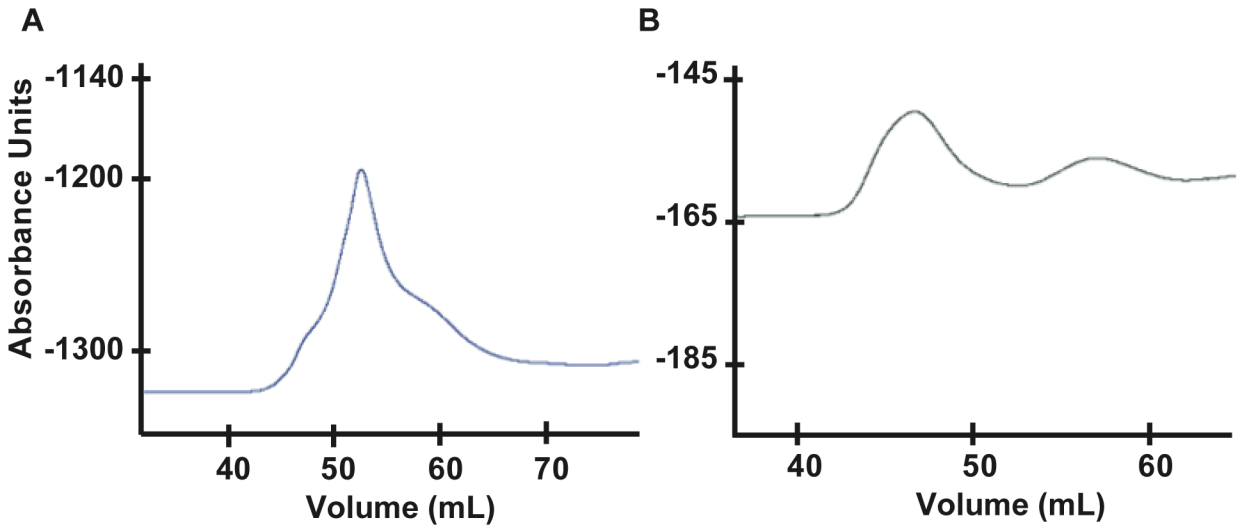


**Figure A5. Gel-filtration analysis** of A) WT β-gal and B) S477A_B mutant β-gal

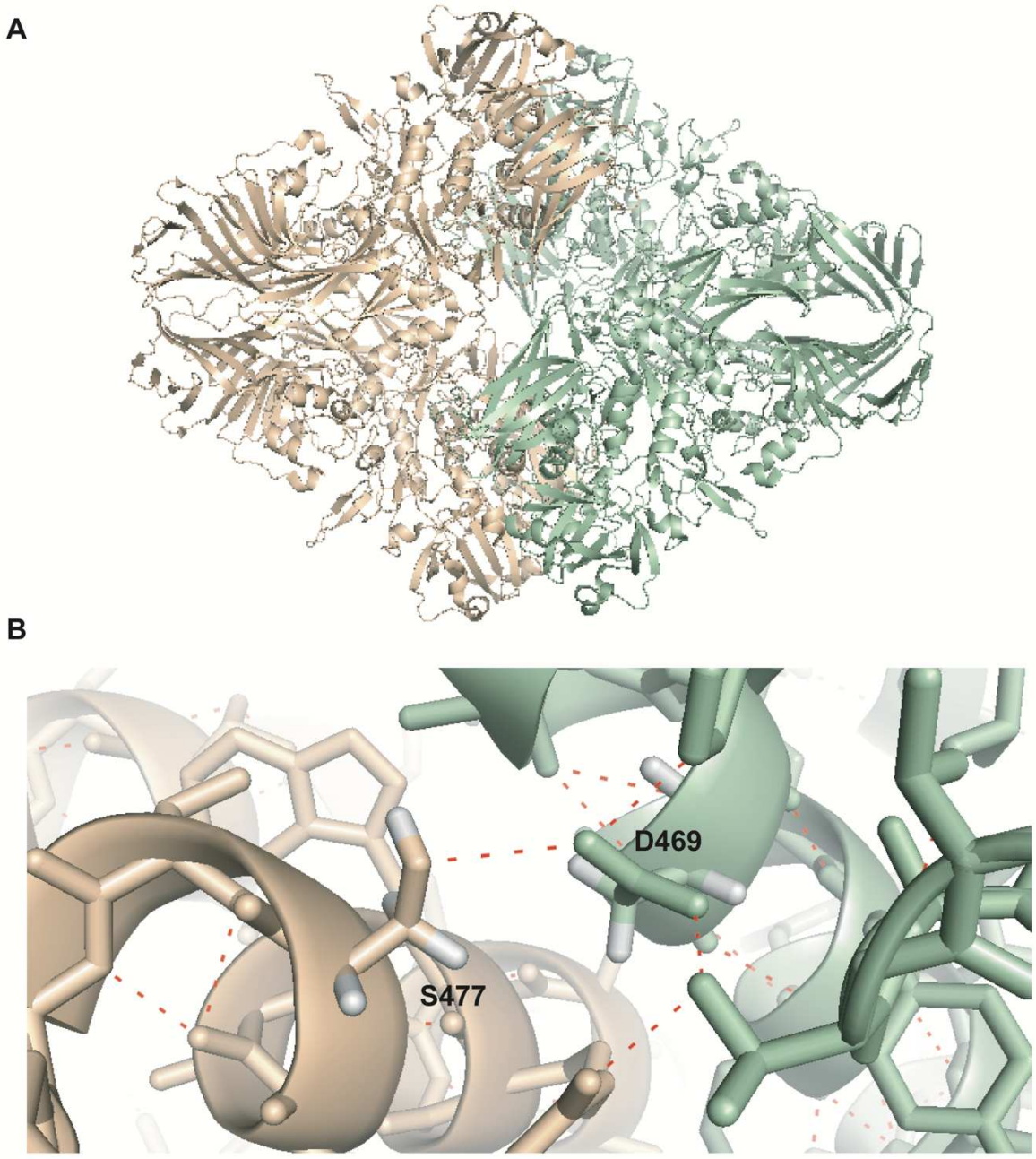


**Figure A6. Schematic of β-galactosidase.** A) WT β-gal tetramer (first dimer in tan, second dimer in green). B) Interaction of S477 with D469 which is involved in tetramerization.

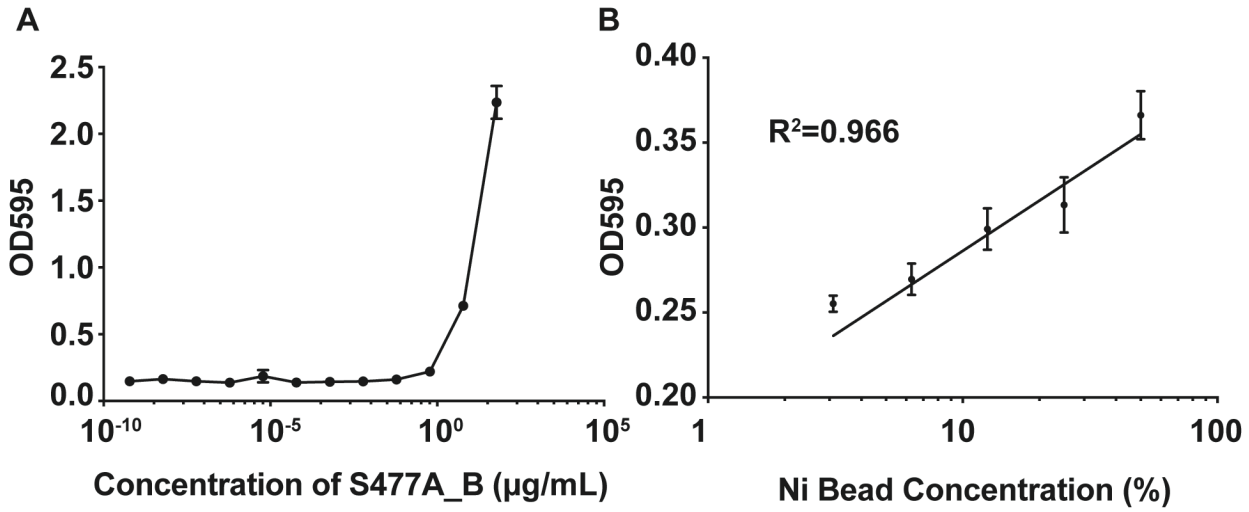


**Figure A7. Enzymatic analysis of S477A_B.** A) Concentration curve of S477A_B mutant β-gal. B) Reconstitution analysis of mutant S477A_B β-gal using Ni beads which bind the dimer's His-tag. (mean ± SEM)